

Three Dimensional Ultrasound Elasticity Imaging

by

Jeffrey Michael Abeysekera

B.A.Sc., The University of British Columbia, 2008

M.A.Sc., The University of British Columbia, 2010

A THESIS SUBMITTED IN PARTIAL FULFILLMENT
OF THE REQUIREMENTS FOR THE DEGREE OF

Doctor of Philosophy

in

THE FACULTY OF GRADUATE AND POSTDOCTORAL STUDIES
(Mechanical Engineering)

The University of British Columbia
(Vancouver)

April 2016

© Jeffrey Michael Abeysekera, 2016

Abstract

Changes in tissue elasticity are correlated with certain pathological changes, such as localized stiffening of malignant tumours or diffuse stiffening of liver fibrosis or placenta dysfunction. Elastography is a field of medical imaging that characterizes the mechanical properties of tissue, such as elasticity and viscosity. The elastography process involves deforming the tissue, measuring the tissue motion using an imaging technique such as ultrasound or magnetic resonance imaging (MRI), and solving the equations of motion. Ultrasound is well suited for elastography, however, it presents challenges such as anisotropic measurement accuracy and providing two dimensional (2D) measurements rather than three dimensional (3D). This thesis focuses on overcoming some of these limitations by improving upon methods of imaging absolute elasticity using 3D ultrasound. In this thesis, techniques are developed for 3D ultrasound acquired from transducers fitted with a motor to sweep the image plane, however many of the techniques can be applied to other forms of 3D acquisition such as matrix arrays. First, a flexible framework for 3D ultrasound elastography system is developed. The system allows for comparison and in depth analysis of errors in current state of the art 3D ultrasound shear wave absolute vibro-elastography (SWAVE). The SWAVE system is then used to measure the viscoelastic properties of placentas, which could be clinically valuable in diagnosing preeclampsia and fetal growth restriction. A novel 3D ultrasound calibration technique is developed which estimates the transducer motor parameters for accurate determination of location and orientation of every data sample, as well as for enabling position tracking of a 3D ultrasound transducer so multiple volumes can be combined. Another calibration technique using assumed motor parameters is developed, and an improvement to an existing N-wire method is presented. The SWAVE

research system is extended to measure shear wave motion vectors with a new acquisition scheme to create synchronous volumes of ultrasound data. Regularization based on tissue incompressibility is used to reduce noise in the motion measurements. Lastly, multiple ultrasound volumes from different angles are combined for measurement of the full motion vector, and demonstrating accurate reconstructions of elasticity are feasible using the techniques developed in this thesis.

Preface

This thesis is primarily based on several manuscripts and conference proceedings, resulting from collaboration of multiple researchers. All publications have been modified to make the thesis coherent.

The work in Chapter 2 was the result of the collaboration of multiple researchers. The author's contribution was designing and building the ultrasound motor controller, helping determine the program structure, developing the ultrasound acquisition and GUI modules, evaluating the phasor measurement accuracy and sensitivity through simulation, and writing the chapter. Julio Lobo helped determine the program structure, tested different experimental configurations, and collected the experimental repeatability measurements. Dr. Hani Eskandari helped determine the program structure and helped developed the software. Dr. Reza Zahiri and Weiqi Wang were the primary developers of the radio frequency (RF) motion tracking C++ and CUDA code. Dr. Ali Baghani and Nabil Lathiff were the primary developers of the phasor fitting and local frequency estimation (LFE) C++ and CUDA code. Dr. Robert Rohling and Dr. Tim Salcudean developed the main research ideas behind the project and provided helpful guidance.

The work in Chapter 3 included a study of human placenta (H15-00974) performed under written informed consent (see Appendix B) after approval by the UBC Children's and Women's Research Ethics Board. The research was the result of the collaboration of multiple researchers. The author's contribution was in helping design the experimental protocol, helping collect experimental data, processing and analysing the data, and writing the chapter. Mehran Pesteie helped design the experimental protocol and helped collect experimental data. Manyou Ma helped collect experimental data. Ashton Ellis and Tamsin Tarling obtained consent from the pa-

tients. Dr. Denise Pugash provided radiology support at BC Women’s Hospital. Support for the elastography system was led by Tim Salcudean and Julio Lobo. Dr. Jeff Terry coordinated placenta handling at BC Women’s Hospital and provided information on placenta anatomy and pathology. Dr. Robert Rohling developed the main research ideas behind the project, helped design the experimental protocol, and provided useful suggestions.

A version of Chapter 4 has been published in

J. M. Abeysekera, M. Najafi, R. Rohling, and S. E. Salcudean, “Calibration for position tracking of swept motor 3-D ultrasound”, *Ultrasound in medicine and biology*, vol. 40, no. 6, pp. 1356–1371, 2014

The author’s contribution in that paper was developing the idea, implementing the methods, verifying the methods through numerical simulations and experiments, and writing the manuscript. Dr. Mohammad Najafi provided the code for his previously published two dimensional (2D) calibration algorithm and the computer-aided design (CAD) file for the calibration phantom. Dr. Robert Rohling and Dr. Tim Salcudean assisted with their suggestions and contributed toward editing the manuscript.

A portion of Chapter 5 was orally presented and published in the conference proceedings in

J. Abeysekera, R. Rohling, and S. Salcudean, “Vibro-elastography: Absolute elasticity from motorized 3D ultrasound measurements of harmonic motion vectors”, in *IEEE International Ultrasonics Symposium*, 2015, pp. 1–4

In addition, another portion of Chapter 5 has also been submitted for publication as

J. M. Abeysekera, M. Honarvar, R. Rohling, and S. E. Salcudean, “3D ultrasound shear wave absolute vibro-elastography (SWAVE) from full vector motion field measurements”, submitted

The author’s contribution was developing the idea, implementing the methods, verifying the methods through experiments, and writing the manuscript. Dr. Mohammad Honarvar reprocessed the experimental measurements using his own inversion

algorithm. Dr. Robert Rohling and Dr. Tim Salcudean assisted with their suggestions and contributed toward editing the manuscript.

A portion of Chapter 6 was orally presented and included in the conference proceedings in

J. M. Abeysekera, M. Honarvar, S. E. Salcudean, and R. Rohling,
“Combining axial measures to estimate 3D motion over an ultrasound
volume”, in *Twelfth International Tissue Elasticity Conference*, 2013,
p. 101

The author’s contribution was developing the idea, implementing the methods, verifying the methods through simulation, and writing the manuscript. Dr. Mohammad Honarvar processed the simulation results using his own inversion algorithm. Dr. Robert Rohling and Dr. Tim Salcudean assisted with their suggestions and contributed toward editing the manuscript.

Table of Contents

Abstract	ii
Preface	iv
Table of Contents	vii
List of Tables	xii
List of Figures	xiii
Glossary	xix
Acknowledgments	xxii
1 Introduction	1
1.1 Motivation	1
1.2 Hypothesis	5
1.3 Thesis Outline	6
1.4 Ultrasound Background	8
1.4.1 Reflection	10
1.4.2 Scattering	11
1.4.3 Transducers	11
1.4.4 Beamforming	13
1.4.5 Image Formation	18
1.4.6 Doppler	21
1.5 Elastography Background	29

1.5.1	Theory	30
1.5.2	Additional Modelling Considerations	33
1.5.3	Motion Measurement	35
1.5.4	Elasticity Estimation	42
1.6	Ultrasound Spatial Calibration Background	59
1.6.1	Calibration Methods	60
1.6.2	Position Tracking	63
2	Development and Analysis of a 3D System for Absolute Elasticity Measurement	69
2.1	Introduction	69
2.2	Methods	72
2.2.1	System Overview	72
2.2.2	Software Design	74
2.2.3	Ultrasound Interface	74
2.2.4	Motor Control	76
2.2.5	Excitation	78
2.2.6	Sampling Sequences	79
2.2.7	Motion Estimation	81
2.2.8	Phasor Fitting	81
2.2.9	Phasor Compensation	83
2.2.10	Synchronization	85
2.2.11	Elasticity Estimation	86
2.3	Simulations	88
2.4	Experiments	91
2.4.1	Motor Attenuation	91
2.4.2	Phasor Synchronization	92
2.4.3	Elasticity Repeatability	93
2.5	Results	95
2.5.1	Phasor Fitting Results	95
2.5.2	Motor Attenuation Results	100
2.5.3	Phasor Synchronization Results	100
2.5.4	Elasticity Repeatability Results	107

2.6	Discussion	109
2.7	Conclusion	112
3	Viscoelastic Characterization of <i>Ex Vivo</i> Placenta Tissue Using SWAVE	114
3.1	Introduction	114
3.2	Methods	116
3.2.1	Rheological Modelling	119
3.3	Results	123
3.4	Discussion	128
3.5	Conclusion	134
4	Spatial Calibration of Swept 3D Ultrasound	136
4.1	Introduction	136
4.2	Methods	141
4.2.1	Data Acquisition	141
4.2.2	N-wire Calibration (N_{2D} , N_{3D} , and N_{3D}^{Full})	143
4.2.3	Planar Calibration (P_{3D})	147
4.2.4	Wedge Calibration on 2D Slices and then Fitting ($W_{2D \rightarrow 3D}$)	151
4.2.5	Validation of the Calibration Methods	154
4.3	Results	156
4.4	Discussion	159
4.5	Conclusion	161
5	Measurement of the Full Shear Wave Motion Vector in SWAVE	163
5.1	Introduction	163
5.2	Methods	169
5.2.1	Synchronization	169
5.2.2	Displacement Estimation	169
5.2.3	Displacement Regularization	172
5.2.4	Elasticity Reconstruction from LFE	174
5.2.5	Elasticity Reconstruction from shear-FEM	175
5.2.6	Phantom Experiment	176
5.2.7	Reconstruction Performance Evaluation	179
5.3	Results	180

5.4	Discussion	188
5.5	Conclusion	195
6	Combining Multiple Views for Increased Accuracy of the Full Shear	
	Wave Motion Vector in SWAVE	197
6.1	Introduction	197
6.2	Methods	199
	6.2.1 Finite Element Simulation	199
	6.2.2 Simulating Displacement Measurements	200
	6.2.3 Solving for 3D Displacement	204
	6.2.4 Simulating Calibration Error	206
	6.2.5 Elasticity Inversion	208
6.3	Results	210
6.4	Discussion	211
6.5	Conclusion	216
7	Conclusion	217
7.1	Summary	217
7.2	Contributions	220
7.3	Limitations	222
7.4	Future Work	223
	Bibliography	226
A	Index Notation	264
B	Placenta Study Consent Form	266
C	N-wire Ambiguity	273
D	Logarithm and Exponential Maps of Dual Quaternions	277
E	Solving for Geodesic Direction on the Quaternion Manifold	279
F	Simulation Test of Rotation Fitting Algorithm	284

G	Linear Least Squares Displacement Gradient	287
----------	---	------------

List of Tables

Table 1.1	Commercially available ultrasound elastography systems. . . .	3
Table 1.2	Technical specifications of common position tracking systems. . . .	66
Table 3.1	Rheological model parameters and root mean square (RMS) error corresponding to the fits to the shear wave speed dispersion for six placenta samples	130
Table 4.1	Standard deviations of the three translation degree(s) of freedom (DOF) (mm) and three rotation DOF (degrees) after 10 trials using a single data set for calibration.	157
Table 5.1	Manufacturer specifications for the CIRS Model 049 elasticity quality assurance phantom. The background and measured inclusion (stiffest of four inclusions) are tabulated.	177
Table 5.2	Performance measures of the reconstructed elasticity values based on the measured and regularized displacements.	187
Table 6.1	Parameter values used for simulating jitter error in the displacement measurements with Equation 6.2.	204

List of Figures

Figure 1.1	A block diagram of an ultrasound system.	9
Figure 1.2	The components of an ultrasound transducer.	12
Figure 1.3	The layout of a linear array and the array coordinates.	13
Figure 1.4	Ultrasound transmit focusing is achieved using variable time delays.	14
Figure 1.5	Ultrasound transmit focusing is achieved using variable time delays.	15
Figure 1.6	Example of apodization weighting functions applied to the elements of an array.	16
Figure 1.7	Simulated response from a point scatterer located at the transducer's focus for the different apodization weightings shown in Figure 1.6.	17
Figure 1.8	Block diagram of in-phase and quadrature (I/Q) processing. . .	18
Figure 1.9	The I/Q demodulation process.	19
Figure 1.10	Example of an RF signal and its corresponding envelope. . . .	20
Figure 1.11	Example of blood flow through the carotid artery as depicted by Pulsed Wave Doppler.	23
Figure 1.12	Example images of blood flow through the carotid artery as depicted by Colour Flow and Power Doppler imaging modes. .	25
Figure 1.13	Example of an RF signal before and after tissue compression. .	35
Figure 1.14	Triangulation configurations for determining three dimensional (3D) marker positions with optical tracking systems.	64
Figure 1.15	Markers for position tracking systems.	65

Figure 2.1	Block diagram of the elasticity measurement system.	73
Figure 2.2	A photograph of the motor control box connected to the Ultra-sonix scanner and a motorized ultrasound transducer.	77
Figure 2.3	Flowchart describing the synchronization between the ultra-sound acquisition and the excitation in the shear wave absolute vibro-elastography (SWAVE) system.	85
Figure 2.4	Simulated excitation signals for analysis of phasor fitting.	89
Figure 2.5	Front view of the CIRS 049 elastography quality assurance phantom with the experimental scanning regions indicated.	93
Figure 2.6	Diagram of the different exciter locations used to test the repeatability of the elasticity measurements as viewed from above the phantom.	94
Figure 2.7	Example phasor fitting result to simulated noisy displacement measurements.	95
Figure 2.8	Error in the least squares fit of a simulated 200 Hz cosine excitation at 10 μm amplitude with varying number of displacement samples, displacement jitter error, and frame rate error.	96
Figure 2.9	A demonstration of a <i>phasor wave artefact</i> observed in experimental bandpass sampled phasor images.	98
Figure 2.10	A profile across the width of an image containing the <i>phasor wave artefact</i>	99
Figure 2.11	Measurements comparing the ultrasound signal strength with and without the motor driver between the transducer and the scanner.	101
Figure 2.12	Results of phase compensation measured with the Porta and Texo ultrasound interfaces.	102
Figure 2.13	Results of phase compensation measured with the BK ultrasound interface.	103
Figure 2.14	Estimated amplitude, noise, and time shifts to minimize the squared error between the first phasor image collected and each subsequent compensated phasor image.	103

Figure 2.15	Results of phase compensation using a trigger to synchronize the start of each phasor image, using the Texo ultrasound interface, with the excitation.	104
Figure 2.16	Example elasticity images of the soft and stiff inclusions measured in the CIRS 049 elastography quality assurance phantom.	105
Figure 2.17	Repeated measurements of the mean elasticity in a stiff and soft inclusion, in a moderately stiff background with different motion sampling techniques.	106
Figure 2.18	Repeated measurements of the mean elasticity in a stiff and soft inclusion, in a moderately stiff background with different exciter positions.	108
Figure 3.1	The experimental apparatus for placenta <i>swave</i> measurements.	117
Figure 3.2	A mechanical schematic of the (a) Voigt, (b) Maxwell, and (c) Zener rheological models.	121
Figure 3.3	The 2D image plane from the centre of the volumetric ultrasound sweep for placenta Sample 5.	124
Figure 3.4	Mean Young's modulus measurements as a function of frequency for the six placenta samples.	125
Figure 3.5	The mean amplitude of the measured phasor for each placenta sample over all excitation frequencies in the region where the mean elasticity was calculated.	126
Figure 3.6	The shear wave speed dispersion relations found using the Voigt, Maxwell, and Zener models for each of the placenta samples.	128
Figure 3.7	The brightness mode (B-MODE) and Young's modulus image planes from the centre of the volumetric ultrasound sweep from three different regions of placenta Sample 4.	129
Figure 3.8	Mean Young's modulus measurements as a function of frequency for placenta Sample 4, repeated at three separate locations.	131
Figure 3.9	The range of mean Young's moduli reported in the elastography literature for normal placenta.	132

Figure 4.1	The coordinate systems used in the calibration procedure. . . .	140
Figure 4.2	The 3D transducer, encased in a holder with infrared light emitting diode (IRED) markers.	142
Figure 4.3	The phantom used for the planar and wedge calibration methods.	143
Figure 4.4	The top view of one row of the N-wire phantom and the intersecting scan plane.	144
Figure 4.5	A 3D view of the three N-wire rows.	145
Figure 4.6	A top view of the same N-wire phantom and scanning geometry as presented in Figure 4.5.	146
Figure 4.7	A rendering of the phantom used for the planar and wedge calibration methods.	148
Figure 4.8	The translation and rotation parameter values plotted for ten independent tests depicting the variation in the solutions. . . .	157
Figure 4.9	Point reconstruction error for the calibration techniques. . . .	158
Figure 5.1	A schematic of the synchronization between the mechanical excitation and the volumetric ultrasound acquisition. At a given motor position, each line in the 2D image plane is triggered sequentially at a common excitation phase which is then repeated for a number of phase offsets. After all phase offsets are collected, the motor is stepped to the next position and the process is repeated. Once the collection is finished for all motor positions, the data are reorganized into volumes that were triggered at a common phase.	170
Figure 5.2	Flowchart of the synchronization between the ultrasound acquisition of each beam line and the excitation signal at multiple phase offsets (extended from Figure 2.3).	176
Figure 5.3	A B-MODE image generated from the envelope of one of the RF images. The hypoechoic circle in the bottom left shows a cross section of the stiff inclusion.	177

Figure 5.4	From left to right, slices through the volume of the displacements measured in the x , y , and z directions. (a)–(c) The displacements estimated using speckle tracking alone, and (d)–(f) the displacements after post-processing the displacement measurements with divergence regularization. The x , y , and z directions roughly correspond to the lateral, axial, and elevational transducer coordinates.	181
Figure 5.5	The estimated Young’s modulus volumes using the LFE and shear-FEM inversion algorithms.	182
Figure 5.6	Profiles of the reconstructed elasticity values passing through the centre of the inclusion in the x , y , and z -directions.	183
Figure 5.7	Boxplots describing the distribution of Young’s modulus values in the inclusion and in the background.	185
Figure 5.8	Plot of the real part of the displacement component along the x -direction, across the x -dimension of the volume, for different values of the regularization parameter, α . The balance between the divergence constraint and the measurement fit is plotted for the same values of α	186
Figure 6.1	The view geometry is described as a rotation about an axis passing through the vertex of a tetrahedron and perpendicular to the opposite face of the tetrahedron.	201
Figure 6.2	Geometry of the multiple view angles with respect to the phantom.	202
Figure 6.3	The ultrasound axial measurement direction over the entire swept volume with an outline of the simulated phantom provided for reference.	203
Figure 6.4	The real part of the complex displacement phasors over the volume shown in three orthogonal cross-sectional slices.	211
Figure 6.5	The estimated elasticity and difference in elasticity from ground truth.	212
Figure 6.6	The ultrasound axial measurement direction over the entire swept volume with an outline of the simulated phantom provided for reference.	213

Figure C.1	By observation of the inter-point distances for one N-wire at a time, the transducer orientation can be constrained to rotate about an axis.	274
Figure C.2	By observation of the inter-point distances for two N-wires at a time, the transducer orientation can be fully constrained. . .	275
Figure C.3	Observing the inter-point distances for all three N-wires at the same time allows for only one coplanar solution.	276
Figure F.1	Plot of the mean and standard deviation of the best fit geodesic error metric after taking the natural logarithm of the set to transform the distribution closer to normal.	285
Figure F.2	A visual demonstration of fitting the rotation samples with axes indicating the rotation orientation.	286

Glossary

1D one dimensional

2D two dimensional

3D three dimensional

ADC analog-to-digital converter

API application programming interface

ARF acoustic radiation force

B-MODE ultrasound brightness mode image

BI-RADS Breast Imaging Reporting and Data System, a tool for breast cancer assessment and categorization

CAD computer-aided design, used for manufacturing

CNR contrast-to-noise ratio

CT computed tomography

CTE contrast-transfer efficiency

DAC digital-to-analog converter

DCT discrete cosine transform

DOF degree(s) of freedom

FEM finite element method

FFT fast Fourier transform

GUI graphical user interface

I/Q in-phase and quadrature, baseband ultrasound signals

IRED infrared light emitting diode

IUGR intrauterine growth restriction

LFE local frequency estimation

MRI magnetic resonance imaging

MRE magnetic resonance imaging elastography

OCT optical coherence tomography

PCA principal component analysis

PET positron emission tomography

PGA principal geodesic analysis

PRF pulse repetition frequency

PSF point spread function

PZT lead-zirconate-titanate, a piezoelectric material

RF radio frequency, unprocessed ultrasound signals

ROI region of interest

RMS root mean square

SDUV shear wave dispersion ultrasound vibrometry

SLAM simultaneous localization and mapping

SMURF spatially modulated ultrasound radiation force

SPECT single-photon emission computed tomography

SNR signal-to-noise ratio

SWAVE shear wave absolute vibro-elastography, a method to provide absolute measurements of tissue elasticity used and developed in this thesis

TCP/IP Transmission Control Protocol/Internet Protocol

TGC time gain compensation

TRUS transrectal ultrasound

Acknowledgments

I would like to thank my supervisors, Professors Robert Rohling and Tim Salcudean, for their valuable guidance and support during the course of this thesis. I am grateful for the many members of the Robotics and Control Lab for their collaborations, insights, and friendship. I would like to acknowledge the funding that supported my research during the course of my thesis from the National Science and Engineering Council, the Canadian Institutes of Health Research, the C. A. Laszlo Chair in Biomedical Engineering, and the UBC Four Year Fellowship scholarship. Finally, this work would not have been possible without the incredible support from my family and friends, who provided the motivation and encouragement needed to achieve my dreams.

Chapter 1

Introduction

1.1 Motivation

It is often desirable to gain insight into the inner workings of the human body. Several techniques have been developed to visualize internal anatomical structures or pathology from measurements of tissue properties. One of the most commonly used medical imaging techniques projects X-rays from one side of the body through the other to create a two dimensional (2D) image of X-ray absorption. The X-ray source and detector may also be rotated around the body to create a cross-sectional slice which forms the basis of computed tomography (CT) imaging. The slice locations may be translated to create a three dimensional (3D) CT image. In positron emission tomography (PET) and single-photon emission computed tomography (SPECT) imaging, a gamma ray detector is rotated around the body to measure rays produced by an injected radioisotope designed to trace specific biochemical reactions. magnetic resonance imaging (MRI) measures the decay rate of proton spins as they relax from an excited state to a lower energy state aligned with a strong magnetic field. Ultrasound imaging measures high frequency acoustic waves reflected back to a transducer caused by reflection of the waves by scatterers and interfaces of different acoustic impedance [263].

Elastography is a branch of medical imaging techniques that provides measurements and images of the mechanical properties of tissue. Most commonly, elastography infers the elastic properties (i.e. Young's modulus or shear modulus) of tissue.

The elastic properties can vary over several orders of magnitude between different types of tissue and between normal and diseased tissues [115]. Both relative and absolute measurements of tissue elasticity have proven useful in several clinical applications such as improving breast cancer classification with Breast Imaging Reporting and Data System (BI-RADS) [101, 147], targeting prostate cancer for biopsy and focal therapy [239, 282], and liver fibrosis assessment and staging [53, 145], among others. Quantifying the absolute elasticity values may be beneficial in characterizing tissue types, determining the different stages of a disease, or monitoring the progress of a treatment [86].

The assessment of tissue elasticity in identifying disease is familiar in medicine. Digital palpation is used in physical examinations to locate stiff tumours of the breast and prostate. A related “mechanical imaging” technique measures the pressure at the tissue surface in order to quantify the sensation felt by the fingertips during palpation [94]. Instead, elastography determines the elastic properties of the tissue by applying a force to the tissue, measuring the resulting internal motion of the tissue, and solving the equations of motion derived from a continuum mechanics model of the tissue behaviour relating the measured motion to the elastic properties. Several approaches have been developed for each of these three steps. For providing measurements of internal tissue motion, the majority of elastography systems rely on ultrasound, with some systems using MRI, and a small number using optical coherence tomography (OCT) and X-ray. A number of ultrasound based systems, described in Table 1.1, are currently commercially available from major manufacturers such as Siemens Healthcare (Erlangen, Germany), Philips Healthcare (Best, Netherlands), GE Healthcare (Little Chalfont, United Kingdom), Echosens (Paris, France), SuperSonic Imagine (Aix-en-Provence, France), Hitachi Medical (Tokyo, Japan), BK Medical (Herlev, Denmark), Toshiba (Otawara, Japan), and Wuxi Hisky Medical Technology (Beijing, China).

Standard medical ultrasound imaging has gained popularity due to its low cost, portability, relatively high frame-rate, ease of use, and safety. Ultrasound uses compressional waves created by short pressure pulses on the surface of the tissue with centre frequencies in the 1 MHz to 20 MHz range. The pressure wave propagates into the tissue and the resulting echoes are recorded. An ultrasound transducer converts between voltages and pressures using piezoelectric crystals. The crys-

Table 1.1: Commercially available ultrasound elastography systems.

System	Type ^a	Absolute Measurement	Measurement Location	Intended Clinical Application
Siemens				
eSie Touch	Strain	No	2D Image	Liver, Breast, Thyroid
VTi	Amplitude	No	2D Image	Liver, Breast, Thyroid
VTq	Transient	Yes	Point ^b	Liver, Breast, Thyroid
VTIQ	Transient	Yes	2D Image	Liver, Breast, Thyroid
Philips				
Elastography	Strain	No	2D Image	Breast
ElastPQ	Transient	Yes	Point ^b	Liver
GE				
Elastography	Strain	No	2D Image	Breast
Shear Wave Elastography	Transient	Yes	2D Image	Liver, Breast
Echosens				
FibroScan	Transient	Yes	Point ^c	Liver
SuperSonic Imagine				
ShearWave Elastography	Transient	Yes	2D/3D Image	Liver, Breast
Hitachi				
Real-time Tissue Elastography	Strain	No	2D Image	Breast, Thyroid Prostate, Pancreas
BK				
Elastography	Strain	No	2D Image	Breast, Prostate
Toshiba				
Elastography	Strain	No	2D Image	Breast
Shear Wave Elastography	Transient	Yes	2D Image	Liver
Wuxi Hisky				
FibroTouch	Transient	Yes	Point ^c	Liver

^a The different types of elastography are described in detail in Section 1.5.4.

^b Average over small 2D region of interest (ROI).

^c Linear regression along one dimensional (1D) line.

tals are grouped in an aperture and electronically pulsed in a timed sequence to create a transmit pressure field. Inhomogeneities in the density and compressibility of the tissue cause the wave to scatter. The returning pressure waves (echoes) are measured over an aperture, delayed, summed, and digitally sampled. The resulting collection of echo signal lines is processed to create a standard brightness mode (B-MODE) image [16, 69].

Due to the complex scattering pattern of ultrasound waves in biological tissues and the highly anisotropic beam pattern, some ultrasound images may be difficult to interpret. 3D ultrasound offers a number of advantages over conventional 2D ultrasound. One clear advantage is that the 3D spatial relationship between structures in the imaging volume is already available in the volume image, in comparison to mentally visualizing the 3D structures from a series of 2D cross-sections. From the 3D image, different 2D imaging planes can be “resliced” from the volume to provide 2D image orientations that would otherwise be impossible to acquire. Alternatively, surface or volume rendered models can be created which may reveal pathology that may be difficult to see in conventional ultrasound images [219]. Imaging in 3D can provide more information on the geometry of anatomical structures and an accurate measure of their volume. 3D ultrasound can also help in needle localization and guidance during biopsy [85].

Use of 3D ultrasound can also benefit elastography. The above mentioned advantages for 3D ultrasound in terms of easing the interpretation of the geometrical relationships in the data and improving the accuracy of geometrical measures still apply [36]. Further, since elastography involves solving the equations of motion derived from a continuum mechanics model, measurement of the variation of the motion over space can help reduce errors when a 2D planar model does not accurately describe the experimental conditions [96]. The most accurate approach would include measurement of motion in all three directions over the volumetric region of interest (ROI) [343].

Since ultrasound is a highly anisotropic imaging modality, the motion measurements with ultrasound are most accurately computed in the axial direction, the primary direction of ultrasound wave propagation. In the other two directions, lateral and elevational, motion measurements are typically an order of magnitude less accurate due to lack of phase information [42], wider extent of the point spread

function [167], and larger sampling intervals [187]. In contrast, magnetic resonance imaging elastography (MRE) is able to measure motion accurately in all three directions, which helps to reduce errors in the elasticity measurements.

One approach to improve ultrasound motion measurements is to move the transducer to different view angles so the accurate axial motion measurements from several directions can be combined [4, 32, 211]. In general this requires a spatial calibration to determine the translation and rotation between each view. The problem of ultrasound spatial calibration has been studied extensively [143, 206], however limited research has investigated 3D ultrasound calibration at accuracies required for elastography applications.

In summary, elastography provides a means of measuring the elastic properties of tissues. Contrast in elastic properties is correlated with clinically relevant pathology. Elastography requires a method of measuring internal tissue motion, with most systems using ultrasound. The use of 3D ultrasound and quantitative absolute elastography techniques may help improve visualization and specification of physiological abnormalities. Improvements in 3D ultrasound spatial calibration may enable more sophisticated methods of measuring 3D tissue motion vectors.

1.2 Hypothesis

The overall hypothesis is that a 3D approach to measurement can be used with ultrasound elastography to provide accurate measurements of tissue elasticity. To examine this hypothesis, the following objectives are set:

- Develop a modular 3D elastography research platform that allows for flexible use of different techniques and equipment for comparison and optimization.
- Test the 3D elastography research platform through simulations and experiments on tissue mimicking phantoms and *ex vivo* tissue.
- Develop highly accurate ultrasound calibration techniques that can be applied to 3D elastography.
- Develop a method for measuring the full shear wave motion vector field over a volume with 3D ultrasound and test on a tissue mimicking phantom.

- Investigate the use of spatial calibration for combining multiple ultrasound volumes from different views to determine the full shear wave motion vector field over a volume through simulation.

1.3 Thesis Outline

The rest of this chapter is devoted to a detailed description of the background in the fields of ultrasound, elastography, and ultrasound spatial calibration. This is meant to provide sufficient information for the non-specialist to understand the rest of this thesis and to provide a more thorough review of relevant literature.

Chapter 2 describes the design, development, and testing of a 3D elastography research platform. The details of the separate components of the system and how they operate are described. Different methods of sampling tissue motion are tested through simulation and experiments. It is shown that single frequency and multi-frequency tissue motion can be recovered with acceptable accuracy using a sub-Nyquist sampling rate, assuming consistent tissue motion, with reasonable assumptions of errors due to measurement jitter and uncertain frame rate, using a range in the number of temporal samples acquired. An artefact from using the sub-Nyquist sampling approach, appearing as a wave with a similar spatial frequency to the waves induced by the applied excitation, is discovered and explained. It is shown that the artefact is less prevalent when using a higher temporal sampling rate. Measurements on a tissue mimicking phantom demonstrate the repeatability of the elasticity measurements for repeated acquisitions and different excitation locations.

In Chapter 3 the 3D elastography research system of Chapter 2 is applied to healthy *ex vivo* human placentas. Measurement of multi-frequency shear waves over a band of 60 Hz to 200 Hz is demonstrated and the feasibility of estimating placenta elasticity is shown. Viscoelastic parameters based on Voigt, Maxwell, and Zener rheological models are estimated, showing a strong viscous dispersion.

In Chapter 4 a novel spatial calibration technique for 3D ultrasound is described. The method makes fewer assumptions about the motor geometry than previous calibration techniques, and thus has the potential to reduce errors introduced through inaccurate scan conversion of ultrasound data from transducer to Cartesian coordinates. The method is based on calibrating individual image slices across the volume

using an accurate 2D calibration technique. A best fit to a subset of slices is performed to decrease data collection time compared to calibrating all of the slices making up the volume, and reduce the influence of random errors in individual calibrations. The method is compared to the widely used N-wire calibration technique. A novel extension of the N-wire calibration is developed to incorporate more data points that are typically discarded and contrasted with the traditional N-wire technique. Finally, another novel 3D ultrasound calibration technique is developed that uses assumed motor geometry and planar calibration features. Experiments show that the proposed multi-slice technique produces the smallest point reconstruction error; at 0.82 mm, the method is the first sub-millimetre 3D ultrasound calibration technique reported.

In Chapter 5 a solution for measuring dynamic motion on the order of hundreds of cycles per second using 3D ultrasound is proposed based on synchronizing the ultrasound acquisition with the mechanical exciter producing the tissue motion. A novel regularization algorithm is developed using a physical constraint of tissue incompressibility to help reduce noise in the motion measurements. The elasticity distribution of a tissue mimicking phantom containing a stiff sphere is estimated using two algorithms; a local frequency estimator and a finite element solution. The best elasticity estimate reaches within 1 kPa of the reference Young's modulus value provided by the phantom manufacturer at the centre of the stiff sphere. Mean elasticity measurements are compared to previous MRE estimates, and are shown to be within the variance of current elastography methods. It is shown that using displacements after regularization results in more than a 2 dB improvement in contrast-to-noise ratio (CNR) ratios of the elasticity images using either algorithm compared to displacements before regularization.

In Chapter 6 the potential of combining multiple ultrasound volumes from different angles for measurement of the full motion vector over a volume is investigated. A method is presented to solve for 3D motion vectors from three volumes of axial motion measurements, and the technique is verified through simulation. The effects of scan conversion, interpolation, and calibration are modelled to study how they affect the displacement and elasticity estimates. It is shown that the proposed multi-view approach can reliably solve for dynamic 3D displacement vectors suitable for elasticity estimation. The error in elasticity increases by less than 8 % for a

typical level of calibration error (< 1 mm and 2°) compared to elasticity measured with no calibration error.

In Chapter 7 the thesis is concluded by relating the results of the preceding chapters to each other and placing the results in the context of the current state of the field of elastography. The strengths and weaknesses of the research are discussed and recommendations for future research directions are provided.

Seven appendices are included at the end of the manuscript. Appendix A provides some useful information on index notation which is used to describe the elastic theory underlying elastography. In Appendix B a copy of the consent form used in the placenta study described in Chapter 3 is provided. In Appendix C the difficulty in determining the location of the edge points in the popular N-wire spatial calibration phantom is demonstrated using geometrical examples, and the particular solution proposed in Chapter 4 is shown to demonstrate how that design leads to the ability to determine the edge points. In Appendix D the exponential and logarithmic mapping to and from the dual quaternion manifold is explained, which is used in the rotation fitting and interpolation used in Chapter 4. In Appendix E the method for determining the direction of the best fit geodesic on the quaternion manifold used in Chapter 4 is described, it is proven that the distance metric used for the geodesic fitting is independent of the choice of coordinate system, and the fitting algorithm is compared in more detail to alternative approaches. In Appendix F a simulation is described that evaluates the rotation fitting algorithm from Chapter 4. In Appendix G a robust method for computing displacement gradients using linear least squares, which is used in the elasticity estimation algorithm in Chapter 6, is described.

1.4 Ultrasound Background

This section describes the physical processes, signal processing, and methods of medical ultrasound imaging. A block diagram providing an overview of an ultrasound imaging system is shown in Figure 1.1.

An ultrasound transducer is applied to the body and is connected to an ultrasound scanner which controls the transducer, and interprets and processes the transducer measurements. A transducer creates acoustic pulses at the surface of the body

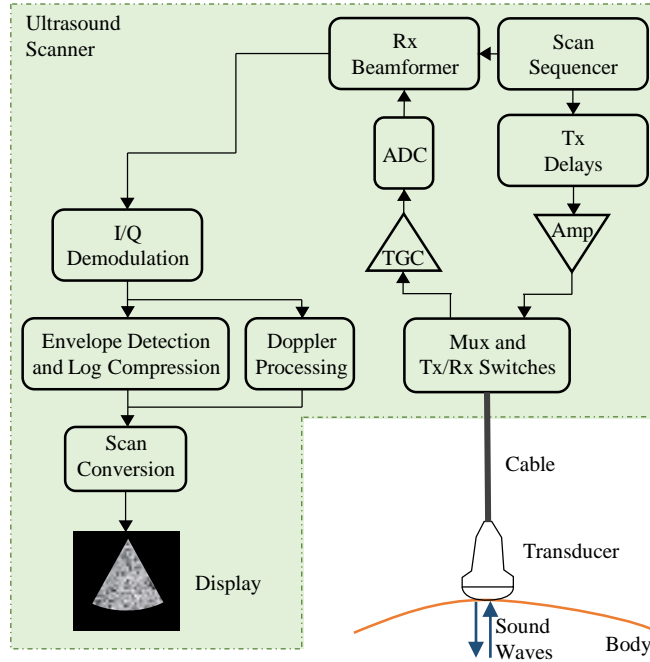


Figure 1.1: A block diagram of an ultrasound system. The scan sequencer controls the transmit (Tx) and receive (Rx) timing. The beamformed received data is then processed for B-MODE/Doppler display.

which transmit waves that travel into the underlying tissue. Echoes are produced by the tissue and are measured by the transducer over time. The distance or depth of the reflecting echoes are resolved, creating a spatial map of the acoustic properties of tissue.

The depth, d , is determined from the time it takes for the ultrasound pulse to travel to the target and back

$$t = \frac{2d}{c}, \quad (1.1)$$

where c is the speed of the ultrasound wave and the factor of 2 accounts for the travel of the transmitted wave to the target and the travel of the reflection back to the transducer, assuming a straight line of travel. Usually a constant speed of sound of 1540 m/s is assumed which corresponds to an average value for tissues typically imaged with ultrasound. Excluding fat, tissues that are usually imaged by ultra-

sound are within 5 % of this value [140]. Some scanners use a different assumed speed of sound using presets depending on the tissue type selected by the user, or will allow the user to set the value directly. This will correct for errors in depth estimation from Equation 1.1, as well as errors in focusing which are discussed in more detail in Section 1.4.4.

Echoes of the ultrasound waves are scattered or reflected by the tissue, where scattering refers to the interaction between waves and particles smaller than the wavelength, and reflection refers to the interaction between the waves and objects larger than the wavelength. The echoes are caused by a combination of changes in the tissue density and compressibility.

1.4.1 Reflection

Tissue structures with features larger than the wavelength, such as interfaces between organs, adipose tissue, cysts, and bone create prominent reflections. The reflections are often described using the characteristic acoustic impedance [161]

$$Z = \rho c, \quad (1.2)$$

where ρ is the mass density and c is the speed of the sound waves travelling in the tissue. It is generally assumed that the propagation of an ultrasound wave in the body can be modelled by a longitudinal wave propagating in a fluid under isentropic conditions [73], resulting in a propagation speed of

$$c^2 = \frac{\partial p}{\partial \rho} = \frac{K}{\rho}, \quad (1.3)$$

where p is the pressure and K is the Bulk modulus.

At a boundary between two objects with impedances Z_1 and Z_2 , the ratio of the reflected pressure of an incident wave normal to the interface is described by the reflection coefficient [69]

$$R = \frac{Z_2 - Z_1}{Z_2 + Z_1}. \quad (1.4)$$

The received ultrasound signal is closely approximated as a convolution between the spatial distribution of the reflection coefficients of the tissue and the point

spread function (PSF) of the imaging system, with the assumptions of linear wave propagation and weak scattering [208]. Typically the reflection coefficient is small for soft tissues, meaning most of the energy of the wave is transmitted through the interface. This is important as it allows echoes to return from structures deeper than the first few reflecting interfaces. Large differences in acoustic impedance, which result in large reflections, can cause a “shadowing” artefact, displaying a dark region below the reflecting object. This is also the reason for using an acoustic coupling gel between a transducer and the skin as there is a large impedance mismatch between air and the body.

1.4.2 Scattering

Inhomogeneities in acoustic impedance of tissue on scales smaller than the wavelength result in scattered echoes. The scattered waves interfere constructively and destructively depending on the relative phases of the waves. This leads to the familiar granular appearance of ultrasound images, also known as speckle. It has been shown that despite its appearance as tissue texture, speckle is not a direct depiction of the underlying tissue structure, but instead carries information dependent on the tissue, transducer, and point spread function [327]. However, the speckle pattern is deterministic, not random, and can be reproduced given the same imaging conditions [306].

1.4.3 Transducers

The transducer is made up of several components, namely piezoelectric elements, a backing layer, a matching layer, and an acoustic lens as shown in Figure 1.2. The piezoelectric elements, commonly composed of lead-zirconate-titanate (PZT), are connected to electrodes leading from the cable attached to the scanner and are used to create the ultrasound waves by applying high voltage pulses (usually 50 V to 100 V), as well as to detect echoes from the body when the reflected waves apply pressure on the transducer face. The backing layer is used to damp the vibrations of the elements which helps to reduce the number of cycles in the pulse, and thus increase the bandwidth. The matching layer reduces the change in acoustic impedance between the transducer and the body which would otherwise cause most of the wave

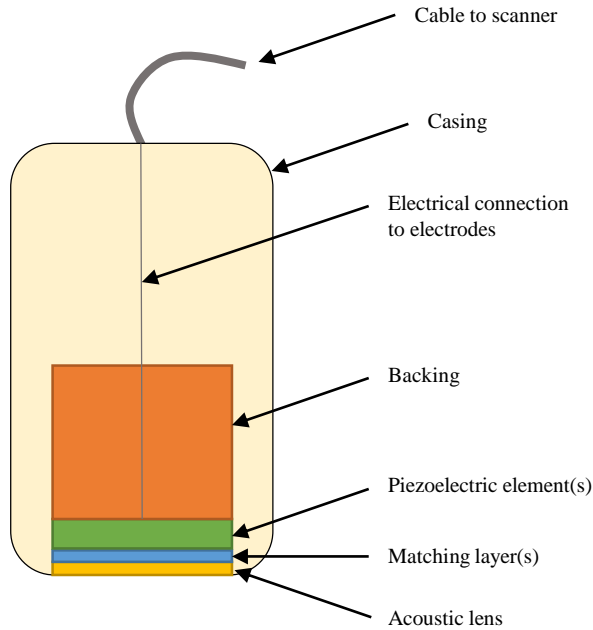


Figure 1.2: The components of an ultrasound transducer.

to reflect before transmitting into the body as explained in Section 1.4.1. The acoustic lens functions to focus the acoustic beam in the elevational direction. The depth of the elevational focus is usually fixed.

While an ultrasound transducer could be made using a single piezoelectric element and the components mentioned in the previous paragraph, only the anatomical information along a single line would be measured. Most modern ultrasound transducers are composed of several piezoelectric elements arranged in a row, called an array. A common configuration is the linear array in which the elements are placed along a straight line, creating rectangular shaped images. Phased arrays use fewer closely packed elements to create a smaller footprint, which allows access to small windows of the body such as between the ribs, and sweep the ultrasound beam across a large range of angles creating a fan shaped image (explained in Section 1.4.4). Curvilinear arrays place the elements along a curved surface, creating an annular sector shaped image which can be useful for imaging large structures such as organs in the abdomen. The layout of a linear array and the coordinate

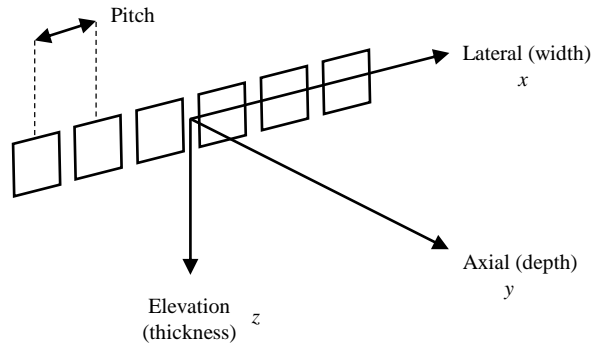


Figure 1.3: The layout of a linear array and the array coordinates. The axial direction corresponds to the 0° direction of sound propagation and thus the depth, the lateral direction (also referred to as azimuth) corresponds to the width of the image, and the elevational direction the thickness of the image. The spacing between the centre of the elements is called the pitch.

system of the array used throughout this thesis is shown in Figure 1.3.

The voltage signal measured by the piezoelectric elements is referred to as an radio frequency (RF) signal. When referring to the voltage from a single element or channel, this would be called prebeamformed RF data. Most ultrasound systems however do not save the channel data, but rather use hardware to combine data from several elements in a process called beamforming.

1.4.4 Beamforming

Beamforming is the process of combining the acoustic energy from a group of elements, or an aperture, to create a beam in which the majority of the acoustic energy is along the beam direction. The postbeamformed RF signal is used to create a line in a B-MODE image. By changing the location or direction of the beam, the multitude of lines can be combined to form an image.

The beam is typically focused by combining the approximately spherical emissions from each element and controlling the pulse timing of each element so that the

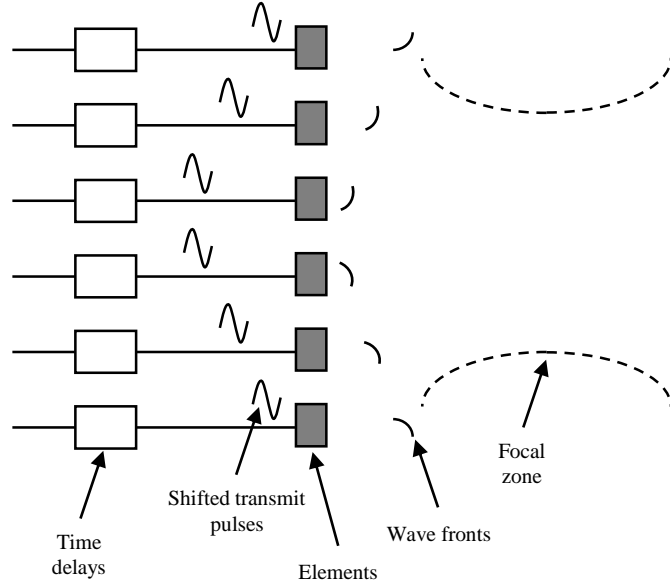


Figure 1.4: Ultrasound transmit focusing is achieved using variable time delays.

waves converge to a focal zone as shown in Figure 1.4. The pulse timing may also be adjusted to steer the beam to different angles. The delays for each element are calculated based on geometry assuming straight line wave propagation as shown in Figure 1.5. The time for the wave emitted by the element located at x to reach the focal point at r at a steering angle of θ is

$$t(x) = \frac{1}{c} \left(\sqrt{r^2 + x^2 - 2rx \sin \theta} - r \right), \quad (1.5)$$

where c is the speed of sound. For a given aperture size, the maximum propagation time can be calculated using Equation 1.5 and used to bias the time delays for each location along the array so the element that is furthest from the focal point will have a delay of zero [12]. Thus the time delay for each element is

$$\tau(x) = t_{max} - t(x). \quad (1.6)$$

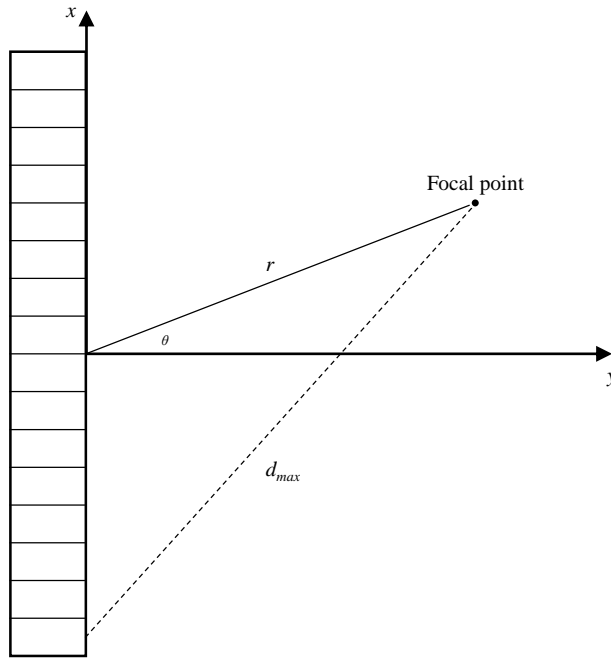


Figure 1.5: Ultrasound transmit focusing is achieved using variable time delays.

Simple receive beamforming essentially performs the reverse of the transmit focusing. The signals across the aperture are aligned in time, using the principle of coherence where coherent signals will add to create a large signal, and incoherent signals will tend to cancel and appear as random low level signal [306]. The delays are computed using geometry as in transmission. However, unlike transmission, which can only use one set of fixed delays to create a physical wave pattern, the receive delays can be changed dynamically. In dynamic receive focusing the delays are adjusted as a function of depth so the entire image is focused. Usually a constant f-number (ratio of the focal distance to the aperture size) is desired, so the number of elements used in the summation is gradually increased with increasing depth.

The received signal can contain energy from directions other than the main beam axis. The off-axis directions containing energy are referred to as side and grating lobes. Apodization, which weights each element in transmit and receive, can help to reduce the amplitude of these lobes with the trade-off of increasing the

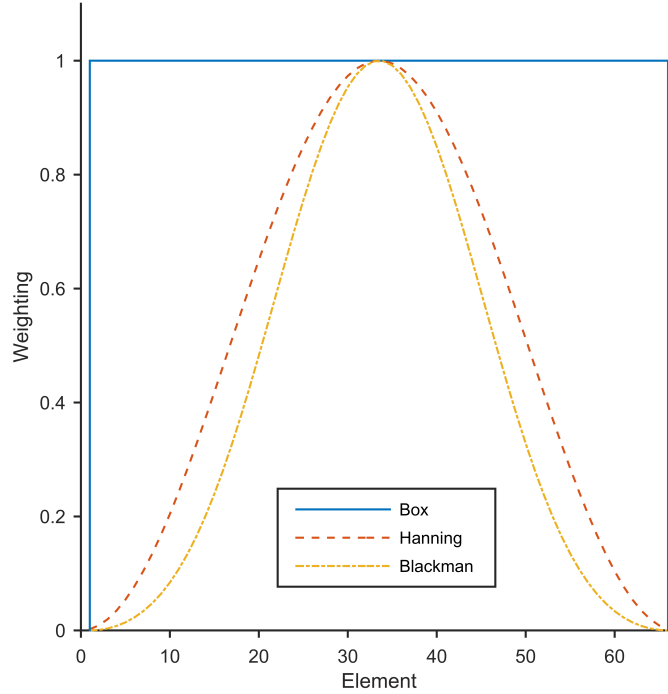


Figure 1.6: Example of apodization weighting functions applied to the elements of an array.

width of the main lobe. Common apodization functions are box, Hanning, and Blackman which are shown in Figure 1.6. To demonstrate the effect of apodization, the reflection from a point scatterer was simulated using Field II [148], a software for simulating the spatial impulse responses of ultrasound transducers, for the apodizations mentioned. The magnitude of the received signal at the axial coordinate of the focus point plotted across the width of the transducer shows the effect on the beam in Figure 1.7. The -6 dB width of the main lobe has increased from about 0.5 mm to 0.8 mm, but the presence of the side lobes and grating lobes has been greatly reduced.

The beamforming delays described in this section are based on the geometry of the elements and the focus. Heterogeneities in the speed of sound cause a change in the geometric time differences to reach to focus because the waves from each

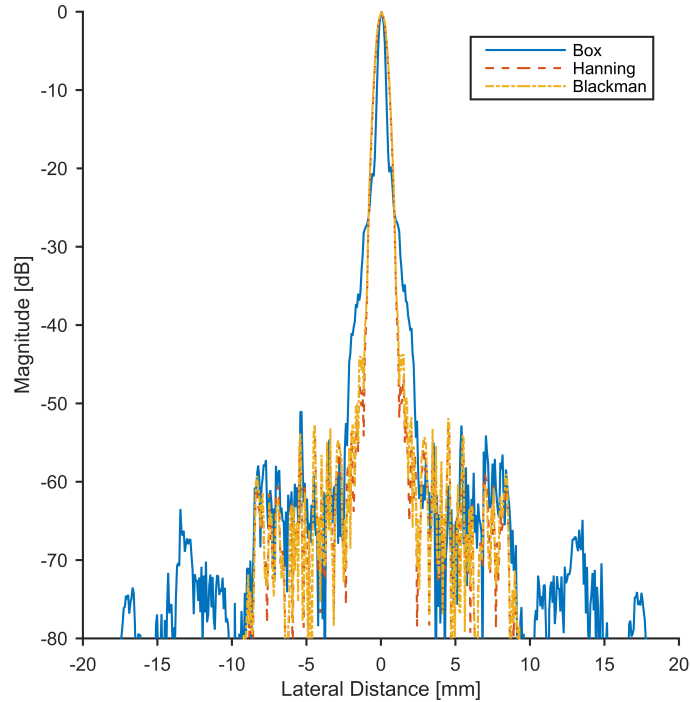


Figure 1.7: Simulated response from a point scatterer located at the transducer’s focus for the different apodization weightings shown in Figure 1.6.

element travel through different paths. The heterogeneities also cause refraction, bending the waves in different directions. These aberrations cause an increase in beam width and decrease in amplitude [316].

An important consideration in ultrasound image formation is the attenuation of the waves due to viscous and scattering effects. Attenuation is depth and frequency dependent and is usually on the order of 1 dB/(cm MHz) [140]. Because the amount of energy lost is a function of how far the waves have travelled, a compensation based on the depth of the received signal is commonly applied in a process called time gain compensation (TGC). The TGC is increased gradually with depth to efficiently use the dynamic range of the analog-to-digital converter (ADC) hardware and to achieve uniform brightness along the depth.

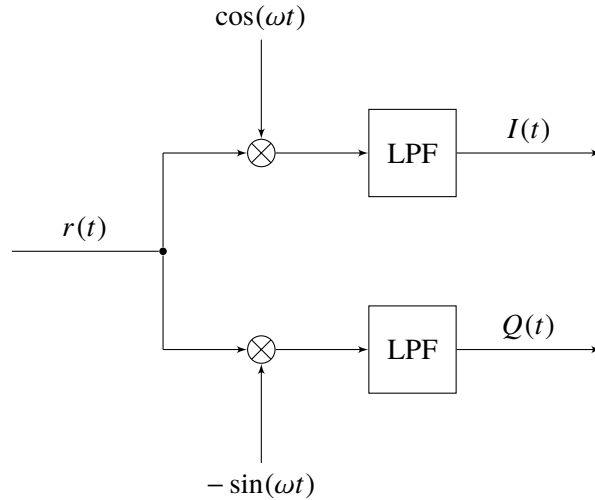


Figure 1.8: Block diagram of I/Q processing.

The resolution of the beamformed ultrasound image is anisotropic and spatially variant. The axial resolution is proportional to the transmit frequency and the fractional bandwidth of the system. The lateral and elevational resolution are also proportional to the transmit frequency, and are directly proportional to the f-number (in the elevational direction the f-number is fixed). The axial resolution is usually higher than the lateral and elevational resolution by factors of 3–8 and 10, respectively [17].

The frequency dependence of resolution and attenuation lead to a fundamental trade-off: short duration, high frequency pulses allow clear separation of fine details in the image; long duration, low frequency pulses allow waves to penetrate deep into the body without images becoming dominated by noise.

1.4.5 Image Formation

The B-MODE image formation process uses beamformed RF data and applies I/Q demodulation, envelope detection, log compression, and scan conversion processes before final display. These processes are described in this section.

The beamformed RF data is an amplitude modulated signal. To retrieve the tissue reflectivity information the carrier frequency is removed in a process called

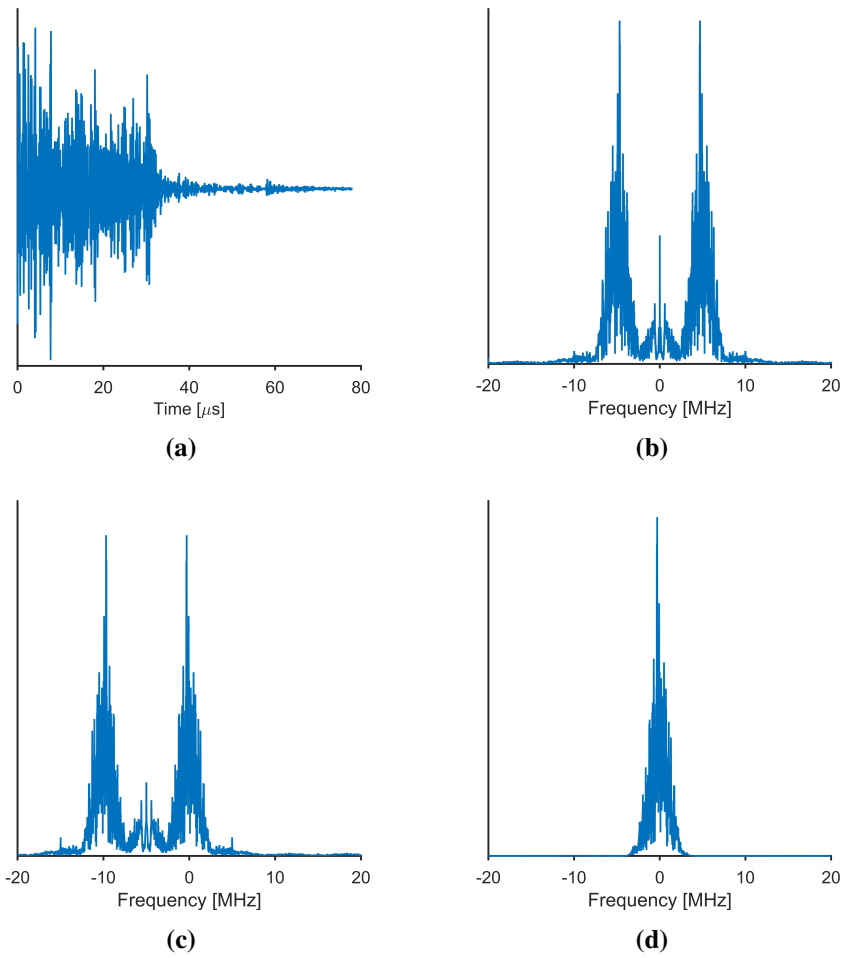


Figure 1.9: The I/Q demodulation process starts with beamformed RF data shown (a) as a function of time and (b) frequency. (c) The spectrum is shifted to the left after down mixing and (d) after low pass filtering the signal only contains a band of energy that was originally centred around the positive centre frequency of the RF signal.

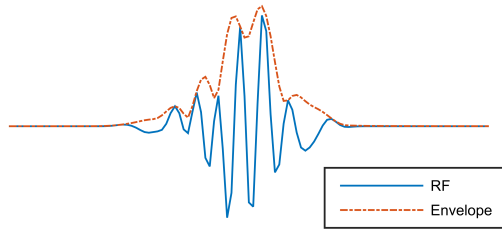


Figure 1.10: Example of an RF signal and its corresponding envelope.

i/Q demodulation, shown schematically in Figure 1.8. First, the RF data is down mixed which shifts the frequency spectrum down. This is commonly achieved by multiplying the RF signal with cosine and sinusoid signals at the centre frequency, or generating the quadrature component by sampling the RF signal with a delay of $1/(4\omega)$ (see [296] for a description of sampling strategies). This can also be accomplished digitally by multiplying with a complex exponential

$$r(t)e^{-j\omega t} = r(t) \cdot (\cos(\omega t) - j\sin(\omega t)) = I(t) + jQ(t), \quad (1.7)$$

where $r(t)$ is the RF signal, $I(t)$ and $Q(t)$ are the in-phase and quadrature i/Q components, and ω is the centre frequency of the RF signal. After down mixing, the signal is low pass filtered to remove the negative frequency spectrum of the real RF signal and noise outside of the desired bandwidth. The spectrum of the signal during the steps of the demodulation process is shown in Figure 1.9. For more efficient storage and processing, the i/Q data is usually downsampled because the sampling rate can be reduced to twice the cut-off frequency of the low pass filter without introducing aliasing. In addition to the B-MODE image formation described below, the i/Q data is also used for Doppler motion detection as described in Section 1.4.6.

The amplitude of the i/Q data, or the envelope, is given by

$$e(t) = \sqrt{I^2(t) + Q^2(t)}. \quad (1.8)$$

Figure 1.10 shows an RF signal and the corresponding envelope. Log compression

follows envelope detection to ensure that the image has an appropriate dynamic range for the display and for human visual perception.

To create a geometrically accurate image for display, the compressed envelope data must be mapped from transducer coordinates to Cartesian coordinates in a process called scan conversion. This can be accomplished by creating a regular grid in transducer coordinates for the envelope data points, a regular grid in Cartesian coordinates for the display, computing the location of the Cartesian grid in transducer coordinates using the beam geometry, and finally using bilinear interpolation to estimate the envelope for the Cartesian grid points.

1.4.6 Doppler

In diagnostic ultrasound, Doppler is used to detect and measure blood flow. First described by Christian Doppler in 1842 in a study of the colour of light from stars, it explains how the frequency of a wave is perceived to change relative to movement. The premise of the Doppler effect is that the apparent frequency of a detected wave will change when the source or receiver is moving.

The Doppler equation for ultrasound waves transmitted and received by a stationary transducer and interacting with a moving scatterer can be derived as follows. Consider a scattering particle moving towards a transducer transmitting a wave with a centre frequency of f_0 . The scatterer is acting as a moving receiver, increasing the rate at which it receives the transmitted sound waves, causing an apparent increase in observed frequency

$$f_S = f_0 \frac{c + v \cos \theta}{c}, \quad (1.9)$$

where f_S is the frequency experienced by the scatterer, v is the velocity of the scatterer, c is the speed of sound in tissue, and θ is the angle between the sound beam and the scatterer. Now part of the sound is echoed by the scatterer back towards the transducer. The scatterer is acting as a moving transmitter, causing an increase in the frequency emitted by the scatterer

$$f_R = f_S \frac{c}{c - v \cos \theta}. \quad (1.10)$$

Substituting Equation 1.9 into Equation 1.10 and defining $f_R = f_0 + f_D$, where f_D

is the Doppler frequency shift measured by the transducer, we obtain

$$f_0 + f_D = f_0 \frac{c + v \cos \theta}{c - v \cos \theta}. \quad (1.11)$$

Considering the flow velocity observed in clinical Doppler examinations is typically 0.1 % of the value of the speed of sound in tissue, Equation 1.11 can be simplified to

$$f_D = 2f_0 \frac{v \cos \theta}{c}. \quad (1.12)$$

Clearly in a real blood vessel in the body the received echo signal will not be from a single scatterer moving at a single velocity, but from a collection of scatterers at different velocities. This results in a spectrum of measured frequency shifts.

A number of blood flow measurement techniques based on the Doppler principle have been developed for ultrasound scanners. The different techniques and their advantages and disadvantages are discussed in the following sections.

Continuous Wave and Pulsed Wave

Continuous Wave Doppler mode on ultrasound scanners continuously transmit sound beam and receive the echoes from the beam. A specialized transducer containing a transmit element and receive element may be used, or an array with separate apertures dedicated to each function. The detected echoes at the receiver undergo I/Q demodulation to shift the spectrum to the base band and remove the high frequency components. The remaining signal contains the spectrum of Doppler shift frequencies, f_D , in the region of the overlapping transmit and receive beams. In addition to the signal due to blood motion, there are contributions from other structures such as the vessel wall which typically have larger echo amplitudes and could overwhelm the blood motion signals. These other structures typically move slower than the blood so a high-pass filter, sometimes referred to as a “wall filter” or a “clutter” filter, can remove these signals from the spectrum [140]. This unfortunately also removes the signal from slow moving blood.

The resulting Doppler shift spectrum for physiological flows is typically in the kHz range, and can be applied to a loudspeaker for audible feedback. Stereo speakers may be used to differentiate between positive and negative flow. The signal is

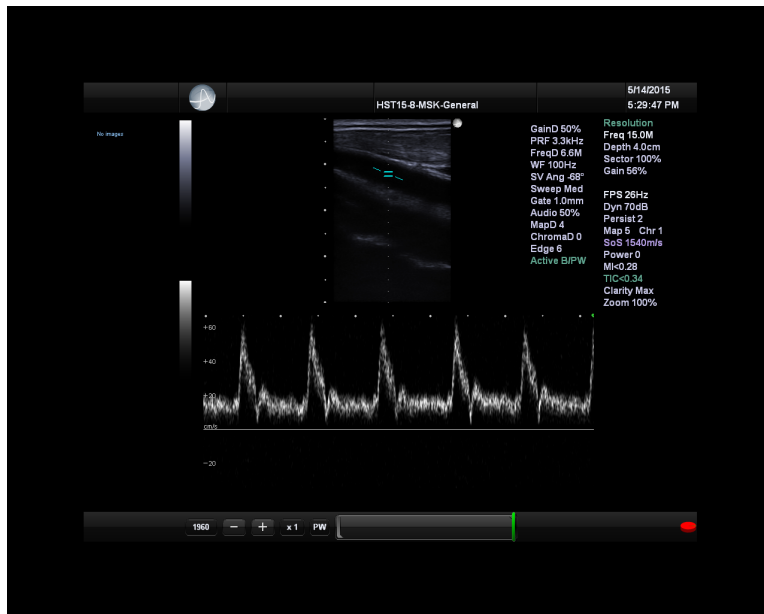


Figure 1.11: Example of blood flow through the carotid artery as depicted by Pulsed Wave Doppler. The horizontal teal lines indicate the gate location, and the angled teal lines indicate the estimated flow angle which was manually set to approximately parallel to the vessel direction. The waveform under the B-MODE image shows the estimated velocity as a function of time. In this case, a purely positive flow is measured (flow towards the transducer), with a peak velocity of approximately 60 cm/s.

also often processed by a fast Fourier transform (FFT) and plotted over time for visual feedback. A broad spectrum often indicates abnormal or turbulent flow. Quantification of the velocity based on the FFT is dependent on the relative angle between the beam and the flow which can be difficult to correct for in Continuous Wave mode, however the ratio between the peak-systolic and end-diastolic values is independent of the angle and can be useful for characterizing the flow [169].

The continuous operation of the transmit and receive operations removes the depth ranging ability of pulse echo ultrasound. This makes it difficult to localize blood flow measurements from Continuous Wave Doppler. Localization may be important for separating flow information from different vessels or to quantify different regions (e.g. turbulent and laminar regions) inside a single vessel. Pulsed

Wave Doppler provides this feature by only providing Doppler shift measurements from a small sample volume or “gate.” The transducer transmits a pulse and the receive signal is ignored until enough time has elapsed for echoes from the start of the gate to return and then is ignored again after the amount of time to reach the end of the gate’s depth. Because the location of the gate is known, the angle of the vessel can be estimated in the region of the gate and corrected for. The signal processing as well as the audio and visual feedback are similar to Continuous Wave. An example of a Pulsed Wave Doppler image is shown in Figure 1.11.

The pulse repetition frequency (PRF) is the effective sampling rate of the Pulsed Wave Doppler signal, which limits the frequency range and thus the maximum velocity that can be measured according to the Nyquist sampling theorem

$$|v| \leq c \frac{f_{\text{PRF}}}{4f_0 \cos \theta}. \quad (1.13)$$

For a deeply placed gate, the waiting time for the echoes to return from the gate location can be long, which could severely limit the PRF. Since the echoes before the start of the gate do not need to be recorded, a high PRF may be achieved by transmitting additional pulses during the period of time before the first pulse returns from the gate [276]. The disadvantage of the high PRF approach is that if there is any motion between the transducer and the gate there will be some ambiguity about where the motion originated.

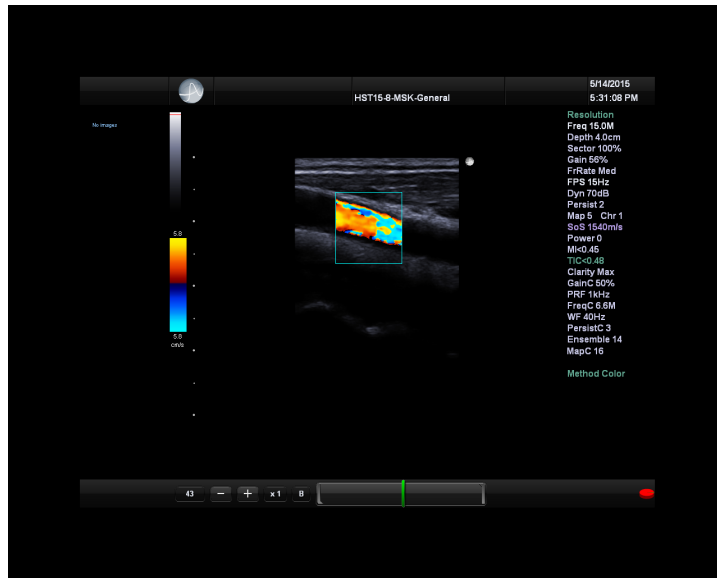
The number of samples, N , for the FFT computation also puts a restriction on the minimum velocity that can be measured with the Pulsed Wave mode, given by [280]

$$|v| \geq c \frac{f_{\text{PRF}}}{2Nf_0 \cos \theta}. \quad (1.14)$$

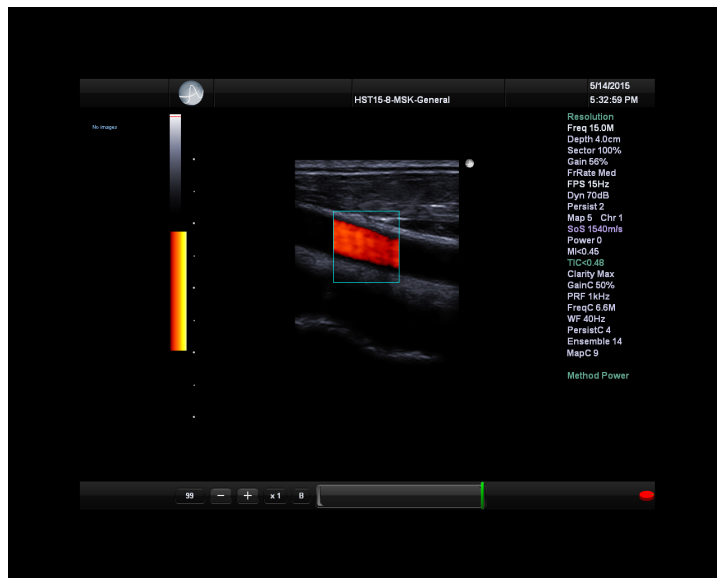
Continuous Wave and Pulsed Wave may be combined in a duplex fashion with conventional B-MODE imaging to provide both Doppler measurements and information about the anatomical structures.

Colour Flow

Colour Flow mode displays measurements of the mean velocity along the beam direction from a number of gates in a region of interest as a 2D image overlaid on



(a)



(b)

Figure 1.12: Example images of blood flow through the carotid artery as depicted by (a) Colour Flow and (b) Power Doppler imaging modes. Rapid transitions from yellow to light blue in the Colour Flow image likely indicate aliasing.

a B-MODE image as shown in Figure 1.12. The colour mapping typically presents flow towards the transducer as red and flow away from the transducer as blue. The gating process is analogous to the Pulsed Doppler gating, except Colour flow will contain multiple different gates along a beam line. The same beam line is transmitted repeatedly at a PRF similar to Pulsed Doppler until a defined number of lines have been acquired, called an ensemble. Adjacent lines over the ROI are acquired sequentially after an ensemble for each line is collected.

Due to the limited number of ensembles causing variability in the FFT output and the computational cost of the FFT operation on each gate across the ROI, different estimators were developed for measuring the mean frequency. Almost all modern scanners use a phase-based estimator [102]. The most common technique is based on the autocorrelation technique introduced in [158]. The technique relates the mean frequency computed from the power spectrum

$$\bar{\omega} = \frac{\int_{-\infty}^{\infty} \omega P(\omega) d\omega}{\int_{-\infty}^{\infty} P(\omega) d\omega} \quad (1.15)$$

to the autocorrelation function using the relationship expressed by the Wiener-Khintchine theorem [59],

$$\Gamma(\tau) = \int_{-\infty}^{\infty} P(\omega) e^{j\omega\tau} d\omega. \quad (1.16)$$

Using Equation 1.15, Equation 1.16, and the derivative of Equation 1.16, it can be shown

$$j\bar{\omega} = \frac{\dot{\Gamma}(0)}{\Gamma(0)}. \quad (1.17)$$

Representing the autocorrelation as

$$\Gamma(\tau) = |\Gamma(\tau)| e^{j\phi(\tau)}, \quad (1.18)$$

the mean Doppler frequency shift is the derivative of the phase of the autocorrela-

tion function which can be approximated as

$$\bar{\omega} = \dot{\phi}(0) \approx \frac{\phi(T_{\text{PRF}}) - \phi(0)}{T_{\text{PRF}}} = \frac{\phi(T_{\text{PRF}})}{T_{\text{PRF}}}, \quad (1.19)$$

where T_{PRF} is the period between pulses.

Using the definition of the discrete autocorrelation at a single lag (T_{PRF}), if the demodulated received signal is represented as a function of ensemble number i , $I(i) + jQ(i)$, then the autocorrelation over an ensemble length of N is

$$\Gamma(T_{\text{PRF}}) = \sum_{i=1}^{N-1} [I(i) + jQ(i)] [I(i-1) - jQ(i-1)], \quad (1.20)$$

and the phase

$$\phi(T_{\text{PRF}}) = \tan^{-1} \left(\frac{\sum_{i=1}^{N-1} Q(i)I(i-1) - I(i)Q(i-1)}{\sum_{i=1}^{N-1} I(i)I(i-1) + Q(i)Q(i-1)} \right). \quad (1.21)$$

Note that the I/Q signals used in Colour Flow processors are often integrated over the depth of a gate, which reduces the samples along the gate to a single sample for each pulse in the ensemble.

The presence of the arctangent function in Equation 1.21 limits the phase estimation to the interval $(-\pi, \pi]$, which puts a restriction on the maximum velocity that can be measured

$$|\bar{v}| \leq c \frac{\bar{\omega}}{2\omega_0 \cos \theta} = c \frac{\pi}{2\omega_0 T_{\text{PRF}} \cos \theta} = c \frac{f_{\text{PRF}}}{4f_0 \cos \theta}, \quad (1.22)$$

which is equivalent to the Nyquist limit from Equation 1.13.

The variance of the spectrum can also be computed with the autocorrelation function

$$\sigma^2 \approx \frac{2}{T_{\text{PRF}}^2} \left(1 - \frac{|\Gamma(T_{\text{PRF}})|}{\Gamma(0)} \right), \quad (1.23)$$

but is less commonly displayed.

Since the flow direction typically varies across the 2D image, angle correction

is often not applied to accurately estimate the actual velocity value. Instead, Colour Flow is usually used to identify interesting flow regions which can then be quantified in detail in Pulsed Wave mode [261].

Significant accuracy improvements can be made by estimating the centre frequency of the backscattered signal rather than assuming that the centre frequency remains constant and is equal to the centre frequency of the transmitted pulse. Additionally, the estimation of both the Doppler shift and centre frequency shift can be made for every sample along the depth of the gate, instead of integrating the I/Q signals. Representing the I/Q signals as a function of ensemble number i and gate sample k , the velocity estimate incorporating these two ideas can be obtained from [194]

$$v \cos \theta = \frac{c}{2T_{\text{PRF}}} \cdot \frac{\tan^{-1} \left(\frac{\sum_{k=1}^M \sum_{i=1}^{N-1} Q(i,k)I(i-1,k) - I(i,k)Q(i-1,k)}{\sum_{k=1}^M \sum_{i=1}^{N-1} I(i,k)I(i-1,k) + Q(i,k)Q(i-1,k)} \right)}{\omega_0 \left(1 + \tan^{-1} \left(\frac{\sum_{k=1}^{M-1} \sum_{i=1}^N Q(i,k)I(i,k-1) - I(i,k)Q(i,k-1)}{\sum_{k=1}^{M-1} \sum_{i=1}^N I(i,k)I(i,k-1) + Q(i,k)Q(i,k-1)} \right) / 2\pi \right)} \quad (1.24)$$

where M is the number of samples contained along the depth of the gate.

Power Doppler

Power Doppler images display the integrated power spectrum of the Doppler signal instead of its mean Doppler frequency shift. While this does not provide quantitative measurements of velocity magnitude or direction, it is useful for detecting the presence of small flow. The images are computed from the zero lag of the autocorrelation function, which is clear from setting $\tau = 0$ in Equation 1.16,

$$\Gamma(0) = \int_{-\infty}^{\infty} P(\omega) d\omega. \quad (1.25)$$

The detection sequence is the same as used in Colour Flow imaging up to the point of computing the autocorrelation. The value of the Power Doppler signal is related to the number and size of the scattering particles, or blood cells, which is non-

linearly dependent on the blood flow velocity, shear rates, and hematocrit level [49, 277].

Compared to Colour Flow imaging, Power Doppler imaging provides several advantages. One critical difference is the noise appears differently. In Colour Flow imaging, the noise as a random process acts to introduce random phase angles into the measurement which may then appear as a random hue. The noise has low power compared to the desired Doppler signal, therefore, in a Power Doppler image, the noise appears over a small range of hues which can easily be visually ignored. This effectively allows the use of a larger gain without the Power Doppler image becoming dominated by noise. The greater sensitivity is useful for detecting small vessels and vessels with low flow velocity, however. Power Doppler also has greater sensitivity when flow within the sample volume occurs in multiple directions, which for Colour Flow will create frequency shifts that tend to cancel each other out when calculating the mean shift, while the Power Doppler integral will add the signal from each shift. Another difference between Colour Flow and Power Doppler modes is that the mean frequency of the Doppler signal will change as a function of the angle, which changes the velocity measurement for Colour Flow, while the energy of the signal does not depend on the angle and therefore does not affect the Power Doppler measurement. The last major advantage is that Power Doppler does not alias like Colour Flow, as the integral of the spectrum is the same whether the phase wraps around or not [198].

The primary disadvantage of Power Doppler compared to Colour Flow is that it does not provide measurements of direction or speed. The greater sensitivity of Power Doppler also makes it more susceptible to motion artefacts such as contraction of the heart organ shift during breathing [213].

1.5 Elastography Background

A brief overview of Elastography was provided earlier in this chapter in 1.1. That overview covered the basic concepts, clinical applications, available commercial systems, and some of the current limitations. This section will go into more detail about the governing principles and the various techniques used to infer tissue elasticity.

1.5.1 Theory

Elastography relies on the field of continuum mechanics. The following section describes how the motion of the material is related to the forces acting upon the material and its material properties. This section introduces some new notation that will be used throughout this thesis unless otherwise specified. Normal fonts denote scalar parameters while vectors are shown in bold lowercase and matrices in bold uppercase. In index notation, the Einstein summation convention is used where repeated indices are summed over. A brief description of index notation is provided in Appendix A.

There are two common descriptions of material motion; Lagrangian and Eulerian. The Lagrangian description studies the motion of a particle that is specified by its initial position. The Eulerian description studies a particle that occupies a specified region of space. In elastography the two descriptions are considered equivalent as the spatial fluctuations in displacement, stress, and strain, are much larger than the amplitudes of the displacements [232].

A fundamental law governing the mechanics of motion is the conservation of linear momentum over a volume V with surface S

$$\frac{\partial}{\partial t} \iiint_V \rho \frac{\partial \mathbf{u}}{\partial t} dV = \iiint_V \mathbf{f} dV + \iint_S \mathbf{T}(\mathbf{n}) dS, \quad (1.26)$$

where ρ is the mass density, \mathbf{u} is the displacement, \mathbf{f} is the body force per unit volume, and $\mathbf{T}(\mathbf{n})$ is the traction on the surface with outward unit normal \mathbf{n} .

The tractions acting on the surface of the volume can be described using the stress tensor

$$T_i = \sigma_{ji} n_j. \quad (1.27)$$

The conservation of angular momentum implies that the stress tensor is symmetric, reducing the number of independent stress components from nine to six.

Using Equation 1.27 and applying Gauss's divergence theorem to Equation 1.26, the equation of motion is obtained

$$\rho \ddot{u}_i = f_i + \sigma_{ij,j}. \quad (1.28)$$

The small deformations observed in elastography can be described in terms of the infinitesimal strain tensor

$$\epsilon_{ij} = \frac{1}{2} (u_{i,j} + u_{j,i}). \quad (1.29)$$

In a linear elastic material, the stress and strain are related through a generalization of Hooke's law

$$\sigma_{ij} = C_{ijkl} \epsilon_{kl}, \quad (1.30)$$

where \mathbf{C} is the fourth-order stiffness tensor. Due to symmetries in σ , ϵ , and \mathbf{C} , the number of independent components of \mathbf{C} is reduced from 81 to 21. It is the goal of elastography to identify the components of \mathbf{C} . To simplify the problem, the tissue is often modelled as an isotropic material, resulting in two independent material parameters

$$C_{ijkl} = \lambda \delta_{ij} \delta_{kl} + \mu (\delta_{ik} \delta_{jl} + \delta_{il} \delta_{jk}), \quad (1.31)$$

where λ and μ are the Lamé parameters, and δ_{ij} is the Kronecker delta (1 for $i = j$ and 0 otherwise). Using Equation 1.31, Hooke's law for isotropic materials can be written as

$$\sigma_{ij} = \lambda \epsilon_{kk} \delta_{ij} + 2\mu \epsilon_{ij}. \quad (1.32)$$

Young's modulus, the ratio of tensile stress to extensional strain, and Poisson's ratio, the ratio of transverse strain to axial strain, are related to the Lamé parameters as

$$E = \frac{\mu (3\lambda + 2\mu)}{\lambda + \mu}, \quad (1.33)$$

and

$$\nu = \frac{\lambda}{2(\lambda + \mu)}. \quad (1.34)$$

Conversely,

$$\mu = \frac{E}{2(1 + \nu)}, \quad (1.35)$$

and

$$\lambda = \frac{\nu E}{(1 + \nu)(1 - 2\nu)}. \quad (1.36)$$

The adiabatic compressibility of tissues is determined primarily by the molecu-

lar content of the tissue and intermolecular interactions [287]. Most tissues imaged by ultrasound are composed of 70 % to 80 % water. Consequently the hydration of soft tissues leads to near incompressible behaviour. The implications of incompressibility on the mechanical properties are Poisson's ratio is almost 0.5 ($\nu \approx 0.5$), through Equation 1.35 Young's modulus is almost three times the shear modulus ($E \approx 3\mu$), and through Equation 1.36 $\lambda \gg \mu$.

Combining the equation of motion described in Equation 1.28 with the definitions of the strain tensor in Equation 1.29 and Hooke's law in Equation 1.32 results in a description of the elastic response in terms of displacements

$$\rho \ddot{u}_i = f_i + \left[\mu (u_{i,j} + u_{j,i}) \right]_{,j} + (\lambda u_{k,k})_{,i}. \quad (1.37)$$

In a homogeneous region, where λ and μ are constant in space, Equation 1.37 can be written as

$$\rho \ddot{u}_i = f_i + \mu u_{i,jj} + (\lambda + \mu) u_{j,ji}. \quad (1.38)$$

In the case of dynamic motion, it is often convenient to represent the motion in terms of propagating waves. According to Helmholtz's decomposition theorem, any square integrable vector field in three dimensions can be resolved into the sum of a divergence-free field and a curl-free field [161]. The divergence-free component is often termed the distortion wave, transverse wave, or shear wave and consists of the component

$$\ddot{u}_i = \frac{\mu}{\rho} u_{i,jj} = c_s^2 u_{i,jj}, \quad (1.39)$$

where c_s is the shear wave speed. The curl-free component is often termed the dilatation wave, longitudinal wave, or compression wave and consists of the component

$$\ddot{u}_i = \frac{\lambda + 2\mu}{\rho} u_{i,jj} = c_p^2 u_{i,jj}, \quad (1.40)$$

where c_p is the compression wave speed [164]. For nearly incompressible materials, such as soft tissues, the compression wave is orders of magnitude faster than the shear wave. The shear wave is typically the component of interest in elastography as it is both easier to measure due to its slower speed, and because its properties are

more directly related to the shear modulus (the compression wave includes the first Lamé parameter).

1.5.2 Additional Modelling Considerations

The previous section provided theory for purely elastic materials because most elastography techniques measure quantities only related to linear elasticity. While in many cases this description is adequate [286], in general soft tissue behaviour is more complex and accounting for these differences can in some situations provide additional information and a more accurate fit to the measurements [173]. Examples of more complicated phenomena include viscoelasticity, anisotropy, and nonlinearity.

Viscoelasticity

Mechanical testing of soft tissue has demonstrated viscoelastic behaviour in which there is a time or frequency dependence for stress and strain [111]. Research on measuring viscosity using elastography techniques has suggested clinical relevance. For example, measurements of the dynamic modulus (complex shear modulus) demonstrated a power law behaviour as a function of excitation frequency in breast lesions, with malignant lesions showing a tendency for larger power law exponents, likely related to high vascularity and more liquid-like behaviour [293]. In addition, the creep behaviour of malignant breast tumours is thought to be related to the pH and collagen density of the tumour micro-environment [146].

In modelling viscoelastic solids, it is generally assumed that the elastic restoring forces are proportional to the displacement and the dissipative forces are proportional to the velocity. It is necessary to choose a tissue model to determine the viscoelastic parameters. Common models include Maxwell (spring and damper in series), Voigt (spring and damper in parallel), and Zener (spring and damper in series and in parallel with another spring) [111]. The appropriate model can depend on the material and the excitation conditions. For example, measurements on *ex vivo* bovine muscle and phantoms of agar gels using a transient planar shear wave excitation showed a Voigt model fit the data better than a Maxwell model [54]. In contrast, a different study of *in vivo* brain and liver tissues undergoing multi-

frequency sinusoidal excitation found that a Maxwell model provided a better fit compared to a Voigt model, while a Zener model provided the best fit [162].

Anisotropy

In soft tissues with highly organized structure, for example the alignment of muscle fibres along particular directions, the mechanics of the material will also depend on the direction of the organization. Measurements on human skeletal muscle have shown shear modulus in the direction parallel to the muscle fibres is greater than that measured perpendicular to the fibres [119]. Myocardial fibre orientation can be mapped by determining the direction in which a shear wave propagates with the greatest velocity, and could be used to detect myofiber disarray associated with cardiac pathologies such as postinfarction myocardial remodelling and hypertrophic cardiomyopathy [181]. White matter tracts in the brain have been observed to act as waveguides for propagating waves and can be modelled using a transverse isotropic model, which has potential for improving accuracy when monitoring clinical changes in the brain [273]. Elastography measurements of the breast in two patients with fibroadenoma and invasive ductal carcinoma found regions of elevated fibre organization corresponding to the two masses, however differentiation was not possible [291].

Nonlinearity

The generalized Hooke's law in Equation 1.30 assumes a linear relationship between stress and strain. However, this assumption only holds over a small range of strains for most soft tissues. For example, the stress-strain relationship is sometimes approximated by three regions; two quasi-linear regions with a relatively low elastic modulus at low stress and a relatively high modulus at high stress, and a region between where there is a constant change in the gradient [89]. The actual stress-strain relationship in real tissue is likely more complex.

There is significant diagnostic potential in differentiating tumours from measurements of nonlinear elastic properties. For example, compression tests of *ex vivo* prostate tissue samples showed a twofold increase in elastic modulus for cancerous tissue between pre-compression levels of 2 % and 4 %, while there was a negligible

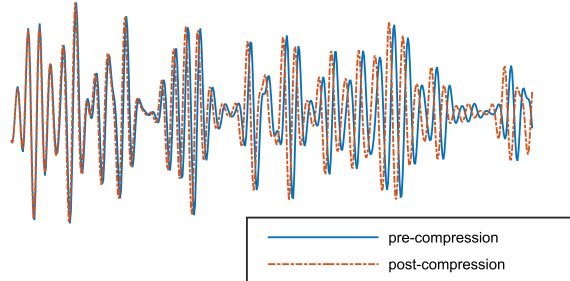


Figure 1.13: Example of an RF signal before and after tissue compression. The data were collected from an Ultrasonix SonixTouch scanner with a L14-5/38 linear array transducer while applying freehand compression with the transducer to a homogeneous polyvinyl chloride tissue mimicking phantom.

change over the same range for normal tissue and benign prostatic hyperplasia [171]. Another study examining *ex vivo* breast tissue compared five hyperelastic models and found almost all of the parameters corresponding to pathological tissues were between two times to two orders of magnitude larger than those from normal tissue, suggesting nonlinear elastography could distinguish between normal and pathological tissues with further potential to classify cancers, especially invasive lobular carcinoma [228]. An *in vivo* imaging study of ten patients with benign and malignant masses demonstrated the potential of nonlinear elastography in distinguishing between the two types, where no statistically significant difference was found between shear moduli for fibroadenomas and invasive ductal carcinomas, however a significant difference was found in the exponential stiffening parameter of a reduced Veronda-Westmann model describing the nonlinearity of the tissues [116].

1.5.3 Motion Measurement

Elastography uses measurements of tissue motion to infer the mechanical properties of tissues using the theory described in Section 1.5.1 and Section 1.5.2. The following section describes the measurement of tissue motion using medical ultrasound.

Speckle Tracking

As mentioned in Section 1.4.2, small scale acoustic inhomogeneities create speckle patterns. If it is assumed that a group of scatterers produces a unique speckle pattern, and the motion of the tissue results in corresponding motion of this pattern, then motion can be measured by matching the speckle pattern over successive signal acquisitions [130]. This assumption holds up well for uniform translation [43], or for small deformations (stretching or compressing) [207], but does not hold for general motion (e.g. for rotations greater than a few degrees [156]). For the motion conditions usually encountered in elastography it has proven adequate.

Figure 1.13 shows an RF signal of tissue before and after undergoing static compression using the probe face to indent the tissue. The post-compression signal clearly has a similar shape to the pre-compression signal. Looking at only a small region of the signal, the change between the two signals can be modelled as a time shift, or temporal translation. Dividing echo signals into small regions, or blocks, and determining the translation between blocks from images captured at different times by finding the best match is the basis of speckle tracking tissue motion measurement. Blocks are selected to be large enough to adequately capture the speckle pattern, while small enough such that the change in the block between frames appears as mainly a shift, instead of a stretch which would change the shape of the signal and make it difficult to match [74].

One method of determining the translation of a block between images is to define a pattern matching function which is maximized/minimized by varying the translation. The most commonly used method is maximizing the normalized cross-correlation, which with the common assumption that the RF is zero mean is computed between two signals s_1 and s_2 by

$$\underset{u}{\text{maximize}} R(u) = \frac{\sum_{i=-B/2}^{B/2} s_1(i) \cdot s_2(i+u)}{\sqrt{\sum_{i=-B/2}^{B/2} s_1(i)^2} \sqrt{\sum_{i=-B/2}^{B/2} s_2(i+u)^2}} \quad (1.41)$$

where i is the sample index, u is the integer sample translation, and B is the number of samples in a block. The normalized cross-correlation has proven to be accu-

rate and robust, however it can be computationally expensive, creating difficulty in tracking tissue motion at rates similar to the ultrasound frame rate. Also, the cyclical nature of the RF signals can lead to finding false matches, called “peak-hopping” errors due to the highest correlation coefficient occurring at a secondary peak in the correlation function [252]. Applying a spatial filter post-processing step can help to reduce the random peak-hopping errors [270]. Starting the search with large blocks and iteratively using smaller blocks (coarse-to-fine) is another approach to reduce the peak-hopping error with a small increase in computational load [62]. Both the speed and peak-hopping problems can be mitigated by bracketing the search region using the previously computed translation from the neighbouring block [345]. Speed can also be improved by using different matching functions with reduced computational complexity, such as minimizing the sum of absolute differences or sum of squared differences between signal blocks, where squared differences provide similar motion estimation precision to normalized correlation, while absolute differences generally performs with less precision [326].

So far this section has discussed estimating motion to the nearest digital sample. For common system parameters of 40 MHz sampling rate and 1540 m/s speed of sound, the spacing between samples computed using Equation 1.1 is 19.25 μm . Often a finer precision is desired so interpolation is used. One option is to interpolate between the samples of the RF signals, however this becomes increasingly computationally expensive for finer precision [253]. Alternatively, the peak of the correlation function can be estimated using discrete computations of the correlation coefficient, either exactly using sinc interpolation, or more commonly using parabolic or cosine interpolation between the three largest samples. Parabolic and cosine interpolation methods are popular because they are computationally inexpensive, however they introduce cyclical bias errors [57].

A popular alternative to cross-correlation peak searching is phase-based tracking. If the RF signal, $s(t)$, is represented analytically

$$\hat{s}(t) = s(t) - j\check{s}(t), \quad (1.42)$$

where $\check{s}(t)$ is the one dimensional (1D) Hilbert transform of $s(t)$, then the magnitude of the complex cross-correlation between two acquisitions will contain the same

maximum as the RF cross-correlation function, and the phase of the complex cross-correlation will cross zero at the location of the maximum [196]. Alternatively, if baseband I/Q signals are used, the phase of the complex cross-correlation is proportional to the displacement at the location of the maximum [226]. The phase-based methods attempt to find the shift that produces a phase angle of zero (for analytic signals), or alternatively finds the phase angle between the two signals (for baseband signals). This second description is reminiscent of the phase-based tracking in Doppler Colour Flow, but in this case only two images are used instead of the several measurements making up a Colour Flow ensemble. Removing T_{PRF} from Equation 1.24 produces a measurement of displacement along the axial beam direction. Phase-based speckle tracking which operates on I/Q data produces a mathematically equivalent result using analytic RF signals, and further, is mathematically equivalent to cross-correlation speckle tracking if it is assumed that the phase varies linearly and that motion produces only shifts of the RF signal [194]. For typical signal-to-noise ratio (SNR) in elastography imaging scenarios (≈ 30 dB) and small displacements ($< 25 \mu\text{m}$) the phase-based Doppler algorithms can provide similar performance to normalized cross-correlation speckle tracking with the advantage of approximately an order of magnitude increase in computation speed [254]. One challenge of using the phase-based tracking method for elastography is aliasing which will occur for any displacement exceeding $(c\pi)/(2\omega_0)$ which is typically around 0.25 mm to 1.0 mm. Aliasing can be reduced by using the neighbouring block's displacement as an initial guess in an iterative Newton search for the root of the cross-correlation phase [251].

While most speckle tracking methods assume that the speckle pattern does not change due to motion, under large deformations it may be necessary to remove the distortions in the pattern. One approach leads to a model that shows the reference image is a filtered version of a motion corrected image, under the assumptions of a linear image formation model and that acoustic impedance is not affected by motion. The filter is dependent on the motion, and corrections for the speckle changes can be applied by solving for an affine transform that minimizes the difference between the filtered image and the reference image [202]. Companding is another approach which warps the reference image by first applying a coarse 2D shift and stretch, then a fine scale 2D shifting, before a final pass of correlation based motion tracking

along the axial direction [60].

A different approach to speckle tracking is to track specific features detected from the speckle patterns. Features of the RF signal such as the zero crossings can be detected using linear interpolation [298], or the peaks using the zero crossings of a wavelet transformed RF signal [95]. Instead of providing the motion measurement for a block of the image, feature tracking methods provide a measurement for every feature location. This generally leads to a higher spatial density of measurements, although the spacing may be nonuniform. The feature tracking algorithms are less susceptible to signal decorrelation due to stretching, however the algorithms can be more sensitive to signal noise.

A continuous representation of the RF data, for example by fitting a piece-wise cubic spline, allows for an analytical solution to the best match of the pattern matching function. Blocks of discrete data from the tracked frame can be compared to the continuous reference frame, and the sum squared error between the two can be minimized by finding where the derivative is zero [325]. This method provides low bias and variance in the motion estimates, however finding the roots of the fifth order polynomial representing the analytical derivative of the sum squared error is generally more computationally demanding compared to other speckle tracking techniques. The size of the signal block used to compute the squared error can be reduced all the way down to a single sample, providing high resolution and comparable accuracy and precision to typical block sizes (on the order of 1 mm), with the trade-off of greater sensitivity to signal noise [346]. Representing both the reference and tracked signals using splines improves accuracy and precision but is computationally more expensive [253].

Speckle tracking methods can be extended to measuring 2D (adding lateral) and 3D (adding elevational) displacement vectors by extending the pattern matching search to those directions, with the exception of phase-based methods because the oscillations at the carrier frequency of the pulsed wave normally only occur along the beam (axial) direction, which means that phase changes cannot be observed in the non-axial directions. The best match (usually the peak of the cross-correlation function) can be found independently in each direction [347], iteratively in each direction [105], or interpolated by fitting a 2D/3D function to the correlation coefficients [67, 349]. The accuracy and precision of the estimates in the lateral and

elevational directions are poor compared to the axial direction, which is in large part caused by a larger sample spacing (typical element pitch is on the order of $300\ \mu\text{m}$ compared to digital sample spacing of $19.25\ \mu\text{m}$), poorer beam resolution in the non-axial directions [195], and a typical lack of phase information in the non-axial directions [42]. Additional RF lines in the lateral and elevational directions can be interpolated to improve the sample spacing [165]. The resolution in the non-axial directions can be improved using a synthetic aperture beamforming approach, however this requires a system that can save pre-beamformed received RF data for each element [167]. Phase information can be introduced into the non-axial directions to improve tracking accuracy. One approach introduced phase information in the lateral direction synthetically by removing either the negative or positive half of the lateral spectrum [66]. Another approach that several groups have investigated is modifying the apodization weightings used in beamforming to introduce oscillations in the other directions [15, 149, 186, 302].

A different approach for estimating 2D and 3D motion vectors is to combine axial measurements from overlapping beams from different directions, often referred to as angular compounding. This takes advantage of the superior measurement accuracy of the axial speckle tracking and uses known geometry of the beams to reconstruct the components of the motion vector mathematically. As only measurements along the beam are used, this technique can also be used with conventional Doppler based velocity tracking and is termed Vector Doppler. The different axial beams can be generated electronically by introducing beamforming delays and using multiple transmit and receive frames at different angles [125, 268], or a single transmit and multiple receive angles computed digitally for a faster sampling rate but poorer SNR [170, 310]. Instead of electronic beamforming methods, multiple angular frames can be created by moving a transducer. For example, a phased array or curvilinear array transducer can be mechanically translated laterally, where each beam line in a conventional image can be rearranged to create an angled image from each translated location [313]. Another example is rotating a transducer around the ROI [211]. Multiple axial beam angles can also be acquired using multiple transducers directed towards the same ROI [4, 33, 90]. An advantage of the moving transducer and multiple transducer techniques over electronic beam steering is that larger inter-beam angles, and thus greater measurement accuracy, can be

achieved. A disadvantage is that the moving and multiple transducer techniques require calibration to spatially align the measurement from each transducer location. The geometry of electronic beam steering methods lends itself well to imaging superficial tissue, such as the carotid arteries, but not for deeper tissue such as liver. The opposite is generally true for moving and multiple transducer methods.

Vibration Doppler

Conventional Doppler, as described in Section 1.4.6, measures the average velocity of a steady and slowly varying flow, and is not suitable for measuring vibrating tissue. While Colour Flow algorithms can be modified to measure the displacement through each gate or block between individual frames as described in the previous section, this requires access to the unprocessed I/Q data. It is still possible however to estimate steady state vibrations using the output of the Doppler processing (i.e. the Doppler spectrum). A vibrating tissue scatterer modulates the Doppler power spectrum, with harmonics spaced proportional to the vibrating frequency and weighted by Bessel functions of the first kind [133]. The modulation parameter of the Bessel functions is related to the vibration amplitude as

$$\beta = \frac{2\xi\omega_0}{c_0}, \quad (1.43)$$

where ξ is the vibration amplitude along the ultrasound beam axis, ω_0 is the centre frequency of the ultrasound pulse, and c_0 is the propagation speed of the ultrasound pulse.

Estimating the modulation parameter, β , leads to an estimate of the vibration amplitude. There are two common methods to do this; one based on estimating the standard deviation of the power spectrum, and the other based on ratios of spectral harmonics. The standard deviation of the Doppler power spectrum is related to the modulation parameter through [144]

$$\beta = \sqrt{2} \frac{\sigma}{\omega_e}, \quad (1.44)$$

where ω_e is the frequency of the vibration.

The amplitude ratio of adjacent Bessel bands in the Doppler power spectrum

are related to the modulation parameter through [339]

$$\frac{A_{i+1}}{A_i} = \left| \frac{J_{i+1}(\beta)}{J_i(\beta)} \right|, \quad (1.45)$$

where A_i is the amplitude of the i th spectral band, and J_i is the i th order Bessel function. The ratio can be computed as a function of β beforehand, and then used to estimate β during the experiment.

The phase of the vibration can be estimated directly from the phase of the Doppler spectra [339].

1.5.4 Elasticity Estimation

Methods for generating images depicting tissue elasticity have been in development for over 20 years, resulting in a diverse set of techniques. The methods can be roughly categorized by the type of tissue excitation applied (static/dynamic) and the type of measurement provided (relative/absolute).

Strain

Under conditions of purely uniaxial compression, from Equation 1.32 and Equation 1.33, Hooke's law reduces to

$$E = \frac{\sigma_{11}}{\epsilon_{11}}. \quad (1.46)$$

Thus, the problem of determining tissue elasticity is reduced to finding the ratio of stress to strain in the direction of compression.

Strain can be computed from ultrasound based motion measurements (see Section 1.5.3) using the slope from a least-squares line fit over a small spatial window [155]. However, it is often difficult to measure the stress distribution in the tissue. A common assumption is a uniform axial stress field. Using a large compressor area can help mitigate errors in this assumption. Since the magnitude of the stress is usually not known, only a relative estimate of the elasticity is possible. Commonly the strain is displayed instead of the relative Young's modulus [233].

Instead of using an extra apparatus for applying compression, it is common to use the ultrasound transducer face to apply quasi-static tissue compression [123]. In

this situation, the pressure is generally higher near the transducer face compared to deep tissue, resulting in a “hardening” artefact which increases apparent elasticity with increasing depth [234].

The relation between strain and stress given in Equation 1.46 applies to the case of uniaxial compression, but achieving this type of loading inside the body is difficult in practice. More generally, the relation between axial strain and stress is

$$\epsilon_{11} = \frac{1}{E} (\sigma_{11} - \nu\sigma_{22} - \nu\sigma_{33}). \quad (1.47)$$

Poisson’s ratio is usually assumed to be approximately 0.5 because most soft tissues are nearly incompressible, leaving the three stresses and Young’s modulus as unknown. It is possible to attempt to estimate the three components of stress using an analytical model and knowledge of the boundary conditions and compressor geometry [256]. However, the stress concentrations caused by elastic heterogeneities are difficult to predict because the underlying Young’s modulus distribution is unknown, and hence the 1D model of Equation 1.46 is usually assumed for strain elastography.

The displacement estimation used for computing strain images produces several artefacts. For example, horizontal “zebra” stripes, caused by cyclical bias errors introduced by sub-sample interpolation in correlation based speckle tracking, and smaller “worm” artefacts caused by large signal overlaps in speckle tracking creating correlated noise patterns [235]. The mechanical compression of the tissue also causes compression of the backscattered signal, meaning the block matching can only match in a certain region of the block, where the location of the match will be biased toward the higher amplitude region of the block [58]. This causes errors in strain computation because the distance between displacement estimates is assumed to be the distance between block centres. Methods to help mitigate this location error include reducing the dynamic range of the echo signals [11], scaling and shifting the pre-compression signal to improve coherence during block matching [60], or correcting for the location of the estimates [188].

In addition to inferring relative Young’s modulus distributions, strain imaging has other clinical uses, such as using shear strain to assess mobility breast lesions to help differentiate between malignant and benign lesions [314], or in measuring

poroelastic behaviour [271]. Creep tests using strain imaging have been used to estimate time constants associated with the extracellular environment of breast lesions, where a shorter time constant has been demonstrated for malignant masses [265].

Another class of elastography methods using strain measurements is directed toward finding a relative distribution of the tissue elasticity based on solving partial differential equations. Starting with Equation 1.28 under conditions of static compression and no body forces, the equation of equilibrium is obtained

$$\sigma_{ij,j} = 0. \quad (1.48)$$

Combining compatibility with Hooke's law as in Equation 1.32, equations relating, strain, spatial derivatives of strain, and spatial derivatives of shear modulus can be obtained. One approach solves the equations under plane strain conditions to find the spatial distribution of the relative shear modulus over 2D using finite differences [294]. A different approach solves the equations under plane stress conditions for the gradient of the relative shear modulus in 2D and calculates the logarithm of the relative shear modulus by integrating the gradient over a path using the relationship between the logarithm and its derivative [305]

$$\frac{\partial \log \left(\frac{g(x)}{g(x_0)} \right)}{\partial x} = \frac{1}{g(x)} \frac{\partial g(x)}{\partial x}, \quad (1.49)$$

where $g(x_0)$ represents a reference shear modulus value at location x_0 . Both of these approaches suffer from requiring third order derivatives of noisy displacement measurements.

An alternative approach that reduces sensitivity to derivatives is using a weak formulation of the equations of motion and elasticity in a finite element method (FEM). The elasticity can be determined using an iterative approach to minimize a functional summing the squared difference between the measured tissue displacements and the displacements computed by the FEM using the current estimate of elasticity [154]. While an initial guess is required for the elasticity, a spatially uniform value can be used and does not affect solution [86]. The elasticity is updated for each iteration by computing the gradient of the functional with respect to the unknown elasticity parameters (e.g. the Young's modulus for every finite element),

resulting in a Jacobian matrix. The columns of the Jacobian matrix, which correspond to the gradient of the functional with respect to a single elasticity parameter, can be computed by solving the FEM forward problem where the forcing function is changed to the product between the current FEM computed displacement field and the partial derivative of the stiffness matrix with respect to the elasticity parameter. This means the Jacobian takes N forward FEM solutions, where N is the number of elements, which is computationally demanding. Instead of the computing the Jacobian, the gradient can be obtained more efficiently using the adjoint method which only requires two forward problem solves per iteration independent of the number of elasticity parameters [225]. Usually the iterative FEM approaches ignore the lateral tissue displacement component because of the poorer displacement measurement accuracy in this direction and the sensitivity of the inverse problem to errors in displacement measurement. Regularization can be used to help solve the equations to compensate for missing data and noise. Typically a plane strain model is assumed to transform the elasticity problem to 2D to accommodate displacement measurements obtained using 2D ultrasound. The FEM problem can also be solved directly by rearranging the equations in terms of the elastic parameters, since the discretized system of equations is linear with respect to the elastic parameters [354].

A slightly different use of FEM in an iterative approach has been proposed to obtain a relative modulus distribution based on Equation 1.47 using strain measurements along the axial direction [255]. The method uses an initial guess for the modulus distribution and uses a 3D FEM to estimate stresses. The modulus is then updated at every pixel location using the estimated stresses and the axial strain measurements, and the process is repeated until the modulus converges. The method requires an assumption for the Poisson's ratio which is typically assumed a constant 0.495.

There has been some work on creating absolute rather than relative measurements of Young's modulus by also measuring the stress distribution over the area of contact between the ultrasound transducer and the tissue. Pressure sensors can be mounted around the outside of the transducer and used to improve estimating 3D stress field [344]. Similarly, a thin film pressure sensor can be placed directly under the transducer with a small reduction in ultrasound signal quality [318]. Instead of using pressure sensors, a thin compliant layer with known elasticity can be placed

between the transducer and the tissue. The strains can be measured in the compliant layer in the same way as is done in tissue, but since the elasticity is known the stress may be computed. This may be accomplished using Equation 1.46 and assuming constant stress along each ultrasound beam line [201], or using a 3D FEM model of the compliant layer with some assumptions about the underlying tissue [160]. While these methods allow for quantification of elasticity values and to correct for nonuniform pressure at the surface of the tissue, the methods cannot reliably predict the stress concentrations caused by inclusions.

Amplitude

Similar to strain imaging, amplitude based elastography displays relative differences in tissue stiffness based on displacement measurements. These methods use a dynamic excitation source as opposed to a static source in strain imaging, and the maximum amplitude of the displacement over the measurement time is displayed at each location. An increase in tissue stiffness results in a decrease in displacement amplitude. For example, an inhomogeneity with an area 0.5 % of the surrounding tissue with a Young's modulus three times greater than the surrounding tissue can be detected by a 20 % drop in shear wave vibration amplitude [113].

“Sonoelasticity” imaging, an amplitude based elastography method, applies steady state vibrations over a band of about 20 Hz to 1000 Hz to the tissue. The amplitude of the wave pattern is measured using the vibration Doppler technique of estimating the power spectrum standard deviation as described in Section 1.5.3. Sonoelasticity methods typically create shear waves in the tissue by applying vibrations on the surface that radiate like a point source such as using an acoustic horn with a tapered cone [183] or a metal rod acting like a piston [312]. Standing waves in the vibration field produce modal patterns with areas of increased or decreased displacement which interferes with the detection of elastic inhomogeneities. To reduce this effect, multiple excitation frequencies can be applied simultaneously to excite a greater number of eigenmodes, which will tend to smooth the overall displacement field [312].

An alternative to using vibrating sources to produce shear waves in tissue is to use the acoustic radiation force (ARF) to create impulsive excitations. High in-

tensity acoustic beams are focused in the tissue using the same ultrasound transducer as used for B-MODE imaging and displacement tracking, creating localized displacements on the order of tens of microns over a volume approximately 1 mm^3 in size [222]. Tissue displacements are typically tracked using correlation based techniques [254]. The advantages of ARF techniques are that the nonuniform stress and modal artefacts seen in the stain and sonoelasticity methods respectively are eliminated, the force can be applied anywhere the imaging system can focus, and no extra equipment is required for applying the tissue excitation. The disadvantages are risks of tissue heating, limiting the number of pushing pulses, and the requirements on the ultrasound scanner being able to produce the high voltages and beam sequences to create the push pulses.

Transfer Function

Considering the tissue as a linear dynamic system, transfer functions of the tissue motion can be used to describe its mechanical response as a function of frequency. The tissue motion can be described by [319]

$$\mathbf{M} \frac{d^2 \mathbf{u}(t)}{dt^2} + \mathbf{B} \frac{d\mathbf{u}(t)}{dt} + \mathbf{K} \mathbf{u}(t) = \mathbf{f}(t), \quad (1.50)$$

where $\mathbf{u}(t)$ and $\mathbf{f}(t)$ are vectors of tissue displacement and force as a function of time, and \mathbf{M} , \mathbf{B} , and \mathbf{K} are matrices representing the mass, damping, and stiffness of the tissue. The matrices are dependent on the mechanical model, but do not have to be specified if model parameters are not desired. The Fourier transform of Equation 1.50 yields the transfer function at a specified location in the tissue

$$H(\omega) = \frac{u(\omega)}{f(\omega)} = \frac{1}{-\omega^2 m + j\omega b + k}. \quad (1.51)$$

From Equation 1.51 it is clear that at $\omega = 0$ the transfer function contains information only about the compliance (inverse of stiffness) of the tissue. Similar to strain imaging, the force is usually not known so a relative estimate of compliance can be obtained by replacing the force with a reference displacement

$$f = k_r u_r. \quad (1.52)$$

If the reference stiffness is set to unity, then the relative compliance between the reference and the i^{th} displacement location is [281]

$$\left|H_r^i(0)\right| = \left|\frac{u_i(0)}{u_r(0)}\right|. \quad (1.53)$$

The transfer function can be computed from the power spectral densities of correlation speckle tracking measurements

$$H_r^i(\omega) = \frac{P_r^i(\omega)}{P_i^i(\omega)}, \quad (1.54)$$

where $P_r^i(\omega)$ is the cross-spectral density between the reference and i^{th} displacement, and $P_i^i(\omega)$ the spectral density of u_i .

Usually it can be assumed that over a small band of low frequencies that the magnitude of the transfer function is flat and therefore the stiffness estimate can be averaged over this band to reduce errors due to measurement noise. A measure of confidence can be used to weight the transfer function over the low frequency band. The coherence function indicates what portion of the input energy from u_r at frequency ω appears at the output in u_i at the same frequency [281]

$$C_r^i(\omega) = \frac{\left|P_r^i(\omega)\right|^2}{P_i^i(\omega)P_r^r(\omega)}. \quad (1.55)$$

The coherence function covers the interval $[0, 1]$, where a value close to 1 indicates a linear system with high SNR. The final weighted intensity value for display can be computed via [210]

$$I_i = \frac{\int_{\omega_1}^{\omega_2} C_r^i(\omega) \cdot \left|H_r^i(\omega)\right| d\omega}{(\omega_2 - \omega_1) \int_{\omega_1}^{\omega_2} C_r^i(\omega) d\omega}, \quad (1.56)$$

where ω_2 and ω_1 are the upper and lower bounds of the frequency band. Typically the excitation is band-pass filtered white noise (ranging from 1 Hz to 20 Hz), applied either via the transducer or through a separate shaker. Compared to strain imaging, transfer function images have demonstrated lower variance and greater accuracy

which may be due to including more temporal and frequency information in the estimation [319].

The magnitude and phase of the transfer functions over a broader frequency range can also be used to estimate the viscoelastic parameters of a material model [97]. This is typically done using a mechanical vibration source. An alternative method is to use the ARF to generate a step response in the tissue. The temporal derivative of the step response is the impulse response, and the Fourier transform of the impulse response is the transfer function between the applied force and tissue displacement [110].

Transient Shear Waves

As mentioned in Section 1.5.1, the behaviour of shear waves is directly related to tissue elasticity. Transient techniques use a short duration, impulse-like excitation to generate a shear wave. The propagation of the wave is measured using speckle tracking techniques over time as the wave travels through the ROI, and the speed of the wave is inferred from the motion measurements. From Equation 1.39, the shear wave speed is proportional to the square root of the shear modulus. Typical shear wave speeds in soft tissue are between 1 m/s to 5 m/s, so the motion must be sampled at a relatively high rate to capture the evolution of the wave over time. The propagation speed of the ultrasound pulse is about three orders of magnitude greater than the shear wave speed, so it is fast enough to sample the motion, however the sequential nature of forming a 2D image results in a frame rate which is too slow to sample the shear wave. Instead the wave can be tracked by using rapid interrogations with a single beam line, repeated with different laterally spaced beam lines across the ROI [223]. Alternatively, full channel parallel receive beamforming hardware can be used which can sample the entire ROI using a planar transmit wave [310].

Mechanical excitation can be used to generate the shear waves, such as using a single element transducer as a piston [283]. The shear wave speed is estimated using linear regression on the phase of the wave as a function of depth, and can be related to the shear modulus through Equation 1.39. The downside of the regression technique is that spatial information is lost (i.e. elastic inhomogeneities which would result in different shear wave speeds along the imaging depth are not captured). This

approach is the basis for the commercial FibroScan and FibroTouch systems used for liver fibrosis examination.

A similar approach is used for 2D imaging, where the shear wave is generated by applying a short pulse using the face of a linear array or two rods on either side of the array in the elevational direction, which creates a shear wave that propagates primarily along the beam axis and does not significantly diffract in the elevational plane [32, 284]. The 2D approach retains spatial information by estimating the shear modulus algebraically using a simplified Helmholtz equation, based on Equation 1.39, using only the axial component of motion and ignoring out of plane derivatives. The simplified Helmholtz equation can be transformed to the frequency domain, either to restrict the inversion to a specific band where the SNR is high, or to examine the complex wave field for viscoelastic parameter estimation [54].

Transient shear waves can also be created using the ARF which creates a point-like source that radiates in an approximately cylindrical shape [288]. The shear modulus can be estimated using the same simplified Helmholtz algebraic inversion [221], however due to the sensitivity to noise when taking second-order derivatives in the algebraic Helmholtz approach, time-of-flight methods have become a popular alternative. The time-of-flight methods assume lateral propagation of the ARF induced shear wave, and measure the time for the peak displacement to occur at laterally spaced locations (adjacent beam lines) [241]. It is also possible to track the shear wave propagation along the pushing beam axis, however it is more challenging as it can be difficult to track the motion along this path, and the time-of-flight has a depth dependence and is affected by the spatial distribution of the ARF, leading to greater variance in the elasticity measurements [329]. Another method for generating transient shear waves is to apply the ARF push at different depths in rapid succession (faster than the speed of the shear waves). The constructive interference of the shear waves from each source creates a planar shaped wave front with greater amplitude, termed the “Mach cone” [34].

In most ARF techniques, an image is constructed from repeated interrogations to enable imaging a large field of view and to average measurements to increase SNR. A single focal ARF excitation can enable measurement over an area approximately $2\text{ cm} \times 2\text{ cm}$ [223], with the axial extent limited by the ARF depth of focus and the lateral extent limited by shear wave attenuation. A “Mach cone” type of excitation

can enable a larger measurement region, however repeated interrogations are still usually required as measurement along the push beam is unreliable because there is no lateral wave front to track and it is still desirable to improve SNR through averaging [311].

In the transient ARF techniques described thus far, each interrogation consists of a single push beam and several tracking beams spaced laterally around the push location to measure the time-of-flight. It is also possible to measure the shear wave time-of-flight by using a single tracking beam at a fixed location and sequentially moving the push beam laterally around the tracking location. This method has the advantage of cancelling out position dependent speckle bias in the motion tracking because the motion is always biased in the same way when the tracking beam is fixed. The disadvantage is that several pushes need to be applied which generally increases the acquisition time [134].

In an effort to increase acquisition speed for transient ARF techniques, a pushing strategy that combines unfocussed ARF beams from multiple small spaced sub-apertures is used to generate multiple shear waves throughout the ROI, a technique termed comb-push [295]. The resulting waves interfere in a complicated pattern making shear wave speed estimation more difficult, however the tissue motion can be directionally filtered to examine waves only propagating from left-to-right and from right-to-left. The wave speed can be easily detected from each of these filtered images and averaged to create a 2D elasticity image from a single ARF interrogation.

In a technique specifically focused on measuring the frequency dependence or viscoelastic properties of tissue, shear wave dispersion ultrasound vibrometry (SDUV) applies a narrow-band oscillatory ARF by modulating the acoustic amplitude. Similar to time-of-flight measurements, the shear wave is interrogated at different laterally spaced locations, but speed is calculated using the known excitation frequency and by measuring the phase change of the wave over the lateral distance (i.e. the spatial frequency) [63]. This is typically repeated for different excitation frequencies to measure the shear wave dispersion.

The SDUV technique uses excitation at a known temporal frequency and measurements of the spatial frequency of the shear wave to determine the shear wave speed. It is also possible to do the opposite by using an excitation of known spatial frequency and measurements of the temporal frequency, a technique termed spa-

tially modulated ultrasound radiation force (SMURF) [203]. In SMURF, the ARF is modulated in the lateral direction, x , taking the form

$$F(x) = (1 + \cos(kx))\psi(x), \quad (1.57)$$

where $\psi(x)$ is a smoothly varying, positive envelope function, such as a Gaussian. The modulation can be created by weighting the transmit apodization with a pair of laterally spaced Gaussians, intersecting two unfocussed (planar) beams at oblique angles to each other, or by rapidly firing multiple push beams laterally. The resulting axial velocity, which can be measured using speckle tracking techniques, takes the form

$$\dot{u}_y(x, t) = (1 + \cos(kx) \cos(\omega t))\psi(x). \quad (1.58)$$

After finding the temporal frequency, ω , from the axial velocity at any tracking location, the shear wave speed can be calculated at the focus of the applied force using

$$c_s = \frac{\omega}{k}. \quad (1.59)$$

By varying the spatial frequency of the force, several temporal frequencies can be examined to observe the dispersion in a similar manner to SDUV.

Steady-State Shear Waves

Steady-state elastography techniques use a continuous harmonic excitation to generate shear waves in tissue. Instead of directly measuring the shear wave propagation speed as in transient techniques, steady-state techniques measure the shear wavelength or wave number (inverse of wavelength) to relate motion measurements to elastic properties. The wave speed is related to the wave number as shown in Equation 1.59. From Equation 1.39, the wave number is inversely proportional to the square root of the shear modulus.

The tissue is typically excited using vibrations applied to the tissue surface at frequencies ranging from 10 Hz to 1000 Hz [138]. The cyclical nature of the excitation has made it popular amongst MRE techniques as the acquisition can be synchronized with different phases of the excitation [214, 278]. For ultrasound elastography, tissue motion may be sampled using a sequence similar to Colour Flow

Doppler and compensated using the known acquisition delays [21], or captured using full parallel receive hardware [205].

One class of elasticity estimation methods using steady state shear waves is algebraic inversion, which directly solves the partial differential equations describing elastic wave motion for the elastic parameters. One approach is to measure and model the full wave field, however this approach can be sensitive to tissue incompressibility since second derivatives of displacement are multiplied by a relatively large value (see Equation 1.38) [290]. If it is assumed that the tissue is fully incompressible, then the motion field will only contain shear waves and the shear modulus can be recovered by measuring only one component of the motion vector over a volume using Equation 1.39 [231]. Instead of ignoring compression waves, they can be removed completely by applying the curl operator to the displacement field before inversion, however this requires measurement of the full 3D vector field over a volume and results in taking third order spatial derivatives of measured displacement for the solution [292].

Similar to the strain methods, the equations of motion can also be described using a weak formulation and discretized using the FEM. Again, a functional minimizing the squared error between the measured displacements and the displacements produced by the FEM for the current elasticity estimate can be iteratively solved [321]. The adjoint method can also be applied to conditions with steady state harmonic excitation to reduce the computational load of the gradient calculation, as was demonstrated for a 2D plane stress condition [352]. The equations of motion can also include viscoelastic parameters, however the solution of these parameters can be more sensitive to noise [96].

Instead of solving an optimization problem iteratively, the FEM problem can also be solved directly by rearranging the equations in terms of the elastic parameters. The equations can be rearranged to directly solve for both Lamé parameters, however this approach can be sensitive to noise for tissue that is nearly incompressible [274]. Instead, the tissue can be assumed to be nearly incompressible with a guess for Poisson's ratio which leaves Young's modulus as the only unknown (optionally also including viscosity) [99]. Another approach to dealing with near

incompressibility is to introduce a pressure term

$$p = \lambda u_{k,k}, \quad (1.60)$$

where λ is the first Lamé parameter and pressure is treated as an unknown quantity [243]. This pressure term can be substituted into Equation 1.37 and discretized using the FEM, avoiding the homogeneity assumption, which has been shown to introduce artefacts into the elasticity estimation. Sparsity inversion has been proposed to help condition the problem with the additional unknowns introduced by including the pressure term [135]. The pressure term can be eliminated to reduce the number of unknowns by applying the curl operator. The curl can be applied directly to Equation 1.37 before being discretized, again avoiding the assumption of local elastic homogeneity [136]. These methods generally require measurement of the full motion vector over a volume. Alternatively, the compression and coupling terms can be removed, while still avoiding the homogeneity assumption, resulting in independent equations relying on only one component of the motion vector [137].

A different approach to determine the elasticity is to extract the wavelength from the measured displacement data. The wave length can be determined by measuring the length between peaks or troughs of the waves [20, 180, 339], fitting a sinusoid along a profile of the displacement data [88, 337], or by computing the gradient of the phase of the wave along a direction [184, 199]. The drawback of these methods is that they assume that the shear wave is propagating locally as a plane wave and they require an estimation of the propagation direction.

The local frequency estimation (LFE) algorithm estimates the wave number of the measured displacement without the assumption of plane wave propagation. As mentioned previously, under the assumptions of incompressibility and homogeneity, the tissue motion can be described with the Helmholtz equation taking the form of Equation 1.39. Oliphant *et al.* [230] showed that the Helmholtz equation can be solved using the ratio of two filters that are related through spatial differentiation. The LFE algorithm makes use of a special case of these pairs of filters: lognormal quadrature filters defined as the product between radial and directional components. A series of filter pairs with different centre frequencies and bandwidths are used to obtain a wideband estimate of the wave number [163, 214]. The LFE approach may

use only a single component measured over a volume or a 2D plane if out-of-plane spatial derivatives are assumed to be negligible. If all components of the motion vector are measured, LFE can be applied to each direction and the results can be averaged [199]. A disadvantage of the LFE approach is that the spatial resolution of the estimate is dependent on the centre frequency and bandwidth of the filter pair that best match the wave number.

While the LFE algorithm naturally contains directional filtering through its filter definition, the techniques based on a plane wave assumption can be improved by adding a directional filtering preprocessing step which helps to reduce the complexity of the wave field from interfering wave fronts. Further, low-pass and high-pass filters can be applied to reduce noise in the displacements and the effects of the compression wave, respectively [200].

Instead of using a directional filter to remove the effects of interfering wave patterns, a model can be designed that incorporates waves travelling in different directions. This approach is used in the Travelling Wave Expansion technique, where the general solution to a Helmholtz decomposition of the displacement field is represented as an integral over a unit sphere [22]

$$f(\mathbf{x}) = \iint_S a(\phi, \theta) e^{jk(\mathbf{n}(\phi, \theta) \cdot \mathbf{x})} d\phi d\theta, \quad (1.61)$$

where this function represents waves with amplitude a and wave number k travelling in the direction \mathbf{n} . The problem is solved by choosing values for a and k that minimize the error between the model and the measured data over small regions assumed to have constant mechanical properties.

In another technique, the centroid of a thresholded spatial Fourier transform of the displacement field is used to determine the principal wave number in a region [204]. The advantage of this method is that it performs well in the presence of noise in the displacement measurements compared to LFE. The disadvantages are that location information is lost so the entire region must be assumed homogeneous, and the region must be large enough to contain at least one wavelength.

The above techniques make use of both the magnitude and phase of the wave motion. When only the amplitude of the waves is available, such as when measur-

ing motion using the vibration Doppler method described in Section 1.5.3, special wave patterns proportional to the shear wavelength or speed can be generating using two vibration sources. When two sources are placed on either side of a ROI and driven at the same frequency and amplitude, the technique is referred to as the static interference approach, and the amplitude of resulting interference pattern has a spatial period equal to half the shear wavelength, assuming plane waves are emitted by the vibration sources. When the two sources are driven with a small frequency difference, one at ω and the other at $\omega + \Delta\omega$, the pattern moves slowly towards the low frequency source at a speed proportional to the shear wave speed

$$c_{\text{pattern}} \approx \frac{\Delta\omega}{2\omega} c_s. \quad (1.62)$$

Because a small frequency difference is used, the observed speed is less than the true shear wave speed, resulting in the term crawling waves, and can be measured without the special techniques used for transient shear wave measurement [338].

Time Reversal

Time reversal elastography measures tissue motion excited by a short transient excitation to obtain information about the impulse response of the tissue at a given location. The technique makes use of principles used in Transfer Function, Transient Shear Wave, and Steady-State Shear Wave elastography methods. The time reversal technique relies on two assumptions, namely time invariance and spatial reciprocity. Time invariance is valid if there are negligible viscous losses, as $u(t)$ and $u(-t)$ are both solutions to the elastic wave equation in Equation 1.37. Spatial reciprocity implies that the excitation source and measurement receiver can be interchanged without a change in measurement, which again is valid for lossless media. While these assumptions may not hold completely in soft tissues, the errors introduced by their violation have proven to be small enough to allow estimation of the elastic properties.

In an acoustic time reversal experiment, first a short excitation pulse is sent through the medium. The scattered waves are recorded, time reversed, and re-applied to the medium from a secondary transducer surrounding all or part of the medium. The opposite scattering propagation occurs through the medium, acting

to refocus the waves toward the original excitation source [103]. A similar approach is used for time reversal elastography, with an additional use of spatial reciprocity to use the same excitation source in both steps to create a focusing of the elastic wave at the measurement location.

The time reversal technique can be applied using either the active approach or the correlation based approach. The active approach is most similar to the acoustic time reversal process just described. In the active approach, first an exciter emits one to two cycles of a sinusoidal signal, usually in the band 60 Hz to 150 Hz. The tissue motion resulting from the excitation is recorded at a single point, \mathbf{x}_o , for a length of time, T , usually on the order of 500 ms. The displacement along the axial direction measured by ultrasound, u_i , can be described in terms of the excitation and the impulse response through convolution

$$u_i(\mathbf{x}_o, t) = f_n(\mathbf{x}_s, t) \otimes h_{ni}(\mathbf{x}_s, \mathbf{x}_o, t), \quad (1.63)$$

where f_n is the excitation applied along direction n at location \mathbf{x}_s , h_{ni} is the impulse response between the excitation and measurement, and \otimes represents the convolution operation. Next, the exciter is programmed with a time reversed recording of the measured motion from the last step. The axial displacement after time reversal is

$$u_i^{\text{TR}}(\mathbf{x}, t) = u_i(\mathbf{x}_o, T - t) \otimes h_{ni}(\mathbf{x}_s, \mathbf{x}, t), \quad (1.64)$$

which can be described in terms of the excitation using Equation 1.63

$$u_i^{\text{TR}}(\mathbf{x}, t) = f_n(\mathbf{x}_s, T - t) \otimes h_{ni}(\mathbf{x}_s, \mathbf{x}_o, T - t) \otimes h_{ni}(\mathbf{x}_s, \mathbf{x}, t). \quad (1.65)$$

Using the principle of reciprocity, if the excitation was applied at the measurement location, \mathbf{x}_o , along the axial direction, the resulting displacement at the location of the exciter, \mathbf{x}_s , along the excitation direction would be the same as the measured displacement

$$u_i(\mathbf{x}_o, t) = u_n(\mathbf{x}_s, t) = f_i(\mathbf{x}_o, t) \otimes h_{in}(\mathbf{x}_o, \mathbf{x}_s, t). \quad (1.66)$$

Since the exciter was programmed to use the time reversed measured displacement,

Equation 1.66 can be substituted into Equation 1.64, resulting in

$$u_i^{\text{TR}}(\mathbf{x}, t) = f_i(\mathbf{x}_o, T - t) \otimes h_{in}(\mathbf{x}_o, \mathbf{x}_s, T - t) \otimes h_{ni}(\mathbf{x}_s, \mathbf{x}, t). \quad (1.67)$$

The tissue motion at the same measurement location, \mathbf{x}_o , will now observe a focusing of energy at time T . The information about the mechanical properties defining the resulting wave motion is contained in the impulse responses h_{in} and h_{ni} , where the observed field is filtered by the excitation [30].

The disadvantages of the active approach are that a fully programmable exciter is required and the entire experiment must be repeated for every point in the ROI. The correlation based approach takes advantage of signal processing to effectively achieve time reversal focusing without needing to re-apply the excitation. Similar to the first step of the active approach, a short duration excitation is applied to the tissue surface and the resulting displacement is measured over a period of time. The temporal cross-correlation is computed

$$R(\mathbf{x}_o, \mathbf{x}, t) = u_i(\mathbf{x}_o, T - t) \otimes u_i(\mathbf{x}, t). \quad (1.68)$$

Using Equation 1.63 and Equation 1.66, the cross-correlation can be expressed in terms of the excitation and impulse response

$$R(\mathbf{x}_o, \mathbf{x}, t) = f_i(\mathbf{x}_o, T - t) \otimes h_{in}(\mathbf{x}_o, \mathbf{x}_s, T - t) \otimes f_n(\mathbf{x}_s, t) \otimes h_{ni}(\mathbf{x}_s, \mathbf{x}, t). \quad (1.69)$$

Noting that the first, second, and fourth terms make up Equation 1.67,

$$R(\mathbf{x}_o, \mathbf{x}, t) = u_i^{\text{TR}}(\mathbf{x}, t) \otimes f_n(\mathbf{x}_s, t), \quad (1.70)$$

demonstrating that the cross-correlation field is the same as the time reversal field, u_i^{TR} , filtered by the excitation [31].

The cross-correlation can be post-processed in the frequency domain to optimize the information obtained. Taking the Fourier transform of the cross-correlation results in the cross-spectral density between \mathbf{x}_o and \mathbf{x} . All of the frequency content in the signal can receive equal weighting by dividing by the magnitude of the cross-spectral density, resulting in

$$\frac{P(\mathbf{x}_o, \mathbf{x}, t)}{|P(\mathbf{x}_o, \mathbf{x}, t)|} = e^{j(\phi(\mathbf{x}, \omega) - \phi(\mathbf{x}_o, \omega))} e^{j2\omega T}, \quad (1.71)$$

where ϕ is the phase of the impulse response. The constant phase offset can be removed and a band pass filter applied to limit the signals to the bandwidth of the excitation.

Due to the complexity of the impulse response, or elastodynamic Green's function, it is difficult to obtain a direct inversion for the shear wave properties from the mix of both near and far field compression and shear wave terms [29]. However, two simple methods based on wave length and wave speed estimation have proven useful. The most widely used to date is the wave length based estimator, probably due to its robustness to low SNR, where it has been confirmed through simulation and experiment that the -6 dB width of the displacement along the axial direction at the focus time is approximately equal to the shear wave length [55]. The wave speed can be determined using the phase as a function of \mathbf{x} , divided by the frequency ω , which provides the time of flight. The slope of a linear regression to the time of flight provides the speed [31].

The time reversal technique works best in highly reflective and reverberant media, as the reverberation acts to increase the effective aperture, increasing the ability to focus waves [104]. Alternatively, multiple uncorrelated random source can also achieve the desired diffuse field [29]. Excitation can be applied through random finger taps, or through passive physiological processes such as arterial pulses to excite the thyroid and brain, or a combination of arterial pulses, heart beats, and muscle contractions to excite the liver [56, 112, 355]. However, the passive techniques typically result in low displacement SNR in ultrasound which can limit the reliability of the results.

1.6 Ultrasound Spatial Calibration Background

Ultrasound spatial calibration describes the problem of determining the position and orientation of ultrasound images with respect to a sensor attached to the ultrasound transducer, which, in turn, is used to track the movement of the transducer with a position tracking system. Most commonly this is used for “freehand 3D ultrasound”, which tracks the movement of a 2D ultrasound image so that multiple

images can be reconstructed into a volume. The same general principles apply when it is desired to track a 3D ultrasound transducer to collect multiple volumes from different positions and orientations. Other applications include tracking needle trajectory in ultrasound-guided needle insertion procedures [218], or ultrasound guided registration of surgical tools to preoperative CT [340].

The position tracking system provides measurements of the sensor mounted on the ultrasound transducer, rather than the ultrasound image itself. Since the location of the image origin and the orientation of the beam lines is not known relative to the transducer casing, the calibration generally cannot be performed through direct measurements of the position of the sensor with respect to the transducer casing. Instead, ultrasound spatial calibration techniques have been developed based on imaging an object of known geometry, also referred to as a calibration phantom. The following sections provide some background on the various calibration techniques as well as the position tracking systems used with them.

1.6.1 Calibration Methods

Many calibration techniques have been developed involving different phantom designs and algorithms. Most phantoms are constructed using a highly acoustically reflective material such as metal, glass, nylon, or rubber, and are placed in a water bath to enable transmission of the ultrasound energy between the transducer and the phantom. Calibration algorithms may be iterative optimization techniques or closed-form solutions, and can vary in the number of unknown parameters. Iterative methods can be sensitive to initial estimates and can result in sub-optimal solutions located in local minima [93]. Iterative methods also typically require more measurements to achieve the same level accuracy as closed-form methods. Reducing the number of unknown parameters also reduces the number of required measurements, and can improve accuracy because the parameters are often coupled and errors in estimation can propagate through the solution.

All calibration methods are affected by the ability to localize image features. The resolution of the ultrasound system, which is both anisotropic and spatially variant causes distortion of the imaged shapes. Variations in speed of sound cause further problems in inaccurate depth estimation and ultrasound beam refraction.

Another related problem is that the ultrasound image is often modelled as a plane, however the beam has a variable thickness. An example that illustrates the problem is locating a point target which can persistently appear in the ultrasound image as the transducer is moved in the elevational direction over several millimetres.

One of the simplest phantom designs is a fixed point target, which can be constructed with a small spherical bead [182], the crossing of two wires [82], or a virtual point located at the centre of a sphere [47]. The point target is scanned from several viewing angles and positions by moving the transducer. The point target when segmented from the ultrasound image and transformed to either the tracker or phantom coordinates should remain in a fixed position. Therefore, the unknown calibration transformation can be found using an iterative optimization algorithm to minimize the spread of the transformed point locations. To help reduce the elevational beam thickness problem in accurately locating the point, a solution using a specialized miniature ultrasound transducer as a phantom that can detect when the main transducer beams reach the phantom and actively send a pulse to locate this point for the main transducer has been proposed [121].

Another simple phantom design is the planar phantom [262, 275]. Similar to fixed point target, the tracked transducer is placed in several different positions. The line feature detected where the planar phantom intersects the imaging plane when transformed to the tracker or phantom coordinate system when using the correct calibration matrix should be in the same plane. The planar method is attractive because it enables automatic segmentation, and unlike the point target, there is no need to carefully align the transducer with the phantom. A solution for the elevational beam thickness problem for planar phantoms has been developed where a transducer is mounted on a moving phantom consisting of a metal bar, with its top edge centred with the axis of a wheel [262]. The wheel is placed on a flat surface and can be translated or rotated to collect multiple images, while the metal bar remains at a fixed height above the flat surface, creating a virtual plane that is detected with ultrasound that is always aligned with the beam. Another planar based technique that reduces the effect of beam thickness is using virtual planes created by pairs of parallel wires [40, 77]. Planar phantoms using a pre-calibration step to determine the location of the plane in tracker coordinates using a calibrated stylus has been used to reduce the number of unknowns in the calibration problem [27], or to obtain

a closed-form formulation [217].

Another method of spatial calibration that does not require knowledge of the phantom location in the tracker coordinate system is the hand-eye calibration problem [35, 39, 41, 68, 176]. In this approach, the goal is to solve the matrix equation

$$AX = XB, \quad (1.72)$$

where A is the rigid transformation between two ultrasound images, B is the rigid transformation between the sensor measurements for the two images, and X is the unknown calibration transformation between the ultrasound image and the sensor. The matrix B is easily computed by chaining together two measurements from the position tracking system, and A can be determined either by registering the ultrasound images directly to one another, or by registering each image to the phantom and chaining the two transformations together. In the case that A is found by registering images to each other, it is possible to achieve calibration without knowledge of the phantom geometry.

Another straightforward approach to calibration is to generate a set of points with known correspondence between the ultrasound and tracker coordinates. This can be accomplished by imaging the tip of a tracked stylus [212]. A similar calibration approach is to use the stylus to locate point features on a phantom which is imaged, resulting in the same corresponding point data [129, 168, 249]. The solution can be obtained iteratively, through geometry, or using a closed-form solution. A proposed solution to the elevational beam thickness problem is to use two cones that meet at a point along the stylus axis a known distance away from the stylus pivot point. The decreasing radii of the cones help to guide the ultrasound plane to the intersection point [142].

A popular phantom that uses known geometry in the tracker coordinate system and corresponding points is the N-wire (or Z-wire) phantom [65, 190, 238]. The N-wire phantom is scanned approximately perpendicular to the plane of the three wires which results in three collinear lines appearing in the ultrasound image. Given knowledge of the end points of the wires in the tracker coordinates through a pre-calibration using a calibrated stylus, the centre point along the diagonal of the N-shape can be determined in tracker coordinates using the geometrical

lengths between the three points measured in the ultrasound image. This creates a corresponding point between the ultrasound image and tracker coordinate systems for each N-shape in each image. Similar to the tracked stylus calibration technique, when at least three non-collinear points are identified the calibration transformation can be solved either iteratively or in closed-form.

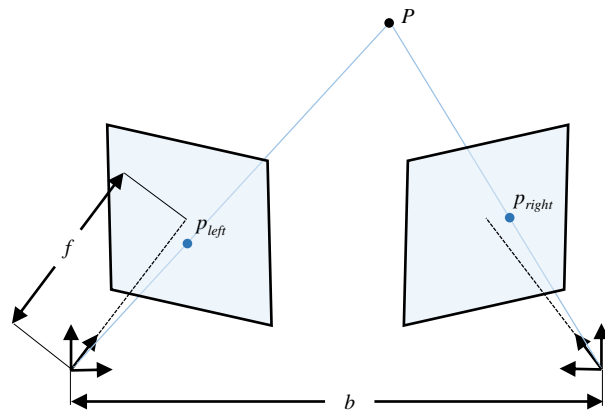
A few iterative techniques for more generic wire phantoms have been developed as well, such as using an optimization algorithm to maximize the correlation between image intensities and a geometrical model of the wire pattern [259]. Another example is using the iterative closest point algorithm to determine the calibration matrix to match segmented points from ultrasound to a random collection of wire targets [334]. Use of the virtual centre point of hollow tubes rather than wires has been proposed to help improve automatic segmentation and line localization [61].

1.6.2 Position Tracking

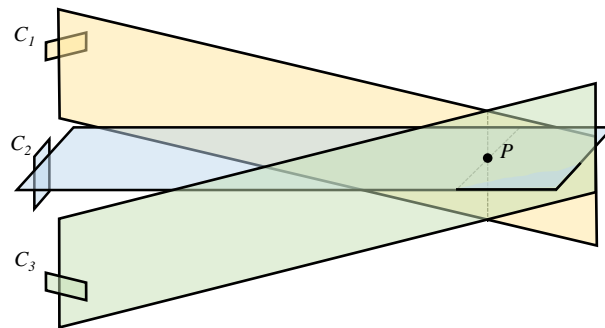
Position tracking systems determine the position and orientation of a sensor mounted on an ultrasound transducer and in some cases a calibration phantom as well. After calibration, the ultrasound image pixels are mapped to the 3D coordinate system of the tracking system using sensor readings during image acquisition. Optical or electromagnetic based tracking systems are commonly used. The following sections describe the two types of systems and Table 1.2 summarizes the technical specifications of commonly used systems.

Optical Systems

Optical tracking systems use cameras to detect markers attached to the object(s) of interest. The position of the markers is determined using triangulation techniques, and the geometry of the marker placement can be used to determine the orientation of the object. A common camera configuration is two 2D cameras which are oriented to view the same scene (i.e. stereo vision). These cameras can be video-based such as the MicronTracker (Claron Technology, Toronto, Ontario, Canada), or infrared-based such as the Polaris (NDI, Waterloo, Ontario, Canada). Another approach is to use three 1D image sensors, such as the infrared-based Certus (NDI). Figure 1.14 demonstrates the triangulation process for both configurations (for more



(a)



(b)

Figure 1.14: Triangulation configurations for determining 3D marker positions with optical tracking systems. (a) Stereo vision uses the geometry of two calibrated cameras that have lens centres separated by a known baseline, b , and known focal distances, f , to determine the 3D position of P based on perspective projections onto the left and right cameras, p_{left} and p_{right} . (b) A combination of three 1D cameras determines the 3D position of P as the intersection between three planes defined by the camera sensor readings (C_{1-3}) and the calibrated relative geometry between the cameras.



Figure 1.15: Markers for position tracking systems. From left to right, a video contrast X-point, a retroreflective infrared sphere, an active IRED, and an electromagnetic sensor coil. Ruler shown for reference scale.

Table 1.2: Technical specifications of common position tracking systems. Accuracy is expressed as root mean squared errors. Fields for which data were not available from the manufacturer are listed as not reported (NR).

Tracking System	Accuracy [mm]	Measurement Rate [Hz]	Maximum Distance [mm]	Minimum Distance [mm]	Resolution [mm]
Optical					
NDI Optotrak Certus	0.1	$\frac{4600}{N+1.3}$ ¹	7000	1500	0.010
NDI Polaris	0.25	60	2400	950	NR
Claron	0.35	20	2000	400	0.015
MicronTracker					
Electromagnetic					
Ascension 3D Guidance	1.4	20–255 ²	250–780 ³	NR	0.5
NDI Aurora	0.7	40	660	50	NR

details see [335] for stereo cameras and [197] for 1D cameras). Some commonly used markers are shown in Figure 1.15. Markers can be passive, such as intersecting high-contrast regions creating an X-point marker or retroreflective infrared spherical markers, or active such as an IRED. The advantages of active markers are that they are less dependent upon lighting conditions affecting reflection and a unique geometry is not required to identify a group of markers representing a single tracked object. The disadvantages of active markers are that usually some time multiplexing must be used to distinguish different markers and a wired connection to the tracking system is usually required. There is no statistically significant difference in the accuracies of passive and active markers [336].

Electromagnetic Systems

Electromagnetic tracking systems track the position of sensor coils in an electromagnetic field generated by a source transmitter. The systems use the principle of electromagnetic induction to measure the induced currents in the sensor coils due to changes created by the source transmitter. If the position of the moving sensor is described with respect to the transmitting source in spherical co-ordinates with distance ρ , azimuth angle α , and elevational angle β , and the orientation of the sensor is described using the angles ψ , ϕ , and θ , then the output current of the sensor coils, \mathbf{y} , is related to the current of the source coils, \mathbf{x} , through [266]

$$\mathbf{y} = \frac{M}{2\pi\rho^3} \mathbf{R}_\phi \mathbf{R}_\theta \mathbf{R}_\psi \mathbf{R}_\alpha^{-1} \mathbf{R}_\beta^{-1} \mathbf{S} \mathbf{R}_\beta \mathbf{R}_\alpha \mathbf{x} \quad (1.73)$$

where M is the magnetic moment of the coil, \mathbf{R} is a rotation matrix for a given subscripted angle, and

$$\mathbf{S} = \begin{bmatrix} 1 & 0 & 0 \\ 0 & -\frac{1}{2} & 0 \\ 0 & 0 & -\frac{1}{2} \end{bmatrix}, \quad (1.74)$$

accounts for the scaling factor between radial and tangential magnetic coupling for aligned source and sensor coils. Assuming that there are only small changes in position and orientation between acquisitions, Equation 1.73 can be linearized and solved using three independent transmission vectors [266].

A line-of-sight is not required between the transmitting source and the tracked sensor coils, which is the primary advantage of electromagnetic systems over optical systems. The primary disadvantage of electromagnetic tracking systems is a sensitivity to environmental factors that alter the magnetic field. For example, power supplies and other electronics generate their own magnetic fields that interfere with the field created by the source transmitter. Ferromagnetic materials such as iron and steel affect the homogeneity of the transmitted magnetic field. For transmitters using alternating current, the presence of conductive material such as copper or aluminum will induce eddy currents causing field distortions. Another disadvantage is the systems usually have a smaller working volume compared to optical systems. Most electromagnetic systems share the drawback of active optical markers in that they require a wired connection between the tracked object and the measurement system. The Calypso system (Calypso Medical Technologies, Seattle, WA, USA) provides wireless tracking by measuring the resonance response of three tuned transponders with a planar sensor array that triangulates the transponder locations [24].

Chapter 2

Development and Analysis of a 3D System for Absolute Elasticity Measurement

2.1 Introduction

Many pathological conditions are associated with a change in the mechanical properties of tissue, such as increased elasticity in focal cancerous lesions [114] and arterial plaques [79], or diffuse diseases such as liver cirrhosis [108] or autoimmune thyroiditis [297]. Elastography is an imaging tool that can depict these changes to help identify, diagnose, monitor, and guide treatment for these conditions. Elastography uses an elastic model to relate the mechanical properties of tissue to its motion in response to a force. The tissue motion is measured inside the body using an imaging modality to track changes over time, most commonly with either ultrasound or MRI.

As mentioned in Chapter 1, current commercial ultrasound elastography systems that produce images of the spatial variation in elastic modulus are based on strain or transient ARF techniques. Strain can be implemented with simple hardware and can acquire images continuously in real-time, however strain only provides relative measures of tissue elasticity. The ARF based approaches require a

cool-down time to limit tissue and transducer heating to safe levels [240], which can limit the acquisition rate and ability to perform continuous acquisition. A further disadvantage is that ARF methods are typically only offered on higher cost ultrasound scanners which have the hardware to provide the necessary power for the push beam [205]. There is also a limit on the depth penetration for measuring the ARF induced transient shear wave. For example, the depth limit on a Siemens Acuson S2000 system is 5.5 cm [84].

Quantifying absolute measures of the elastic modulus, rather than relative measures of elasticity, can reduce dependence on operator skill and improve reproducibility [8, 52], and can be useful in determining the different stages of a disease [307]. In static or quasi-static low frequency deformation (<20 Hz) such as in strain imaging, with the force boundary conditions unknown, the absolute values of the elastic modulus cannot be obtained. Dynamic excitation produces inertial forces inside the tissue and enables the calculation of the absolute values of elasticity. While the ARF technique provides a convenient way of applying dynamic excitation integrated with the imaging system, external mechanical harmonic vibrations can also be used for absolute elastography without the previously mentioned drawbacks of ARF [214, 290, 339]. Of course, such methods also have disadvantages to be explored later.

Measurement of dynamic tissue motion is challenging because acquisition rates must be sufficient to capture the full spectral content of the motion, and acquisition over a ROI should describe a common motion state (i.e. the tissue deformation at an instant in time should be captured). Under the assumption of consistent and repeatable cyclical tissue motion, MRE approaches solve this problem by using synchronization between a mechanical exciter and the MRI scanning sequence [290]. For ultrasound measurement of transient ARF propagation, a small imaging region can be used to achieve a high effective temporal sampling rate, and repeated interrogations can be used to scan a larger ROI [222]. Some ultrasound scanners can receive data in parallel across all channels, allowing for ultrafast acquisition on the order of 1000 Hz using planar transmit beams [34].

Conventional ultrasound measures 2D image planes, however tissue deformation is 3D in general. Measurement in 3D allows for a more accurate description of tissue mechanics, which is one of the main advantages of MRE over conventional

ultrasound elastography [87]. Volumes of ultrasound data can be acquired using motorized swept ultrasound transducers, or more sophisticated matrix array transducers. Measurements of motion over a volume can improve the precision of shear wave time-of-flight measurements [331], reduce shear wave diffraction bias [343], and enable characterization of anisotropic behaviour [330].

Transient ARF elastography techniques have become well-known with many commercial and research systems developed for a wide variety of clinical applications. These techniques are limited in measurement depth and fundamental compromises of tissue heating, transducer heating, and the size of the ROI. MRE systems have the advantage of measuring the full 3D displacement vector over a volume of interest, using steady state, low frequency vibrations that can penetrate deep into tissue. However, MRE has disadvantages in long acquisition time (usually several minutes), and high cost of equipment relative to ultrasound. It is worth exploring steady state excitation with 3D ultrasound to investigate the possible advantages and determine the limitations of this type of elastography system.

Previously a 3D ultrasound elastography system was developed at UBC based on repetitive acquisition of small sectors for a high effective frame rate of tissue motion [23]. An alternative bandpass motion sampling technique that is compatible with conventional ultrasound B-MODE sequences was developed and implemented in 2D with an Ultrasonix scanner (Richmond, BC, Canada) [98]. The latter technique was also adapted to work with a BK scanner (Herlev, Denmark) with a transrectal ultrasound (TRUS) transducer mounted on a motorized cradle for 3D imaging [191].

The three systems described in the previous paragraph were developed for the specific configuration used in the application. It is desirable to create a generic research platform that can flexibly adapt to different hardware and approaches. This will allow for comparison between the different approaches, as well as selection of the optimal tools for a given application. The focus of the work presented in this chapter is to present a unified framework that combines the different techniques developed at UBC. The system has been termed shear wave absolute vibro-elastography (SWAVE), as it uses mechanical vibrations to generate shear waves within the tissue to quantify absolute measures of elasticity. Details of the configuration options that have currently been developed are described, and an analysis of the reliability of the system under expected experimental conditions are quantified

through simulation and experiment on a tissue mimicking phantom.

Specifically, a modular software project is developed that implements the previously developed 3D sector based Ultrasonix system, the 3D bandpass based BK system, and the 2D bandpass based Ultrasonix system. The flexibility of the system is demonstrated by adapting the system for the first implementation of a 3D bandpass based Ultrasonix system. A new motor control hardware unit is described which can be used to interface with any swept motor 3D ultrasound transducer without modification. A new triggering system is described which is used to synchronize ultrasound acquisition with mechanical excitation. Methods for detecting complex motion phasors from time harmonic displacement measurements are described and simulations are used to investigate the sensitivity of the phasor detection in the presence of errors in frame rate and displacement measurement, as a function of the number of temporal measurements. The ability to synchronize measurements of tissue motion over the ROI is tested experimentally for various configurations. The repeatability of elasticity measurements is investigated using experiments comparing the measurements from bandpass based and sector based motion measurement, and from different excitation geometry.

2.2 Methods

2.2.1 System Overview

The main components of the system are the ultrasound interface to the scanner and transducer, the motor control of the ultrasound transducer to collect volumetric data, the excitation control of the function generator and vibration shaker, and the elastography processing sub-system that comprises motion tracking and elasticity estimation. The components are controlled by a user through a graphical user interface (GUI) on the scanner which also provides real-time display of B-MODE, tissue motion, and elasticity images, as well as data saving for offline use. Presets designed for specific hardware and measurement applications can be loaded by the GUI to initialize the different components to appropriate settings. The components and their connections are shown in the block diagram in [Figure 2.1](#).

The ultrasound component is used to interrogate the tissue over a period of

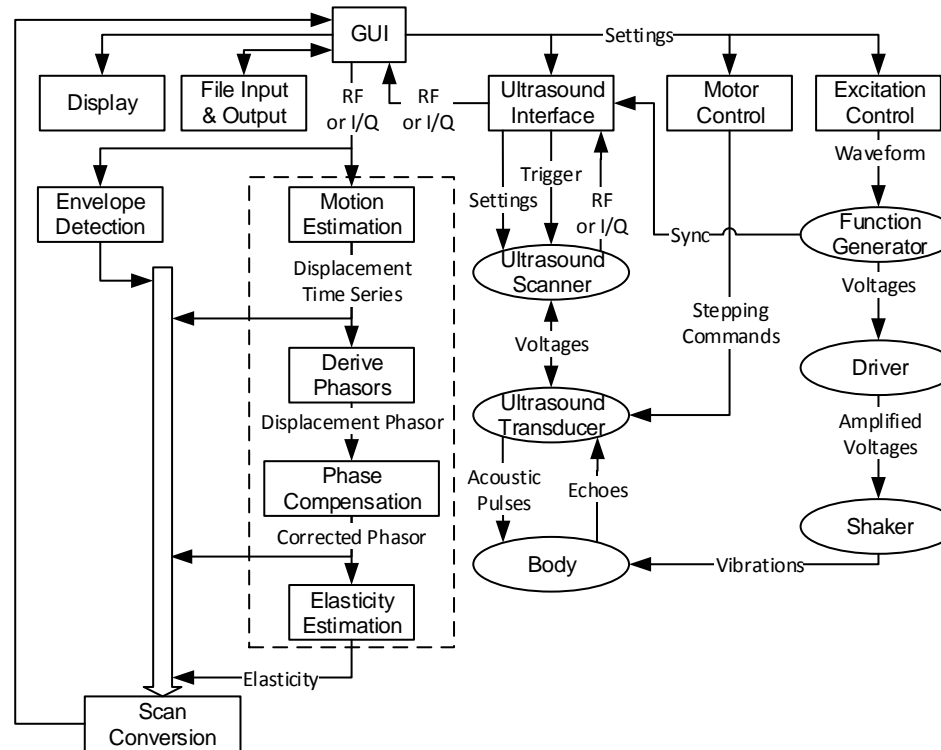


Figure 2.1: Block diagram of the elasticity measurement system. In this diagram the ellipses represent physical objects and the rectangles represent programming modules, or classes. The elastography processing sub-system is contained in the dashed box.

time while steady-state multi-frequency vibrations are applied to the tissue surface by the excitation component. The ultrasound image is swept over a volume using a customized motor control component. The tissue motion caused by the excitation is estimated along the axial direction using correlation-based displacement tracking from the collected ultrasound data. The temporal displacements are converted into a phasor representation in the frequency domain and elasticity is estimated based on the shear wavelength over the volume.

2.2.2 Software Design

The rectangular components shown in Figure 2.1 correspond to different classes or collections of classes separated to achieve a specific task in the elasticity measurement process. Each component consists of a base class which defines a common interface and typically contains multiple derived classes for different hardware or software implementations. Configuration of software projects for different component combinations is controlled through CMake (Kitware Inc., Clifton Park, NY, USA), a cross-platform open-source build system. Allowing CMake to include and exclude certain components provides the advantage that a given system only requires the dependencies for the desired combination of components, rather than needing to install the dependencies for every combination. Because each component uses a common interface, different configurations can easily be swapped and new hardware can be implemented without affecting the other components of the system.

Projects were developed with Microsoft Visual C++ (Redmond, WA, USA). Processes for motion tracking, elasticity estimation, envelope detection, and scan conversion were accelerated using the CUDA application programming interface (API) to work with an NVIDIA 580 GTX GPU (Santa Clara, CA, USA) or greater. The Ultrasonix scanner was modified to include this GPU and a larger power supply, while the BK system used an external PC with the GPU installed.

2.2.3 Ultrasound Interface

The primary role of the ultrasound interface is to communicate with the scanner to obtain RF or I/Q ultrasound data as it becomes available and to record the time

when the data is acquired. When possible, it also enables controlling acquisition settings and timing. The interface has specific implementations to work with Ultrasonix and BK scanners in real-time. The Ultrasonix systems are primarily used with hand-held swept motor 3D ultrasound transducers which can be used to scan various organs such as the breast, liver, kidney, or thyroid. A longer term goal with the Ultrasonix systems is to implement the system with the Sonix Embrace automated breast scanner. The BK scanner is used primarily with a TRUS transducer with a sagittal array, mounted in a cradle driven by an external stepper motor for acquiring 3D ultrasound volumes of the prostate.

The Ultrasonix interface actually has three implementations based on different APIs offered and runs directly on the scanner. It is designed to work with the current generation scanner, the SonixTouch, as well as the older MDP and RP models. The first Ultrasonix interface is based on the Porta API which provides access to the imaging “engine backend.” It uses C-style callbacks to transfer RF data directly from the “cineloop” buffer and provides various functions for controlling the scanner. The advantages of the Porta API are a lightweight interface for communicating with the scanner and access to the clinical exam B-MODE images which are computed using a proprietary algorithm and cannot be reproduced exactly from the RF signals. The disadvantage of the Porta API is a lack of fine level control of the scanner, such as sequence parameters. The second Ultrasonix interface is based on the Texo API, which solves the limitation of Porta by providing access to the sequencing and beamforming parameters of the scanner. Similar to Porta, it provides callbacks and functions to communicate with the scanner. However, the Texo API only provides RF data. While this is the data of interest for elastography as an input for motion estimation, it is difficult to use it in clinical settings because the B-MODE is computed from the RF by the research software and has not been approved for clinical use. The third Ultrasonix interface is based on the Ulterius API which uses Transmission Control Protocol/Internet Protocol (TCP/IP) to stream RF data from the Ultrasonix clinical exam software to a client application. The advantages of the Ulterius API are that the familiar clinical interface is available for user to change ultrasound imaging settings, as well as the clinical exam B-MODE as with Porta. The disadvantages are shared with Porta, with additional problems with dropped frames due to TCP/IP packet loss and increased CPU usage because

the clinical exam software. Acquisition timing information for all three Ultrasonix interfaces is determined using a frame counter and interrogating the scanner frame rate or frame period.

The BK interface is designed to work with the Pro Focus 2202 scanner equipped with a research interface to stream i/Q data to an external PC through a DALSA Xcelera-CL PX4 frame grabber card (Teledyne DALSA, Waterloo, ON, Canada). Settings may be controlled via the Grabbie API which communicates over TCP/IP, however in practice the settings are often set manually on the scanner by the user. Timing information for each frame is provided by time stamps from the frame grabber.

The system is capable of working with only 2D images (no motorized sweep), but 3D is preferred for greater accuracy.

2.2.4 Motor Control

In a conventional 3D ultrasound scan, the scan plane is swept over the ROI in the elevation direction in slow steady motion. The sweeping rate is limited by the 2D frame rate of the ultrasound system which in turn is limited by the amount of time for the ultrasound waves to reach the imaging depth and back and the number of beam lines across the 2D frame. The motor can either briefly pause at each motor position while a 2D frame is acquired, or can move continuously but slowly enough that the distortion caused by acquiring a frame while moving is negligible. This results in a volumetric sample on the order of one volume per second.

In the development of the 3D ultrasound elastography research system, it was desired to gain greater control over the motion of the scan plane during imaging. Specifically, for measuring dynamic motion on the order of 20 Hz to 300 Hz, a reasonable sampling rate and number of samples can be achieved by stepping the motor to a position, collecting several frames (for motion measurements), and then stepping motor to the next position in the sweep. The designed motor control box provides motor commands to the transducer without any modification to the transducer or scanner. The motor control box is placed between the transducer and scanner as shown in Figure 2.2. The motor control box passes ultrasound signals straight through but intercepts motor signals from the scanner and provides its own motor



Figure 2.2: A photograph of the motor control box connected to the Ultra-sonix scanner and a motorized ultrasound transducer.

commands as directed by the software running on the PC. The motor control box contains the same receptacle as the scanner for inserting the transducer. On the other end of the motor control box, the same type of plug as the transducer is used to connect the box to the scanner. From the scanner's perspective, the transducer appears as if it is normally connected.

The ultrasound signals are routed directly from the transducer receptacle to the scanner plug on a 12-layer PCB. Finger stock gaskets are used to couple the transducer shield to the motor driver shield and the scanner chassis shield to limit noise entering the system. A stepper motor driver circuit is placed on the same PCB as

is connected to the transducer motor pins via the transducer receptacle. Any motor signals from the scanner via the plug are left floating. The stepper motor circuit receives step and direction signals from two pins of the parallel port of the on-board scanner PC which can be controlled from the developed software. An external 12 V DC supply provides power to the motor driver circuit.

2.2.5 Excitation

Some previous elastography methods have applied vibrations to tissue using an exciter oriented in a transverse direction to the tissue surface in order to generate shear waves [38, 46, 113, 173]. Conceptually this is the most straight forward way to generate shear waves, as the applied deformation is a shear at the surface. For simple geometry, the resulting waves have a planar wave pattern, allowing for some simplifying assumptions in the elasticity inversion process. However, the wave penetration using transverse surface vibrations can be poor, limiting the available imaging region, especially for larger depths. Alternatively, longitudinal vibrations applied normal to the tissue surface can be applied which generally provide better wave penetration into the body [290, 322, 339, 353]. These longitudinal vibrations will still generate shear waves, since an incident elastic wave at the interface of two media can result in the reflection and refraction of both compression and shear waves, regardless of the type of incident wave [164]. Further, the types of waves generated by the excitation source are dependent on geometry. For example, a finite sized rectangular strip or circular disk radiates both compression and shear waves [209]. To achieve deep tissue penetration, the *SWAVE* system typically applies longitudinal vibration to the surface of the tissue with a small circular disk at the end of a rod, vibrating normally to the surface of the medium. Mode conversion results in shear waves at depth.

Excitation signals are defined using a data array in software with each entry in the array corresponding to a voltage at a specific time. The signals can be arbitrary, but are typically sinusoidal. Multi-frequency signals are created by adding multiple sinusoids together. The excitation frequencies are usually picked within a band of 20 Hz to 400 Hz, which balance a trade-off of greater wave penetration at lower frequencies and finer elasticity resolution with higher frequencies. The sig-

nal generating hardware is programmed with the excitation signal arrays over USB. The current system supports three hardware signal generators: Agilent 33220A and U2761A function generators (Santa Clara, CA, USA), as well as the Data Translation DT9812 digital-to-analog converter (DAC) (Marlboro, MA, USA).

The output signal power of the signal generators is amplified before being sent to the vibration shaker. Any amplifier with sufficient bandwidth and wattage can be used.

2.2.6 Sampling Sequences

As mentioned in the previous section, the SWAVE system requires measurement of tissue motion within a band of 20 Hz to 400 Hz. The SWAVE system has been designed to be able to switch between two ultrasound sequences capable of measuring this motion. The first sequence, called *sector-based scanning*, divides the width of image into small sectors which are repetitively scanned at a high effective sampling rate [21]. The second sequence, called *bandpass sampling*, uses a conventional B-MODE sequence of single continuous scanning, and uses knowledge of the ultrasound frame rate and the excitation frequencies to reconstruct the amplitude and phase of the motion while sampling at a rate lower than the Nyquist rate [98].

The ultrasound acquisition rate is determined by the time of flight of the ultrasound pulse to reach the imaging depth and reflect back to the transducer (Equation 1.1), and the number of beam lines across the width of the image. In a conventional B-MODE sequence, the beam lines are acquired one-by-one starting with the first line at one end of the array, and ending with the last line at the opposite end of the array. This constitutes a single frame of data. For a typical image with 128 beam lines, a depth of 5 cm, and a speed of sound of 1540 m/s, the maximum possible frame rate is 120 Hz and therefore tissue motion measurements will be aliased.

The *sector-based scanning* method divides the image into sectors, typically containing between 1 and 16 beam lines, and changes the sequence in which the beam lines are acquired such that each sector is repeated immediately for the desired number of temporal motion samples to increase the sampling rate over the sector region. For example, if an image consisting of 128 beam lines is divided into sectors of 8 beam lines each, the effective sampling rate of each sector is 16 times greater than

when acquiring entire image frames sequentially. However, the total acquisition time remains the same as the same total number of beam lines are acquired in the sequence. After motion detection, the phase of the motion measured within each sector is aligned across the image using knowledge of the acquisition delays, which is described in more detail in Section 2.2.9.

In the *bandpass sampling* method, because the sampling rate and the frequency content of the excitation signal are known, the amplitude and phase of the tissue motion can be reconstructed from the displacement time series without having to satisfy the Nyquist sampling rate requirement of a sampling rate greater than twice the highest frequency component in the signal. Given the excitation frequency and sampling rate, the aliased motion signal will appear at a known frequency in the measurable frequency band. The sampling requirement can be restated for a real-valued band-limited time-domain signal as requiring the sampling rate to be greater than twice the positive spectral bandwidth of the signal. This will result in a replica of the signal spectrum in the measurable baseband as long as the sampling frequency, f_s , satisfies

$$\frac{2f_0 + B}{m + 1} \leq f_s \leq \frac{2f_0 - B}{m}, \quad (2.1)$$

where f_0 is the centre frequency of the signal, B is the positive frequency bandwidth, and m is an integer corresponding to the minimum number of spectral half-shifts required to project the original signal to the baseband. While the excitation is typically a single frequency signal, or a combination of widely spaced single frequency signals, a bandwidth of about 10 Hz around each frequency component is usually assumed to account for the effect of finite-time windowing and distortion. The aliased signal will have the same amplitude as the true signal, and the phase of the signal will either match the true signal or be 180° out of phase depending on the known number of spectral half shifts due to aliasing. The spectral shifting of the spectrum to the baseband frequencies causes a decrease in SNR proportional to the number of shifts

$$\text{SNR} = \frac{P_S}{(m + 1)P_N}, \quad (2.2)$$

where P_S and P_N are the spectral power densities of the signal and white noise, respectively. For multi-frequency excitation, one further note about the *bandpass sampling* method is the sampling frequency should be chosen carefully to avoid

overlap between the aliased spectral bands.

2.2.7 Motion Estimation

Tissue motion is estimated between sequences of RF data provided by the ultrasound interface. In the cases when I/Q data are provided by the ultrasound interface instead, the RF signals are reconstructed by reversing the demodulation process. The RF data is divided into overlapping blocks of several data samples and the maximum normalized cross-correlation is found along the beam axis for each block. Neighbouring blocks which have already been computed are used to bracket the search region to improve speed and reduce errors [345]. Displacement shifts at sub-sample resolution are obtained by estimating the cross-correlation peak using cosine interpolation on the discrete normalized correlation coefficients [57]. The output of the motion estimation block is the displacement component along the beam axis for every block location and every acquisition of a given line. Every block represents the tissue motion at the block's location over the sampling time. Subsequent analysis is carried out in the frequency domain as described in the following sections.

2.2.8 Phasor Fitting

To provide input data for the inverse elasticity algorithm the speckle tracking measurements which describe the displacement between ultrasound frames in time need to be converted into displacement phasors at each excitation frequency. Given N_s speckle tracking measurements, the displacement in the time domain at a given location can be described by

$$u(t_k) = \sum_{m=1}^{N_f} A_m \cos(\omega_m t_k + \theta_m), \quad (2.3)$$

where t_k represents a discrete time sample, $k \in 1 \dots N_s$, N_f is the number of excitation frequencies used, ω_m is the excitation frequency, and A_m and θ_m are the amplitude and phase at a given excitation frequency. The displacements can also

be described using the complex exponential by

$$u(t_k) = \sum_{m=1}^{N_f} \Re \left\{ A_m e^{j\theta_m} e^{j\omega_m t_k} \right\}. \quad (2.4)$$

Replacing the complex exponentials with their trigonometric representations and then taking the real part results in

$$u(t_k) = \sum_{m=1}^{N_f} \underbrace{A_m \cos(\theta_m)}_{x_r} \cos(\omega_m t_k) - \underbrace{A_m \sin(\theta_m)}_{x_i} \sin(\omega_m t_k). \quad (2.5)$$

The two identified scalars, x_r and x_i , are calculated to find the best fit phasor to the speckle tracking measurements.

The values of x_r and x_i are identified for each frequency by expressing Equation 2.5 in matrix form, $\mathbf{M}\mathbf{x} = \mathbf{u}$, where

$$\mathbf{M} = \begin{bmatrix} \cos(\omega_1 t_1) & \sin(\omega_1 t_1) & \dots & \cos(\omega_{N_f} t_1) & \sin(\omega_{N_f} t_1) & 1 \\ \vdots & \vdots & \vdots & \vdots & \vdots & \vdots \\ \cos(\omega_1 t_{N_s}) & \sin(\omega_1 t_{N_s}) & \dots & \cos(\omega_{N_f} t_{N_s}) & \sin(\omega_{N_f} t_{N_s}) & 1 \end{bmatrix}, \quad (2.6)$$

$$\mathbf{u} = \begin{bmatrix} u(t_1) \\ \vdots \\ u(t_{N_s}) \end{bmatrix}, \quad (2.7)$$

$$\mathbf{x} = \begin{bmatrix} x_{r1} \\ x_{i1} \\ \vdots \\ x_{rN_f} \\ x_{iN_f} \\ C \end{bmatrix}, \quad (2.8)$$

where C accounts for a DC offset in the measurements. The solution is found in the least squares sense

$$\mathbf{x} = (\mathbf{M}^T \mathbf{M})^{-1} \mathbf{M}^T \mathbf{u}. \quad (2.9)$$

The phasor at a given frequency is

$$U(\omega_m) = A_m e^{j\theta_m} \quad (2.10)$$

$$= A_m \cos(\theta_m) + jA_m \sin(\theta_m) \quad (2.11)$$

$$= x_r + j(-x_i). \quad (2.12)$$

To provide feedback on the goodness of the fit, a quality factor is computed using the ratio of the signal energy of the fit and the summation of the energy of the fit and the difference between the fit and the original data. This is expressed as

$$\frac{\|\mathbf{M}_0 \mathbf{x}\|^2}{\|\mathbf{M}_0 \mathbf{x}\|^2 + \|\mathbf{M} \mathbf{x} - \mathbf{u}\|^2}, \quad (2.13)$$

where \mathbf{M}_0 is the same as \mathbf{M} except the last column is set to zeros to remove the DC component from the fit.

2.2.9 Phasor Compensation

It is the nature of ultrasound acquisition that leads to the sampling of each displacement signal to occur at different times dependent on spatial location. The finite propagation speed of the ultrasound pulses means that points located deeper within the tissue are sampled at a later time relative to the shallower depths. Typically ultrasound scanners create a 2D image by sequentially scanning beam lines, meaning that each line is also separated in time. To use spatial information about the measured motions and relate the information to tissue mechanics, the displacement measurements should be synchronous. For periodic motions, under the assumptions that the transducer does not move relative to the tissue and the ultrasound speed of sound is constant through the ROI, the time delays can be compensated in the frequency domain as described by Baghani *et al.* [21]. The technique corrects for the acquisition delays by multiplying the phasors at each spatial location by a complex exponential to shift the phase of the phasor proportional to the time difference from the first measured phasor.

$$U_{\text{comp}}(a, b, c) = U_{\text{meas}}(a, b, c) e^{-j2\pi f_e \Delta t} \quad (2.14)$$

where $U_{\text{meas}}(a, b, p)$ is the phasor fitted to the temporal displacements at beam line a and depth b in the p^{th} 2D image plane, $U_{\text{comp}}(a, b, p)$ is the phasor after compensation, f_e is the excitation frequency, and Δt is the acquisition time difference between the phasor at (a, b, p) and the phasor at the origin. The time difference can be decomposed into intraline, interline, intersector, and interplane compensations. The intraline compensation accounts for the time delay between acquiring ultrasound echo signals along the axial or depth dimension, which is the time for the ultrasound pulse to reach the phasor at depth b and return to the transducer, where the wave travels at a speed of c , resulting in

$$\Delta t_{\text{intra}} = \frac{2b}{c}. \quad (2.15)$$

The interline compensation accounts for the delay between the acquisition of each beam line. Given the pulse repetition period, T_{PRF} , which is typically the time for the ultrasound pulse to reach the maximum depth in the image and back, $2d/c$, then the time delay between the a^{th} line and the first is

$$\Delta t_{\text{inter}} = T_{\text{PRF}}(a - 1). \quad (2.16)$$

The interplane compensation accounts for the delay between the acquisition of subsequent 2D phasor image planes, and is typically computed using the difference between the time stamp of the first ultrasound RF frame used in the first phasor computation, and the time stamp of the first ultrasound RF frame used for the p^{th} phasor image plane.

If a sector-based high frame rate sequence is used to sample the tissue motion, then the interline compensation would be applied independently to each individual sector using the first line in the sector as the reference, and a fourth compensation would be applied to account for the delay between each sector acquisition. For L lines in a sector, each scanned K times, the delay between the first line in the first sector and the s^{th} sector is

$$\Delta t_{\text{sector}} = LKT_{\text{PRF}}(s - 1). \quad (2.17)$$

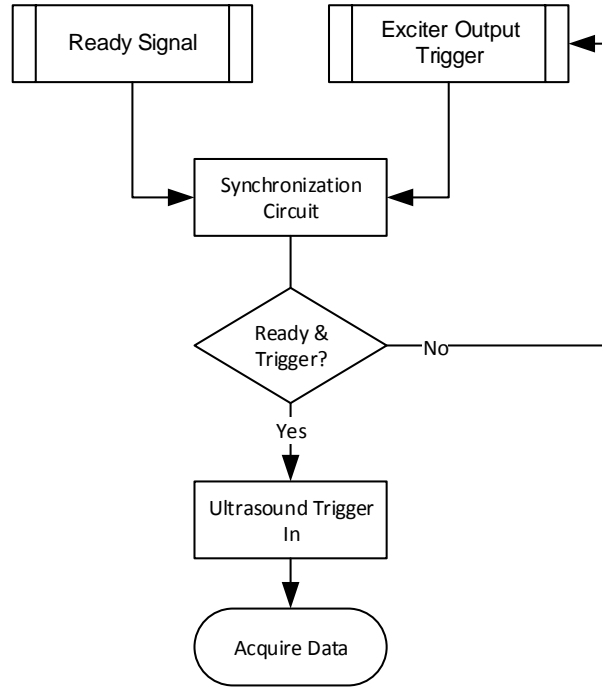


Figure 2.3: Flowchart describing the synchronization between the ultrasound acquisition and the excitation in the swAVE system.

2.2.10 Synchronization

Synchronization between the ultrasound acquisition and the excitation signal can be used as a complement or replacement for the phasor compensation described in the previous section. One option is to trigger the start of the acquisition of a defined number of ultrasound frames for computing a phasor image, with each trigger occurring at a common excitation phase. This would remove the need for interplane compensation, and might be more reliable than frame time stamps over long acquisition periods. Another option is to trigger the acquisition of each ultrasound frame. In this case, triggers would need to shift to different phases over the excitation to detect tissue motion between ultrasound frames. Synchronizing each ultrasound frame also removes the need for interplane compensation, while providing finer control over the exact motion phases that are measured rather than measuring mo-

tion phases depending on the ultrasound frame rate. Finally, each ultrasound beam line can be triggered, again while shifting the phase of the trigger for subsequent acquisitions to observe motion. This final synchronization scheme removes the need for interline compensation, and can enable tracking of all components of the motion vector as discussed in more detail in Chapter 5.

The implementation of the synchronization for the Ultrasonix systems is described by the flowchart in Figure 2.3. A custom synchronization circuit is used to output a trigger pulse to the ultrasound machine which collects the specified ultrasound data (one beam line, one frame, or a defined number of frames) in its standard sequence after receiving the trigger. The synchronization circuit takes two inputs. One input is a ready signal from the ultrasound machine which allows the program to indicate when it would like to acquire a beam line which is realized through a pulse sent through the parallel port of the ultrasound machine. Once the synchronization circuit has received the ready signal, it will wait for the function generator to output a trigger pulse, which happens when the function generator reaches the programmed phase. The synchronization circuit then outputs a pulse which is sent to the ultrasound machine, and resets itself to wait for the next ready signal. The synchronization circuit is realized using two flip-flop chips. The ultrasound scanner transmits and receives as soon as the trigger pulse is received from the synchronization circuit. The process is repeated until all of the desired data are collected.

2.2.11 Elasticity Estimation

The linear elastic wave equation relating the displacement in the frequency domain to the mechanical properties of the tissue is given by Equation 1.37, which for harmonic excitation at a frequency of ω is written in matrix form as

$$\nabla \cdot [\mu (\nabla \mathbf{d} + (\nabla \mathbf{d})^T) + \lambda (\nabla \cdot \mathbf{d}) \mathbf{I}] = -\rho \omega^2 \mathbf{d}, \quad (2.18)$$

where λ and μ are the Lamé parameters, ρ is the density, and \mathbf{d} is the tissue displacement. The density of most soft tissue is close to the density of water, so ρ is usually assumed to be uniformly 1000 kg/m^3 . Tissues imaged in elastography are often considered nearly incompressible ($\nabla \cdot \mathbf{d} \approx 0$), which implies the Poisson's ratio, ν , is approximately 0.5 and the Young's modulus is related to the shear modulus

through

$$E = 2\mu(1 + \nu) \quad (2.19)$$

$$\approx 3\mu. \quad (2.20)$$

To simplify the problem, the shear modulus is usually assumed to be locally constant (i.e. homogeneity assumption) meaning that the spatial derivatives of the shear modulus are negligible. These assumptions allow Equation 2.18 to be simplified to a Helmholtz equation

$$\mu \nabla^2 \mathbf{d}_\gamma = -\rho \omega^2 \mathbf{d}_\gamma, \quad (2.21)$$

which is independently satisfied by each orthogonal displacement component γ . The shear modulus can be determined using a ratio of the output of two filters operating on the displacement [230]. This can be accomplished over a broadband range of elastic wave spatial frequencies with a collection of lognormal quadrature filters, defined as a product between radial and directional components [163]

$$\mathbf{q}_i(\mathbf{k}) = \mathbf{r}_i(k) \sum_p \mathbf{n}_p(\mathbf{k}), \quad (2.22)$$

where \mathbf{k} is the spatial frequency variable, $k = \|\mathbf{k}\|$ is the wave number, and p is the number of directions. The radial component is defined as

$$\mathbf{r}_i(k) = e^{-\frac{1}{2\ln 2} \ln^2\left(\frac{k}{k_i}\right)}, \quad (2.23)$$

where k_i is the centre frequency of the filter. In this work, the filter banks consist of 11 frequencies spaced an octave apart, with the highest frequency corresponding to a wavelength of two pixels. For a 200 Hz excitation frequency with 1 mm pixel spacing, this results in the filter banks containing a centre frequency range corresponding to Young's modulus values of approximately 0.5 kPa to 500 MPa.

The directional component of the filters have a \cos^2 dependence in the half-space of the selected direction, and zero in the other half-space, with selected directions corresponding to the positive and negative x , y , and z axes [200]. This

filter design helps to separate interfering waves due to reflection and refraction so they can be processed separately and combined.

Let \mathbf{s} represent the result of the convolution between a quadrature filter and the displacement; then, the frequency estimate for a pair of filters is

$$\hat{k}_i = \Re \left(\frac{\mathbf{s}_{i+1}}{\mathbf{s}_i} \right) \sqrt{k_i k_{i+1}}. \quad (2.24)$$

The final local frequency estimate is a weighted summation of the estimates from the pairs of filters

$$\bar{k} = \frac{\sum_{i=1}^{N-1} \|\Re(\mathbf{s}_i)\| \hat{k}_i}{\sum_{i=1}^{N-1} \|\Re(\mathbf{s}_i)\|}. \quad (2.25)$$

Once the local spatial frequency has been determined, the Young's modulus can be estimated

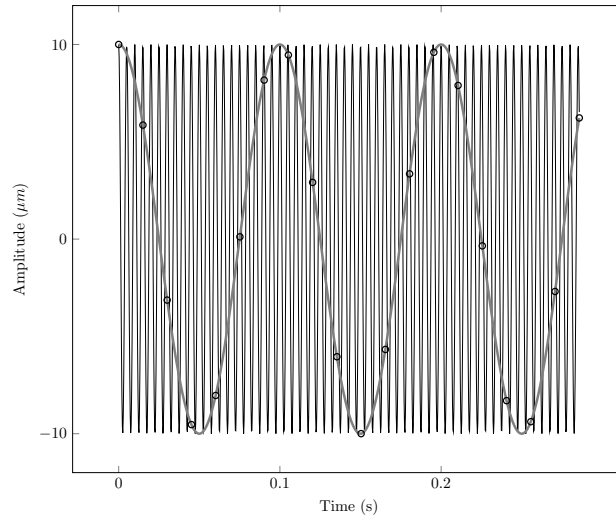
$$E = 3\rho \frac{\omega^2}{\bar{k}^2}. \quad (2.26)$$

This method has been used for MRE inversion and has been termed LFE. In the SWAVE system, axial displacement phasor image planes are computed at each excitation frequency for each motor position in the 3D sweep of the ultrasound transducer and scan converted to a 3D Cartesian grid before applying the LFE inversion algorithm to estimate elasticity over the volume. If the elasticity can be considered to be independent of frequency, for example if the tissue is not significantly viscous, or if the excitation frequencies are similar enough that dispersive effects are negligible, then the elasticity can be averaged over each excitation frequency. This can help reduce artefacts caused by low amplitude nodes in the tissue motion modal pattern, as each frequency should produce a different pattern [312].

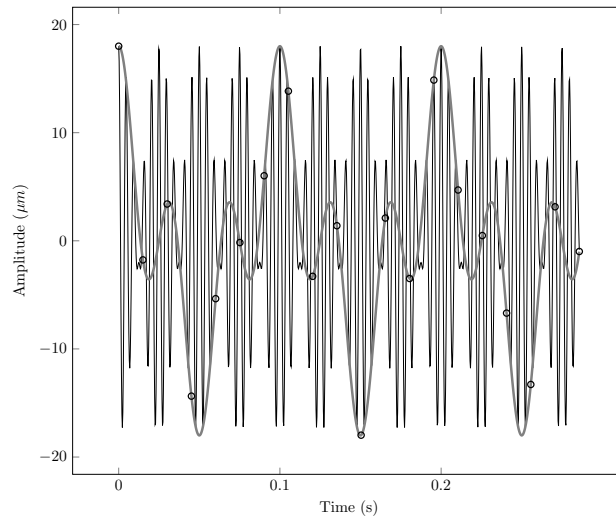
2.3 Simulations

Simulation was used to study the errors in the phasor calculation for common use cases and expected errors in the system. Synthetic speckle tracking measurements were generated for a single location in space by sampling a synthetic excitation signal at a given frame rate for a given number of desired measurements, then adding a random error to the displacement value representing jitter error.

The phasor calculation was first tested using a single frequency cosine signal.



(a)



(b)

Figure 2.4: Simulated excitation signals for analysis of phasor fitting. (a) Single frequency excitation signal consisting of a cosine at 200 Hz with a $10\ \mu\text{m}$ amplitude and 0° phase. (b) Multi-frequency excitation signal created from the summation of the signal (a) and a second cosine signal at 240 Hz with a $8\ \mu\text{m}$ amplitude and 30° phase. The true signal is shown in black and the signal in the base band is shown in grey. The circles represent 20 displacement samples acquired at a frame rate of 70 Hz.

The signal had a frequency of 200 Hz, an amplitude of $10\ \mu\text{m}$, and a phase of 0° . This is a typical excitation used with the elastography system. The chosen frequency is low enough to provide adequate penetration into the tissue without substantial attenuation, and high enough such that the measured elastic wavelengths fit within the region of interest and allow for identification of small scale variations in elasticity. The amplitude is at a level typically observed *in vivo* and is measured accurately with speckle tracking. The amplitude is small enough to limit observable nonlinear effects in the Young's modulus.

The number of samples acquired is limited by the amount of time to perform the measurement and the number of scan lines that can be programmed in the ultrasound sequencer. The time to perform the measurement is ideally as small as possible to limit possible artefacts from patient motion as well as to provide results faster. The scan lines are programmed in the ultrasound sequencer to acquire ultrasound images for a given number of repetitions to provide the number of desired speckle tracking measurements. The limit is typically somewhere between 1000 and 2000 lines. The transducers on the Ultrasonix machines have 128 elements. Although the sequence does not necessarily have to program 128 lines, reducing the number of lines also reduces either the field of view or the lateral spatial spacing of the displacement samples. For most practical sequences the number of speckle measurements is limited to be between 10 and 30 samples. This study looked between that range in increments of 5 samples.

A nominal frame rate of 70 Hz was used to sample the speckle tracking measurements. The maximum frame rate possible is limited by the time required for the ultrasound acoustic pulse to reach the desired imaging depth and reflect back to the transducer surface as described by Equation 1.1, and the number of beam lines in a frame. For a conventional ultrasound sequence with depths between 6 cm and 15 cm and 128 beam lines across the image, the maximum frame rate is somewhere between 30 Hz and 100 Hz. The frame rate is chosen to be below this limit to ensure that no frames are dropped, but close to this limit to ensure a short acquisition time.

After an ultrasound sequence is programmed on the machine, the software requests the scanner to report the frame rate it is using. There is potentially a small difference between the frame rate reported by the scanner and the actual frame rate. The frame period is provided by the Ultrasonix APIs at a resolution of $1\ \mu\text{s}$. The

time stamps from the frame grabber used with the BK scanners are provided at a resolution of $1\ \mu\text{s}$ as well. At a frame rate of 70 Hz, an error in the frame period of $1\ \mu\text{s}$ would result in a error in the frame rate of 0.05 dHz. Even though the resolution of the frame period is $1\ \mu\text{s}$, the error could potentially be larger. When setting the frame rate on the Ultrasonix scanners, the maximum resolution is 1 dHz. The error in the actual frame rate is likely much less than this, but it serves as an upper bound for the expected error. This study investigated the frame rate error between 0 dHz and 0.2 dHz, in increments of 0.05 dHz.

The jitter error is expected to be under $4\ \mu\text{m}$ for speckle tracking under typical conditions [254]. The jitter was modelled as normally distributed with standard deviations starting from $0\ \mu\text{m}$ and incremented by $1\ \mu\text{m}$ to $4\ \mu\text{m}$. The jitter was randomly sampled for each displacement measurement and added to the displacement value. The error was randomly sampled 1000 times for each test case and the results were averaged over the 1000 trials.

The simulation compared the phasor fit to the synthetic speckle tracking measurements to the known true signal. The difference between the phasor amplitude and phase were computed, as well as the quality factor of the fit as computed by Equation 2.13.

2.4 Experiments

2.4.1 Motor Attenuation

Placing the motor control box between the transducer and the scanner poses the risk of attenuating the ultrasound signals by passing them through two additional connectors and a few centimetres of copper trace (approximately 3 cm to 7 cm long, 0.2 mm wide, and $36\ \mu\text{m}$ thick traces). The attenuation could reduce SNR and limit the depth of penetration of the ultrasound. To test whether the motor control box causes significant attenuation, a 4DL14-5/38 motorized ultrasound transducer was used to image a CIRS 040 general purpose multi-tissue phantom. The phantom consists of Zerdine, a proprietary elastic polymer that mimics the mechanical and acoustic properties of tissue. The phantom was measured by the manufacturer to have a speed of sound of 1541 m/s and attenuation of 0.63 dB/(cm MHz). The

phantom contains multiple nylon monofilament wire targets which appear as bright point reflectors in ultrasound. A group of wires aligned along a vertical column and spaced by 1 cm was imaged to examine the amplitude of the ultrasound signal as a function of depth. Plots of the amplitude were used to compare the signal strength with and without the motor control box.

2.4.2 Phasor Synchronization

While the phasor calculation simulation investigated the ability of the fitting algorithm to recover a phasor when the frame rate is unknown, it did not investigate the errors introduced by the phase compensation when an incorrect frame rate is used. To study how this might affect the phasor measurement, a transducer is fixed over a tissue mimicking phantom and 2D image frames are collected over a period roughly 40–60 seconds long while steady-state harmonic motion is applied to the surface of the phantom. Phasors are computed using every 20 consecutive image frames and compensated according to Equation 2.14. Each computed phasor image in the set should be the same after compensation, so the effect of an incorrect frame rate can be observed by computing the root mean square (RMS) error between the first phasor image and each subsequent phasor image

$$U_{\text{RMS}}(i) = \sqrt{\frac{\sum_{a=1}^{N_c} \sum_{b=1}^{N_r} (U_{i+1}(a, b) - U_1(a, b))^2}{N_c N_r}}, \quad (2.27)$$

where U_γ is the γ^{th} phasor image, N_c and N_r are the number of columns and rows in the ROI, $i \in 1 \dots N_p - 1$, and N_p is the number of phasor images.

The study was done with the Porta and Texo Ultrasonix ultrasound interfaces using a 4DL14/38 transducer on a CIRS 049 elastography phantom, and the BK frame grabber interface using a 8848 TRUS transducer on a CIRS 066 prostate elastography phantom.

An estimate of any phase shift present in the phasor images due to systemic or constant timing errors is quantified using an optimization to minimize the squared difference between the first phasor image, U_1 , and the k^{th} phasor image, U_k , where the k^{th} phasor image is shifted by phase θ , amplitude weighted by A , and adjusted

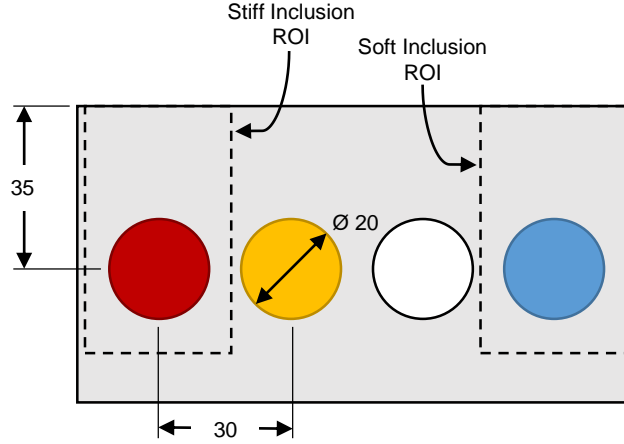


Figure 2.5: Front view of the CIRS 049 elastography quality assurance phantom with the experimental scanning regions indicated (not to scale).

for the DC component of noise η

$$\underset{\theta, A, \eta}{\text{minimize}} \left\| U_1 - AU_k e^{j\theta} - \eta \right\|^2. \quad (2.28)$$

The experiment was also repeated using the trigger described in Section 2.2.10 with the Texo ultrasound interface to synchronize each phasor image with the excitation (i.e. every 20th ultrasound frame was triggered). If there is a constant error in the frame time stamps, then the synchronization should limit the error in the phasor measurements.

2.4.3 Elasticity Repeatability

An important aspect of the system is the ability to reliably provide the same measurement of absolute elasticity over repeated tests. To test the repeatability of the measurements, five volumes were acquired sequentially using an Ultrasonix Sonix-Touch scanner with a 4DL14-5/38 motorized linear transducer. The experiment was repeated using both the Porta ultrasound interface with the *bandpass sampling* method and Texo ultrasound interface with the *sector-based scanning* method. Note that the *bandpass sampling* method can be implemented on either the Porta or Texo

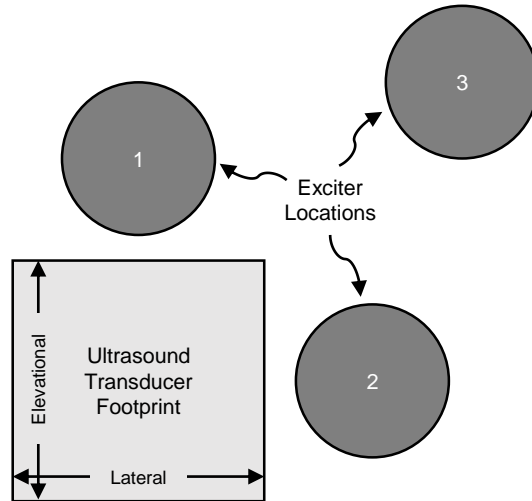


Figure 2.6: Diagram of the different exciter locations used to test the repeatability of the elasticity measurements as viewed from above the phantom. The positions are shown for measuring the stiff inclusion. The exciter positions were mirrored about the vertical when measuring the soft inclusion to keep them on the surface of the phantom.

interfaces, while the *sector-based scanning* method can only be implemented with the Texo interface at this time. For clinical studies, the Porta interface would be preferred as it can stream the clinically approved B-MODE image from the scanner’s exam software.

The transducer was placed over two regions of a CIRS 049 elastography quality assurance phantom to capture data for the stiffest (62 kPa) and the softest (6 kPa) spheres in the phantom, as shown in Figure 2.5. The mean elasticity within the inclusions and in the surrounding background (29 kPa) was computed and compared for each volume. To study the effect of different boundary conditions, the measurements were repeated using three different exciter placements as shown in Figure 2.6.

Ultrasound images were acquired to a depth of 5 cm using a centre frequency of 5 MHz for the transmit pulses. The phasors were fit using 25 displacement measurements at each location in the volume. The Porta interface, using the *bandpass*

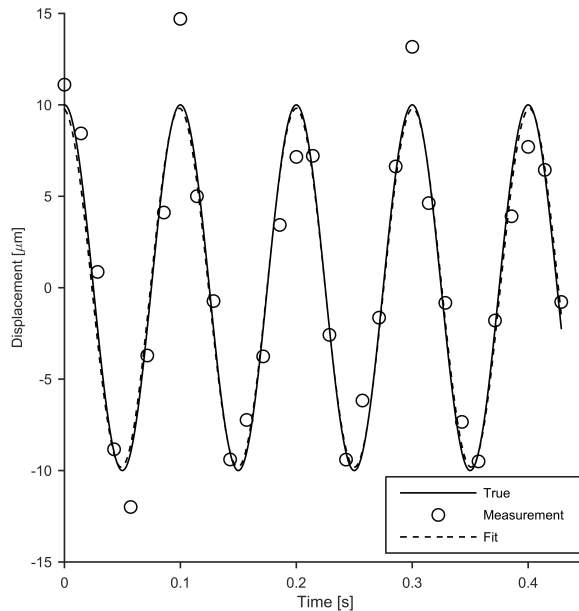


Figure 2.7: Example phasor fitting result to simulated noisy displacement measurements.

sampling method, acquired each 2D ultrasound image, consisting of 128 beam lines, at a rate of 72 Hz. The Texo interface, using the *sector-based scanning* method, divided each 2D ultrasound image into 8 adjacent sectors of 16 beam lines, and each sector was acquired at a rate of 625 Hz. The 2D images were swept into a thin 3D volume using 9 motor steps in 0.45° increments. Excitation was applied at 200 Hz.

2.5 Results

2.5.1 Phasor Fitting Results

An example of a phasor fitting result is shown in Figure 2.7. The fitted signal closely matches the true simulated signal despite the presence of displacement measurement errors.

The first row of Figure 2.8 shows how the error in the magnitude of the phasor

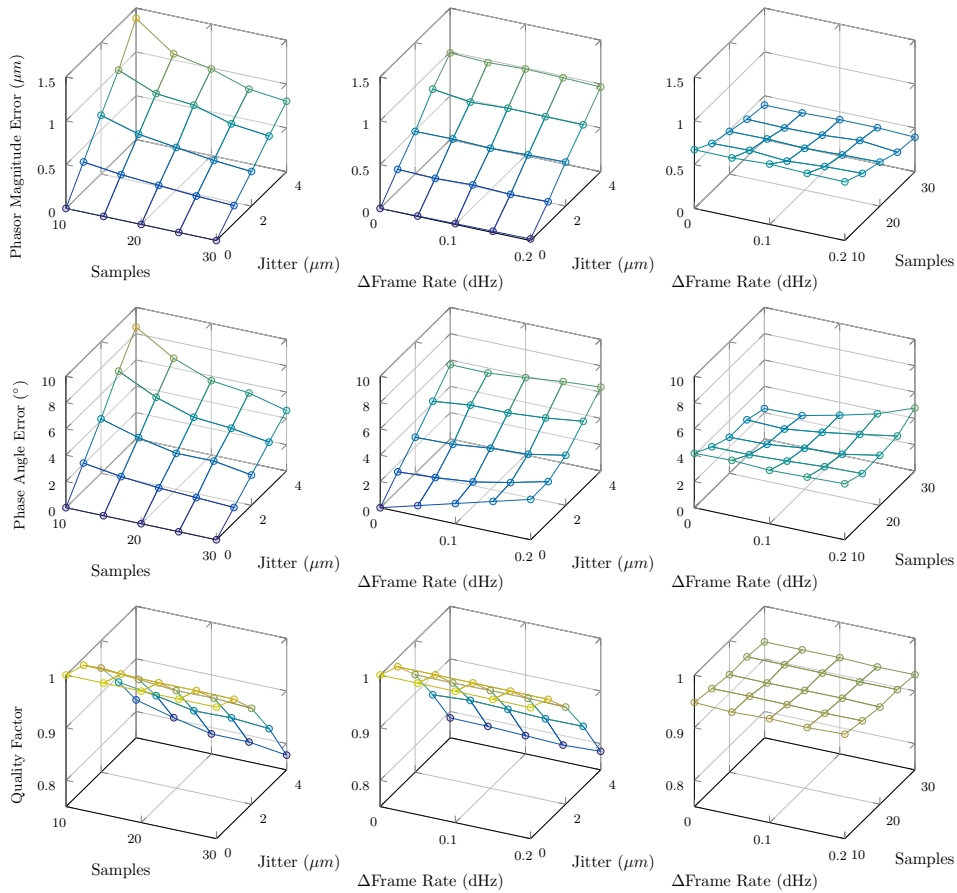


Figure 2.8: Error in the least squares fit of a simulated 200 Hz cosine excitation at $10\ \mu\text{m}$ amplitude with varying number of displacement samples, displacement jitter error, and frame rate error. The first row shows the difference between the fitted phasor magnitude and the excitation reference, the second row the difference between the recovered phasor angle and the excitation reference, and the third row the quality factor of the fit as defined in Equation 2.13. The first column shows results with no error in the frame rate. The second column displays the fitting results using 20 displacement samples. The third column has a fixed jitter error of $2\ \mu\text{m}$.

changes with the number of displacement samples, the displacement jitter error, and the frame rate error. The results show that for a fixed level of jitter error ($2\ \mu\text{m}$), the magnitude error varies from 3.9% with 30 samples and no frame rate error, to 6.7% with 10 samples and 0.2 dHz frame rate error. For a fixed number of 20 samples, the magnitude error increases approximately linearly with jitter error from 0 to 9.9%, while the frame rate error contributes to less than 0.4% change in the error varying from 0 dHz to 0.2 dHz. Looking at the error in estimating the phasor magnitude varying only the jitter error and number of samples with no frame rate error, the magnitude error again increases approximately linearly with jitter error, while decreasing the number of samples increases the slope of the error line exponentially.

In the second row of Figure 2.8 the phase angle error is analysed. The phase angle error increases dramatically at large jitter error levels, especially with fewer displacement samples. The phase angle error also generally increases with greater error in the frame rate. At a level of 0.2 dHz frame rate error, the phase angle error actually worsens when more samples are collected, from 4.3° at 10 samples to 4.8° at 30 samples. This is explained by the longer amount of time required to collect the samples, allowing the error in frame rate to accumulate.

In the third row of Figure 2.8 it can be seen that the quality factor drops off as the jitter error in the displacements increases. The quality factor does not seem to be strongly affected by the level of error in the frame rate or the number of displacement samples collected.

A second test was conducted for multiple frequencies by adding a second cosine signal at 240 Hz with an amplitude of $8\ \mu\text{m}$ and phase angle of 30° to the previously described 200 Hz cosine signal. The signal is shown in Figure 2.4 (b). Of the 125 different cases using different combinations of displacement samples, displacement jitter error, and frame rate error, the recovered 200 Hz signal was almost identical to the single frequency case. The largest differences in magnitude and phase were $0.015\ \mu\text{m}$ and 0.18° .

Experimental measurements applying the bandpass sampling technique showed a wave pattern polarized in the horizontal direction of the image, regardless of the excitation position. In fact, the pattern can be observed without any excitation force and will be referred to as the *phasor wave artefact*. An example is shown in Fig-

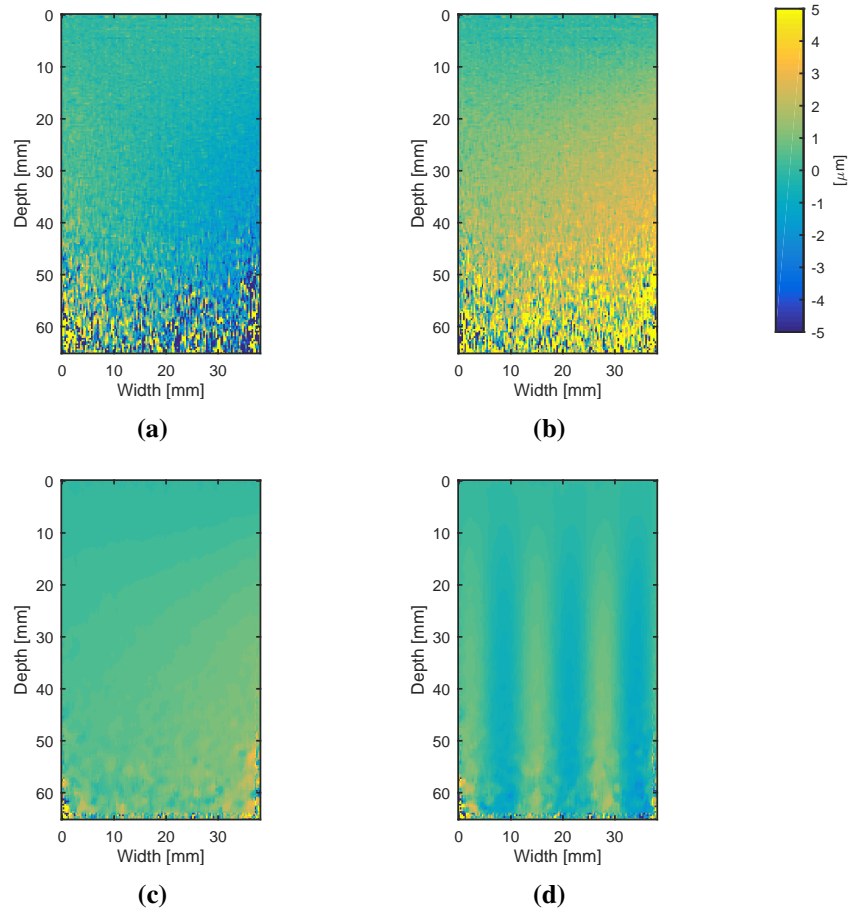


Figure 2.9: A demonstration of a *phasor wave artefact* observed in experimental bandpass sampled phasor images. The temporal displacements measured from (a) a frame early in the acquisition and (b) a frame collected later in time show small shifts across the image. The fitted phasor (c) before applying interline compensation shows a small uniform amplitude as a result from the temporal displacements, and (d) after applying interline compensation shows a wave pattern across the horizontal dimension.

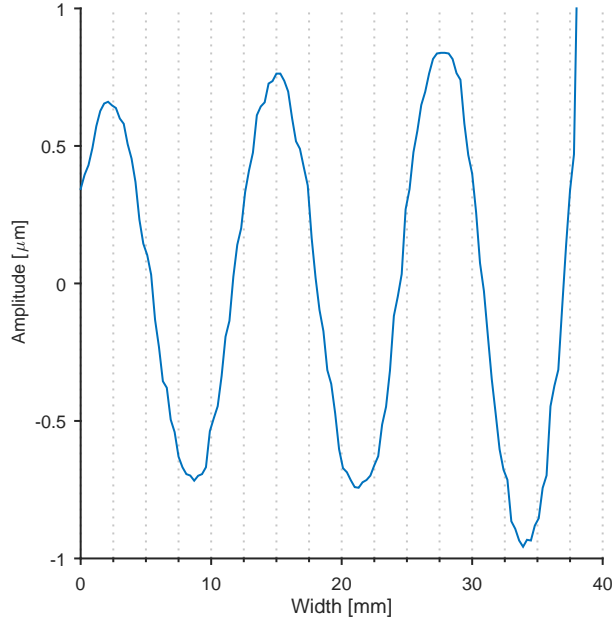


Figure 2.10: A profile across the width of an image containing the *phasor wave artefact*.

Figure 2.9. The pattern is caused by fluctuations in the displacement tracking and the interline compensation. The temporal displacement frames can contain random displacement shifts on the order of a micron either towards or away from the transducer as shown in Figure 2.9 (a) and Figure 2.9 (b). This noise can cover a wide band, and can therefore appear at one of the excitation frequency components, shown as a mostly uniform displacement across the frame in the real part of the fitted phasor in Figure 2.9 (c). This inaccuracy on its own should have little effect on the elasticity measurements because of its low magnitude and low spatial frequency which is removed during the LFE processing. However, the interline compensation, which is supposed to correct for the phase shift of the measured excitation wave pattern caused by sequential line acquisition, when applied to this uniform shift introduces a phase change across the lateral direction. Figure 2.10 shows a profile of the wave pattern across the width of the image. Measuring the distance from crest-to-crest and trough-to-trough gives an estimated wave length of approximately 13 mm. The

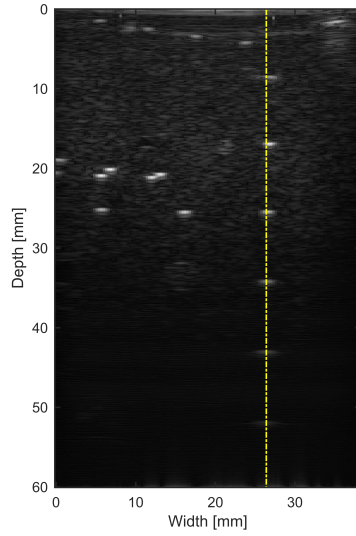
significance of this length on the measurements and how it can be predicted is discussed in Section 2.6.

2.5.2 Motor Attenuation Results

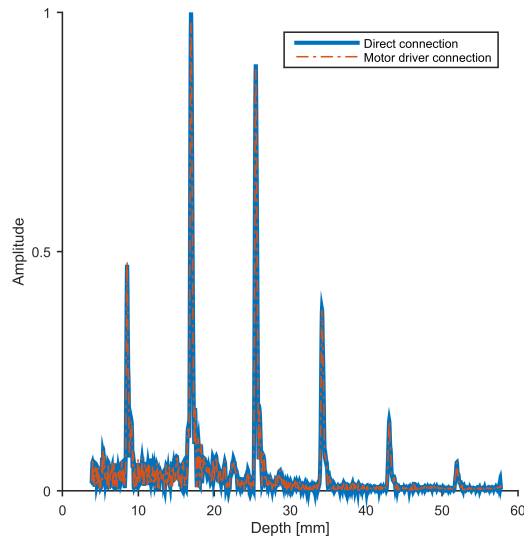
The results from comparing the ultrasound signal strength with and without the motor control box placed between the transducer and the scanner are shown in Figure 2.11. The B-MODE shows the vertical column of strong point reflectors used for the comparison. From top-to-bottom, the brightness increases as the focus depth is reached, then gradually decreases as the signal is absorbed by the phantom material. Looking at just the RF envelope amplitude along the beam line intersecting the vertical column, it is evident that the peak signal amplitude from each point target with the motor control box inserted is within 2 % of the peak signal amplitude when connecting the transducer directly to the scanner.

2.5.3 Phasor Synchronization Results

The results from measuring the same repeated motion over a period of 40–60 seconds using the Ultrasonix Porta and Texo interfaces on a CIRS 049 elastography quality assurance phantom are plotted in Figure 2.12. The vibration was applied at 200 Hz and was measured at a frame rate of 72 Hz, measuring a peak phasor amplitude of 4 μm . The RMS error when considering only the absolute part of the phasor remains small in magnitude and flat over time, indicating that the same wave amplitudes are being detected. There is a 0.41 μm jump over about 0.5 seconds for the absolute phasor at around 35 seconds in the Porta dataset. A 0.17 μm jump is also visible at around 42 seconds in the Texo dataset. These jumps were possibly caused by someone walking near the apparatus during the acquisitions, or an accidental bump of the ultrasound scanner, transducer clamp, or phantom. The real and imaginary parts of the phasor show a gradual increase in RMS error over time, indicating that the phase of the measurements is slowly drifting and causing a difference compared to the first detected phasor. There is a sudden increase of 0.59 μm and 0.44 μm in the error for the real and imaginary components for the Porta measurements at around 25 seconds. The Porta timing is provided by a frame counter and the frame rate, and the sudden increase occurs when the frame counter reaches



(a)



(b)

Figure 2.11: Measurements comparing the ultrasound signal strength with and without the motor driver between the transducer and the scanner.
 (a) The B-MODE image with a yellow dashed line indicating the line in (b) which is used to plot the signal in both cases.

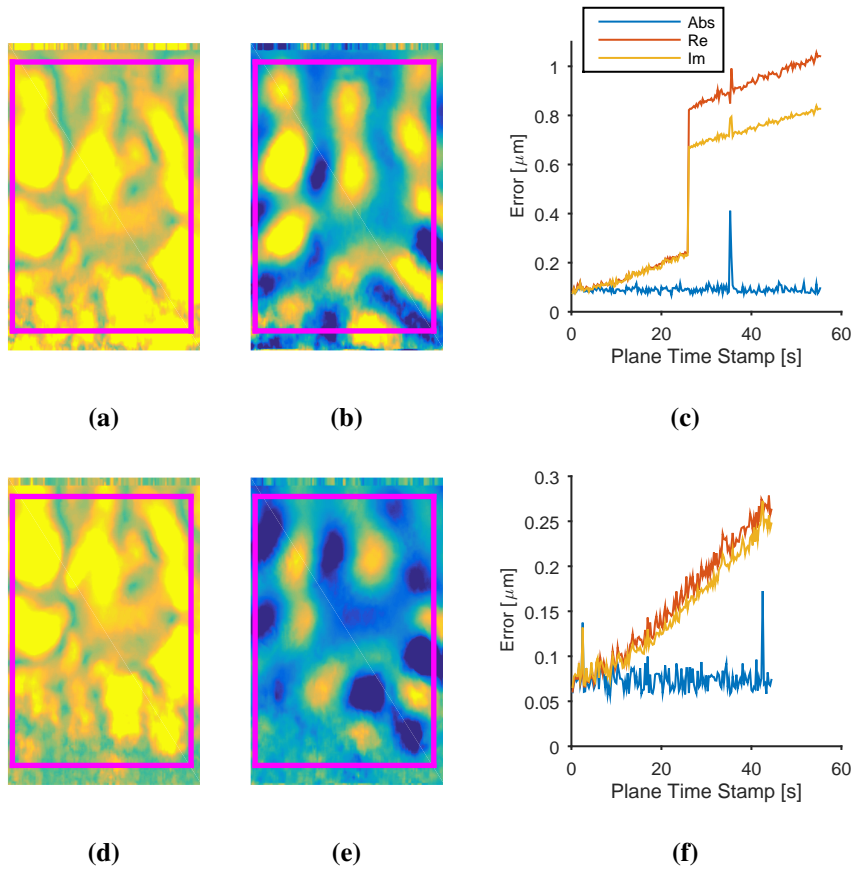


Figure 2.12: Results of phase compensation measured with the (top) Porta and (bottom) Texo ultrasound interfaces showing from left-to-right the absolute magnitude of the phasor, the real part of the phasor, and a plot of the phasor RMS error over time for the absolute, real, and imaginary components of the phasor. The magenta box indicates the region that the RMS is calculated over.

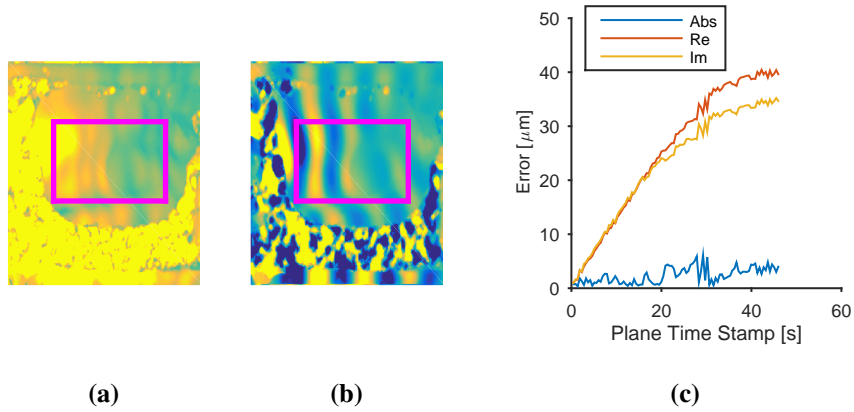


Figure 2.13: Results of phase compensation measured with the BK ultrasound interface showing from left-to-right the absolute magnitude of the phasor, the real part of the phasor, and a plot of the phasor RMS error over time for the absolute, real, and imaginary components of the phasor. The magenta box indicates the region that the RMS is calculated over.

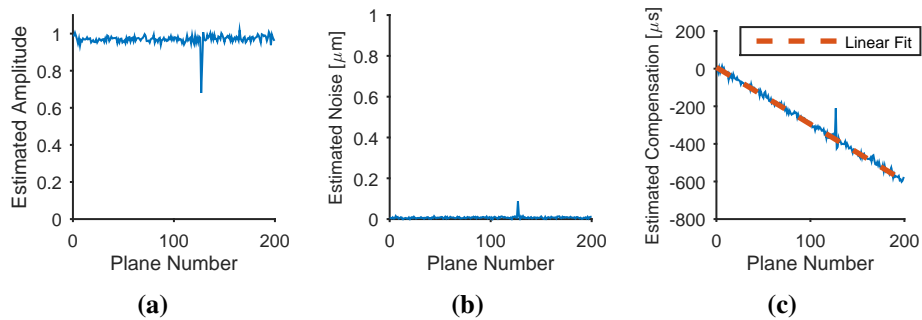


Figure 2.14: Estimated amplitude, noise, and time shifts to minimize the squared error between the first phasor image collected and each subsequent compensated phasor image, corresponding to the Porta ultrasound interface measurements.

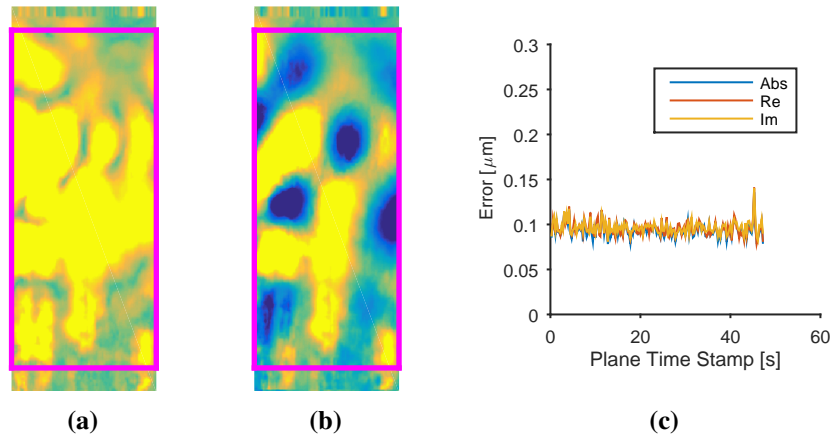


Figure 2.15: Results of phase compensation using a trigger to synchronize the start of each phasor image, using the Texo ultrasound interface, with the excitation. From left-to-right are the absolute magnitude of the phasor, the real part of the phasor, and a plot of the phasor RMS error over time for the absolute, real, and imaginary components of the phasor. The magenta box indicates the region that the RMS is calculated over.

its maximum allowable value (experimentally determined to be 16000) and starts counting up again from zero. Since the maximum counter number is fixed it can be detected and corrected for.

The test was also applied to the BK ultrasound interface, instead using a CIRS 066 prostate elastography phantom, resulting in the measurements plotted in Figure 2.13. In this case, the vibration was applied at 165 Hz and was measured at a frame rate of 43 Hz, measuring a peak phasor amplitude of 78 μm . The ROI in the phasor images is smaller than in the previous results because the waves are only measured properly within the ellipse shaped prostate mimicking region. Similar to the results obtained with the Ultrasonix interfaces, the RMS error of the absolute part of the phasor remains flat over time, while the RMS error in the real and imaginary parts increases with time. The magnitude of the error appears to be larger for the BK measurements, but this might be partially explained by the larger phasor amplitudes.

The larger phase drift in the BK measurements is confirmed in the results obtained by applying the optimization in Equation 2.28 to estimate the phase shift

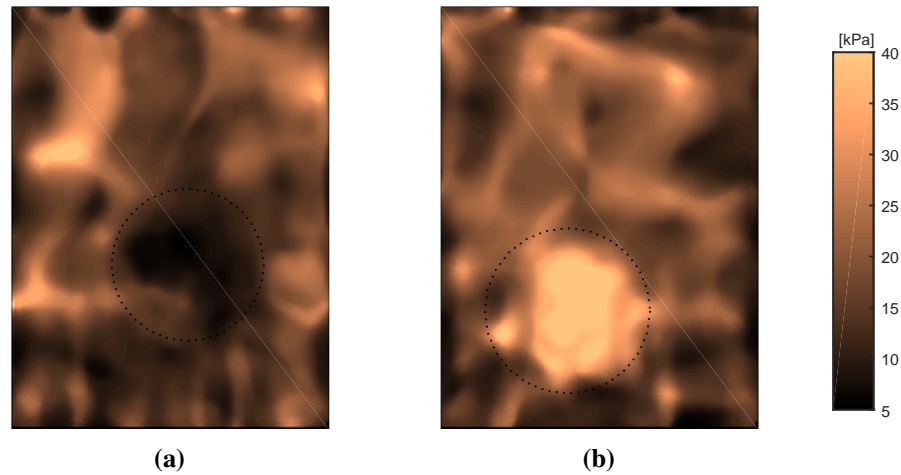
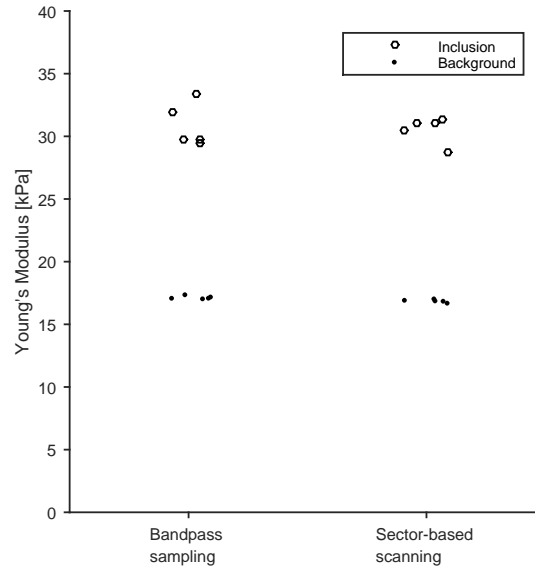


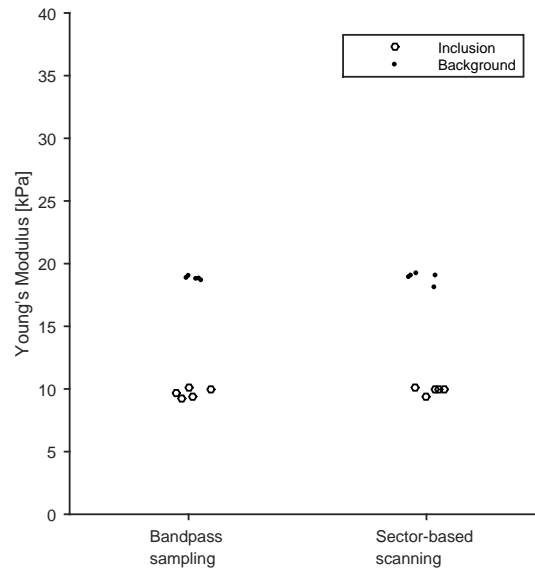
Figure 2.16: Example elasticity images of the (a) soft and (b) stiff inclusions measured in the CIRS 049 elastography quality assurance phantom using the Porta ultrasound interface on an Ultrasonix scanner. These images are taken from the centre 2D image slice of the swept volume. The dotted circles correspond to the inclusion location. Excitation was applied at 200 Hz.

between phasor images. For the Porta interface, the estimated phase shift for each plane to correct for the drift of the phasor images over time was $3.03 \mu\text{s}$, after correcting for the discontinuity in the real and imaginary parts of the phasor due to the frame counter roll-over. The Texo interface had an estimated shift of $2.07 \mu\text{s}$, and the BK interface $30.2 \mu\text{s}$ per phasor image. In all cases, the fit to Equation 2.28 produced amplitude weightings consistently close to unity, noise at a fraction of a micron, and time delays that increased in magnitude linearly for each phasor image, even in the BK case despite the curving in the RMS error. An example of the fit for the Porta interface is shown in Figure 2.14.

The RMS error over time when triggering the ultrasound acquisition with the exciter is shown in Figure 2.15. In this case, the error remains flat over time for all of the absolute, real, and imaginary parts of the phasor.



(a)



(b)

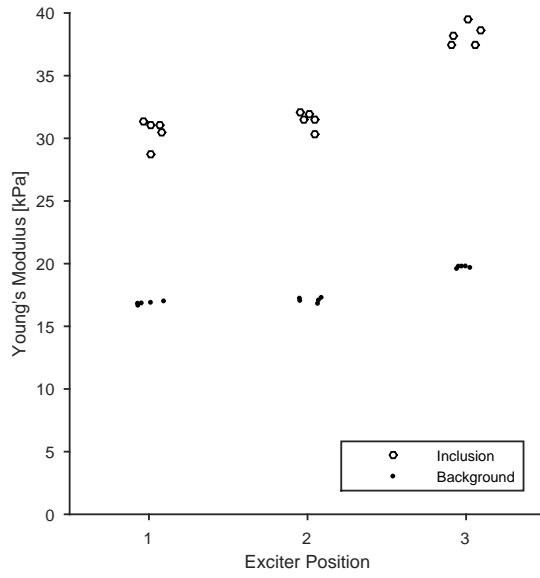
Figure 2.17: Repeated measurements of the mean elasticity in a (a) stiff and (b) soft inclusion, in a moderately stiff background with different motion sampling techniques. Excitation was applied at 200 Hz.

2.5.4 Elasticity Repeatability Results

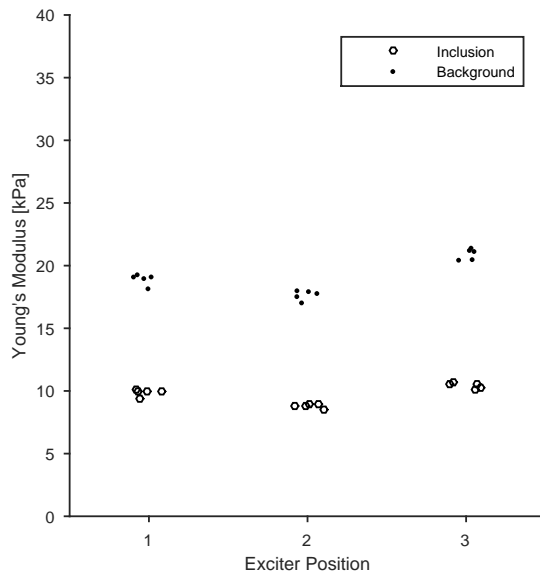
Figure 2.16 displays example elasticity images of the soft and stiff inclusions in the CIRS 049 elastography quality assurance phantom. The displayed images correspond to the centre image slice in one of the volumetric acquisitions using the *bandpass sampling* technique with the Porta ultrasound interface. The location of the inclusions was determined through manual segmentation of the B-MODE ultrasound images, and are indicated with dotted circles in Figure 2.16. As expected, the estimated elasticity values are lower within the soft inclusion region, and higher in the stiff inclusion region, relative to the background. Some variation in the estimated elasticity is observed in regions expected to be homogeneous. This variation is likely caused by regions of low displacement amplitude, or nodes in the wave field, which result in poor estimation of derivatives and corrupt the elasticity measurements [136, 199].

The following repeatability results averaged the Young's modulus values within the segmented region to obtain a measure for the inclusion elasticity, and outside of the segmented region for a measure of the background elasticity. The measurements of the mean elasticity of the stiff and soft CIRS inclusions and the background from five separate volumetric acquisitions using either *bandpass sampling* or *sector-based scanning* are shown in Figure 2.17. The measurements of the background elasticity in the region near the stiff inclusion are consistent, all near 17 kPa with a range of less than 0.5 kPa. The measurements of the background in the region near the soft inclusion are also consistent but are slightly larger in magnitude at around 19 kPa, with a range of less than 1 kPa. Measurements of the stiff inclusion elasticity show the greatest variation in these results with a range of 4 kPa around a mean of about 31 kPa. The soft inclusion measurements show repeatability similar to the background, with an average stiffness of about 9.5 kPa and a range of values spanning less than 1 kPa. For all of these measurements there appears to be no substantial difference between the *bandpass sampling* or *sector-based scanning* methods.

The repeatability of mean elasticity measurements as a function of exciter position are shown in Figure 2.18. For the measurements around the stiff inclusion, exciter positions 1 and 2 demonstrate similar results to the previous measurements



(a)



(b)

Figure 2.18: Repeated measurements of the mean elasticity in a (a) stiff and (b) soft inclusion, in a moderately stiff background collected using *sector-based scanning* at three exciter positions. Excitation was applied at 200 Hz.

both in terms of mean elasticity and spread and in both the inclusion and background. At exciter position 3, both the inclusion and background show increases in mean elasticity by approximately 7 kPa and 2.5 kPa, respectively. The measurements however have a similar spread compared to the other exciter positions. The measurements around the soft inclusion show a similar trend, with increased mean elasticity of approximately 0.5 kPa and 2 kPa for the inclusion and background, respectively, again with a similar spread for repeated volume acquisitions.

2.6 Discussion

An important aspect of the system is the elasticity image frame rate. The total computational time for motion tracking and elasticity inversion using a GPU-based implementation is 71 ms [23]. The frame rate of the elasticity images is limited by the rate of ultrasound data collection rather than computation time for typical imaging settings. For example, an acquisition with an imaging depth of 6 cm and 128 laterally spaced beam lines, using 20 ultrasound frames to estimate the motion phasor, the 2D elasticity image could be updated at a rate of 5 Hz. Elasticity measurements have shown improvements from 3D volumes with as few as 5 to 7 elevationally spaced planes, with a volumetric elasticity update every one to two seconds [23]. To obtain a full volumetric sweep, using a 4DL14-5/38 motorized linear array transducer with a default motor step of 0.45°, a total of 61 planes is required which reduces the volumetric acquisition time to around 10–20 seconds. In all cases, the acquisition can be repeated continuously for an indefinite time, providing updated elasticity measurements during a procedure.

Care must be taken in selecting multi-frequency signals so that they do not overlap in the base band. For example, excitation frequencies of 200 Hz and 270 Hz sampled at a frame rate of 70 Hz both appear at 10 Hz in the base band. In this case the phasor calculation is no longer unique and therefore they cannot be reliably found. The solution to the least squares fit is no longer unique because the matrix \mathbf{M} defined in Equation 2.6 becomes rank deficient. Observing that the time samples, t_k , are taken at multiples of the sampling rate, and

$$\frac{\omega_1}{f_s} \pmod{\pi} = \frac{\omega_2}{f_s} \pmod{\pi}, \quad (2.29)$$

it is clear that

$$\cos(\omega_1 t_k) = \cos(\omega_2 t_k) \quad (2.30)$$

and

$$\sin(\omega_1 t_k) = \sin(\omega_2 t_k). \quad (2.31)$$

The phasor fitting results in this chapter were presented by fitting a signal at the excitation frequency, however the procedure can also be accomplished using the base band frequencies instead. For the test cases mentioned in this section, the difference between the results was close to the machine precision, indicating no difference between the two methods.

In the phasor fitting results, it was revealed in Figure 2.9 that small random shifts in the displacement estimates from experimental measurements resulted in a *phasor wave artefact* across the lateral dimension of the phasor image. The wave appearance is caused by the interline compensation which is used to shift the phase of tissue motion collected at different times. Ignoring any motion induced by the excitation, from Equation 2.14 the wave appears across the lateral coordinate as a plane wave

$$Ae^{-j2\pi f_e T_{\text{PRF}} l + \theta}, \quad (2.32)$$

where T_{PRF} is the time delay between acquiring adjacent beam lines, l is the beam line number, A is the amplitude of the phasor fitted to the random displacement shifts appearing in the band at the excitation frequency, f_e , and θ is a random phase resulting from the phasor fit. For a linear array transducer, this will appear in Cartesian coordinates as a horizontally polarized plane wave. The elasticity measured by the LFE algorithm can be predicted by computing the wave number from Equation 2.32

$$k = \frac{d\phi}{dx} = \frac{f_e T_{\text{PRF}}}{\Delta x}, \quad (2.33)$$

where Δx is the spacing between beam lines. For curvilinear transducers, the wave will no longer appear purely as a plane wave in Cartesian coordinates, but will be stretched with increasing depth, which would show as an increase in elasticity with depth. For the example in Figure 2.9, the data was acquired with a linear array, the excitation frequency was 210 Hz, the interline time was 110 μs , and the line spacing was 0.3 mm, resulting in a wave number of 0.077 mm^{-1} which corresponds

to a wave length of approximately 13 mm which matches the wave length estimated from Figure 2.10. The elasticity, as computed from Equation 2.26 is 22 kPa, which is within the range of soft tissue elasticity. This makes it difficult to filter the *phasor wave artefact* from the phasor images because the spatial frequency is within the band of the expected shear wave measurements, unlike the compression wave which can be filtered due to its low spatial frequency away from the measurements. It may be possible to apply a filter before applying the interline compensation. Further investigation into whether this could affect the measured shear wave field would be an interesting area of future research.

The phasor synchronization results show that the wave pattern can slowly drift out of phase over time if it is not synchronized with the exciter. The fact that the RMS error does not increase over time for the absolute part of the phasor, but does for the real and imaginary parts indicate that it is a timing issue. This is further confirmed by the elimination of the increase in error with time when the acquisition is triggered by the excitation module. The underlying cause is likely either an error in estimating the frame time stamps, or clock skew caused by different clocks used for the ultrasound scanner and excitation modules. The latter might be solved by driving both by a master clock. If the master clock is sufficient for removing the phase drift error, it may become the preferred method in most use cases compared to the triggered synchronization proposed in this work, since there would never be a lag introduced by waiting for a trigger pulse to start the next ultrasound acquisition.

The elasticity measurements of the CIRS 049 elastography phantom are slightly different from the values reported by the manufacturer. For soft inclusion there is an overestimation of the reported elasticity, and for the stiff inclusion and the background there is an underestimation of the reported elasticity. This is consistent with previous measurements by our group at UBC using both ultrasound and MRI based elastography methods, with a variety of different inversion algorithms [22, 135–137]. The reasons for this discrepancy could be the difference in temperature, excitation frequency, or changes of the material properties of the phantom over time. The measurements done by CIRS were performed in a temperature controlled environment at 22 °C, using quasi-static compression, and at the time of manufacture approximately 10 years before the measurements were collected for this work. In this work, the temperature was at the ambient room temperature of the laboratory,

and was not controlled or measured. The frequency dependence of the elastic modulus of the phantom is not known, however there could be substantial difference between 0 Hz and 200 Hz.

The elasticity measurements at different exciter locations show a systemic increase in elasticity values for the third exciter location. This location is the furthest from the transducer. The increase can be explained as a diffraction bias, where the wave motion is no longer primarily along the axial direction, and therefore the projected motion vector results in an underestimation of the wave number. The decrease in wave amplitude due to the greater wave attenuation over the longer distance also likely contributes to greater error in the elasticity measurements for the third location.

2.7 Conclusion

This chapter has described the design and analysis of a flexible research based elastography platform. The implementation details for several different ultrasound interfaces has been described. The system is generic and can be adapted to any ultrasound scanner that allows access to beamformed RF or I/Q echo signals (using the *bandpass sampling* method). Simulations demonstrated that a conventional B-MODE pulse sequence can be used to measure steady state shear wave motion, and the phasor motion estimation is robust to speckle tracking jitter and errors in estimating the frame time stamps or frame rate. A customized ultrasound motor driver was developed that can interface with any motorized ultrasound transducer without modification, which provides greater control over the ultrasound acquisition without reducing ultrasound signal quality. Experimental measurements showed a gradual shift in motion phase over long acquisitions. For most cases, the acquisition time should be short enough to safely ignore the error, but for large volumetric acquisitions, or for combining multiple measurements over a long period of time, a synchronization between the excitation and ultrasound scanner using a trigger can eliminate the problem. The elasticity estimates are repeatable, but have a slight dependence on excitation conditions.

The following chapter describes some initial measurements obtained by applying the system to *ex vivo* placenta tissue. The system is also being used concurrently

by other researchers at UBC for studies of liver, kidney, and prostate elasticity.

Chapter 3

Viscoelastic Characterization of *Ex Vivo* Placenta Tissue Using SWAVE

3.1 Introduction

The placenta is the organ connecting a developing fetus to the uterine wall, and is responsible for the exchange of oxygen, nutrients, and waste between the mother and fetus. The fetal blood circulates through the umbilical cord to the placenta where it branches into vessels and eventually a network of branching chorionic villi. Placental abnormalities, such as preeclampsia and intrauterine growth restriction (IUGR), can have long-term impacts on both maternal and fetal health. Preeclampsia is a progressive hypertensive disorder of pregnancy, and is associated with approximately one third of severe obstetric morbidity [332]. IUGR is the pathologic restriction of fetal growth due to adverse genetic or environmental factors, characterized by an estimated fetal weight below the 10th percentile. The incidence of IUGR is estimated to be 5% to 7% of all pregnancies and results in an increased risk of perinatal, childhood, and adult morbidities [48]. The etiologies of both conditions are associated with placental factors such as poor uteroplacental perfusion, abnormal villous structure, and placental infarction [132, 285].

Due to the vascular nature of the placenta, medical Doppler ultrasound serves as a natural tool to assess placental function. The pulsatility index of the uterine artery, which is calculated as the difference between peak systolic and end diastolic flow divided by the mean velocity, is the most predictive Doppler measurement for diagnosis of preeclampsia or IUGR. The presence of a prediastolic notch in the velocity waveform provides further predictive power [72]. However, the sensitivity of Doppler ranges from 20% to 60%, with a positive predictive values of 6% to 40%, and therefore Doppler assessment alone has limited value as a screening test [26].

Histology indicates that abnormal placenta microstructure is significantly different from normal placenta, and is suggested as a cause of significant differences in elastic and viscous properties in mechanical testing [179]. Elastography offers a non-invasive method of characterizing changes in mechanical properties *in vivo*. Recently, a few studies have investigated applying elastography to the placenta in both *ex vivo* and *in vivo* settings [51, 185]. Initial studies have shown promise in identifying placental abnormalities. For example, Kılıç *et al.* [159] estimated elasticity using ARF induced shear wave speed measurements and found a significant difference in placental elasticity between women diagnosed with preeclampsia and healthy controls for gestational ages between 28–35 weeks. Similarly, significant increases in elasticity have been found for measurements during the second trimester of pregnancy using shear wave speed [70], and relative stiffness inferred from strain [71]. A significant increase in shear wave speed for pregnancies diagnosed with either fetal growth restriction or pregnancy induced hypertension has been observed [229]. Sugitani *et al.* [301] found a significant difference between normal and growth restricted placental shear wave speed, but did not find a significant difference for pregnancy induced hypertension.

Elastography can also determine the viscous properties of tissue by examining the frequency dependence of the shear waves [63, 81, 162]. Measurement of the viscous properties of placenta tissue is limited, though a dependence on the deformation rate has been observed in mechanical testing [333]. A recent elastography study of the placenta fit a power law rheological model to account for shear wave dispersion over a band of 20 Hz to 80 Hz [51].

Most elastography studies of the placenta to date have been based on ARF tran-

sient shear wave speed measurements at a single point on anterior placentas. The application of ARF to other placenta locations might be difficult due to depth limitations. For example, one study was unable to study placentas located at depths greater than 8 cm [70]. The SWAVE system uses longitudinal vibration which generates shear waves deep into the body. The placement of the excitation source can also be selected by the operator, so it could be placed in a location optimized for the placenta location without affecting the placement of the ultrasound transducer. Elasticity is computed quickly over a large volumetric ROI which can provide additional information about the spatial variability of placenta elasticity.

The purpose of this study is to obtain initial placenta data using the SWAVE system and to select appropriate experimental factors and SWAVE parameters. The SWAVE system is used to measure the Young's modulus of six placenta samples over a band of 60 Hz to 200 Hz. The frequency dependence is observed and the viscosity is quantified by fitting rheological models to the data. This is meant as a proof-of-concept to demonstrate the SWAVE system and start work on better understanding the placenta, and not meant as a final diagnostic tool for a specific medical condition.

3.2 Methods

SWAVE measurements were applied to six healthy intact placenta samples. The placentas were obtained after full-term delivery, and were measured approximately 4 hours after delivery on average, with a maximum delay of 10 hours after delivery. This study (H15-00974) was performed under written informed consent after approval by the UBC Children's and Women's Research Ethics Board. The consent form used for this study is provided in Appendix B. Study data were collected and managed using REDCap electronic data capture tools hosted at BC Women's and Children's Hospital [128].

Samples were stored immediately after delivery in a refrigerator at 4°C, and were heated to 37°C to approximate *in vivo* temperature just before SWAVE measurements by submerging the samples in a constant temperature water bath (Cole-Parmer, Montreal, Quebec, Canada). The maternal side of the placenta was placed on over an acoustic absorbing pad to reduce reverberation artefacts, and both the placenta and pad were placed on top of a steel plate and wrapped loosely in a mesh



Figure 3.1: The experimental apparatus for placenta SWAVE measurements. The placenta (1) is submerged in the water bath after being placed on a acoustically absorbent pad and a steel plate and wrapped loosely in a mesh bag. The ultrasound transducer (2) is submerged in the water bath and is imaging the fetal side of the placenta. The transducer is placed in a holder and positioned using a flexible arm. The disk at the end of the exciter (3) makes contact with the fetal side of the placenta to generate shear waves.

bag to keep the placenta submerged and stationary in the water bath. The exciter used to generate shear waves in the placenta was partially submerged into the water bath to make contact with the fetal side of the placenta. The exciter consisted of a 3 cm diameter circular steel plate which was placed in contact with the placenta on one end and at the other attached to a 10 cm long steel shaft threaded into a voice coil actuator (LDS V203, Brüel & Kjær, Nærum, Denmark) which was held stationary above the water bath using a 3-prong clamp (Fisher Scientific, Waltham, MA, USA). A 4DL14-5/38 motorized swept volume ultrasound transducer (Vermon, Tours, France) was placed in a custom made 3D printed case which was used to attach the transducer to a flexible positioning arm (CIVCO Medical Solutions, Kalona, IA, USA). The transducer face was submerged in the water bath and was fixed by the positioning arm with light contact on the fetal side of the placenta or with a small gap of less than a few millimetres. This placement was used to avoid pre-compression effects which could potentially increase the observed elasticity. The experimental apparatus is shown in Figure 3.1.

The ultrasound transducer was connected to a SonixTouch ultrasound machine

(Ultrasonix Medical Corp., Richmond, BC, Canada). The *swave* system was configured with the Porta ultrasound interface, the Data Translation excitation generator, and the custom stepper motor driver for Ultrasonix machines to control the volume acquisition, all described in Chapter 2. The ultrasound scanner transmitted pulses centred at 5 MHz, which corresponds to the recommended abdominal transducer frequency for obstetric examinations by the American Institute of Ultrasound in Medicine [14]. The thickness of a full term placenta is expected to be between 1.5 cm to 2.5 cm [157], so the scanner was set to a depth of 3 cm to capture the full thickness of all placentas and allow for a small water gap between the transducer and placenta. Monochromatic harmonic excitation was used to generate shear waves in the placentas. A single ultrasound volume was collected for each of six excitation frequencies at 60 Hz, 80 Hz, 90 Hz, 100 Hz, 120 Hz, and 200 Hz. The excitation frequencies were chosen to cover a wide range to examine the frequency dependence of the elasticity measurements, to line up nicely within the baseband so they could easily be differentiated, and to create at least one wavelength across the depth of the placenta sample to ensure LFE algorithm reached the correct estimate because it requires a transition zone of half a wavelength into a region [199]. The scanner collected 2D RF image frames at a rate of 72 Hz, so the excitation frequencies were placed at -12 Hz, 8 Hz, 18 Hz, 28 Hz, -24 Hz, and -16 Hz in the baseband. Using measurements of placenta elasticity from the literature [229], the average healthy placenta has a Young's modulus of approximately 5 kPa, so the chosen excitation frequencies result in expected wavelengths of 2.2 cm, 1.6 cm, 1.4 cm, 1.3 cm, 1.1 cm, and 0.65 cm. Based on the simulations from Chapter 2, a total of 25 ultrasound RF image frames were collected at each motor position in the volume for measuring tissue displacement and accurately fitting phasors at each excitation frequency. The motor was stepped to 10 positions, subtending an angle of approximately 4.5° . This relatively thin motor sweep decreased the acquisition time, which helped to limit the phase drift error described in Chapter 2, while still covering enough distance in the elevation direction to fit at least a quarter of a shear wavelength based on estimates of placenta elasticity from the literature and the excitation frequencies chosen in this study. The thin volume approach has produced accurate results on phantoms in a previous study [23]. Shear wave motion was estimated along the axial direction of the transducer, and the Young's modulus at each

excitation frequency was computed from the scan converted motion phasors using the LFE algorithm and Equation 2.26.

To ensure quality measurements, the phasor amplitude was monitored after starting the excitation at 60 Hz to check that the amplitude adequately penetrated the ROI and had a magnitude between 5 μm to 50 μm which is in a range accurately tracked by the cross-correlation speckle tracking algorithm. The accuracy of the speckle tracking was monitored by observing images of the normalized correlation coefficient and ensuring that the value was greater than 0.95 over the majority of the ROI. The phasor fit to the displacement measurements was monitored by ensuring the quality factor, as computed by Equation 2.13, was greater than 0.8, averaged over the entire image. Real-time display of the B-MODE, phasor amplitude, and Young's modulus images during acquisition also provided quality control. Data were saved for offline processing.

For each placenta sample the images were examined and an annular sector ROI was manually selected containing placenta tissue (avoiding regions in the ultrasound volumes that imaged outside of the placenta) with good wave amplitude (trying to avoid nodes in the wave pattern). This ROI generally covered the majority of the image volume. The mean and standard deviation of the Young's modulus was computed for each excitation frequency on each placenta sample. To help gain insight into the frequency dependence of the results, viscoelastic models were fit to the measurements as described in the following section.

3.2.1 Rheological Modelling

The viscoelastic properties of tissue can be determined by examining the frequency dependence or dispersive behaviour of the shear waves. The frequency dependence can be modelled by replacing the shear modulus with the complex shear modulus

$$\mu^* = \mu + j\mu'. \quad (3.1)$$

The shear wave number also becomes complex

$$k^* = \sqrt{\frac{\rho\omega^2}{\mu^*}}. \quad (3.2)$$

The shear wave speed can be obtained from the real part of the shear wave number [227]

$$c_s = \frac{\omega}{\Re(k^*)}. \quad (3.3)$$

As mentioned in Section 1.5.4, the LFE algorithm provides measurements of the wave number, so the SWAVE system can easily convert its output to shear wave speed using Equation 3.3. For this work, the mean wave number over the ROI is used. Using Equation 3.1 and Equation 3.2, the shear wave speed can be related to the complex shear modulus using

$$c_s = \sqrt{\frac{2(\Re(\mu^*)^2 + \Im(\mu^*)^2)}{\rho(\Re(\mu^*) + \sqrt{\Re(\mu^*)^2 + \Im(\mu^*)^2})}}. \quad (3.4)$$

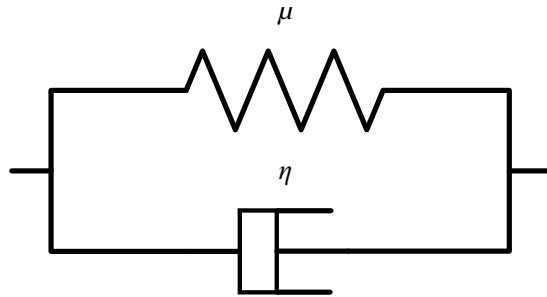
The complex shear modulus can be related to the viscoelastic properties using rheological models. Commonly used models for biological soft tissues include Voigt, Maxwell, and Zener [111]. A mechanical schematic representation of the models is shown in Figure 3.2. To derive the complex shear modulus for these models, it is convenient to use mechanical impedance, which measures how much a structure resists motion. It is usually expressed as a ratio of force to velocity, but in this chapter in order to relate impedance to continuum mechanics, shear stress replaces force and shear strain rate replaces velocity, which in the frequency domain results in

$$Z = \frac{\sigma(\omega)}{j\omega\epsilon(\omega)}. \quad (3.5)$$

Since the shear modulus is the ratio of shear stress and shear strain, the shear modulus can be expressed in terms of impedance as

$$\mu^* = j\omega Z. \quad (3.6)$$

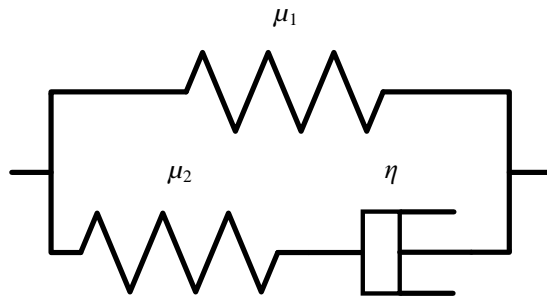
This makes it simple to determine the shear modulus from the schematic representations in Figure 3.2, and then obtain the shear wave speed from Equation 3.4. The total impedance of components in parallel is the summation of the component impedances. For components in series, the inverse total impedance is the sum of



(a)



(b)



(c)

Figure 3.2: A mechanical schematic of the (a) Voigt, (b) Maxwell, and (c) Zener rheological models.

the inverses of the component impedances. The impedance of a spring element parametrized by μ is

$$Z = \frac{\mu}{j\omega}, \quad (3.7)$$

and for a dashpot parametrized by η is

$$Z = \eta. \quad (3.8)$$

For the Voigt model, this results in a shear modulus of

$$\mu^* = \mu + j\omega\eta, \quad (3.9)$$

and a shear wave speed of

$$c_s = \sqrt{\frac{2(\mu^2 + \omega^2\eta^2)}{\rho(\mu + \sqrt{\mu^2 + \omega^2\eta^2})}}, \quad (3.10)$$

where μ and η refer to the spring and dashpot parameters in Figure 3.2a.

For the Maxwell model, the shear modulus is

$$\mu^* = \frac{j\omega\mu\eta}{\mu + j\omega\eta}, \quad (3.11)$$

and the shear wave speed

$$c_s = \sqrt{\frac{2\mu}{\rho\left(1 + \sqrt{1 + \frac{\mu^2}{\omega^2\eta^2}}\right)}}. \quad (3.12)$$

For the Zener model, the shear modulus is

$$\mu^* = \frac{\mu_1\mu_2 + j\omega(\mu_1\eta + \mu_2\eta)}{\mu_2 + j\omega\eta}, \quad (3.13)$$

and the shear wave speed

$$c_s = \sqrt{\frac{2 \left(\mu_1^2 \mu_2^2 + \omega^2 \eta^2 (\mu_1 + \mu_2)^2 \right)}{\rho \left(\mu_1 \mu_2^2 + \omega^2 \eta^2 (\mu_1 + \mu_2) + \sqrt{\left(\mu_1^2 \mu_2^2 + \omega^2 \eta^2 (\mu_1 + \mu_2)^2 \right) \left(\mu_2^2 + \omega^2 \eta^2 \right)} \right)}}. \quad (3.14)$$

To estimate the parameters in each of the models, a least squares fit over the six excitation frequencies is found between the model and the measured shear wave speed from `SWAVE`

$$\begin{aligned} & \underset{\boldsymbol{\chi}}{\text{minimize}} && \sum_{i=1}^6 (c_s(\omega_i, \boldsymbol{\chi}) - \hat{c}_s(\omega_i))^2 \\ & \text{subject to} && \chi_a \geq 0, a = 1, \dots, n, \end{aligned} \quad (3.15)$$

where $\boldsymbol{\chi}$ is a vector of n rheological parameters, and $\hat{c}_s(\omega_i)$ is the measured shear wave speed from `SWAVE` at excitation frequency ω_i . The lower bound constraint was applied to avoid non-physical solutions for the rheological parameters. The goodness of the fit is evaluated using the RMS error

$$c_{\text{RMS}} = \sqrt{\frac{1}{6} \sum_{i=1}^6 (c_s(\omega_i, \boldsymbol{\chi}) - \hat{c}_s(\omega_i))^2}. \quad (3.16)$$

3.3 Results

An example of the waves measured inside of a placenta sample is displayed in Figure 3.3. The `B-MODE` image shows mostly uniform speckle through the imaging region, with some bright reflections near the centre of the image likely caused by a collagenous matrix encasing damaged villi (discussed further later). The acoustically absorbent pad is visible at the bottom of the image at a small angle to the horizontal and a dark region in the top left of the image is created from waves passing through water where the exciter has depressed the tissue away from the face of the ultrasound transducer. The real part of the complex motion phasor shows the wave pattern at one phase of the excitation. The waves appear to be propagating roughly from left to right. The wavelength appears to decrease with increasing ex-

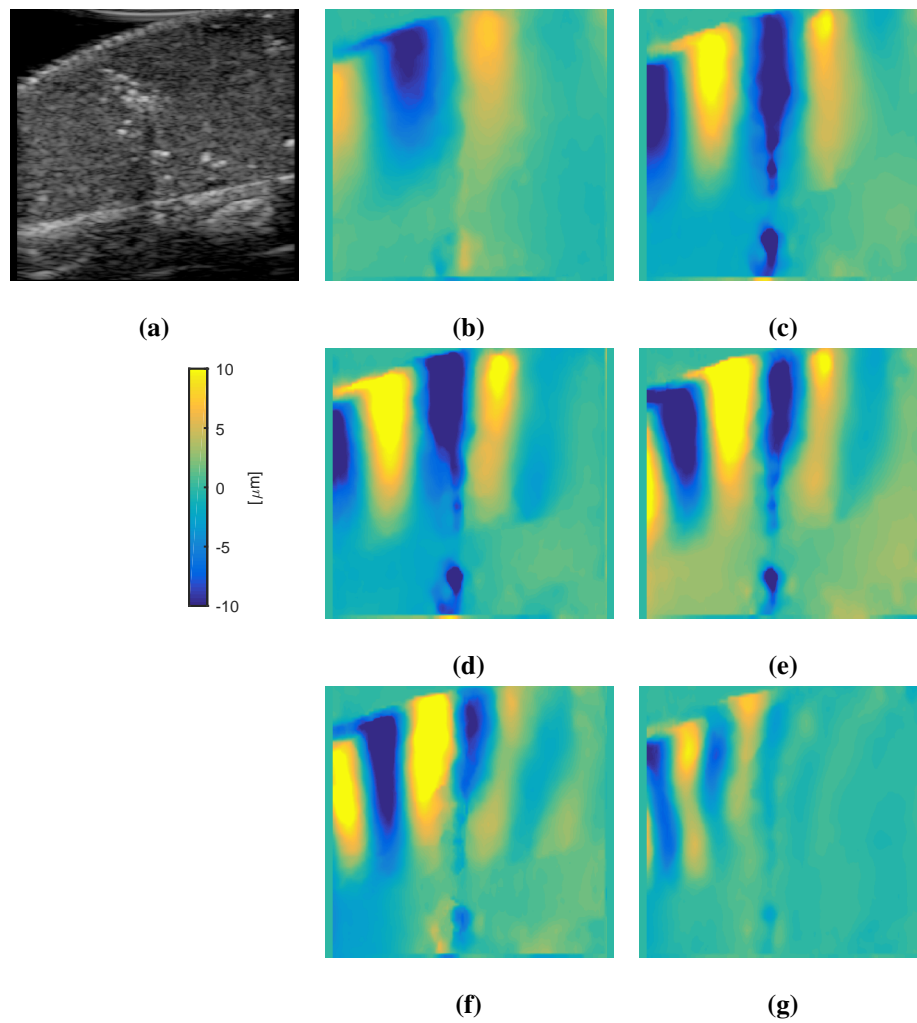


Figure 3.3: The 2D image plane from the centre of the volumetric ultrasound sweep for placenta Sample 5. (a) The B-MODE image shows the placenta, with bright reflections near the centre of the image. The corresponding real part of the complex motion phasor is shown at the excitation frequencies (b) 60 Hz, (c) 80 Hz, (d) 90 Hz, (e) 100 Hz, (f) 120 Hz, and (g) 200 Hz. All images have a depth of 3 cm and width of 3.8 cm.

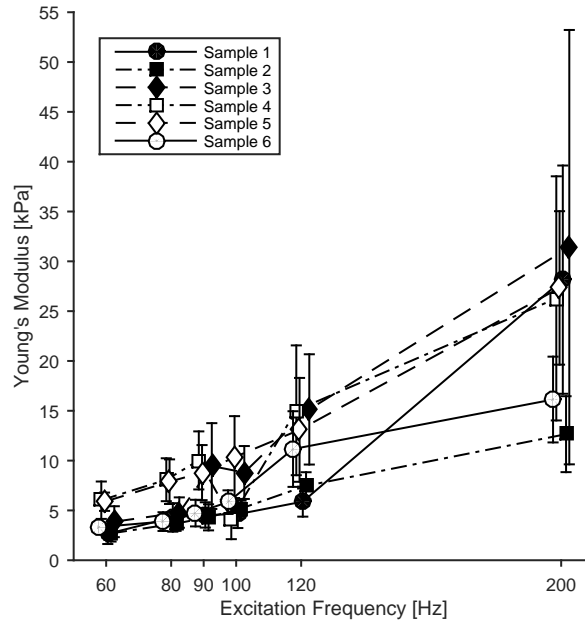


Figure 3.4: Mean Young’s modulus measurements as a function of frequency for the six placenta samples (standard deviation shown as bars). The plot markers are spread a small amount about each excitation frequency to improve visualization—this does not correspond to actual variations in the physically applied excitation frequency.

citation frequency. The region containing the damaged villi seems to change the wave pattern slightly which is especially visible at higher frequencies.

Mean Young’s modulus measurements, as computed by the LFE algorithm and Equation 2.26, as a function of excitation frequency for the six placenta samples are plotted in Figure 3.4. All samples show a general trend of increasing elasticity with increased excitation frequency as expected because Equation 2.26 does not include a separate viscous term. The mean elasticity values between samples are similar at each excitation frequency, with greater spread occurring at higher frequencies. The variance of the elasticity within a sample also increases with frequency. This may be partially explained by the decrease in excitation amplitude, as shown in Figure 3.5, possibly leading to a poorer SNR at high frequencies.

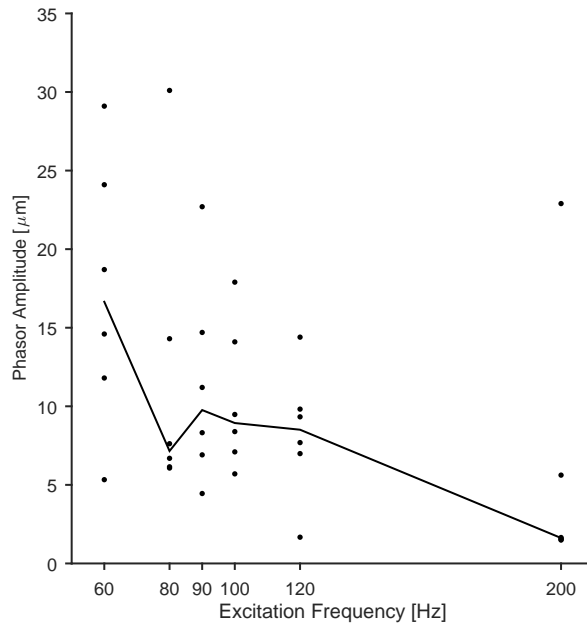
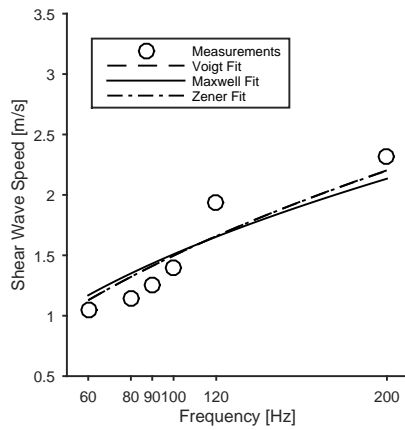


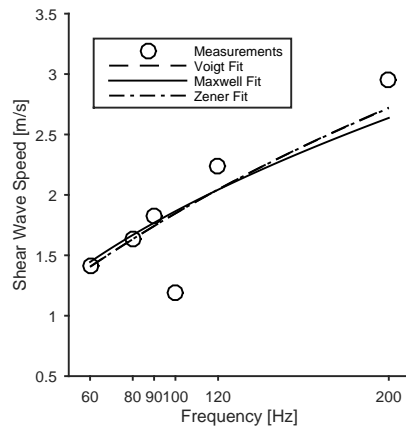
Figure 3.5: The mean amplitude of the measured phasor for each placenta sample over all excitation frequencies in the region where the mean elasticity was calculated. The solid line connects the median of the means for each frequency, indicating that the general trend is decreasing phasor amplitude with frequency.

Figure 3.6 shows the fits to the shear wave speed dispersion using the Voigt, Maxwell, and Zener models. The viscoelastic parameters which correspond to the fitted models for each sample and the RMS error in the fits are provided in Table 3.1. All of the models provide a similar fit to the measurements, with the Voigt and Zener models providing an almost identical curve. For this data set the Voigt model provides the best fit in terms of RMS error.

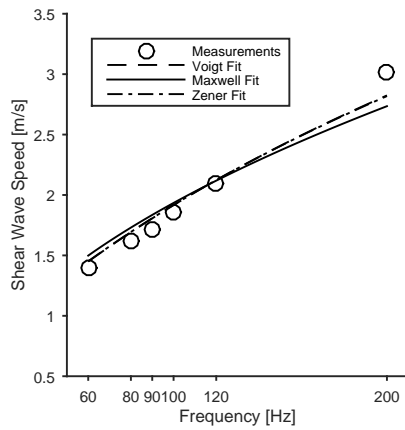
Although most of each placenta appears as uniformly textured tissue in B-MODE images, some placentas did exhibit some heterogeneities which were also investigated. Measurements were repeated in three different locations on placenta Sample 4. The B-MODE and Young's modulus (computed at 120 Hz) images for the different regions are shown in Figure 3.7. The elasticity in the first measurement region



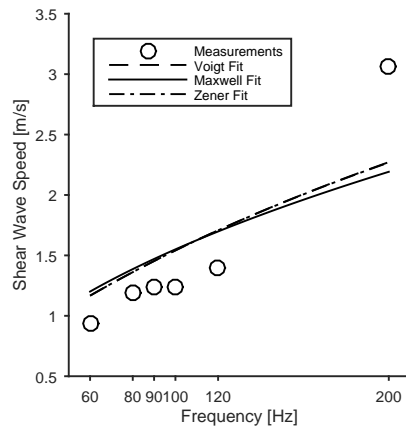
(a)



(b)



(c)



(d)

(continued)

is mostly uniform with increasing elasticity with increasing depth. Computing the mean Young's modulus over the first 3 mm and last 3 mm depth quantifies the increase from 6.5 kPa to 16.4 kPa. The second measurement region contains a dark circular region near the centre of both B-MODE and elasticity images, likely corresponding to a blood clot. The third measurement region contains some bright reflections near the bottom centre of the B-MODE image, again likely caused by damaged villi as in Figure 3.3, and an increase in elasticity seems to correspond to this area. The mean and standard deviation of the elasticity for each of these regions

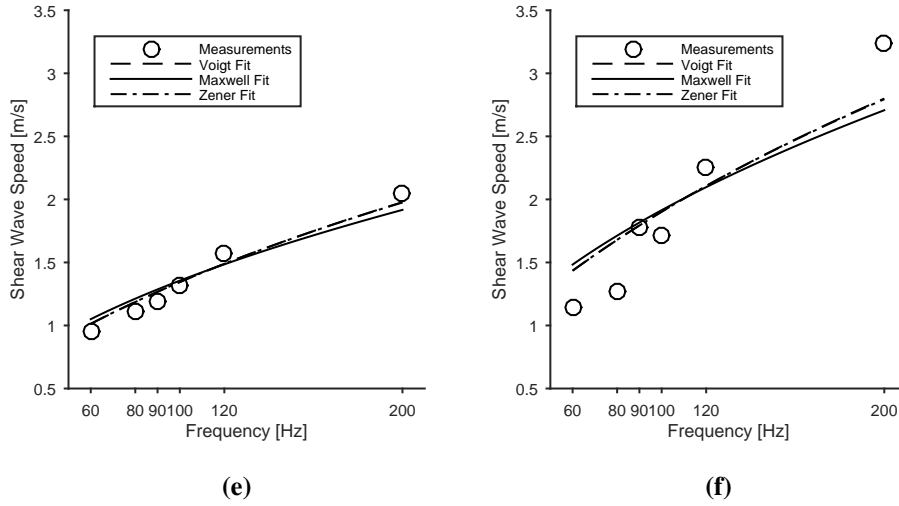


Figure 3.6: The shear wave speed dispersion relations found using the Voigt, Maxwell, and Zener models for each of the placenta samples ((a)–(f) correspond to samples 1–6).

over the full range of excitation frequencies is shown in Figure 3.8. For computing the statistics, the second region did not include the blood clot, but the third region did contain the damaged villi. Visually the mean elasticity measured in the first two regions appears very similar, especially for frequencies ≤ 120 Hz, however there is a statistically significant difference between the two regions over all frequencies, using the Student's t-test for comparison ($p < 0.001$). The third region shows an increase in elasticity compared to the other two regions over all frequencies which is likely due to the presence of the damaged villi.

3.4 Discussion

The elasticity values measured in this work can be compared with previous placenta elastography studies. Figure 3.9 summarizes the range of mean Young's moduli from several studies. When necessary, measurements were converted from shear wave speed to Young's modulus using

$$E = 3c_s^2\rho, \quad (3.17)$$

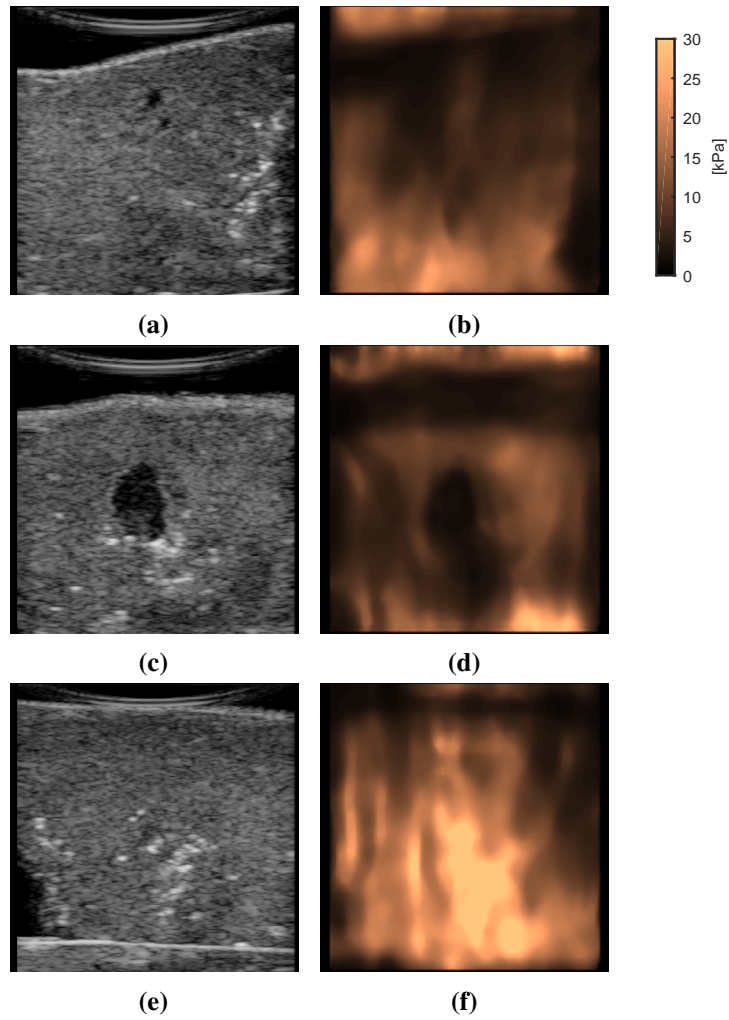


Figure 3.7: The B-MODE (first column) and Young's modulus (second column) image planes from the centre of the volumetric ultrasound sweep from three different regions of placenta Sample 4. The Young's modulus images shown here were computed from waves excited at 120 Hz.

Table 3.1: Rheological model parameters and RMS error corresponding to the fits to the shear wave speed dispersion shown in Figure 3.6 for six placenta samples. The final column shows the inter-sample mean of each quantity (standard deviation in brackets).

Model	Sample						Mean
	1	2	3	4	5	6	
Voigt							
μ (kPa)	0.369	0.733	0.690	0.451	0.295	0.607	0.524 (0.179)
η (Pa s)	13.6	21.4	22.7	14.7	11.0	22.1	17.6 (5.05)
c_{RMS} (m/s)	0.164	0.301	0.099	0.396	0.070	0.291	0.220 (0.129)
Maxwell							
μ (MPa)	7.64	9.15	5.64	19.8	3.82	13.6	9.95 (5.89)
η (Pa s)	11.4	17.4	18.7	12.0	9.19	18.3	14.5 (4.12)
c_{RMS} (m/s)	0.189	0.320	0.144	0.429	0.098	0.333	0.252 (0.128)
Zener							
μ_1 (kPa)	0.367	0.731	0.692	0.455	0.296	0.609	0.525 (0.179)
μ_2 (kPa)	413	486	456	498	326	489	445 (65.9)
η (Pa s)	13.7	21.4	22.7	14.7	11.0	22.1	17.6 (5.07)
c_{RMS} (m/s)	0.164	0.301	0.102	0.397	0.071	0.293	0.221 (0.129)

where ρ was assumed to be 1000 kg/m^3 , and the tissue was implicitly assumed to be completely incompressible. The low frequency measurements from this work correspond to the low end of the previously reported range, and some of the high frequency measurements extend beyond the high end of the previously reported range. Only the study by Callé *et al.* [51] used mechanical excitation, however it used transient rather than steady-state excitation, and the reported speeds were extracted from the spectrum at 50 Hz. The other studies used ARF excitation, however the spectral content of the excitation for the commercial systems used is not reported.

The repeated measurement of elasticity for a single placenta at different locations showed similar mean elasticity results but with a significant difference. Previ-

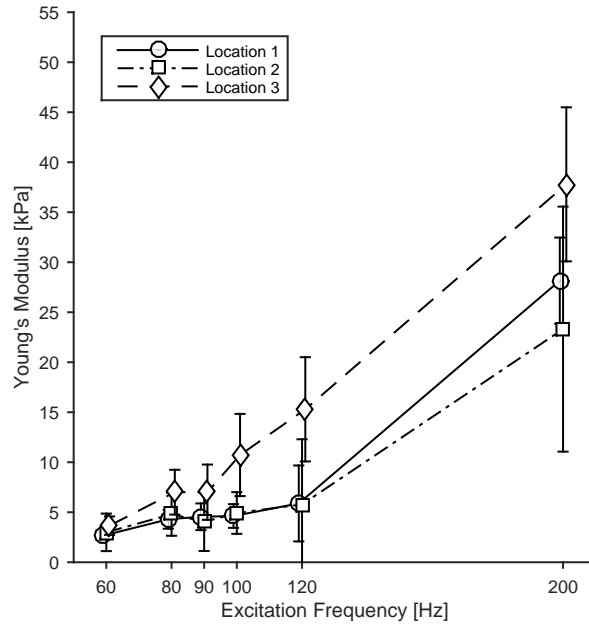


Figure 3.8: Mean Young’s modulus measurements as a function of frequency for placenta Sample 4, repeated at three separate locations (standard deviation shown as bars). The plot markers are spread a small amount about each excitation frequency to improve visualization—this does not correspond to actual variations in the physically applied excitation frequency.

ous studies have compared mean elasticity measurements from different regions of the placenta with one finding differences [301], one not finding differences [185], and one finding difference for abnormal placenta tissue but no difference for healthy placenta tissue [159]. The results in this work are not directly comparable because the difference in mean elasticity is compared within a single placenta sample, rather than the differences between groups of mean elasticity as in the literature. The results here add additional insights that the particular structures in the ROI can affect the elasticity measurements.

Kılıç *et al.* [159] measured a larger maximum elastic modulus on the maternal surface of the placenta than on the fetal surface. The maternal side corresponds to the deeper region in our measurements, so the observation of increased elastic-

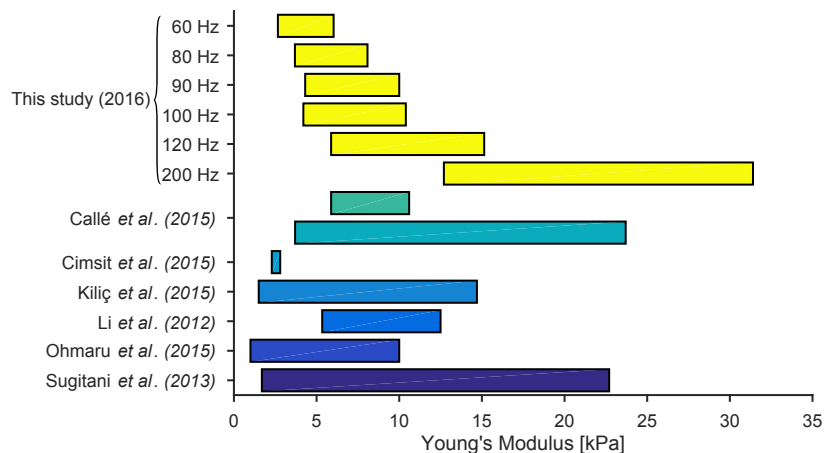


Figure 3.9: The range of mean Young’s moduli reported in the elastography literature for normal placenta, with the range of mean Young’s moduli from this study at each frequency provided for comparison. The values were extracted from Callé *et al.* [51], Cimsit *et al.* [70], Kılıç *et al.* [159], Li *et al.* [185], Ohmaru *et al.* [229], and Sugitani *et al.* [301]. The Callé *et al.* [51] work includes two transient excitation methods, the topmost corresponding to ARF induced shear waves, and the lower a mechanical excitation.

ity with depth in Figure 3.7 seems to match the previous measurements. Further research into the biophysical basis for differences in elasticity between the chorionic plate, intervillous space, and basal plate would be helpful for explaining these observations. Based on our current understanding, our best explanation is the increased stiffness is caused by a collagenous layer separating the fetal and maternal tissues. The placenta is organized into cotyledons that each correspond to a single major fetal vascular unit. At term, the three dimensional organization of placental cotyledons resembles an egg carton. The lateral and deep margins of each cotyledon are defined by a transition from fetal placental tissue to maternal decidual tissue under and between each cotyledon. At the border of this transition the placenta exudes a contiguous layer of collagenous material which effectively separates the fetal and maternal solid tissues. Because this layer is solid and contiguous, this likely represents areas of increased stiffness at the base of the placenta and intermittently

where the lateral aspect of bordering cotyledons are included in the scanned area. When placental villi are damaged, which occurs in all placentas including clinically normal placentas, a similar collagenous matrix is produced which encases the damaged villi and frequently concatenates adjacent villi. This process is a likely explanation for focal areas of increased stiffness and density seen away from the basal and lateral cotyledon margins. Occasionally these areas, particularly along the basal aspect in placentas over 40 week gestational age, may calcify and this would contribute to increased echogenicity and stiffness (e.g. bright spots in Figure 3.3(a) and Figure 3.7(e)).

The placenta elasticity measurements demonstrated a strong frequency dependence. This agrees with previous mechanical testing that concluded that the mechanical response of placenta tissue is dependent on strain rate [333]. It is difficult to compare the results to previous elastography studies of the placenta as they have not reported viscosity values. Comparing the mean viscosity of 17.6 Pa s using the Voigt model for the placenta measurements from this work to other tissues reported in the literature indicates that the placenta is highly viscous. For example, measurements of breast tissue have reported a much lower mean viscosity at 2.4 Pa s for malignant cancer, 2.1 Pa s for fibroadenoma, and 0.55 Pa s for surrounding breast tissue [292]. The mean viscosity for healthy brain and liver tissue is also lower at 6.7 Pa s and 5.5 Pa s, respectively [162]. The viscosity of the vastus medialis muscle in the thigh when actively contracting is closer to but still smaller than the placenta at 12 Pa s [80].

There are several limitations in the estimation of viscoelastic properties in this work. These limitations include lower tissue displacement SNR at higher frequencies, simplifications in the LFE inversion algorithm for determining the shear wave number, lack of consideration for fitting attenuation, lack of spatial information, and simplifications in rheological modelling. The tissue displacement SNR affects the viscoelastic parameter estimation in a similar way to the Young's modulus estimation, where the low amplitude of the waves at higher frequencies leads to greater uncertainty in the LFE output. The LFE inversion algorithm also includes simplifications which do not account for any dispersive effects, which likely leads to inaccuracies in the shear wave speed estimation. A more sophisticated inversion method that can directly obtain the complex shear modulus or complex shear wave number

directly would likely be more accurate. One possible approach to find the imaginary part of the complex wave number is to measure the phase angle between the shear wave and the applied force [323].

The lack of spatial information in the viscoelastic results is due to using an averaged wave number over a ROI for the wave speed calculation. This was done to simplify the fitting operation from applying it to many thousands of voxels for each placenta sample to applying it just once per sample. This also made interpreting the results simpler and easier to compare between rheological models and different placenta samples. However, just as the spatial distribution of Young's modulus can contain interesting information as demonstrated in Figure 3.7, the change in viscosity over space could provide some useful diagnostic information.

The rheological modelling was simplified by ignoring inertial terms. Elastography studies typically do not model inertial effects as the fits to experimental results appear to be adequate without the need for adding an additional parameter. While inertial effects could play a role, the strong effect of viscosity likely produces a highly overdamped second order system [97, 246].

The different excitation frequencies applied in this work were applied in a sequential manner, with an independent volumetric ultrasound displacement measurement acquired for each frequency. This allowed complete isolation of each frequency component to help interpret the quality of acquisition of each component and their influence on the system. For the *ex vivo* setting this was an acceptable compromise, but for *in vivo* applications, the multiple acquisitions may not be able to be matched sequentially due to motion of the mother or fetus between excitation frequencies. A multi-frequency excitation approach, which combines the excitation signals of each desired frequency, is the recommended approach for *in vivo* measurements in order to reduce acquisition time. This efficacy of the simultaneous multi-frequency approach has previously been demonstrated for *in vivo* prostate tissue [191].

3.5 Conclusion

The feasibility of applying the SWAVE technique to placenta tissue has been demonstrated. Measurement of six healthy placenta samples produced similar elasticity

measurements over a band of excitation frequencies of 60 Hz to 200 Hz, with values agreeing with previous elastography measurements in the literature.

This is the first study to apply Voigt, Maxwell, and Zener rheological models to elastography measurements of placental tissue. Results indicate that all models provide a similar fit, with the Voigt model providing the best fit by a slim margin based on RMS error. The results indicate the placenta is a very viscous organ, which corroborates with its highly vascular structure.

Future work will compare elastic and viscoelastic measurements of placentas from normal pregnancies to those diagnosed with preeclampsia or fetal growth restriction, to determine if there are differences that may be used to help detect disease. Applying the SWAVE system *in vivo* should include a study optimizing the exciter design and placement for sufficient generation of shear waves within the placenta, but it would otherwise be straightforward to measure the placenta viscoelastic behaviour during pregnancy with this system. Increased accuracy in elasticity inversion could be obtained by measuring the full 3D displacement vector. The following chapters describe methods for improving the accuracy in measuring the full 3D displacement vector for SWAVE.

Chapter 4

Spatial Calibration of Swept 3D Ultrasound

4.1 Introduction

Ultrasound has gained popularity because it is low cost, portable, safe, and has a high frame-rate. While the majority of diagnostic ultrasound procedures use 2D imaging, 3D imaging can provide significant advantages [85, 219]. For example, different 2D imaging planes may be “re-sliced” from the 3D ultrasound volume to provide 2D image orientations that would be otherwise impossible to acquire, such as parallel to the skin surface. Additionally, surface or volume rendered models can be generated which may reveal pathology that is more difficult to discern in conventional ultrasound images. Imaging in 3D can provide more information on the geometry of anatomical structures and more accurate measures such as volume. 3D ultrasound can also help in needle localization and guidance during biopsy [28]. In this thesis, 2D imaging refers to planar cross-sectioned images produced by transducers such as linear, curvilinear, or phased arrays, and 3D imaging refers to ultrasound volumes produced from swept motor transducers.

3D ultrasound data can be especially beneficial in elastography. While inducing low frequency vibration of the tissue, 3D ultrasound can observe the waves propagating in all 3 dimensions over a volume [260]. 3D measurements can reduce overestimation of elasticity calculations by up to 60% compared to 2D measure-

ments [23].

Typically a swept motor transducer relies on a model of the motor geometry to calculate the location of 2D image slices with respect to another. In elastography, the effect of uncertainty or error in the parameters, such as sweep angle, sweep step size, scale of the voxels, and other geometry used by the ultrasound machine to reconstruct each sweep of image slices into a Cartesian volume, has not been studied in detail. While most of these errors are generally not considered large enough to pose a problem with 3D diagnostic ultrasound imaging, errors in the parameters could be expected to contribute to elastography errors in two major ways. The first is by incorrect geometrical placement of image data, which for SWAVE techniques would affect the apparent shear wavelength, resulting in misestimation of elasticity. The other contribution from errors in the parameters is errors in the assumed direction of motion measurement. Previous work has demonstrated that assuming a purely vertical measurement direction for motion that is actually measured in a cylindrical coordinate system leads to underestimation of elasticity [137]. Some form of calibration to solve for these parameters for an individual transducer may help reduce these errors.

A further extension of applying 3D ultrasound to elastography is the possibility to combine multiple intersecting volumes tilted at different angles which would allow for accurate measurement of the full 3D motion vector, rather than the 1D component of the motion vector that is typically measured with ultrasound [4]. A position tracking sensor can be attached to a swept motor transducer to allow tracking of multiple 3D ultrasound volumes. Using the position tracking sensor measurements, these volumes can be transformed to a global coordinate system and combined into a composite volume. 3D ultrasound spatial tracking of this nature has other clinical applications including intra-operative visualization [237], ablation guidance [19], and spatial compounding [172], among others.

Generally, position tracking systems measure the pose of a sensor mounted on the ultrasound transducer with respect to a fixed base; therefore, it is necessary to calibrate the pose of the image with respect to the sensor to enable these tracking techniques. Typically, this calibration is accomplished by collecting ultrasound images of objects, called phantoms, with known geometry and calculating the rotation and translation parameters of the calibration that best match the image features to

the geometry. Phantoms are typically constructed from spherical beads [182], nylon wires [262], and planar surfaces [275].

Ultrasound calibration remains a critical factor in the overall system accuracy of many ultrasound guided procedures [189]. The 2D ultrasound calibration problem has been studied extensively, with reviews of many of the techniques published [143, 206]. However, it is generally not straightforward to extend 2D techniques to make use of the extra data available in 3D ultrasound volumes. Various aspects of the 3D ultrasound calibration problem have been investigated. One study used a 2D technique to calibrate a 2D transducer mounted on a motor to replicate the action of a 3D transducer [45]; however, in commercially available swept motor 3D transducers, the array is enclosed in the transducer housing, so tracking the array location as the motor is swept is infeasible. Tracking both the transducer and phantom has shown greater accuracy compared to registering ultrasound volumes to each other, as in hand-eye techniques [35]. Point phantoms have been used for 3D calibration, and are easier to use in 3D compared to 2D because aligning the point phantom precisely with the scan plane is not as difficult with many regularly spaced slices in the volume [175, 259]. For wire phantoms, the intensities of the wire reflections over the volume are iteratively matched to a reference model of the straight lines matching the phantom geometry [35, 258]. A few techniques have also used planar features, and are solved by either using intensity information to iteratively match a reference, similar to the wire methods [177], or matching the zero component of the reference model of the plane to points on the plane in the volume [27, 258].

As previously mentioned, a swept motor transducer relies on several geometrical parameters to calculate a volume based on the location of a set of 2D image slices. Reliance on these parameters is considered to contribute to spatial calibration error [258]. It is a problem during calibration acquisition, since each volume observing the phantom will incorrectly locate the phantom's features. It further becomes a problem after calibration when tracking the transducer, as not only are the calibration transforms incorrect, leading to placing the volumes in the wrong position and orientation in the global coordinate system, but each volume in the collection is distorted with respect to the local transducer coordinates as well. Previous work has studied the distortions caused by errors in the sweep parameters for an untracked swept motor transducer, where highly accurate measures of organ

volume were desired, and a method was presented for estimating the parameters assuming accurate alignment of the transducer with two specially designed phantoms [315].

The work presented in this chapter aims to reduce errors caused by uncertainty in the motor parameters in tracked 3D ultrasound. This should help to reduce errors in 3D elastography which relies upon these parameters, as well as provide improvement to 3D ultrasound spatial calibration which can be applied to advanced elastography methods and several other clinical application. Since recent techniques developed for 2D calibration demonstrate very high accuracy, and, assuming motor positioning is repeatable such that each image slice in a swept volume can be considered a 2D imaging source, a novel technique is proposed that calibrates multiple individual 2D image slices along the sweep, instead of scan converting the slices to a Cartesian volume and then performing a single 3D calibration. For example, a study of a closed-form 2D calibration using differential measurements from inclined wedges reported a point reconstruction error under 0.3 mm [215]. While it is difficult to compare calibration accuracy across the literature, sub-millimetre point reconstruction accuracy has not been previously demonstrated in 3D calibration techniques.

Ideally, 2D calibration would be performed for each slice in the volume to achieve ultimate accuracy. However, it is impractical and unnecessary to calibrate every slice. Instead, a best fit path through calibration solutions calculated for a subset of the images slices along the sweep is used. The fit will be used to determine the calibration transforms between the calibrated slices. The fit can also reduce the influence of error in individual calibrations, analogous to a least-squares model fitting to noisy linear data to reduce error of individual measurements.

In particular, a method for fitting calibrations is presented which separately fits the translation and rotation parameters. The translation parameters are found by fitting an arc to the origin of each calibration. The rotation parameters are found by solving for the best fit geodesic on the quaternion manifold, with each calibration's rotation component representing one quaternion sample on the manifold. The fitting method presented in this work is general and would function to extend any 2D calibration technique to a 3D swept motor transducer. The 2D differential wedge technique is used in this work due to its high accuracy [215]. Since the technique

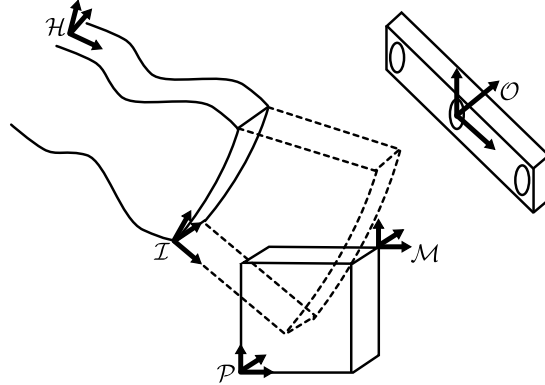


Figure 4.1: The coordinate systems used in the calibration procedure.

uses multiple 2D slices of the wedge phantom over a 3D volume, this technique is labelled “ $W_{2D \rightarrow 3D}$ ”.

The proposed multi-slice calibration approach is evaluated by comparing it to several single-calibration (slice or reconstructed volume) techniques. One approach is to use a 2D technique on a single slice in the volume, such as the well known N-wire (or Z-wire) [75, 238], and rely on the motor parameters to locate all other points in the volume relative to the calibrated slice (“ N_{2D} ”). Since this calibration technique ignores data at all locations along the sweep except one slice, there is potential for a lever arm effect to magnify errors when the motor is swept far from the calibrated slice. To reduce the lever arm effect, a novel technique is developed to extend the N-wire concept to a reconstructed volume (3D) by first scan converting the segmented points into a 3D point cloud before solving for the calibration parameters (“ N_{3D} ”). A possible improvement to the general N-wire calibration concept is also presented by solving for the outside edge points of the N-wire, in addition to the centre point used in previous works (“ N_{3D}^{Full} ”), explained in detail later. The N-wire technique provides the advantage of a closed form solution compared to an iterative optimization, but has the disadvantage of providing sparse point features compared to feature-rich planes [262]. For a final comparison, a novel closed form planar-fitting calibration technique is presented that relies on scan converted 3D data (“ P_{3D} ”). Details of these methods are provided below.

4.2 Methods

This section describes the calibration problem and the five techniques used in this chapter to solve it. An illustration of the components and coordinate systems for the calibration is shown in Figure 4.1. The goal of calibration is to determine the fixed, rigid rotation and translation relating the image coordinate system, \mathcal{I} , and the coordinate system of the position sensor on the transducer holder, \mathcal{H} . Here the position sensor consists of markers on the holder that are tracked by a fixed optical camera system, \mathcal{O} , which also tracks markers mounted on the phantom body, \mathcal{M} . Often it is convenient to define the coordinate system of the phantom not at \mathcal{M} , but with respect to a geometrical feature that appears in the images. This coordinate system is called \mathcal{P} , and the fixed relationship between \mathcal{P} and \mathcal{M} is determined separately *a priori* with tracked stylus measurements (using an optical tracking system with 0.02 mm mean error as explained later in Section 4.4).

4.2.1 Data Acquisition

All images were acquired on a SonixTouch ultrasound machine (Ultrasonix Medical Corp., Richmond, BC, Canada), equipped with a 4DL14-5 linear array swept motor transducer, operating at a transmit frequency of 10 MHz and a depth setting of 45 mm. The transducer and phantoms were submersed in a solution of 9% by volume glycerol combined with distilled water to create a medium for the ultrasound waves to travel through at 1540 m/s to match the ultrasound machine's settings [224].

Based on data from the transducer manufacturer (Vermon, Tours, France), the radius of the motor is 81 mm and has an angular travel of 0.45° between slices. Both parameters were used for 3D scan conversion. To gain complete control over the transducer's stepper motor, an intermediate circuit was constructed and placed between the transducer and the ultrasound machine (see Section 2.2.4). The circuit passed the ultrasound signals directly through the connectors, but provided its own stepper motor signals controlled by the parallel port on the SonixTouch.

The transducer and phantoms used for calibration had IRED markers mounted to their bodies which were optically tracked by an Optotrak Certus motion capture system (Northern Digital Inc., Waterloo, Ontario, Canada). This provided both

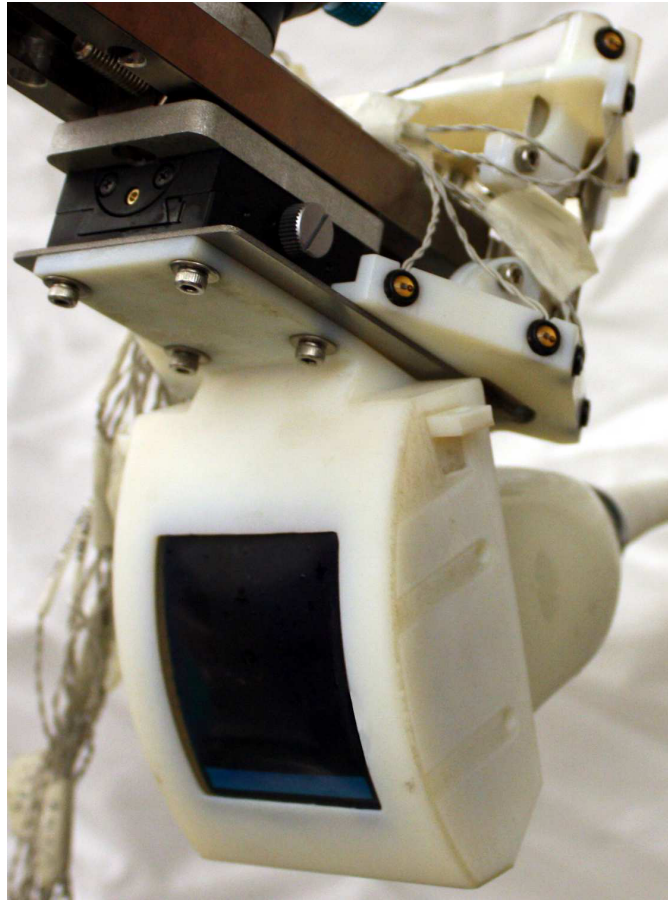


Figure 4.2: The 3D transducer, encased in a holder with IRED markers.

position and orientation of coordinate systems defined using the markers on the transducer and phantom bodies with respect to the Optotrak coordinate system. To find the relationship between the IRED markers on the phantom body and the image features on the phantom, an Optotrak 4 Marker Digitizing Probe stylus with a known 1.5 mm radius ball tip was used to locate points in \mathcal{M} with known correspondence in \mathcal{P} .

The transducer was placed inside a holder that was precisely manufactured to match its outer dimensions with an Objet30 3D printer (Objet Inc., Billerica, MA, USA) and held in place using constraining pins pushing against the top of the transducer. The IRED markers were press fit into small circular bore holes in the holder,

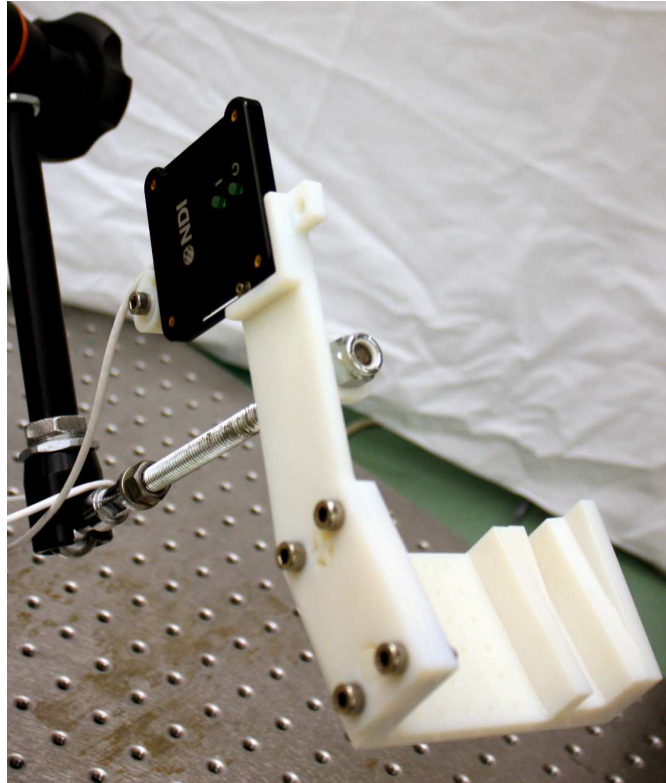


Figure 4.3: The phantom used for the planar and wedge calibration methods.

which was reinforced with a stainless steel frame to reduce the possibility of the holder flexing and changing the markers' positions. The holder was mounted on a goniometer, a linear translation stage, and a rotary stage to allow fine adjustments of the transducer pose, before being attached to a positioning arm (model 811-002; CIVCO Medical Solutions, Kalona, IA, USA) to fix the assembly in space. The phantoms were also attached to a positioning arm (model 244; Manfrotto, Cassola, Italy) to keep the phantom fixed while recording data. The holder and one of the calibration phantoms are pictured in Figure 4.2 and Figure 4.3.

4.2.2 N-wire Calibration (N_{2D} , N_{3D} , and N_{3D}^{Full})

In N-wire calibration, the geometry of the N shape is used to calculate the position of the centre point, \vec{f} , based on measurements from an ultrasound image. Once

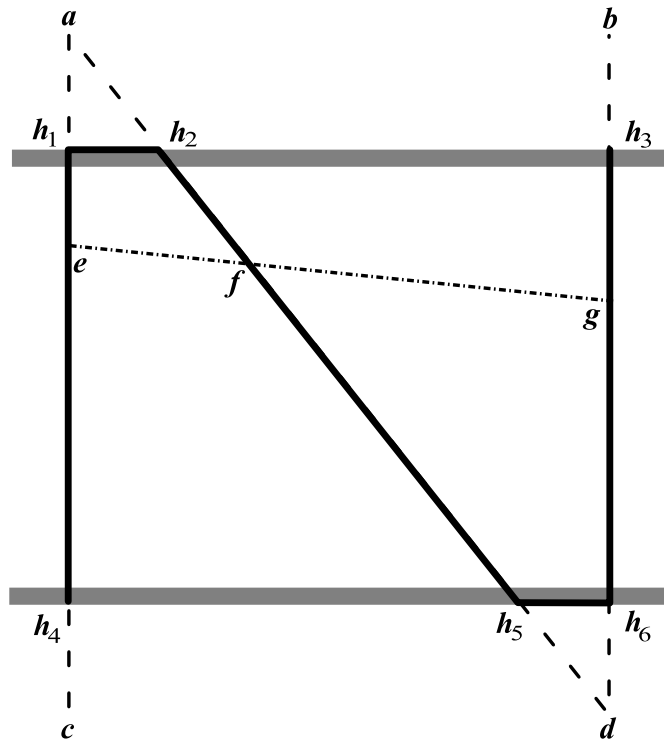


Figure 4.4: The top view of one row of the N-wire phantom and the intersecting scan plane.

at least three non-collinear centre points have been found in both coordinate systems, the transform that best matches the points provides the calibration solution. Multiple centre points can be obtained by acquiring an image with more than one N-wire shape visible, or acquiring additional images after transducer motion. Both techniques are used in this work to obtain an over-constrained set of points, with a phantom containing three N-wire shapes, and a collection of 10 ultrasound volumes from different positions and orientations.

The phantom was constructed with 0.3 mm nylon wire interwoven through six holes (\vec{h}_{1-6}) in a N shape, as shown in Figure 4.4. In total the phantom contained three rows of N-wires, each spaced by 5 mm. The top row geometry had 30 mm between \vec{h}_1 and \vec{h}_3 , 50 mm between \vec{h}_1 and \vec{h}_4 , and 20 mm horizontally between \vec{h}_2 and \vec{h}_5 . The middle row had the same dimensions, but the N shape was mirrored.

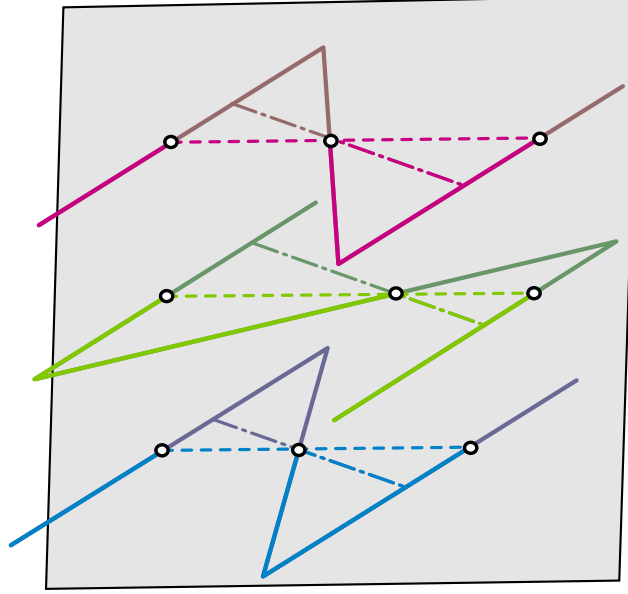


Figure 4.5: A 3D view of the three N-wire rows. The ultrasound scan plane, shown in grey, intersects each N-wire at three points, shown by the circles. A dashed line is shown connecting the intersection points in the scan plane. Based on the same inter-point distances, the lines could be mirrored to alternate orientations, shown as dash-dot lines.

The bottom row had the same orientation as the top, but \vec{h}_3 , \vec{h}_5 , and \vec{h}_6 were shifted 5 mm to the left. The holes were precisely located by manufacturing a rectangular block with the 3D printer (0.028 mm resolution and 0.1 mm accuracy, as stated by the manufacturer).

The geometry of the N-wire was defined by the points \vec{a} , \vec{b} , \vec{c} , and \vec{d} which were identified in the phantom markers' coordinate system, \mathcal{M} , with a stylus and the Optotrak system. The stylus measured the hole locations, $\vec{h}_{1..6}$, and used the known geometry to find the corners of the N shape. The corner \vec{a} was located some scalar distance ξ along the direction $(\vec{h}_1 - \vec{h}_4)$ from the point \vec{h}_1 . The scalar distance was determined using the triangle formed by

$$\xi (\vec{h}_1 - \vec{h}_4) + \xi (\vec{h}_5 - \vec{h}_2) = \vec{h}_2 - \vec{h}_1. \quad (4.1)$$

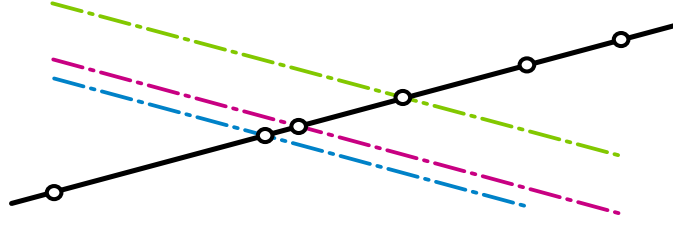


Figure 4.6: A top view of the same N-wire phantom and scanning geometry as presented in Figure 4.5. The N-shapes are omitted in this view, but the intersection points are shown as hollow circles along the ultrasound scan plane, shown in black. The dashed lines from Figure 4.5 all lie within the scan plane and are occluded by the black line. Considering only one N-wire row at a time, the inter-point distances could be created by the scan plane being aligned along the dash-dot line for the top (pink), middle (green), or bottom (blue) rows. Noting equal depth between each dash-dot line into the page from this view, it would be impossible for the scan plane to possibly pass through all three of the dash-dot lines at the same time, or any combination of dash-dot and dashed (occluded by the black) lines.

The other corner points were found in a similar manner.

The nine points in each slice in the ultrasound volume were automatically segmented by performing morphological opening operations to reduce speckle and then searching for parallel lines of three collinear dots [65]. Using the segmented points, the location of the centre point in the phantom marker coordinates was calculated

$${}^M\vec{f} = {}^M\vec{a} + \frac{\|{}^I\vec{e} - {}^I\vec{f}\|}{\|{}^I\vec{e} - {}^I\vec{g}\|} ({}^M\vec{d} - {}^M\vec{a}), \quad (4.2)$$

where ${}^M\vec{f}$ and ${}^I\vec{f}$ are located in the marker and image coordinate systems, respectively. The N_{3D} technique used all of the segmented points, while the N_{2D} only used the points segmented in the centre slice. For each calibration technique, 10 volumes were acquired.

The collection of points described in \mathcal{M} can be transformed to \mathcal{H} using Optotrak measurements. The calibration transform can be found by matching corresponding points between \mathcal{I} and \mathcal{H} . The translation vector is the difference between the centroid of the two sets of points, and the quaternion describing the rotation is

found by solving an eigenvalue problem [139].

The description thus far has only demonstrated how to estimate the location of the centre point along the angled segment of the N-wire, as used previously in the literature, ignoring the points on the parallel outside wires (\vec{e} and \vec{g} in Figure 4.4). Including the outside points could improve the corresponding point transformation estimation. The reason that these points were ignored in previous works might be the fact that the location of the outside points in the phantom's coordinate system is not unique when based only on the lengths from the ultrasound image used to find the centre point. In fact there are two possible locations for the outside points, mirrored about a line perpendicular to outside wires and passing through the centre point as shown in Figure 4.5 and Figure 4.6. Considering only one N-wire at a time, the ultrasound scan plane could pass through either the dashed line or the dash-dot line in Figure 4.5 and still produce the same inter-point distances in the image. However, it is possible to determine the correct line when considering all three N-wires. Considering the three interior points in Figure 4.5, and all the possible exterior points (intersections of dashed and dash-dot lines with exterior wires), there are $2^3 = 8$ possible sets of nine points that could lie on the ultrasound plane. In general, only one of these sets lies in a plane. In Figure 4.6, it is clear that a plane could not pass through any set of three lines that contains any of the dash-dot lines, leaving the combination of the three dashed lines as the only possibility in this example. To select the correct set of points in this work, a plane is fitted for each case, and the plane with the smallest mean squared distance to the points is selected. Further discussion on the ambiguity of transducer pose based on N-wire lengths measured in ultrasound is explored in Appendix C.

4.2.3 Planar Calibration (P_{3D})

The method of planar calibration presented here is similar to a technique developed for simultaneous localization and mapping (SLAM) [247]. The SLAM technique was applied to a laser range finding sensor, mounted on a mobile robot, which obtained a cloud of points to be segmented into planar surfaces. The planes were then matched after a change in position or orientation of the sensor to estimate the motion of the sensor. Our method does not match two sets of segmented data. Rather, it matches

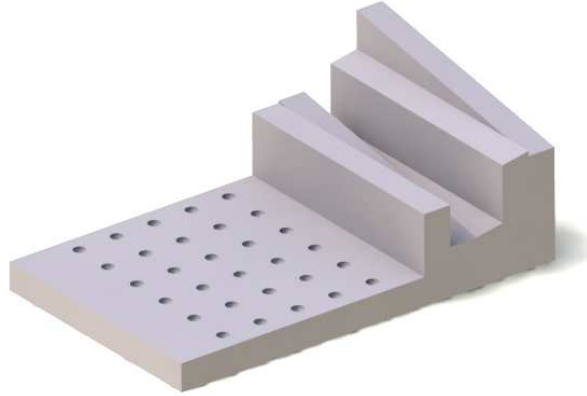


Figure 4.7: A rendering of the phantom used for the planar and wedge calibration methods, excluding the IRED marker attachment. The phantom includes a grid of hemispherical indents for the stylus to measure the rigid transformation between the phantom coordinate system and the mounted IRED markers.

planes segmented in ultrasound, \mathcal{I} , to a mathematical model of the planes described in the phantom coordinate system, \mathcal{P} . Only one reconstructed ultrasound volume is required. However, collecting additional volumes after transducer motion can serve to reduce errors in calibration calculations via averaging. Our method uses a phantom designed for ultrasound calibration, where the angles for the planes were chosen to balance image quality and reliable feature extraction, while providing angles that reduce the sensitivity of the calibration to measurement errors [215]. The calibration solution is found in two steps. First, the rotation is found by aligning the normal vectors of the planes segmented in the ultrasound volumes to the mathematical model. Next, the translation is found using the rotation solved in the first step, and by satisfying the planar equation in both the phantom and image coordinate systems.

Previous studies using planar features in 3D swept ultrasound have not attempted to detect planes using 3D data, instead using 2D data to create clouds of points defined by maximum intensity gradients [177], Canny edge detection [259], and 2D Hough transforms [27]. These studies have used iterative methods to solve the

calibration problem. The technique presented here uses total least squares to find the best fit planes to 3D data and has a closed form solution. Based on research on 2D calibration, both aspects tend to provide more accurate solutions [216, 262].

The phantom was manufactured with the 3D printer, containing five planar surfaces as pictured in Figure 4.3. The phantom also contains a 6×5 grid of hemispherical indents, spaced 10 mm apart in each direction, pictured in Figure 4.7. The location of the indents with respect to the planar surfaces is known to within the tolerance of the 3D printer, and the radius of the hemispheres matches the radius of the stylus tip. The points are reliably located in both the phantom, \mathcal{P} , and marker, \mathcal{M} , coordinate systems with a stylus. The rigid transformation between \mathcal{P} and \mathcal{M} is determined with a corresponding point algorithm [139].

The lines produced by the phantom surfaces are segmented in each slice in the sweep by finding the maximum intensity along each scan line. The user identifies local regions where each unique plane is located in the image. Best fit planes are fit to the collection of maximum intensity points using principal component analysis (PCA) to minimize the orthogonal distances of the points to the plane [153].

A plane can be described by the equation

$$\vec{n} \cdot \vec{x} = d, \quad (4.3)$$

where \vec{n} is the unit normal of the plane and the distance to the origin is d . To find the rotation from the ultrasound volume to the phantom, the dot product is maximized between the normal vectors detected from the ultrasound volume and the normal vectors of the planes known from the phantom's manufactured geometry described in the phantom coordinate system (i.e. the corresponding normal vectors are made as close to parallel as possible). Using unit quaternions to represent rotation, the algorithm finds the unit quaternion ${}^{\mathcal{P}}_I q$ that maximizes:

$$\sum_{i=1}^k \left({}^{\mathcal{P}}_I q {}^I n_i {}^{\mathcal{P}}_I q^* \right) \cdot {}^{\mathcal{P}} n_i, \quad (4.4)$$

where ${}^I n_i$ is the i^{th} normal vector in the ultrasound volume coordinate system, written as a purely imaginary quaternion $\left[0, \vec{n}_i^T \right]^T$, q^* is the conjugate of q , and k is

the number of planes in the volume. This equation is essentially the same as finding the rotation in the corresponding point problem with quaternions. The difference is using normal direction vectors instead of position location vectors. The quaternion that maximizes Equation 4.4 can be determined by finding the eigenvector corresponding to the maximum eigenvalue of a 4×4 symmetric matrix composed of sums of products of the elements of the normal vectors [139].

The next step is to find the translation vector from the ultrasound volume to the phantom. Consider transforming a point from one of the planes in the ultrasound volume coordinate system to the phantom coordinate system

$${}^{\mathcal{P}}\vec{p} = {}^{\mathcal{P}}R^I \vec{p} + {}^{\mathcal{P}}\vec{t}, \quad (4.5)$$

where ${}^{\mathcal{P}}R$ is the rotation found from Equation 4.4, but expressed as a 3×3 rotation matrix to simplify the notation, and ${}^{\mathcal{P}}\vec{t}$ is the translation to solve for between the two coordinate systems. Using Equation 4.3, the translation vector is related to the plane parameters via

$$\begin{aligned} {}^{\mathcal{P}}d &= {}^{\mathcal{P}}\vec{n} \cdot {}^{\mathcal{P}}\vec{p} \\ &= {}^{\mathcal{P}}\vec{n}^T \left({}^{\mathcal{P}}R^I \vec{p} + {}^{\mathcal{P}}\vec{t} \right) \\ &= \left({}^{\mathcal{P}}R^I \vec{n} \right)^T {}^{\mathcal{P}}R^I \vec{p} + {}^{\mathcal{P}}\vec{n}^T {}^{\mathcal{P}}\vec{t} \\ &= {}^I\vec{n}^T {}^I\vec{p} + {}^{\mathcal{P}}\vec{n}^T {}^{\mathcal{P}}\vec{t} \\ &= {}^I d + {}^{\mathcal{P}}\vec{n}^T {}^{\mathcal{P}}\vec{t}. \end{aligned} \quad (4.6)$$

Given three or more planes in the ultrasound volume, ${}^{\mathcal{P}}\vec{t}$ can be solved for in the least squares sense

$${}^{\mathcal{P}}\vec{t} = \left(A^T A \right)^{-1} A^T \vec{d}, \quad (4.7)$$

where

$$A = \begin{bmatrix} {}^{\mathcal{P}}\vec{n}_1^T \\ \vdots \\ {}^{\mathcal{P}}\vec{n}_k^T \end{bmatrix}, \quad (4.8)$$

and

$$\vec{d} = \begin{bmatrix} \mathcal{P} d_1 - \mathcal{I} d_1 \\ \vdots \\ \mathcal{P} d_k - \mathcal{I} d_k \end{bmatrix}. \quad (4.9)$$

The five planes in the phantom used in this experiment already provide redundant information with a single ultrasound volume. To match the other techniques, ten volumes in total were acquired.

4.2.4 Wedge Calibration on 2D Slices and then Fitting ($W_{2D \rightarrow 3D}$)

The methods described thus far rely upon knowing the geometry of the transducer and motor precisely to determine where each of the 2D image slices in the ultrasound volume is located with respect to another to scan convert the slices into a 3D volume before identifying phantom features. To reduce errors introduced from 3D scan conversion, 2D calibrations are performed at multiple slice locations and the best fit path through the 2D calibrations is found to link them together. Any 2D calibration technique may be applied in this framework. For this work, a recently developed highly accurate technique is chosen which uses slope measurements of wedge features from the phantom in Figure 4.3 [215]. Calibrations on five slices evenly distributed across the motor sweep are used to fit the 3D calibration path. The trade-off of improving the best fit path with more calibrated slices is the time required to collect data. The 2D wedge calibration typically requires at least ten unique images and poses per slice for a reliable result. Collecting data for each slice would require $10 \times 64 = 640$ unique images and poses compared to the 50 chosen to be collected here. Using the information from the 50 poses, the calibration transforms at intermediate positions are found by interpolating along the best fit path. This method does not rely on the motor geometry, however in-plane scan conversion is assumed to be correct (i.e. the piezoelectric element spacing is known). In addition, it is assumed that the array travels along a circular arc and the relative angular positions produced by the stepper motor are accurate and repeatable. The rest of this subsection describes the method of interpolating between 2D calibrations.

The translation and rotation parts of the calibration interpolation are considered

separately. The translation is found using the best fit circle to the individual translation samples from each slice calibration along the arc. In this work, circle fitting is performed using a closed form algebraic fit, optimized to eliminate bias in the estimation [10].

The rotation is found using the best fit geodesic on the unit quaternion manifold. The advantages of parametrizing the rotation using quaternions are that they are intuitively and compactly described by a rotation axis and angle, and it is simple to remove computational drift and restore a valid rotation through vector normalization. The quaternion manifold is a 3-sphere (S^3) sitting in four dimensional space. A number of researchers have focused on the problem of interpolating rotations, where the resulting path must pass through the set of control points. Examples include spherical linear interpolation [289], acceleration minimizing cubics [245], and spherical splines [50]. The problem of finding a best fit path through regression on the manifold is far less studied. One example attempts to find a geodesic on S^3 using the analogous slope and intercept for linear regression in Euclidean space with an optimization algorithm minimizing distances to the rotation samples [106]. The method presented here is similar, however the mean of the rotation samples is used to locate the geodesic on the manifold, and only the direction of the geodesic is optimized instead of solving for both quantities simultaneously. The method here is only one such method of fitting the calibration methods. Other approaches are discussed in Appendix E.

In Euclidean space, \mathbb{R}^3 , a best fit line can be parametrized by a point on the line and a direction vector. The line passes through the centroid, or mean, of the sample points, and the sum of the orthogonal distances between the samples and the line is minimized. This line can be written as

$$\vec{x} = \vec{x}_m + t\vec{v}, \quad (4.10)$$

where \vec{x}_m is the mean point, \vec{v} is the direction of the line, and t is the scalar parameter of the line.

This same procedure can be extended to finding a best fit geodesic on a quaternion manifold. The direction of the line in Equation 4.10 can be interpreted as lying in the tangent space at the mean point. On a quaternion manifold, some mapping is

required to pull the tangent back to the manifold. This is called the exponential map, which also has an inverse mapping from the manifold to the tangent space called the logarithmic map. The correspondence between the two can be seen as follows. A quaternion, q , describing a rotation around the normalized axis of rotation, \vec{u} , by an angle, θ , can be written as [13]

$$\begin{aligned} q &= \cos\left(\frac{1}{2}\theta\right) + \sin\left(\frac{1}{2}\theta\right)\vec{u} \\ &= e^{\frac{1}{2}\theta\vec{u}}. \end{aligned} \quad (4.11)$$

Taking the logarithm of Equation 4.11 results in

$$\vec{v} = \frac{1}{2}\theta\vec{u}. \quad (4.12)$$

The logarithmic and exponential maps are explained in more detail in Appendix D. The $+$ operator in Equation 4.10 is replaced by the Lie group operator, which for unit quaternions is multiplication. Therefore, the best fit geodesic on the quaternion manifold can be written using the mean quaternion, q_m of the set of sample quaternions, and a tangent vector at the mean quaternion, \vec{v}

$$q = q_m \exp(t\vec{v}). \quad (4.13)$$

The mean quaternion, is found using spherical averages by first calculating a Euclidean average and projecting back to the 3-sphere, then iteratively mapping the sample points to the tangent space at the current estimate of the mean, calculating the Euclidean average in the tangent space, then mapping back to the sphere by the exponential map until the iterations converge to a single point on the sphere [50].

The tangent vector at the mean quaternion, \vec{v} , is found by solving a gradient descent minimization problem, described in Appendix E. A simulation verifying the efficacy of the algorithm is provided in Appendix F.

The interpolated rotation path is bi-invariant, which means that the result is independent of the choice of coordinate system for the transducer holder (left-invariance), \mathcal{H} , as well as the image slices (right-invariance), \mathcal{I} . See Appendix E for a demonstration of the left- and right-invariance of the distance metric used

for optimization. If all of the quaternion sample points were left multiplied by an arbitrary quaternion, a , then the resulting path would be

$$q = a q_m \exp (t\vec{v}) . \quad (4.14)$$

Right multiplication of the quaternions would result in the path

$$q = q_m \exp (t\vec{v}) a . \quad (4.15)$$

In other words, if any of the axes of our co-ordinate systems were redefined, the rotation describing the redefinition would be the same as the rotation between the original and new solution paths. This is an intuitive and desirable property, but it is not guaranteed in general for paths on the manifold. If bi-invariance was not satisfied, the path would depend upon the definitions of the co-ordinate systems which can be defined arbitrarily.

4.2.5 Validation of the Calibration Methods

Validation of the calibration methods was performed by assessing repeatability and accuracy. Repeatability refers to how similar calibration solutions are to each other given different input data—repeating calibrations with different images should ideally still give the same transform between \mathcal{I} and \mathcal{H} because it is fixed. Accuracy refers to how close the calibration solution is to the true transform between \mathcal{I} and \mathcal{H} . Since this is unknown, accuracy cannot be measured directly. Instead, accuracy is inferred by reconstructing physical quantities with known location or dimension.

To evaluate the repeatability, the standard deviation of the six degrees of freedom can be calculated after calibration with multiple independent data sets [2, 39]. In this work, since 10 data sets were acquired for each technique, and each technique can be solved using only one data set, the standard deviation for each technique is calculated for 10 independent trials. In the case of $W_{2D \rightarrow 3D}$, the standard deviation is calculated after applying fits to 10 randomly selected unique combinations of the 10 calibrations at each of the five calibration locations.

Two point reconstruction tests were used to evaluate the calibration accuracy. Point reconstruction tests calculate the difference between points with known lo-

cations and segmented points transformed to the same coordinate system using a calibration solution. In both of the tests, all 10 data sets were used to solve for a single least squares solution for each method.

The first point reconstruction test used a tracked stylus as the object to be imaged [258]. The stylus and transducer were both moved between each of 25 volume acquisitions. The ball tip was manually segmented by finding the slice in each volume with the strongest comet-tail reverberation, centring a line along the reverberation, and selecting the top of the bright intensity response of the tip [7]. The bright response corresponds to the top of the sphere [122]; the centre of the sphere was estimated by adding a distance equal to the radius along the direction of the scan line. The point reconstruction error is calculated between the stylus tip, as measured by the Optotrak system, and the tip segmented in the images and then transformed into the Optotrak coordinates using the calibration solution

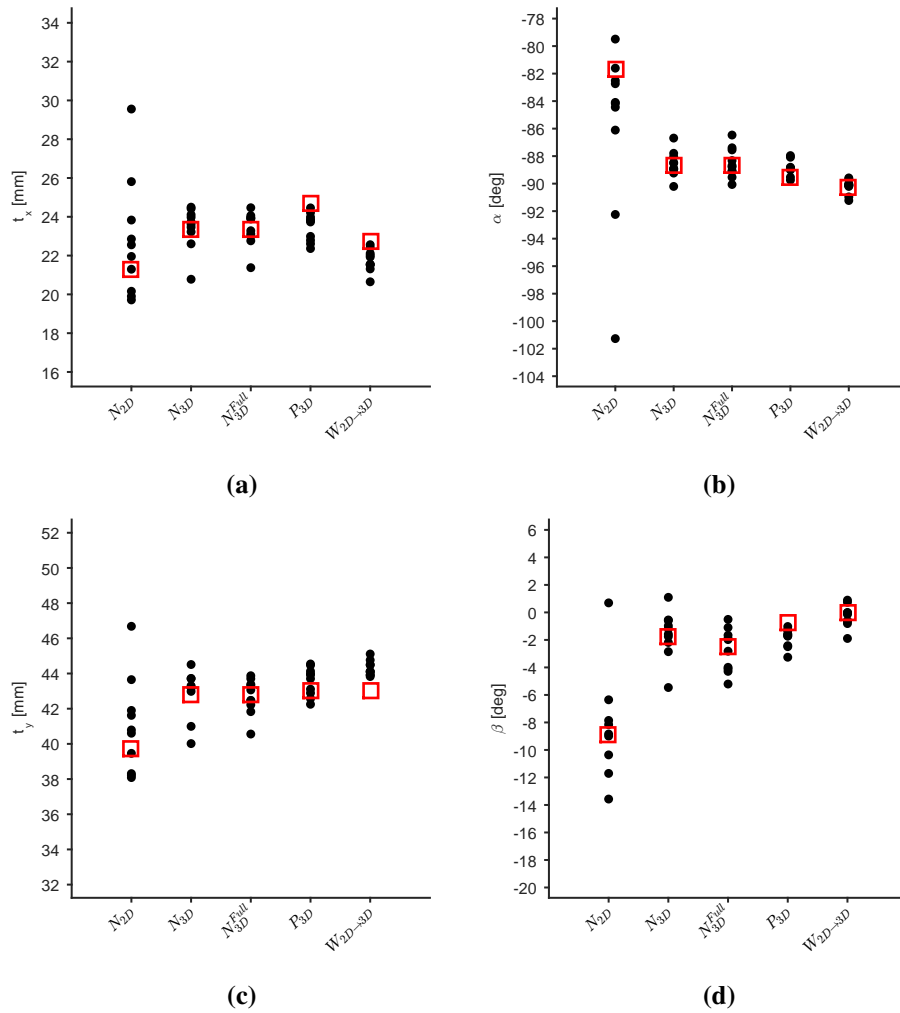
$$E_s(v) = \|\mathcal{O}\vec{x} - \mathcal{O}_v T_v \mathcal{H} T^I \vec{x}\|, \quad (4.16)$$

where the \vec{x} is the stylus tip, T describes the rigid transformation operation, error is calculated for the v^{th} volume acquired of the stylus tip.

The second point reconstruction test used the N-wire phantom [215]. A single volume of the phantom was acquired, distinct from the 10 used in the N-wire calibrations. Only the centre points of each N shape were used for evaluation with a total of 78 centre points segmented in the volume. The centre points are known in \mathcal{M} from geometry as described in the Methods section. These points can be transformed to \mathcal{H} using the Optotrak measurements. The same centre points in \mathcal{I} can be transformed to \mathcal{H} using the calibration solution. The error is the magnitude of the difference between these two sets of points

$$E_n(i, v) = \|\mathcal{O}_v T_v^{-1} \mathcal{O}_v T_v \mathcal{M} \vec{x}_i - \mathcal{H} T^I \vec{x}_i\|, \quad (4.17)$$

where the error is calculated for $i \in [1 \dots 3]$ centre points in each volume.



(continued)

4.3 Results

The calibration results from each of the 10 data sets for all of the calibration methods are plotted in Figure 4.8. The results are separated into six DOF; translation from the image to the holder (t_x , t_y , t_z) and Euler angles defined using the fixed image coordinate axes and applying first a rotation by γ around the x -axis, followed by a rotation by β around the y -axis, and finally a rotation by α around the z -axis. It should be noted that these results cannot be used to assess the accuracy of the

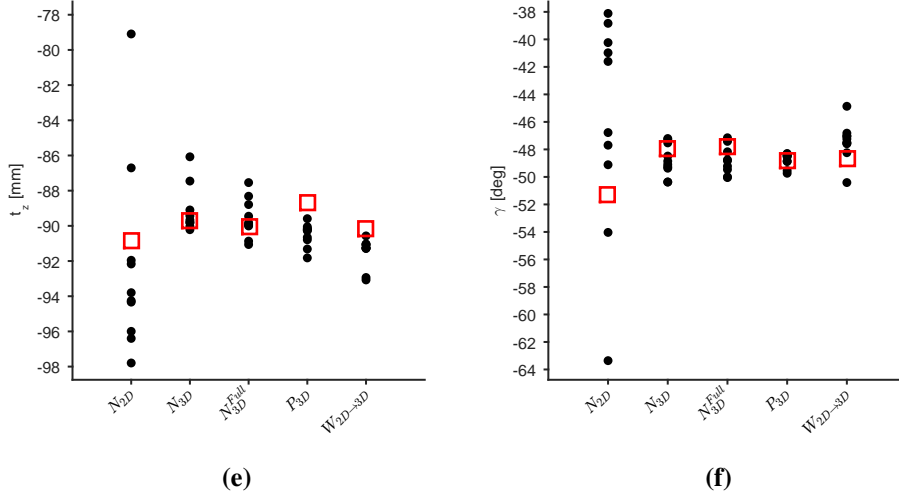


Figure 4.8: The translation and rotation parameter values plotted for ten independent tests (\bullet), depicting the variation in the solutions. Note, N_{2D} results are converted to the same coordinates as the other methods (i.e. the first slice of the sweep) using the assumed motor geometry. The parameters corresponding to a least squares solution (\square) using all of the data sets are also plotted.

Table 4.1: Standard deviations of the three translation DOF (mm) and three rotation DOF (degrees) after 10 trials using a single data set for calibration.

	N_{2D}	N_{3D}	N_{3D}^{Full}	P_{3D}	$W_{2D \rightarrow 3D}$
t_x	3.05	1.09	0.89	0.73	0.63
t_y	2.72	1.35	1.00	0.80	0.44
t_z	5.55	1.31	1.09	0.66	0.92
α	6.38	0.94	1.09	0.55	0.58
β	7.13	1.73	1.57	0.68	0.89
γ	7.96	1.16	1.08	0.51	1.54

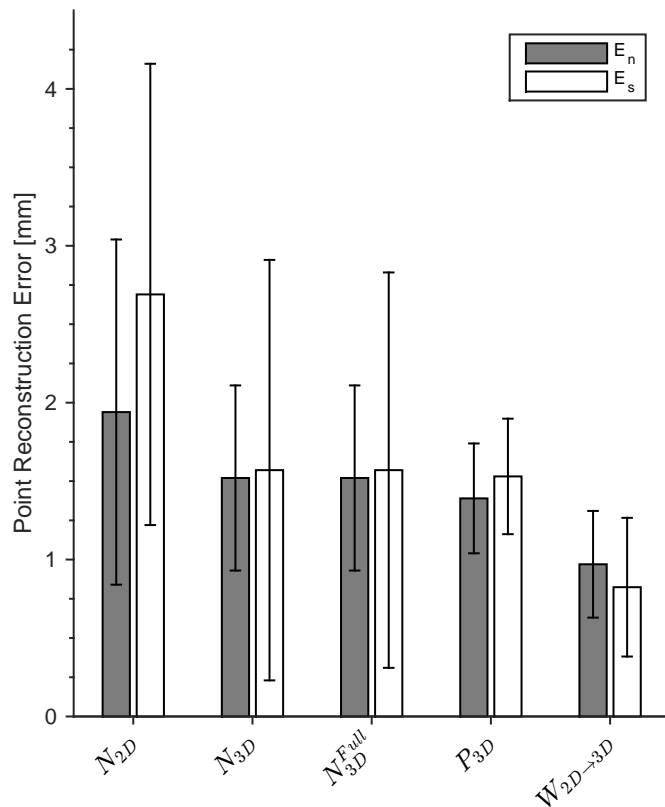


Figure 4.9: Point reconstruction error for the calibration techniques, using the N-wire phantom as validation (E_n) and the stylus (E_s). The bars indicate the mean and the error bands indicate the standard deviation.

calibration methods, as the true calibration solution is unknown, however it does provide a measure of the calibration repeatability. A calibration method is more repeatable when the solutions are more closely spaced. Based on Figure 4.8, the most repeatable methods are P_{3D} and $W_{2D \rightarrow 3D}$. This is quantified later in the results section using standard deviation. The least squares solution using all of the 10 data sets for each calibration method is also plotted. While a few points appear to be outliers, the outliers do not correspond to each other across the six DOF (e.g. an outlier in t_x does not correspond to an outlier in t_y). The least squares solution is clearly not a mean of the individual solutions in each DOF, and does not necessarily

even lie within the spread of the individual solutions in each DOF, because the least squares solution fits all six degrees of freedom at once.

The standard deviations of the six DOF for each of the calibration techniques are presented in Table 4.1. A smaller standard deviation indicates that the solutions are repeatable with a different input of transducer poses and images. This is desirable as it demonstrates that the method is not sensitive to the exact motion of the transducer used to collect the images as well as the image quality. The most repeatable calibration based on the standard deviation results is $W_{2D \rightarrow 3D}$ for t_x and t_y and P_{3D} for the remaining DOF.

The mean and standard deviation of the point reconstruction error as calculated using both the N-wire phantom and stylus tip as validation tools are presented in Figure 4.9. These results serve as an indirect measure of calibration accuracy. Based on the mean error, $W_{2D \rightarrow 3D}$ is significantly the most accurate technique in both the E_n and E_s tests, where significance is found using the Student's t-test ($p < 0.01$). All of the techniques are significantly more accurate than N_{2D} .

4.4 Discussion

The stylus used in this study served two purposes; to measure the coordinate systems for the phantoms, and to provide points measured in the tracker's coordinate system for validation in the point reconstruction test. To understand how the stylus contributed to the errors in this study, a study of how well the stylus measures known distances, as well as how much the stylus location varies at a measurement point was done. The columns of the stylus grid on the slope phantom are 50 mm in total length. Averaging over the five columns, the mean and standard deviation of the absolute error in the distance measurement using the stylus were 0.02 mm and 0.03 mm, respectively. To measure how much the stylus location varies, the standard deviation of the stylus location at each of the 30 grid points was averaged, resulting in a value of 0.11 mm. These results suggest stylus error has little effect on calibration or the point reconstruction test.

Comparing the performance of the calibration methods studied in this chapter to previous results produced by other research groups should be done with caution due to differences in materials, equipment, and acquisition protocol. In addition,

not all methods in the literature evaluate the calibrations using the same definitions of point reconstruction error. One study matched five tracked ultrasound volumes to a model of a phantom containing two egg-shaped 3D features to calibrate, and simulating optical tracking errors found a mean point reconstruction error of 2.0 mm [176]. A study using only a single volume and four point fiducials for calibration measured RMS point reconstruction errors of 5.1 mm and 5.5 mm, over two cross-wire point measurements repeated 10 times each and located in tracker coordinates using a stylus [258]. A study comparing three calibration methods (IXI-wire, cube, and stylus) found RMS point reconstruction errors over 10 stylus validation points of 2.15 mm, 4.91 mm, and 2.36 mm, using one, one, and five tracked ultrasound volumes, respectively [259]. Another study comparing separable and combined hand-eye calibrations (the phantom is not tracked) as well as a tracked phantom approach, all with a cross-wire phantom, calculated error between points sets generated over a 50^3 mm^3 volume spaced by 5 mm in each direction, and found mean errors of 5.9 mm, 3.5 mm, and 3.3 mm, respectively [35]. To the best of our knowledge, $W_{2D \rightarrow 3D}$ is the first 3D ultrasound calibration to demonstrate potential for sub-millimetre point reconstruction accuracy with a mean of 0.82 mm with the stylus validation, and 0.97 mm with the N-wire validation. To compare to the results in the literature reported as RMS values, the RMS error for the $W_{2D \rightarrow 3D}$ method with the stylus validation was 0.93 mm, and 1.03 mm with the N-wire validation.

Including the outside points for the full N-wire calibration (N_{3D}^{Full}) did not provide a significant improvement in accuracy compared to the traditional centre point N-wire calibration (N_{3D}). However, N_{3D}^{Full} did provide a small improvement in repeatability. It is important to remember that these results used multiple volumetric sweeps over the phantom, resulting in thousands of corresponding points used for calibration. In cases where the number of points may be more limited, for example in the case of 2D calibration, the full N-wire technique may prove to be of greater practical significance. Using a single 2D image for calibration, including the outside points reduced the standard deviation of the six DOF ($t_x, t_y, t_z, \alpha, \beta, \gamma$) over ten independent trials by 29 %, 11 %, 10 %, 28 %, 8 %, and 22 %, respectively.

The N-wire configuration used in this experiment enabled unique determination of the edge points for N_{3D}^{Full} . The edge points cannot be determined for all possible N-wire configurations. For example, using only two rows of the config-

uration presented in this chapter allows the possibility of the plane tilting to pass through two of the alternate lines shown in Figure 4.6. However, finding the common plane to the three row configuration presented in this chapter is not the only method of determining the edge points. One possible alternative is to place two N-wires side-by-side. In this configuration, the alternate line for one of the N-wires would produce incorrect inter-point distances in the second N-wire. The trade-off for the side-by-side configuration is a lower sensitivity because of a shallower angle for the diagonal segments to fit the width of the image.

4.5 Conclusion

The process of scan conversion to convert swept ultrasound data into a Cartesian volume relies on estimates of motor parameters which can introduce errors into the calibration process. To overcome the reliance on motor parameters, a novel approach was proposed in which multiple 2D calibrations are performed and a best fit path through them is found ($W_{2D \rightarrow 3D}$). The proposed method can be used with any 2D calibration technique, however a wedge phantom was chosen due to its high accuracy in 2D. Four other techniques were developed to compare against the fitting method. Three were based on extending the 2D N-wire calibration technique into 3D. The fourth (P_{3D}) used planar features for calibration, and is the first planar technique to have a closed form solution for 3D swept ultrasound.

The repeatability of the calibrations was evaluated using the standard deviation of the six DOF after multiple trials on independent input data, and it was found P_{3D} was the most repeatable. Overall accuracy was evaluated using two point reconstruction tests and $W_{2D \rightarrow 3D}$ demonstrated the highest accuracy in both tests. The accuracy and repeatability of the N-wire phantom methods were improved by using 3D data compared to sweeping from a 2D calibration.

The fitted calibration approach, $W_{2D \rightarrow 3D}$, was able to obtain sub-millimetre accuracy. Based on previous work, sub-millimetre tracking accuracy is required in elastography applications to realize the benefits of multiple ultrasound views for tissue motion measurements compared to beam steering methods [4]. This should enable use of tracked swept motor ultrasound in elastography to improve 3D tissue motion estimates. Future work will investigate the benefits of using tracked 3D ul-

trasound to measure tissue motion and calculate elasticity. In Chapter 5 the fitted calibration parameters are used in the scan conversion process to convert 3D speckle tracking displacement measurements from transducer coordinates to Cartesian coordinates. In Chapter 6 three ultrasound volumes are combined to compute 3D displacement measurements and elasticity, with calibration errors simulated based on the errors measured in this chapter.

Chapter 5

Measurement of the Full Shear Wave Motion Vector in SWAVE

5.1 Introduction

Elastography measures the mechanical properties of tissue and tissue elasticity (e.g. Young's modulus) is the most common quantity inferred from these measurements. Determining tissue elasticity is clinically relevant because changes in tissue elasticity are correlated with certain pathological changes, such as stiff cancerous tumours surrounded by soft normal tissue [236]. Elastography has found clinical applications in improving breast cancer BI-RADS classification [101, 147], targeting prostate cancer for biopsy and focal therapy [239, 282], and liver fibrosis assessment and staging [53, 145], among others.

Tissue elasticity is determined by applying a mechanical excitation to the tissue, measuring the resulting tissue displacements, typically with ultrasound or MRI, and reconstructing the elasticity distribution from the measured displacements by applying the laws of continuum mechanics [25, 308]. The mechanical excitation can be quasi-static, where the strain computed from the displacements provides information on the relative elasticity distribution, or dynamic, where the inertial forces in the tissue allow for calculation of absolute values of elasticity [135]. The SWAVE technique uses dynamic multi-frequency mechanical excitation to deform the tissue and estimate absolute elasticity values. Quantifying the absolute elasticity values

may be beneficial in characterizing tissue types, determining the different stages of a disease, or monitoring the progress of a treatment [86].

One of the main advantages of MRE over conventional ultrasound elastography is that displacement can be measured accurately in all three directions over a volume [87]. Elasticity reconstructions based on the full 3D displacement field measurements are more accurate than 2D or 1D approaches [299]. Conventional ultrasound measures 2D image planes. Volumes of ultrasound data can be collected with a swept ultrasound transducer that contains a stepper motor to sweep the 2D image plane over a 3D field of view. Volumes may also be acquired with matrix array transducers that contain multiple rows of elements [220].

Motion measurement, or speckle tracking, is typically measured in ultrasound by dividing the echo signals into small regions or blocks and matching the blocks between successive acquisitions, for example by maximizing the correlation coefficient between blocks [254, 326, 345]. Previous studies have demonstrated tracking 3D motion components over ultrasound volumes by extending block matching methods to 3D [67, 105, 317]. Most of these studies measure quasi-static compression motion to generate strain images. In comparison, dynamic motion is a challenge as each ultrasound beam line must be collected at a common motion state to allow for block matching in 3D.

In most conventional ultrasound scanners, beam lines are scanned individually from one side of the array to the other. For performing 3D measurements of dynamic motion, this presents two problems. First, the frame rate is limited by the acoustic propagation speed of the ultrasonic pulses and the number of beam lines in a frame. Second, within each frame as each subsequent scan line is acquired the tissue scatterers will continue to move to different locations, making speckle pattern matching across lines unreliable.

As a result of the first problem, in most imaging scenarios the motion must be limited to under 50 Hz based on the Nyquist sampling criterion. For band-limited periodic motion, the magnitude and phase of the displacement can be recovered from the undersampled measurements in the baseband using knowledge of the excitation and sampling frequencies [98]. The frame rate can be increased by receiving a collection of lines, usually four, beamformed in parallel within the transmitted beamwidth with minimal changes to conventional hardware, which has been used to

measure motion in ARF imaging [76]. In a 3D cardiac strain imaging study, a matrix array was triggered to collect sub-volumes synchronized with an ECG, resulting in a high frame rate relative to the heart rate [193]. For measuring periodic motion, the effective sampling rate can be increased using a different sequence, similar to color Doppler, acquiring a small sector of lines repeatedly before moving to the next sector. After measuring displacement in one direction along the lines, the delays between each line and each sector can be compensated using the known delays between acquisitions [21].

The second problem with measuring 3D dynamic motion, that of tissue scatterers being in different locations when each scan line is acquired, results in errors in the speckle tracking process. The displacement measured from block matching is the average motion of the scatterers of the block, ignoring biases towards higher signal amplitudes [58]. If an entire block was acquired at the same time, most of the scatterers would be expected to generally move in the same direction because the shear wavelength is typically much larger than the block size. If a 3D block contains lines acquired at different times, then the shear wave will have travelled between acquisitions and the scatterers will no longer generally move in the same direction across the block. In addition, the change in speckle pattern during the acquisition of a frame caused by scatterer motion may cause biases because the speckle pattern may match over a larger volume. A solution to the problem is to synchronize the excitation and ultrasound acquisition. One study triggered the start of a single element ultrasound transducer acquisition with the start of harmonic tone burst excitations, reaching an effective sampling rate of 10 kHz, and repeated the procedure at different locations to create a 2D image [91]. Similarly, a single element transducer was used to visualize heart contraction by triggering the start of acquisition from the R-wave peak of an ECG and recording the signal over several cardiac cycles before moving the transducer laterally and repeating to create a 2D image [250]. The same concept has been used with a linear array by triggering the start of one beam line with the start of a mechanical excitation, where additional beam lines were collected subsequently in the same manner by electronically changing the position of the beam centre with the linear array and repeating the mechanical excitation to measure both harmonic and transient motions [131]. In a study measuring the shear wave propagation from a vibrating needle, the start of acquisition of a small

sector of lines was triggered by the actuator controller and, after a period of recording time, the procedure was repeated to collect additional sectors until the entire image was collected [83]. A method that programs the ultrasound sequencer to use a line repetition frequency that is an integer multiple of the excitation frequency, and acquires one line per excitation period can achieve synchronization without a trigger [350]. All of these methods ensure that, across the image, the motion was measured at the same relative temporal sample points and could potentially be used to match speckle patterns across lines for multi-dimensional motion measurement. However, these studies only measured one component of the motion vector.

Combining ultrasound planar transmit (the pulse is applied to all array elements at the same time) with hardware that receives and samples echoes on each element channel individually in parallel results in very high frame rates by collecting an entire image in one transmit and receive event [309]. The lack of transmit focusing results in a lower acoustic energy density and larger errors in displacement measurements, however coded pulses can be used to compensate for the loss in acoustic energy [320]. Because all beam lines are active at the same time, they all measure the motion at the same time and there is no need for additional synchronization within an image. Extending this concept to a matrix array might allow synchronous acquisition of a volume [264], however a swept ultrasound transducer would require synchronization between each motor position in the sweep. While not using a packaged swept ultrasound transducer, a similar concept has been used to collect volumes of ultrasound data with linear arrays mounted on stepper motors either configured as two perpendicular arrays intersecting at a line [33], or with a single array rotated around the circumference of a phantom [211], using plane wave transmission and parallel receive hardware to quickly measure several phases of motion with synchronization to the excitation applied at each motor position. These works were able to obtain measurements of the full vector shear wave motion field over a volume, the same goal as this work, but used 1D displacement measurements from different angles to reconstruct the motion vector.

In MRE, the start of the motion sensitive gradient used to measure tissue displacements is triggered by the mechanical actuator at several different excitation phase offsets for each motion encoding direction [199, 290]. Our work on ultrasound follows a similar approach by triggering each beam line with a function gen-

erator applying harmonic excitation. For successive frames, the phase of the excitation signal is shifted such that each frame measures a different phase of the motion. This approach creates volumes of beamformed ultrasound data at common motion states. The frame rate or effective temporal sampling rate is no longer an issue because the time to acquire a single line is almost negligible compared to the period of excitation, and the temporal samples of the excitation signal are not related to the line repetition rate, but are chosen by selecting the trigger offsets.

It should be noted that the motion measurements with ultrasound are most accurately computed in the axial direction, or the direction of ultrasound wave propagation. The other two directions, lateral and elevational, are typically an order of magnitude less accurate due to lack of phase information [42], wider extent of the point spread function [167], and larger sampling intervals [187]. It is desirable to mitigate the measurement errors in the other two directions, as elasticity reconstruction methods are sensitive to noise [231]. The motion measurements can be improved using special beamforming strategies such as introducing phase information in other directions through transverse oscillations [186], improving the resolution of the point spread function using synthetic aperture techniques [167], or electronically steering the ultrasound beam to combine axial measures in different directions [267]. All require changes to standard *B-MODE* imaging.

Alternatively the displacement measurements can be processed to reduce errors, for example through spatial filtering with a median filter [270], however such a filter does not have a meaningful relationship to the physics of the motion. Applying a physical constraint on the motion using reasonable assumptions can be used as an alternative to spatial filtering. A common physical constraint on the motion to reduce displacement estimation error is continuity. For example, during block matching the 2D displacement in a local neighbourhood was estimated by simultaneously minimizing the speckle decorrelation and a continuity penalty based on sums of the derivative of the motion in each direction [151]. Other examples of enforcing continuity on the displacement include using a cost function minimizing the squared difference in the displacement measurement in adjacent samples in the axial and lateral directions [272], or in a local neighbourhood [248], while minimizing the sum squared or absolute difference between images. Another regularization penalty based on the strain energy in a deformable mesh has also been used [341].

For vector measurements, regularization based on the divergence and curl of the vector field has been proposed as a method to include every derivative-based quantity that has a direct physical interpretation [18]. In the case of elastography, a common assumption of tissue incompressibility can be enforced by minimizing the divergence. In MRE it is common to process the measured displacements to obtain a divergence-free field, for example by applying the curl operator [292], performing Helmholtz-Hodge decomposition [291], or applying a high pass filter to remove contributions from compressional waves and a low pass filter to remove noise [162, 200]. For quasi-static ultrasound elastography, an algorithm for reducing the variance in lateral displacement estimates based on an integral of the axial strain and an average of the lateral displacement speckle tracking measurements in a plane strain incompressible condition demonstrated signal-to-noise improvements in the lateral displacement of a factor greater than 10 [195]. Under similar experimental conditions, a recent study applied a penalty on the divergence of the 2D displacement to iteratively reduce noise in both the axial and lateral speckle tracking measurements by up to a factor of 17 [120]. Displacement vectors in 3D after static compression were estimated by simultaneously minimizing the squared intensity differences between two volumes, and penalties on the smoothness and divergence of the displacement, approximated using a finite element mesh [269]. A similar approach has been used as a post processing step on MRE displacement data, finding a new displacement field that minimizes the difference between the new field and the measurements as well as the new field's smoothness and divergence [243]. Our work attempts to reduce noise in all three components of the displacement by applying a regularization based on the divergence, with no assumption on the deformation condition, and is solved directly based on a least squares formulation.

In summary, there is a need for full vector motion field measurement with standard 3D ultrasound to obtain absolute measures of elasticity. The goal of this chapter is to develop a novel method that measures harmonic tissue motion vectors over a volume with a standard swept B-MODE ultrasound transducer, applies a novel regularization to the motion to improve measurements, and produces elasticity estimates comparable to MRE. The method is validated on measurements of a tissue mimicking phantom, and the results are compared to a previous MRE study on the same phantom. Elasticity is estimated using both the LFE method and a state-of-the-art

FEM based inversion algorithm to evaluate the effect of the inversion model on the elasticity estimates. Several metrics are used to compare the inversion algorithms and the difference between using the measured displacements and regularized displacements as inputs to the algorithms. This work also includes a study of how the regularization parameter affects the displacement.

5.2 Methods

5.2.1 Synchronization

Analogous to MRE, a steady-state mechanical excitation is applied externally to generate shear waves in the tissue. Beamformed ultrasound RF data are acquired over a volume of tissue by collecting 2D frames of standard delay and summed channel data at a given motor position for a period of time before stepping the motor to the next position in the volumetric sweep. To enable displacement speckle tracking of 3D blocks of RF data shifted over a 3D volume, volumes of RF data at common motion states are acquired by synchronizing each ultrasound beam line in a 2D frame with the mechanical excitation. Once a 2D frame is collected, the exciter is reprogrammed to synchronize at a phase shifted point along its cycle, and another 2D frame is collected. When the motor is stepped to the new position, the exciter is reprogrammed to the first synchronization phase used in the previous motor position. This is shown in Figure 5.1 and the pseudo-code provided in Algorithm 5.1. It is assumed that the motion within the tissue is consistent across all cycles of the excitation. Once the entire collection is complete the RF lines are rearranged into volumes that were triggered at common phases. Displacements are then estimated by comparing the volumes to each other, resulting in a complete volume of displacement vectors for each common excitation phase.

5.2.2 Displacement Estimation

Once the volumes of RF data at several excitation phases are collected, 3D speckle tracking and scan conversion is used to find the 3D displacement vectors over the volumes, as done in previous work on static 3D displacement tracking [260]. Blocks of RF data approximately $1.2 \text{ mm} \times 1.5 \text{ mm} \times 2.25^\circ$ in the axial, lateral, and eleva-

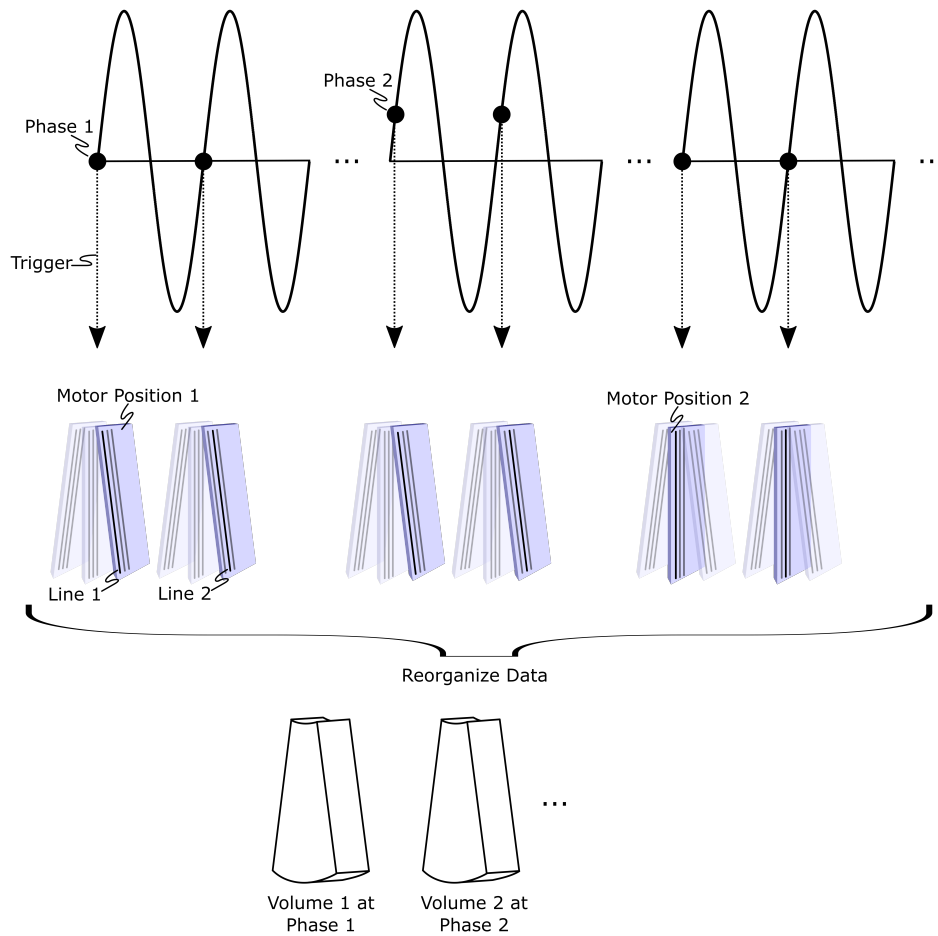


Figure 5.1: A schematic of the synchronization between the mechanical excitation and the volumetric ultrasound acquisition. At a given motor position, each line in the 2D image plane is triggered sequentially at a common excitation phase which is then repeated for a number of phase offsets. After all phase offsets are collected, the motor is stepped to the next position and the process is repeated. Once the collection is finished for all motor positions, the data are reorganized into volumes that were triggered at a common phase.

Algorithm 5.1 Ultrasound pulse sequence to synchronize with excitation.

```

Start exciter
for  $\phi \leftarrow -\Phi$  to  $+\Phi$  do                                 $\triangleright$  for all motor angles
  for  $\theta \leftarrow 0$  to  $\Theta$  do                                 $\triangleright$  for all phase offsets
    for  $l \leftarrow 0$  to  $L$  do                                 $\triangleright$  for all beam lines
      Send ready signal
      Wait for next trigger
      Acquire line  $l$  at phase  $\theta$  and motor angle  $\phi$ 
    end for
  end for
end for

```

tional directions of the transducer were used for speckle tracking, and were overlapped by spacing the blocks by approximately $0.3 \text{ mm} \times 0.3 \text{ mm} \times 0.45^\circ$. Sub-sample displacement shifts in transducer coordinates are estimated by maximizing the normalized cross-correlation in 3D. First, a coarse estimate of the axial shift is estimated using a 1D search for the maximum correlation along an RF line, bracketed by the previous block's estimated shift to improve speed and reduce peak hopping errors [345]. Next, the correlation is computed at the neighbouring sample points in the axial, lateral, and elevational directions, resulting in a $3 \times 3 \times 3$ volume of correlation coefficients. A 23 coefficient 3D polynomial of the form

$$\begin{aligned}
g(u, v, w) = & a_0 + a_1u + a_2v + a_3w + a_4uv + a_5uw \\
& + a_6vw + a_7u^2 + a_8v^2 + a_9w^2 + a_{10}u^2v \\
& + a_{11}u^2w + a_{12}v^2u + a_{13}v^2w + a_{14}w^2u \\
& + a_{15}w^2v + a_{16}uvw + a_{17}u^2v^2 + a_{18}u^2w^2 \\
& + a_{19}v^2w^2 + a_{20}u^2vw + a_{21}v^2uw \\
& + a_{22}w^2uv
\end{aligned} \tag{5.1}$$

is fit to the correlation coefficients, and the maximum of the polynomial is computed using Newton's method, providing the sub-sample shifts in each direction [349]. All correlations are computed using the volume triggered at zero phase as a reference.

The displacements in Cartesian coordinates are calculated by using scan conversion to compute the location of the blocks both before a displacement shift and

after a displacement shift and taking the difference between these points. Usually the scan conversion parameters can be obtained through the transducer manufacturer. To achieve greater accuracy, in this work the scan conversion parameters were determined using the $W_{2D \rightarrow 3D}$ calibration technique described in Chapter 4.

Using a least squares fit, the multiple volumes of displacement measurements at different excitation phases are converted to a single volume (for each measurement direction) of complex phasors in the form $Ae^{j\theta}$ (see Section 2.2.8).

5.2.3 Displacement Regularization

As mentioned, the displacement measurements are often precise in the axial direction, but contain an order of magnitude larger variance in the lateral and elevational directions. Generally, elasticity estimation algorithms are sensitive to this variance so it is desirable to find a way to smooth the displacement field. While a spatial filter could be used, a regularization of the displacements that uses *a priori* information may be more appropriate. One possible constraint is assuming tissue incompressibility, which is applicable to most soft tissues due to the high volume fraction of water, provided that the water does not diffuse out of the local tissue region during mechanical excitation. The incompressibility constraint can be expressed mathematically as minimizing the divergence of the displacements. A displacement field, \mathbf{d} , that balances a fit to the displacement measurements, \mathbf{m} , with minimizing the field's divergence can be found via

$$\underset{\mathbf{d}}{\text{minimize}} \quad \|\mathbf{d} - \mathbf{m}\|^2 + \alpha^2 \|\nabla \cdot \mathbf{d}\|^2, \quad (5.2)$$

where α is a regularization parameter. The displacement measurements in Cartesian coordinates in Equation 5.2 have been arranged in a single vector

$$\mathbf{m} = \begin{bmatrix} m_x[0] \\ m_y[0] \\ m_z[0] \\ \vdots \\ m_z[N-1] \end{bmatrix}, \quad (5.3)$$

where $m_\gamma[i]$ is the measurement at the i^{th} pixel in the γ direction, and N is the

total number of pixels, resulting in \mathbf{m} containing $3N$ entries. The pixel ordering is organized to first traverse the x direction, then the y direction, and finally the z direction. The divergence operator is approximated using finite differences

$$\nabla \cdot \mathbf{d} = \frac{\partial \mathbf{d}_x}{\partial x} + \frac{\partial \mathbf{d}_y}{\partial y} + \frac{\partial \mathbf{d}_z}{\partial z} \quad (5.4)$$

$$\approx \mathbf{Ld} \quad (5.5)$$

$$\approx \frac{1}{h} (\mathbf{L}_x + \mathbf{L}_y + \mathbf{L}_z) \mathbf{d}, \quad (5.6)$$

where h is the pixel spacing (assumed uniform in each direction) and \mathbf{L}_x , \mathbf{L}_y , and \mathbf{L}_z are sparse arrays with difference kernels of

$$\mathbf{l}_x = [1 \ 0 \ 0 \ -1], \quad (5.7)$$

$$\mathbf{l}_y = [1 \ \mathbf{0}_{1 \times 3N_x+1} \ -1], \quad (5.8)$$

and

$$\mathbf{l}_z = [1 \ \mathbf{0}_{1 \times 3N_x N_y + 2} \ -1], \quad (5.9)$$

starting at the first, second, and third columns of the arrays, respectively, and shifting by three columns for every row of the arrays. The kernels perform a simple finite difference between adjacent pixels in the x , y , and z directions, with the zeros in the centre of the kernels accounting for the three components in the displacement vector and the number of pixels in each direction of the volume, denoted N_x , N_y , and N_z . Differences at the boundary are taken to be zero.

The minimization problem in Equation 5.2 can be solved by taking the derivative with respect to \mathbf{d} and setting it equal to 0, resulting in

$$\mathbf{d} = (\mathbf{I} + \alpha^2 \mathbf{L}^T \mathbf{L})^{-1} \mathbf{m}, \quad (5.10)$$

where \mathbf{I} is a $3N \times 3N$ identity matrix. This is equivalent to the least squares solution to

$$\begin{bmatrix} \mathbf{I} \\ \alpha \mathbf{L} \end{bmatrix} \mathbf{d} = \begin{bmatrix} \mathbf{m} \\ \mathbf{0} \end{bmatrix}, \quad (5.11)$$

where $\mathbf{0}$ is a $3N \times 1$ vector of zeros. The solution to Equation 5.11 can be computed

directly using matrix factorization [127]. The uncertainty in the measurements can be accounted for by applying the weighting

$$\mathbf{W} = \begin{bmatrix} 1/\sigma_x & & & \\ & 1/\sigma_y & & \\ & & 1/\sigma_z & \\ & & & \dots \end{bmatrix}, \quad (5.12)$$

where σ_γ is the standard deviation of the measurement in the γ direction. The standard deviation values used in this work are taken from a planar motion test in a previous study [260]. The least squares problem in Equation 5.11 with the weighting applied becomes

$$\begin{bmatrix} \mathbf{W} \\ \alpha \mathbf{L} \end{bmatrix} \mathbf{d} = \begin{bmatrix} \mathbf{Wm} \\ \mathbf{0} \end{bmatrix}. \quad (5.13)$$

The choice of the regularization parameter, α , affects how much influence the divergence penalty is given. A small value will provide little influence and the result will be very close to the displacement measurements and a value that is too large will produce a result that does not resemble the displacement measurements. Several values of α between 10^{-10} to 10^6 are tested and based on the results presented later in this paper, the elasticity is reconstructed using a value of 10^2 .

5.2.4 Elasticity Reconstruction from LFE

As described in Chapter 2 in Section 2.2.11, under the assumptions that the elastic properties of the tissue are linear, isotropic, lossless, and locally constant, and the tissue can be considered incompressible, the motion can be described with an independent Helmholtz equation in each direction

$$\mu \nabla^2 \mathbf{d}_\gamma = -\rho \omega^2 \mathbf{d}_\gamma, \quad (5.14)$$

where λ and μ are the Lamé parameters, ρ is the density, ω is the frequency of excitation, and γ is the chosen direction. The LFE inversion method uses the output of the ratio of pairs of filters from a filter bank that spans a large range of spatial frequencies corresponding to the range of possible shear wave numbers. In Chapter 2,

only axial displacement measurements were collected, so Equation 5.14 was solved using only the axial component. With all three components of the displacement vector measured in this chapter, the final LFE reconstructions are averages of separate reconstructions calculated from the x , y , and z displacement data sets [199].

5.2.5 Elasticity Reconstruction from shear-FEM

In the derivation of the Helmholtz equation in Equation 5.14 for the LFE reconstruction, one of the assumptions is that the spatial derivatives of the shear modulus are negligible (homogeneity assumption). For heterogeneous media, this assumption breaks down at the boundary of the two materials. In LFE, the spatial support of the filters is proportional to the wavelength, and thus creates a transition zone in the results where the elasticity gradually changes between the two materials with a resolution of one-half of the wavelength [199].

It is also possible to formulate the inverse problem without this assumption. Starting from Equation 2.18 and removing all coupling and compression terms results in

$$\nabla \cdot (\mu \nabla \mathbf{d}_y) = -\rho \omega^2 \mathbf{d}_y. \quad (5.15)$$

This model for the tissue motion is discretized using the FEM, and has been termed the shear-FEM method [137]. The FEM implementation uses linear shape functions for the displacement and test functions, and piece-wise constant shape functions for the shear modulus. The equations are arranged in terms of shear modulus so the system of equations can be solved directly

$$\mathbf{K} \boldsymbol{\mu} = \mathbf{f}, \quad (5.16)$$

where \mathbf{K} and \mathbf{f} are formed using any one of the displacement components. Since all three displacement components are measured, the equations can be formed for each and then stacked and solved simultaneously [138]

$$\begin{bmatrix} \mathbf{K}_x \\ \mathbf{K}_y \\ \mathbf{K}_z \end{bmatrix} \boldsymbol{\mu} = \begin{bmatrix} \mathbf{f}_x \\ \mathbf{f}_y \\ \mathbf{f}_z \end{bmatrix}. \quad (5.17)$$

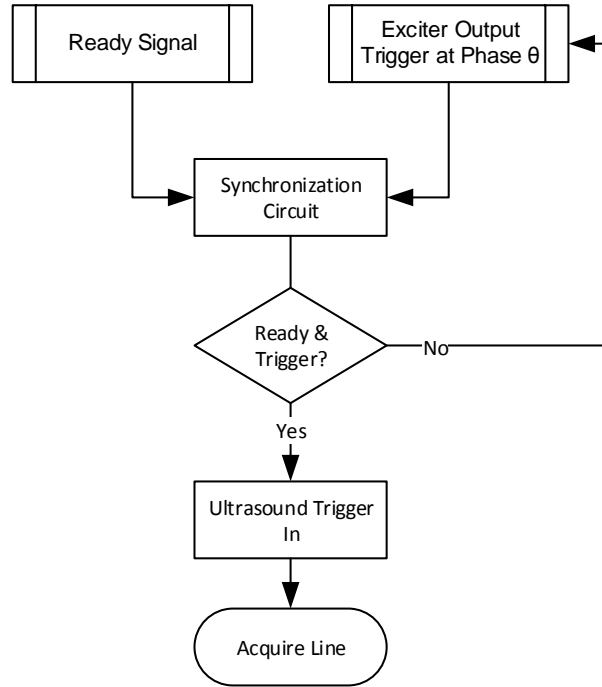


Figure 5.2: Flowchart of the synchronization between the ultrasound acquisition of each beam line and the excitation signal at multiple phase offsets (extended from Figure 2.3).

The inverse problem is stabilized using sparsity regularization, choosing a truncated discrete cosine transform to approximate the solution [135]. The volume is meshed using eight-node hexahedral elements, with a length of 1.5 mm which is near the optimal element size to elastic wavelength ratio which balances the trade-off in increasing inertial forces with decreasing derivative accuracy [138].

5.2.6 Phantom Experiment

To test the methods, ultrasound data were captured from an elastography quality assurance phantom (Model 049, CIRS Inc, Norfolk, VA, USA). This phantom was chosen because the manufacturer provides reference elasticity values based on quasi-static compression tests on batch samples, and MRE measurements of the same

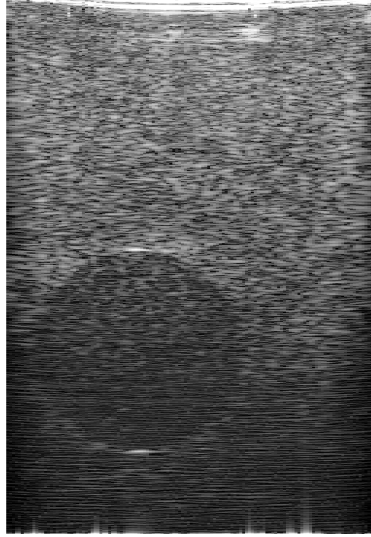


Figure 5.3: A B-MODE image generated from the envelope of one of the RF images. The hypoechoic circle in the bottom left shows a cross section of the stiff inclusion.

Table 5.1: Manufacturer specifications for the CIRS Model 049 elasticity quality assurance phantom. The background and measured inclusion (stiffest of four inclusions) are tabulated.

	Background	Inclusion
Speed of Sound [m/s]	1545	1541
Attenuation [dB/(cm MHz)]	0.5	0.53
Elasticity [kPa]	29	62

phantom have been performed in a previous study [22]. The CIRS phantom is composed of an elastic tissue mimicking material called Zerdine, and contains two sets (10 mm and 20 mm diameter) of four spherical inclusions constructed with elasticities ranging from soft to stiff. Images of the stiffest 20 mm diameter inclusion of the phantom were acquired. The phantom specifications measured by the manufacturer are provided in Table 5.1.

The images were acquired with a 4DL14-5 motorized linear array ultrasound transducer connected to an SonixTouch scanner (Ultrasonix Medical Corp., Richmond, BC, Canada). Each beam line was synchronized with an exciter (33220A, Agilent, Santa Clara, CA, USA) applying 200 Hz vibrations before reprogramming the exciter to a total of 25 phases distributed evenly across the excitation period. After collecting one 2D image frame for each exciter phase, the transducer motor was stepped to the next position in the sweep. The sweep comprised a total of 31 motor positions, subtending an angle of approximately 14° .

The synchronization between the ultrasound acquisition and the excitation is shown in more detail in Figure 5.2, which is a specialized version of the general synchronization scheme for the SWAVE system in Figure 2.3. As shown in the flowchart, a custom synchronization circuit is used to output a trigger signal to the ultrasound machine which is programmed to collect one beam line in its standard sequence after receiving the trigger. The ultrasound machine transmits and receives a beam line as soon as the trigger pulse is received from the synchronization circuit. The process is repeated until all of the data are collected as described in Algorithm 5.1.

The location of the stiff inclusion was determined using its known geometry provided by the manufacturer and comparing it to features in corresponding B-MODE images. The inclusion appeared as a slightly hypoechoic circle in individual B-MODE slices through the volume as shown in Figure 5.3. The edges of the inclusion were manually segmented in several slices, creating a cloud of points over the volume. The centre of a 10 mm radius sphere was calculated by minimizing the distance between the edge of the sphere and the point cloud. To reduce the influence of the boundary artefacts, the background region was cropped 1 cm from the edges of the volume.

5.2.7 Reconstruction Performance Evaluation

The RMS error can be used to compare the performance of the two elasticity reconstruction techniques, LFE and shear-FEM, using both the regularized displacements and unprocessed displacements as inputs. It is defined as

$$E_{\text{RMS}} = \sqrt{\frac{1}{N} \sum_{i=1}^N (E - E^*)^2}, \quad (5.18)$$

where E and E^* are the Young's modulus values at each voxel in the volume estimated by the reconstruction technique and provided by the manufacturer, respectively, and N is the number of voxels.

It is also of interest to compare the elasticity reconstructions from the measured motion from 3D ultrasound in this work to a previous study using MRE measurements. Using RMS error in this case would be difficult because it would contain registration errors from aligning the two data sets. Instead the mean value in the inclusion and background regions are compared and reported as a percentage, resulting in the MRE error metric

$$E_{\text{US} \rightarrow \text{MR}} = \frac{|E_{\text{USE}} - E_{\text{MRE}}|}{E_{\text{MRE}}} \times 100\%, \quad (5.19)$$

where E_{USE} and E_{MRE} are the mean Young's modulus values in a region computed from ultrasound elastography and MRE measurements, respectively.

The elastographic CNR is commonly used to quantify the detectability of an inclusions or inhomogeneity [37]. In this work it is computed from the reconstructed Young's modulus values

$$\text{CNR} = 20 \log_{10} \left(\frac{2 (E_{\text{inc}} - E_{\text{bkg}})^2}{\sigma_{\text{inc}}^2 + \sigma_{\text{bkg}}^2} \right), \quad (5.20)$$

where E_{inc} and E_{bkg} are the mean moduli, and σ_{inc}^2 and σ_{bkg}^2 the variance of the moduli in the inclusion and background regions, respectively.

The elastographic SNR can be used as a measure of how much variation or noise is present in a homogeneous region [324]. In this work it is computed from the

reconstructed Young's modulus values in regions that should have a constant elasticity value

$$SNR = 20 \log_{10} \left(\frac{E}{\sigma} \right), \quad (5.21)$$

where E and σ are the mean and standard deviation of the reconstructed Young's modulus values in the ROI. The SNR is computed for both the inclusion and background regions.

The contrast-transfer efficiency (CTE) describes the efficiency with which levels of true modulus contrast are converted into levels of contrast in the reconstructed elasticity image. It is defined as the ratio of the observed contrast to the true contrast [257]. Expressed in decibels, it is given by

$$CTE = 20 \log_{10} \left(\frac{E_{inc}}{E_{bkg}} \right) - 20 \log_{10} \left(\frac{E_{inc}^*}{E_{bkg}^*} \right), \quad (5.22)$$

where E_{inc}^* and E_{bkg}^* are the Young's modulus values for the inclusion and background, respectively, provided by the manufacturer.

5.3 Results

The motion measured over the ultrasound volume in the x , y , and z directions are presented in Figure 5.4. The figure displays the real part of the displacement phasor for both the speckle tracking measurements and the regularized displacement. The regularized displacements show a reduction in variance, particularly in the x and z directions, as these measurements are more influenced by the poorer speckle tracking ability in the lateral and elevational directions, respectively.

The volumes of reconstructed elasticity using the LFE and shear-FEM methods from both displacement measurements and regularized displacement are shown in Figure 5.5. All of the elasticity images show a stiff inclusion in a homogeneous background as expected. The location and size of the inclusion appears to agree with the location estimated from segmenting the inclusion in B-MODE images.

Profiles of the elasticity images through the centre of the inclusion in the x , y , and z -directions are shown in Figure 5.6, using the B-MODE segmentation to define the inclusion centre. For the LFE reconstruction using 1D displacement, the peak

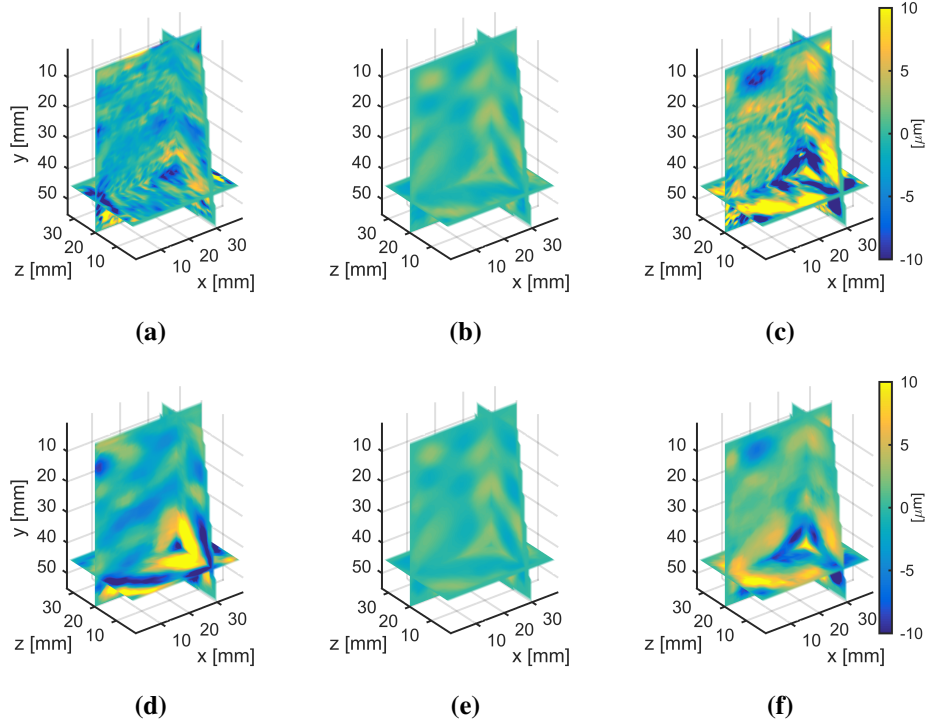


Figure 5.4: From left to right, slices through the volume of the displacements measured in the x , y , and z directions. (a)–(c) The displacements estimated using speckle tracking alone, and (d)–(f) the displacements after post-processing the displacement measurements with divergence regularization. The x , y , and z directions roughly correspond to the lateral, axial, and elevational transducer coordinates.

elasticity reaches close to the manufacturer’s specification in each direction, with the peak occurring a few millimetres off centre. The LFE reconstruction using 3D displacement slightly underestimates manufacturer’s specification of the inclusion elasticity, but the peak of the profiles appears more centred. The LFE reconstruction using the regularized 3D displacement produces more of an underestimation, but the profiles appear to maintain a more consistent elasticity value within the inclusion. For the shear-FEM reconstruction with 1D displacement the inclusion elasticity is mostly underestimated, however a large peak appears off centre along the x direction. The reconstruction with 3D displacement has a similar underestimation of

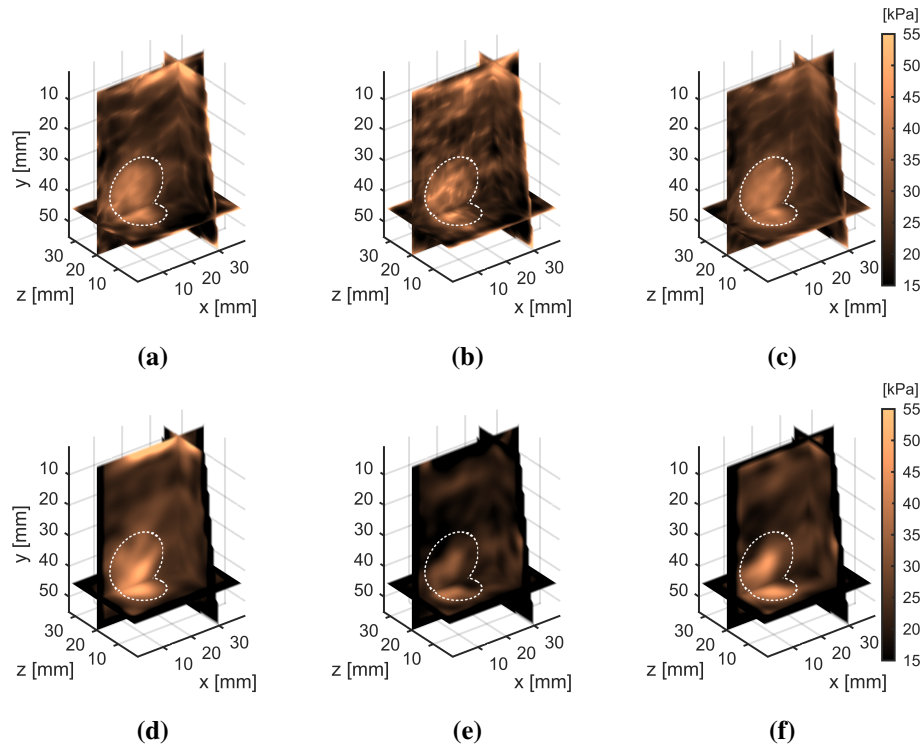


Figure 5.5: The estimated Young's modulus volumes using the (top row) LFE and (bottom row) shear-FEM inversion algorithms. The first column uses only the displacement component along the y direction, the second column uses all three displacement components, and the third column uses all three displacement components after applying regularization. The white dotted outline indicates the intersection between the edges of the spherical stiff inclusion and the displayed cross-sectional planes. The x , y , and z directions roughly correspond to the lateral, axial, and elevational transducer coordinates.

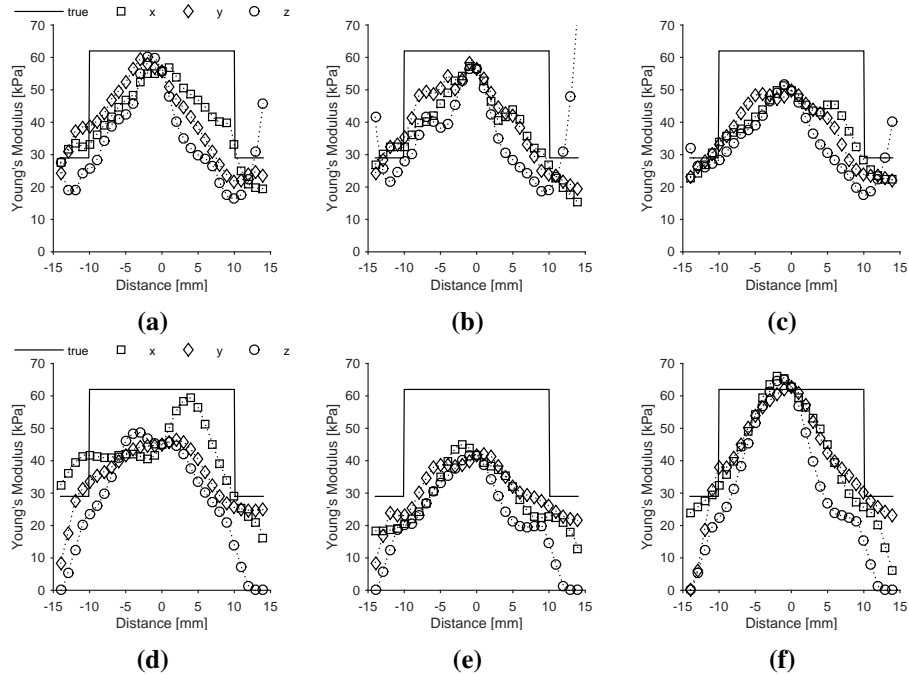


Figure 5.6: Profiles of the reconstructed elasticity values passing through the centre of the inclusion in the x , y , and z -directions using the (top row) LFE and (bottom row) shear-FEM inversion algorithms. The first column uses only the displacement component along the y direction, the second column uses all three displacement components, and the third column uses all three displacement components after applying regularization. The “true” elasticity profile based on the manufacturer’s specifications is shown as the solid line. The distance along the abscissae is measured from the centre of the inclusion.

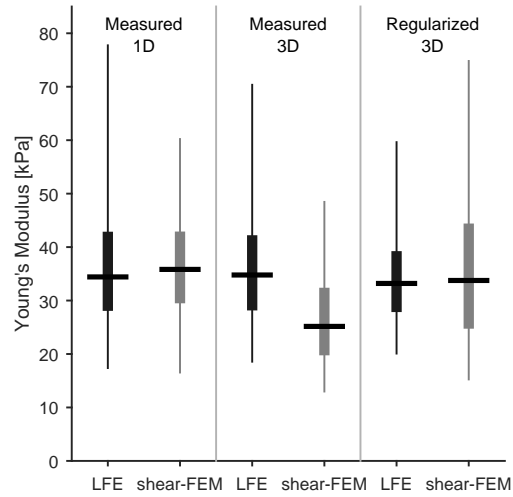
the inclusion elasticity, but without the large peak. The regularized displacements produce a smooth bell shaped profile with a peak located in the centre of the inclusion that slightly overestimates the expected elasticity. A boundary artefact causes the estimated elasticity values to rise rapidly toward the edges of the LFE plots in the z -direction (bright edges in Figure 5.6(a), Figure 5.6(b), and Figure 5.6(c)). Similarly, the values decrease to zero for the shear-FEM plots near the edges (dark edges in Figure 5.6(d), Figure 5.6(e), and Figure 5.6(f)). The boundary effect appears larger for the shear-FEM and for this reason is also visible in the profile across

the x -direction.

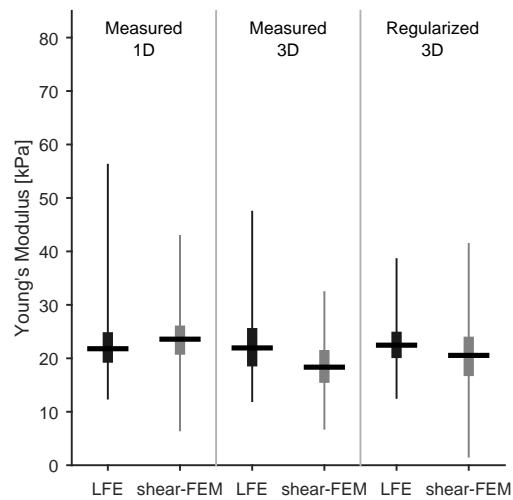
The distribution of the elasticity values within the inclusion and outside of the inclusion are shown for all of the methods in Figure 5.7. In all cases the median values underestimate the manufacturer's specification. For the LFE reconstructions, the range of elasticity values decreases when changing the input from 1D to 3D displacements, and from 3D displacements to regularized 3D displacements. For the shear-FEM reconstructions, the range of elasticity values decreases when changing the input from 1D to 3D displacements, but increases from 3D displacements to regularized 3D displacements. Decreasing the variance is desirable since the regions represented in these box plots are expected to have a single homogeneous elasticity. However, a decrease in variance should not come at the cost of decreased accuracy in the estimate. This balance is quantified in the performance measure presented next.

The performance metrics for the LFE and shear-FEM methods using unprocessed 1D and 3D displacements, as well as regularized 3D displacements as inputs for estimating the elasticity are summarized in Table 5.2. In terms of RMS error, the shear-FEM reconstruction using 1D displacements provided the best performance, while LFE performed better in both 3D displacement cases. Using previous MRE measurements on the same phantom as a reference [22], the percent error for the mean inclusion value was lowest (6.79 %) for the shear-FEM method using the 1D displacements, closely followed by the shear-FEM reconstruction using the regularized 3D displacements (8.44 %). For the background, LFE with the regularized 3D displacements produced the lowest error (9.63 %). The reconstructions show at least a 2 dB improvement in CNR from unprocessed 3D displacements to regularized displacements with both methods. Similarly, a 2 dB improvement in SNR is observed in the inclusion and 3 dB in the background for LFE from unprocessed 3D displacements to regularized displacements, however there is drop in SNR for the shear-FEM method which seems to be caused by the larger variance as observed in Figure 5.7. The CTE shows that the shear-FEM method using the regularized 3D displacements does the best job of displaying the true contrast of the phantom (-1.38 dB away from zero).

The effect of the regularization parameter, α , on the displacements is examined in Figure 5.8. Profiles of the real part of the displacement component along

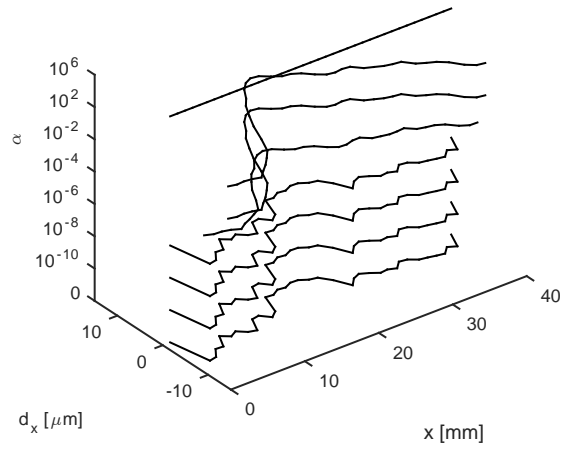


(a)

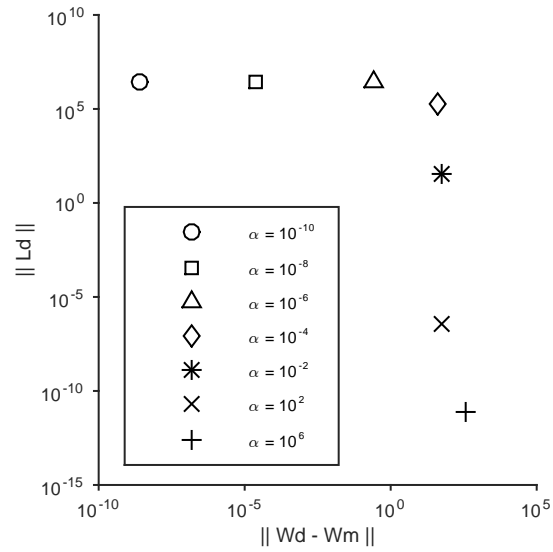


(b)

Figure 5.7: Boxplots describing the distribution of Young's modulus in the (a) inclusion and (b) background. Each plot is divided into three sections, with the leftmost based on 1D displacement measurements, the middle based on 3D displacement measurements, and the rightmost based on 3D displacements after divergence regularization.



(a)



(b)

Figure 5.8: (a) Plot of the real part of the displacement component along the x -direction at $y = 10$ mm and $z = 15$ mm across the x -dimension of the volume for different values of the regularization parameter, α . (b) The balance between the divergence constraint and the measurement fit is plotted for the same values of α .

Table 5.2: Performance measures of the reconstructed elasticity values based on the measured and regularized displacements. The 1D displacement measurements correspond to the y component of motion. Some measures are specific to the stiff inclusion (inc) or soft background (bkg) regions.

	E_{RMS} [kPa]	$E_{US \rightarrow MR_{inc}}$ [%]	$E_{US \rightarrow MR_{bkg}}$ [%]	CNR [dB]	SNR_{inc} [dB]	SNR_{bkg} [dB]	CTE [dB]
Measured 1D Displacement							
LFE	14.4	16.5	10.9	12.7	12.4	16.0	-2.45
shear-FEM	13.8	6.79	10.4	12.9	13.3	15.7	-2.74
Measured 3D Displacement							
LFE	14.5	16.6	11.0	12.4	12.4	14.8	-2.46
shear-FEM	19.5	32.3	29.1	6.54	11.1	14.1	-2.98
Regularized Displacement							
LFE	14.7	21.2	9.63	14.6	14.4	17.8	-3.06
shear-FEM	16.8	8.44	24.7	8.63	9.30	9.53	-1.38

the x -direction are shown in Figure 5.8(a) for several values of α , at the location $y = 10$ mm and $z = 15$ mm in the volume. The regularization initially shows little change in the displacement profile for increasing α , then starts to produce smoothing before dominating the solution and no longer fitting the measurements. There is a visible change between the profiles at $\alpha = 10^{-4}$ and 10^{-6} . There appears to be little change in the profiles between 10^{-2} and 10^2 , indicating that increasing the regularization is not producing any further improvement. At very large values of α , the regularization term dominates and a field with no displacement and thus zero divergence is found. A common method to visualize the balance between fitting the measurements and fitting the regularization term is to plot the norm of the residual for each term against each other for different values of regularization [127]. This is done in Figure 5.8(b) using the terms from Equation 5.13 with the divergence norm, $\|\mathbf{Ld}\|$, along the ordinate, and the weighted difference between the solution and the measurements, $\|\mathbf{Wd} - \mathbf{Wm}\|$, along the abscissa. This plot confirms the findings from Figure 5.8(a), with small values of α not affecting the divergence residual and showing the measurement residual increases but remains small (measured in microns and summed across the entire volume in three displacement directions). The point at $\alpha = 10^{-4}$ shows a change in the divergence residual, corresponding to the start of visual smoothing in Figure 5.8(a). The divergence residual continues to decrease as α increases without change in the measurement residual until a very large α is used, corresponding to the zero displacement solution.

5.4 Discussion

Compared to the values of elasticity reported by the phantom manufacturer, the mean and median values of all reconstructions underestimate the inclusion (62 kPa) and the background (29 kPa). This discrepancy was also observed in Chapter 2. A previous MRE study on the same phantom describes possible reasons for the discrepancy between the manufacturer's values and the elasticity estimates, such as differences in temperature, excitation frequency, or change in properties due to ageing [22]. The same reasons also apply to discrepancies between the elasticity estimates from the MRE study and this study, with differences such as segmentation of the inclusion also contributing.

The LFE elasticity estimates based on the 1D displacement measurements are similar to the measurements reported in Chapter 2. The mean Young’s modulus computed in the inclusion is 36 kPa compared to 31 kPa in Chapter 2, and in the background is 23 kPa compared to 17 kPa in Chapter 2. The data in this chapter were acquired by triggering every beam line in the sequence, while there was no triggering at all in the Chapter 2 data used for the elasticity comparison, so phasors had to be compensated based on estimated timing. The volume sweep in this chapter is also more than three times larger than the sweep used in Chapter 2. Another important difference is that while only a single component of displacement was used in this chapter, the tracking was done in 3D. Tracking in 3D improves accuracy by reducing signal decorrelation because the blocks of RF data can shift in more than one direction to get the best match, and by improving SNR by increasing the amount of RF data in each block by extending it along each dimension [141]. The y component of the displacement used in the 1D elasticity estimation in this chapter also corrects for geometrical errors caused by different motor angles creating a different angle for the axial measurements across the volume.

The magnitude of the $E_{US \rightarrow MR}$ error reported in Table 5.2, comparing the inversions from the ultrasound data collected in this work to MRE measurements from a previous work, appears large in some cases. While closer agreement is desirable, the field of elastography has been challenged by the inability to obtain the same quantitative elasticity measurements between different methods. For example, using the same MRE measured motion field with the LFE inversion algorithm and an algebraic inversion algorithm produced a difference in mean Young’s modulus of 24.1 % [199]. A study comparing MRE measurements and ultrasound comb shaped ARF elastography found a 15 % difference in modulus [295]. Another study comparing different commercial ultrasound elastography methods found an error of 31.5 % comparing the 25th and 75th percentiles from modulus measurements using a Philips system [124]. The same study found the percent error between Philips and Siemens median modulus measurements was 12.4 %. The study also detected a dependence on transducer type and measurement depth. Despite these differences, for a given modality, algorithm, and measurement protocol, valuable clinical data are obtained which can be used for liver fibrosis staging [53] and breast cancer BI-RADS classification [101], among other applications.

Using the regularized 3D displacements rather than the unprocessed 3D displacement measurements as an input to the shear-FEM algorithm improves the result in every metric except for SNR. It does not provide as clear a benefit to the LFE algorithm, where the CNR, SNR and $E_{\text{US} \rightarrow \text{MR}}$ error in the background region all improve, but the RMS error, CTE, and $E_{\text{US} \rightarrow \text{MR}}$ error in the inclusion all worsen. The same can be said for the LFE algorithm when comparing the 1D displacement to the regularized 3D displacement. The shear-FEM inversion using 1D displacements outperforms the regularized 3D displacements in all metrics except the CTE. While a better result is expected using 3D motion measurements, this indicates that there are likely still errors in the x and z displacement components that are corrupting the FEM solution. This is further backed up by the inability of a full FEM based inversion with coupled displacement terms to produce a reasonable elasticity estimate (results not reported). Ideally, all three components would have the best (axial) accuracy, which is the goal of Chapter 6.

The method of regularizing the displacement field by minimizing the field's divergence presented in this work operates on a phasor representation of the displacements. It is also possible to apply the smoothing operation on each volume of displacements, representing a measurement at different phase or time samples, and then derive the phasor representation of the smoothed displacement measurements. Based on the data collected in this work, there is no difference in the resulting phasor between the two methods up to about machine precision. The choice to apply the smoothing on the phasor representation instead of the raw displacement measurements was made to reduce the computation time since the operation only needs to be applied once instead of 25 times (number of phase offsets).

The regularization parameter, α in Equation 5.13, was chosen manually by starting with a small value and slowly increasing it until a visually smooth displacement field was produced. The L-curve criterion can be used as an automated approach to choosing the regularization parameter [127]. Figure 5.8(b) is a plot of the residuals, however it does not display an L-shape for the values of α examined, suggesting it may not be appropriate for picking the parameter in this case. In another work using divergence regularization on the displacement field, it is suggested that minimizing the divergence term should not be considered a true regularization term, but a constraint being enforced by a penalty, and it should be chosen as the largest value after

which no improvement is observed in the displacement [269]. This is essentially the manual approach used in this work.

Based on the displacement phasors shown in Figure 5.4, the regularization appears to have the greatest smoothing effect on the x -component of the displacement. The x -component is based on the lateral speckle tracking measurements, while the y - and z -components have spatially varying dependencies on the axial and elevational speckle tracking measurements. Since the axial component is measured most accurately, the y - and z -components in Cartesian coordinates are expected to be more accurate than the x -component. This is observed in a previous translational motion tracking experiment of volumetric displacement components [260]. The variances measured in that experiment are also used to weight the different components during regularization as described in Equation 5.13, meaning the measurements of the x -component contribute less to the final regularized solution of the displacement vector field (the y - and z -components contribute 50 and 2.5 times more to the solution, respectively).

The displacement measurement weighting matrix as defined in Equation 5.12 assumes spatially uniform variance in each of the vector components. However, since the point spread function in ultrasound is spatially variant, better performance might be observed using a spatially varying weighting [304]. Instead of using experimental translation motion tests to estimate the variances, which depend on the transducer and imaging system characteristics, theoretical lower bounds on the estimation accuracy could be used [166], eliminating the need to repeat the experiments for different imaging scenarios.

The synchronization between the mechanical excitation and the acquisition of each beam line increases the total acquisition time compared to standard imaging without synchronization. In standard ultrasound *B-MODE* imaging, the minimum time required to acquire a beam line is determined by the depth that the ultrasonic pulse needs to travel to and back and the speed at which the pulse travels. For example, typical values of 5 cm depth and 1540 m/s speed of sound results in a time of approximately 65 μ s. The synchronization used in this work triggered a beam line once every excitation period, which at 200 Hz is 5000 μ s. For an acquisition with 31 motor positions, 25 frames in each position, and 128 beam lines in each frame, the total acquisition time is 496 s with synchronization, compared to 6.45 s without

synchronization. This is a worst case comparison as these timings do not account for any pauses for motor movement, which is not a significant factor for the synchronized case because of the long time between beam line triggers, but would increase the time for the case without synchronization. It is difficult to directly compare the timing to MRE since the acquisition is dependent on a number of factors such as the MRI sequence, echo times, volume dimensions and resolution, excitation frequency, and number of phase offset measurements. The MRE study used for comparison in this work reported an acquisition time of 300 s, however the volume was thin and wide compared to the ultrasound volume used in this work, and the number of phase offsets was 8 compared to 25 [22].

The acquisition time could be improved by designing a new synchronization sequence. For example, when a beam line is triggered, it could be repeatedly fired with known delays between firing to collect all desired phase offsets before one excitation period is complete, and then the next line could be triggered at the start of the next period. This would reduce the time in the above example by a factor of 25 (number of frames in each motor position) for a total acquisition time of approximately 19.8 s. This would be similar to the work sequence and synchronization used in previous works of dynamic motion measurement [83, 91, 131, 250]. The spacing between the phase offsets as determined by the line repetition time could also be set such that the acquisition of subsequent lines is frequency-locked to the excitation frequency, eliminating the need to trigger between each line [350], though some form of synchronization would be required between motor positions to collect synchronous volumes. The disadvantage of this method is it requires reprogramming of the pulse sequence which is possible on Ultrasonix machines, but not all others. In the method used in this work, the only requirement is being able to trigger each transmission; there is no modification to the standard ultrasound sequence. If full channel parallel receive hardware is available such that all 128 lines could be received at the same instant, in combination with a planar transmit as in [309], entire frames could be acquired in 65 μ s and the trigger at the start of an excitation period would only be necessary for each motor position, resulting in an acquisition time of approximately 0.16 s, neglecting pauses for motor movement. It might also be possible to eliminate the need for synchronization if tissue motion is constrained to primarily the axial direction by applying compensation to the RF signals for the

delay in acquiring subsequent beam lines, similar to previous work applying compensation for transducer motion [283].

Methods for the acquisition of the full 3D vector shear wave motion over a volume using ultrasound have been described before using a different approach [33, 211]. In these works a plane wave transmit and full channel parallel receive hardware was used to measure the motion at a high rate. These works use a linear array mounted on a stepper motor to obtain a volume which is similar to a swept motor ultrasound transducer but with the motor not integrated into the casing and cabling. Synchronization between the exciter and pulse sequence is applied at each motor position. Elasticity is estimated by applying the curl operator to the displacement field and solving an Helmholtz equation algebraically which is similar in concept to the LFE inversion used in this work. The main difference between the work described in this paper and these previous works is the previous works use 1D displacement tracking from multiple angles, obtained through both beamforming and physical repositioning of the ultrasound array, and combine these 1D measures into a 3D vector. This paper uses 3D displacement tracking to obtain the 3D vector directly. The advantages of 3D tracking over 1D are greater measurement accuracy due to the ability to shift in multiple directions to reduce signal decorrelation and the option to use signal blocks that span all three directions which should improve SNR, and the ability to use a single view angle for the full 3D displacement vector which reduces system complexity and acquisition time. Combining multiple transducer view angles has the advantage of using axial displacement measures which are more accurate than lateral and elevational measures and therefore the regularization used in this work to reduce noise is not as important [4, 5]. However, the number of organs which multiple transducers may be applied is limited by geometry and the need to surround the organ from different transducer viewing positions. It is also important that the multiple transducers do not change the mechanical boundary conditions (e.g. changing the areas of transducer contact with the patient) during acquisition, otherwise the elastic wave field will change and it would be impossible to combine the measurements into a 3D vector. For these reasons, a specialized breast scanner using a water bath between the transducer and tissue has been used in the previous studies [33, 211].

Longer acquisition times, such as those caused by the synchronization used in

this work, are more susceptible to errors caused by patient or transducer motion. Some 3D ultrasound procedures might be able to restrict some undesired motions such as an automated breast scan [351], or TRUS imaging of the prostate [281], so such errors could be minimized.

The measurement of tissue motion in this work relies upon the assumption that consistent reproducible motion is produced, and thus a snapshot of the motion can be measured over a region at different acquisition times but identical mechanical exciter states. In a clinical setting, patient motion (e.g. through breath or heartbeat) breaks this assumption and would introduce error into the measurements. As mentioned in the previous paragraph, the long acquisition time for the method proposed in this work is more susceptible to these errors, but certain clinical applications, such as automated breast scanning, where motion is restricted may be able to reduce the magnitude of these errors. MRE is susceptible to these same problems but has been used *in vivo* [162, 290, 342]. Several ultrasound based tissue motion measurement methods also use this assumption, for example for *ex vivo* liver [83] and *in vivo* cardiac [250] measurements. Based on the success of tissue motion sampling in these previous studies, it seems that error introduced by patient motion can be managed to acceptable levels. There remains the question of whether the proposed method can measure consistent reproducible motion in an ideal setting when the patient does not contribute any additional motion. Forced harmonic vibrations approach steady state in exponential time for a nearly incompressible 3D elastic body [152]. To quantify the time to reach steady state, a simplified analysis of 1D damped forced vibration can be used as an approximation of tissue motion. The solution to the differential equation governing a mass-spring-damper vibration excited by a harmonic forcing function results in a transient term that oscillates at the damped natural frequency of the system and decays exponentially, and a steady-state term that oscillates at the forcing frequency. The exponentially decaying term takes the form

$$e^{-\frac{\eta}{2m}t} = e^{-\frac{t}{\tau}}, \quad (5.23)$$

where η and m are the local lumped damping and mass parameters, τ is the time constant of the exponential decay, and t is the elapsed time. A rough guideline is to ignore transient effects when $t/\tau \geq 5$ (the exponential decay is less than 0.67 % of

its original amplitude) [300]. To estimate the time constant, following the methodology of Turgay *et al.* [319], the ratio of viscous damping to the local lumped mass is estimated to be 4000 Pa s/kg. This means that transient effects can be ignored after 2.5 ms have elapsed. In this work care was taken to only start sampling ultrasound data a few seconds after starting the vibration source so a consistent and reproducible steady-state motion should be expected in the phantom experiments.

Another potential change that could disrupt the assumption of consistent reproducible motion is thermal effects. Repeated acoustic pulses from the ultrasound transducer may increase tissue temperature, changing the elastic properties of the tissue and the speckle pattern used for motion tracking. Previous research has shown these thermal effects to be small, with a temperature change under 2 °C and a shift of under 5 % of a sample in the speckle pattern (under one micron) [78].

This study used monochromatic mechanical excitation. Multi-frequency vibrations have been measured in MRE [162], so the synchronization presented in this work should allow for ultrasound measurement of multi-frequency displacement vector components over a volume. The multi-frequency data can mitigate measurement noise by changing locations of small displacement [242], and increasing the number of the equations to improve the conditioning of the inverse problem [136], or can also be used for spectral analysis [81, 97].

5.5 Conclusion

This study has demonstrated measurement of the full 3D harmonic motion vector over a volume by adding a synchronization step to the tracking steps and adding divergence-based regularization. Using a physical constraint consistent with soft tissues, divergence regularization post-processing creates a smoother field of displacement vectors. The regularized displacements produce a more accurate volume of elasticity estimates using the shear-FEM inversion method compared to using the unprocessed 3D displacement measurements. The accuracy does not seem to improve with LFE inversion using the regularized displacements, however improvements in CNR and SNR are observed. It is difficult to determine which inversion method is superior, however the profile of shear-FEM shows a symmetric and consistent profile in each direction with a peak at the centre of the inclusion that is

within 1 kPa of the manufacturer's specification. Results similar to *MRE* are generated using either method.

Future work will investigate the use of more sophisticated elasticity estimation algorithms, measurements on tissue instead of phantom material, and improvements in acquisition speed. Investigating repeatability and sensitivity to different boundary conditions and excitation modes are also of interest for particular clinical applications.

Chapter 6

Combining Multiple Views for Increased Accuracy of the Full Shear Wave Motion Vector in SWAVE

6.1 Introduction

Images of tissue elasticity are formed by measuring tissue motion in response to a mechanical stimulus. This field of medical imaging, called elastography, is commonly based on ultrasound measurements of tissue motion because ultrasound is ubiquitous, non-invasive, safe, inexpensive, and portable.

High quality measurements of the full 3D displacement vector over a volume are necessary to accurately solve the inverse problem for elastic parameters [96, 299]. Unfortunately, in the directions orthogonal to the ultrasound beam axis, the lack of phase information, poorer resolution, and larger sample spacing leads to over an order of magnitude increase in displacement measurement uncertainty compared to measurements along the beam axis [42, 167, 187]. The measurement noise in these directions can cause errors so large in the inversion process that replacing the measurements with a false assumption of no motion in the orthogonal direc-

tions can lead to more accurate estimates of the elastic parameters [99]. In Chapter 5, a method for measuring 3D displacement vectors using cross-correlation based speckle tracking on synchronized ultrasound acquisition with a motorized 3D transducer was proposed, and a technique for reducing noise in the displacement measurements using regularization based on tissue incompressibility was implemented. However, the two inversion methods used in that study decoupled the displacement components in the equations of motion, because inversion based on a fully coupled 3D motion model was not able to properly estimate elasticity.

One way to obtain multiple displacement components is to vary the ultrasound beam angle to obtain different axial measurements. Angular compounding is a technique which electronically steers the ultrasound beam axis to different angles, and combines the displacement measurements from each of these angles to compute the displacement vector components [267, 348]. The angular compounding technique improves displacement estimates by using multiple accurate axial displacement measurements of the projected displacement vector, however the steering angle is usually limited to angles up to 15° to maintain acceptable image quality, and even in special cases the angle is typically limited to 45° at most [126]. The maximum imaging depth becomes limited with increasing steering angles because the vector components can only be estimated in the region where the beams from each angle overlap.

An alternative approach is to use multiple transducer views with overlapping beams crossing at different angles. This has been successfully used in a customized Doppler instrument for measuring the blood velocity vector at a point in space [109]. A more recent work used multiple volumes collected by a hand held matrix array to compute 3D velocity vectors in the heart [118]. There has been some research interest in using this approach in elastography to improve displacement measurement accuracy in different directions. Some studies have used a transducer oriented orthogonal to the applied compression so that accurate axial displacement measurements could be used to measure the strains transverse to the primary excitation direction [60, 303]. Another study used two coplanar and orthogonal linear array transducers to measure 2D strains over a plane using axial displacement measurements from each transducer to obtain symmetric accuracy in the measurement directions [150]. In my master's research [4], I compared 2D displacement and

strain measurement accuracy using 2D correlation speckle tracking, angular compounding, and two coplanar linear arrays with relative beam angles varied between 40° to 90° and investigated errors introduced by inaccurate calibration between the two transducers.

A combination approach of multiple transducer views and angular compounding has been used in an elastography study measuring shear waves using two orthogonal linear arrays, oriented such that their image planes intersect along a line, mounted on stepper motors to measure 3D displacements over a 3D grid [33]. A similar approach is used by Muller *et al.* [211], using a single linear array mounted on a rotating table to circle the ROI from multiple view directions.

In this chapter it is proposed to combine axial measurements from different motorized 3D ultrasound transducers scanning the same volume from different angles, or, alternatively, a single tracked motorized 3D ultrasound transducer sequentially scanning a volume from different angles. It is the focus of this chapter to solve for 3D motion vectors from three volumes of axial motion measurements, and to study the effects of scan conversion, interpolation, and calibration on the displacement and elasticity estimates. Practical issues of the possibility of applying the technique clinically for breast cancer imaging are examined by simulating feasible scanning geometry and realistic calibration errors based on the results of Chapter 4.

6.2 Methods

6.2.1 Finite Element Simulation

A 3D FEM simulation was used to investigate the effectiveness of the proposed multiple view method in a controlled and repeatable environment. The FEM solution provided synthetic displacement data to generate simulated ultrasound speckle tracking measurements and a ground truth for comparing the elasticity results. A $40 \times 40 \times 40 \text{ mm}^3$ cube with a 5 mm radius stiff sphere was modelled using ANSYS FEM software (Cecil Township, PA, USA). The simulated phantom was meshed with 10-node tetrahedral elements (SOLID187) with a 0.5 mm nominal side length. The stiff sphere was modelled with a Young's modulus of 62 kPa, with the rest of the cube modelled with a background Young's modulus of 29 kPa. All elements were

modelled with a density of 1000 kg/m^3 and a Poisson's ratio of 0.495 to simulate soft tissue. A 300 Hz harmonic excitation with an amplitude of 0.6 mm was applied to the top surface of the cube in the normal direction of the top surface (longitudinal vibration in the y direction). The bottom surface of the cube was constrained in its normal direction (y), and constrained in the x and z directions along their respective lines of symmetry. All other sides of the cube were left free to deform.

6.2.2 Simulating Displacement Measurements

Ultrasound volumes were modelled using the geometry of a 4DL14-5/38 transducer (Vermon, Tours, France). Each volume contained 61 2D image slices swept over an arc in 0.45° increments with a radius of 81 mm between the centre of rotation and the start of the image. Each 2D image was 38.1 mm wide and 60 mm deep.

In total three ultrasound volume views were modelled to measure different components of the phantom motion vector using axial measurements from each ultrasound volume. To obtain the highest quality vector displacements from combined ultrasound axial displacement measurements, three orthogonal views should be used such that each axial measurement corresponds to one component of the vector. The volumetric sweep the 3D motorized ultrasound transducer changes the direction of axial measurement as a function of motor position, making it difficult to ensure the views are orthogonal over the full volume. Instead, it was decided to make the central 2D image plane of the motor sweep from each view orthogonal, while the other image planes would deviate slightly from the ideal measurement geometry. To make the method easy to adapt to experimental and clinical settings, it was desired to design the geometry such that the transducer views all generally pointed downwards so that they could all be placed on the top surface of a water bath, or flipped and placed under a prone patient. This geometry can be achieved by orienting the axial direction of the centre image plane at an angle of 35.4° downward from the horizontal, and rotating the transducer about a vertical axis in 120° increments to obtain the three views. The geometry can be described as rotating around the top face of a tetrahedron as depicted in Figure 6.1.

With respect to the FEM model, the first transducer view was placed such that the central 2D image plane had a 5 mm gap between the transducer face and the

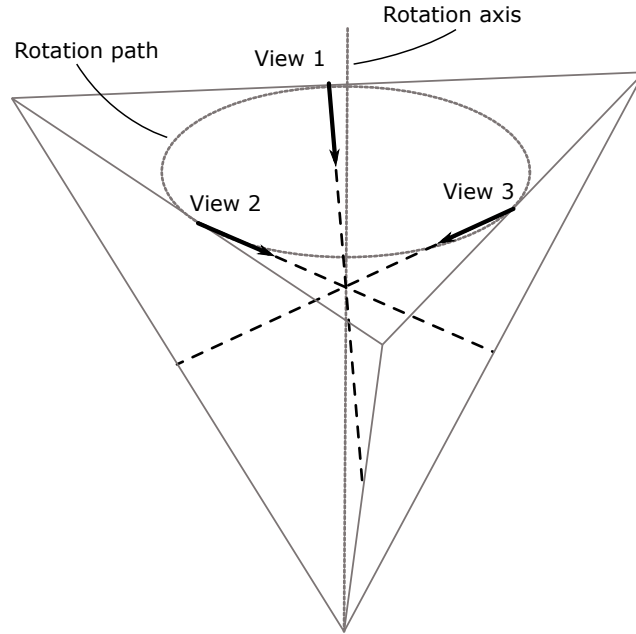


Figure 6.1: The view geometry is described as a rotation about an axis (dashed grey line) passing through a vertex of a tetrahedron and perpendicular to the opposite face of the tetrahedron (shown here as the top face). The views follow a 120° rotation along a circular path (grey dashed circle) on the top face of the tetrahedron, with each view centred on one of the tetrahedron edges and directed to the centre of the opposite edge (black arrows and dashed lines). The three views intersect at a common point and are orthogonal.

phantom, and the start of the image corresponded to the same height as the top of the phantom. The second and third transducer views were obtained by rotating the first view about the centre of the cube. The axes of the central image planes for each of the three views around the phantom are shown in Figure 6.2. The geometry of the sweep of the first view with respect to the phantom is shown in Figure 6.3.

Time-varying axial displacement measurements were generated by projecting the FEM solution onto the axial directional cosines of each image slice. Let $\mathbf{u}(\mathbf{x}, t)$ represent the displacements computed by ANSYS at position \mathbf{x} at time t , and $\mathbf{n}_\gamma(\mathbf{x})$ represent the axial directional cosines of the γ^{th} view, then the simulated axial dis-

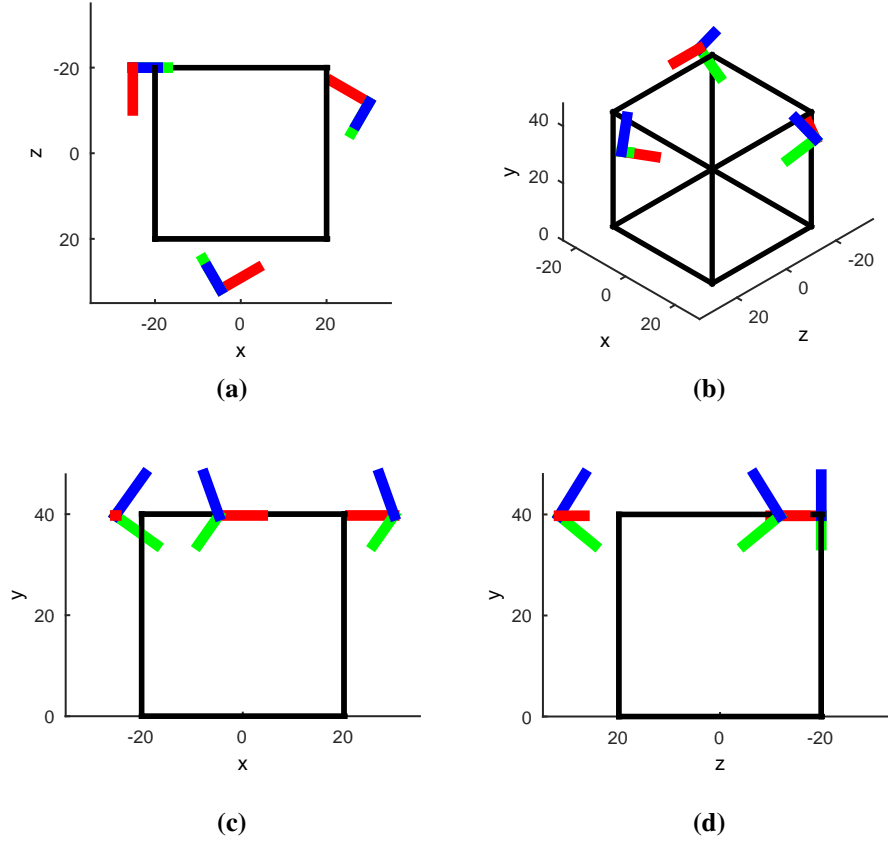


Figure 6.2: Geometry of the multiple view angles with respect to the phantom, showing (a) top, (c) front, (d) side, and (b) isometric views of the simulation. The black lines indicate the edges of the phantom and the red, green, and blue lines indicate the x , y , and z axes of the centre plane of the volume for each view, respectively.

placement is computed as a dot product

$$a(\mathbf{x}, t) = \mathbf{n}_y(\mathbf{x}) \cdot \mathbf{u}(\mathbf{x}, t) + \eta(\mathbf{x}, t), \quad (6.1)$$

where η represents jitter error in the ultrasound speckle tracking process. The jitter error in the motion measurements was simulated by adding zero mean Gaussian noise with variance equal to the Cramér-Rao lower bound for partially decorrelated

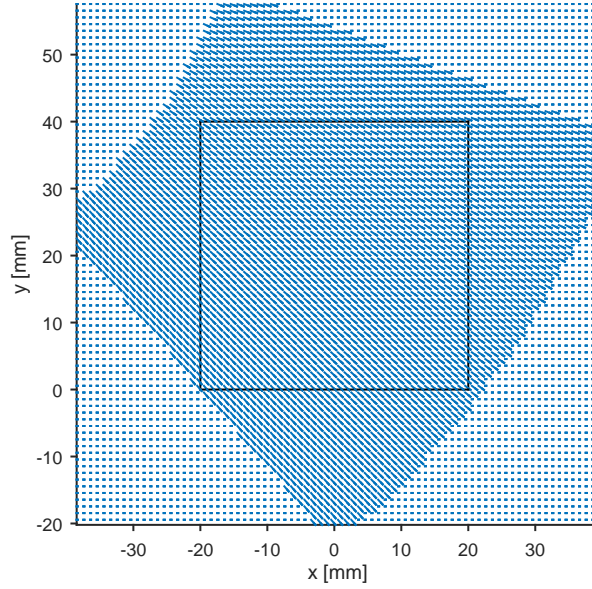


Figure 6.3: The ultrasound axial measurement direction over the entire swept volume (blue arrows) with an outline of the simulated phantom provided for reference (black square).

speckle [328]

$$\sigma = \frac{c}{2} \cdot \sqrt{\frac{3}{2\pi f_0^3 T (B^3 + 12B)} \left(\frac{1}{R^2} \left(1 + \frac{1}{\text{SNR}^2} \right)^2 - 1 \right)}, \quad (6.2)$$

where c is the ultrasound pulse speed, f_0 is the centre frequency of the ultrasound pulse, T is the displacement block length (measured in terms of echo time), B is the fractional bandwidth of the ultrasound system, R is the normalized cross-correlation coefficient, and SNR is the ultrasound signal-to-noise ratio based on signal corruption due to electronic noise. The parameter values used in this study are shown in Table 6.1 and were chosen to match the 4DL14-5/38 transducer and expected experimental measurement conditions.

Table 6.1: Parameter values used for simulating jitter error in the displacement measurements with Equation 6.2.

c	1540 m/s
f_0	10 MHz
T	1.3 μ s
B	0.7
R	0.98
SNR	40 dB

6.2.3 Solving for 3D Displacement

The axial displacements from each volume were mapped to a common grid, covering the extent of the overlapping region of the volumes, using 3D linear interpolation. The grid was regularly spaced, with a resolution of 1 mm in each direction chosen to achieve balance for the inversion algorithm in the element size trade-off in increasing inertial forces with decreasing derivative accuracy [138]. The axial directional cosines of each volume was also mapped to the common grid, and a least squares solution, similar to beam steering methods [313], was used to calculate the displacement vectors in terms of the FEM coordinate system. The relationship between the unknown displacement, \mathbf{d} , and the axial measurements is modelled as

$$\mathbf{V}\mathbf{d} = \mathbf{a}, \quad (6.3)$$

where

$$\mathbf{V} = \begin{bmatrix} \mathbf{n}_1^T[0] & \mathbf{0}_{1 \times 3} & \dots & \mathbf{0}_{1 \times 3} \\ \mathbf{0}_{1 \times 3} & \mathbf{n}_1^T[1] & & \vdots \\ \vdots & & \ddots & \\ \mathbf{0}_{1 \times 3} & & & \mathbf{n}_1^T[N-1] \\ \mathbf{n}_2^T[0] & \mathbf{0}_{1 \times 3} & \dots & \mathbf{0}_{1 \times 3} \\ \mathbf{0}_{1 \times 3} & \mathbf{n}_2^T[1] & & \vdots \\ \vdots & & \ddots & \\ \mathbf{0}_{1 \times 3} & & & \mathbf{n}_2^T[N-1] \\ \mathbf{n}_3^T[0] & \mathbf{0}_{1 \times 3} & \dots & \mathbf{0}_{1 \times 3} \\ \mathbf{0}_{1 \times 3} & \mathbf{n}_3^T[1] & & \vdots \\ \vdots & & \ddots & \\ \mathbf{0}_{1 \times 3} & & & \mathbf{n}_3^T[N-1] \end{bmatrix}, \quad (6.4)$$

$\mathbf{n}_\gamma[i]$ is the axial directional cosine vector for the γ^{th} view at the i^{th} grid location, N is the total number of grid locations,

$$\mathbf{d} = \begin{bmatrix} d_x[0] \\ d_y[0] \\ d_z[0] \\ \vdots \\ d_z[N-1] \end{bmatrix}, \quad (6.5)$$

d_x , d_y , and d_z are the x , y , and z components of the displacement vector at each

grid location,

$$\mathbf{a} = \begin{bmatrix} a_1[0] \\ a_1[1] \\ \vdots \\ a_1[N-1] \\ a_2[0] \\ \vdots \\ a_2[N-1] \\ a_3[0] \\ \vdots \\ a_3[N-1] \end{bmatrix}, \quad (6.6)$$

and a_γ is the axial measurement for the γ^{th} view at each grid location. The least squares solution for \mathbf{d} is computed as

$$\mathbf{d} = (\mathbf{V}^T \mathbf{V})^{-1} \mathbf{V}^T \mathbf{a}. \quad (6.7)$$

6.2.4 Simulating Calibration Error

The process of mapping each volume of data to a common grid requires knowledge of the spatial transformations between each of the volumes. This requires a calibration procedure, which could consist of determining the transformation between a transducer and a tracking sensor as described in Chapter 4, or could consist of a registration to align ultrasound volumes scanning the same target from different positions. In either case, some residual error in the translation and rotation parameters is expected. This will contribute to errors both in spatially aligning the data from each volume, and in describing the measurement directions accurately in the model as described by Equation 6.3.

Conceptually, the calibration error in this work models the situation where the data are measured at the nominal locations and directions as described in Section 6.2.2, but the calibration provides the wrong measurement location and direction. Before calibration error is introduced, the axial displacement data are given by Equation 6.1 at spatial location \mathbf{x}_0 . If the calibration error is described by a translation, \mathbf{s}_Λ , and a rotation, \mathbf{R}_Θ , then the axial displacement measurements from the

γ^{th} view are mapped to a new location

$$\mathbf{x} = \mathbf{R}_\gamma^\top \mathbf{R}_\Theta \mathbf{R}_\gamma \mathbf{x}_0 + \mathbf{R}_\gamma \mathbf{s}_\Lambda, \quad (6.8)$$

where \mathbf{R}_γ describes the rotation from phantom coordinates to the central image plane of the γ^{th} view. The application of \mathbf{R}_γ in Equation 6.8 is to ensure the calibration error is the same for each of the three views in the local view coordinates. In addition to mapping the data to a new location, the axial directional cosines are modified

$$\mathbf{m}_\gamma[i] = \mathbf{R}_\gamma^\top \mathbf{R}_\Theta \mathbf{R}_\gamma \mathbf{n}_\gamma[i], \quad (6.9)$$

where the matrix \mathbf{V} in Equation 6.4 is now constructed using the modified directional cosines, $\mathbf{m}_\gamma[i]$.

The calibration errors are composed of a magnitude and a direction. For the translation, this is just a scalar distance, Λ , multiplied by a unit vector

$$\mathbf{s}_\Lambda = \Lambda \hat{\mathbf{v}}_\Lambda. \quad (6.10)$$

For the rotation, Rodrigues' rotation formula is used to obtain the rotation matrix from the rotation axis unit vector and rotation angle magnitude

$$\mathbf{R}_\Theta = \mathbf{I} + \sin(\Theta) [\hat{\mathbf{v}}_\Theta]_\times + (1 - \cos(\Theta)) [\hat{\mathbf{v}}_\Theta]_\times^2, \quad (6.11)$$

where \mathbf{I} is a 3×3 identity matrix and $[\hat{\mathbf{v}}_\Theta]_\times$ is a skew symmetric cross product matrix constructed from the components of the rotation axis unit vector

$$[\hat{\mathbf{v}}_\Theta]_\times = \begin{bmatrix} 0 & -\hat{\mathbf{v}}_\Theta[2] & \hat{\mathbf{v}}_\Theta[1] \\ \hat{\mathbf{v}}_\Theta[2] & 0 & -\hat{\mathbf{v}}_\Theta[0] \\ -\hat{\mathbf{v}}_\Theta[1] & \hat{\mathbf{v}}_\Theta[0] & 0 \end{bmatrix}. \quad (6.12)$$

To investigate the error in estimating elasticity as a function of calibration error, Λ and Θ were tested at several values. The magnitude of calibration errors can be difficult to estimate because there often is no gold standard to compare a calibration result against. In Chapter 4, calibration error was quantified by calculating the the point-to-point distance in mapping the tip of a tracked stylus to a global coordinate

system using the calibration solution and position tracking measurements. Based on the results of Chapter 4, the best calibration method, $W_{2D \rightarrow 3D}$ had an error reaching up to 1.0 mm (95 % confidence interval using the Student's t-distribution). It is also of interest to investigate the effect of larger calibration errors, so based on the results of Chapter 4, and neglecting the N_{2D} method as a naive approach for 3D calibration, the worst calibration errors were observed with N_{3D} , reaching 2.7 mm (95 % confidence interval). Unfortunately this calibration error metric cannot separate errors in the the translation and rotation parameters, so instead the magnitude of the translation error was assumed to vary up to 2 mm, and the rotation parameters caused a position error on the order of 0.7 mm to 2.7 mm, which corresponds to approximately 1° to 3° for at an imaging depth of 60 mm. For the simulations, Λ was tested at values of 0 mm, 0.5 mm, 1 mm, 1.5 mm, and 2 mm, and Θ at 0° , 1° , 2° , and 3° . At each value of Λ and Θ , 50 random trials were simulated, each with a unique translation direction, \hat{v}_Λ , and rotation axis, \hat{v}_Θ . These vectors were sampled uniformly over all directions using the direction defined by uniform random quaternions [174].

6.2.5 Elasticity Inversion

Estimates of Young's modulus were therefore obtained using a recently developed direct (rather than iterative) inversion algorithm based on a dynamic displacement-pressure FEM, or mixed-FEM, formulation with sparsity regularization [135]. The mixed-FEM technique uses a full volumetric model of 3D elastic deformation without assumptions about elastic parameter homogeneity, or material incompressibility. As a result of the more realistic model, this inversion algorithm has demonstrated high quality results when all three displacement components are accurately measured, as in MRE, with both phantom and patient data [279]. Since ultrasound based displacement measurements using the multiple view approach should be of similar accuracy, this inversion algorithm is well suited for this work.

Using the governing equation of motion for a linear isotropic elastic material undergoing a time harmonic excitation (Equation 1.37), and defining the hydrostatic pressure (as in Equation 1.60) as an additional unknown, the tissue mechanics are

described by

$$\nabla \cdot [\mu (\nabla \mathbf{d} + (\nabla \mathbf{d})^T) + p \mathbf{I}] = -\rho \omega^2 \mathbf{d}, \quad (6.13)$$

where μ is the shear modulus, p the pressure, \mathbf{d} the displacement, ρ the density, and ω the frequency of excitation. The density of most soft tissue is close to the density of water, so ρ is assumed to be uniformly 1000 kg/m³.

For the FEM formulation, Equation 6.13 is written in weak form and discretized using 8-node hexahedral elements, with piece-wise constant shape functions for the shear modulus and pressure and linear shape functions for the displacement. The inverse problem can be written in matrix form as

$$\begin{bmatrix} \mathbf{A} & \mathbf{C} \end{bmatrix} \begin{bmatrix} \boldsymbol{\mu} \\ \mathbf{p} \end{bmatrix} = \mathbf{f}. \quad (6.14)$$

Sparsity regularization is used to ensure that the problem is full rank, to improve the condition number of the matrix, and to reduce the sensitivity of the solution to noise. The shear modulus and the pressure are assumed to have a sparse representation in the discrete cosine transform (DCT) domain, and can be represented using the lower frequency part of the domain. In this work, the DCT domain is truncated to select 85 % and 90 % of the coefficients for the shear modulus and pressure, respectively. Let \mathbf{T}_μ and \mathbf{T}_p represent the inverse truncated DCT transforms for the shear modulus and pressure respectively, then the regularized inverse problem becomes

$$\begin{bmatrix} (\mathbf{A}\mathbf{T}_\mu)^\top (\mathbf{A}\mathbf{T}_\mu) & (\mathbf{A}\mathbf{T}_\mu)^\top (\mathbf{C}\mathbf{T}_p) \\ (\mathbf{C}\mathbf{T}_p)^\top (\mathbf{A}\mathbf{T}_\mu) & (\mathbf{C}\mathbf{T}_p)^\top (\mathbf{C}\mathbf{T}_p) \end{bmatrix} \begin{bmatrix} \tilde{\boldsymbol{\mu}} \\ \tilde{\mathbf{p}} \end{bmatrix} = \begin{bmatrix} (\mathbf{A}\mathbf{T}_\mu)^\top \mathbf{f} \\ (\mathbf{C}\mathbf{T}_p)^\top \mathbf{f} \end{bmatrix}, \quad (6.15)$$

where $\tilde{\boldsymbol{\mu}}$ and $\tilde{\mathbf{p}}$ are approximated DCT transform domain shear modulus and pressure. After solving Equation 6.15, the shear modulus is obtained via

$$\boldsymbol{\mu} = \mathbf{T}_\mu \tilde{\boldsymbol{\mu}}. \quad (6.16)$$

In this work, the shear modulus values calculated by the inversion algorithm are converted to Young's modulus assuming fully incompressible tissue, resulting in a simple scalar relation $E \approx 3\mu$.

To decrease the computation time, the ROI is divided into several $13 \times 13 \times 13$

sub-domains and the solution is computed independently in each sub-domain. The total computation time using Matlab (Mathworks, Natick, MA, USA) running on a 3 GHz Intel Core2 Duo PC for a full elasticity volume was approximately two minutes on average.

The inversion process is sensitive to errors introduced by taking derivatives of noisy displacement measurements. A linear least squares fit in overlapping $3 \times 3 \times 3$ regions is used as a robust method to calculate the spatial gradient of the displacements used in the inversion. This is described in more detail in [Appendix G](#).

6.3 Results

The real part of the complex phasor motion field is shown in [Figure 6.4](#) for both the ANSYS solution and the displacement computed from three simulated axial displacement volumes. All three components are recovered from the combination of axial displacements and the wave pattern closely resembles the ANSYS solution. The common overlapping volume of the three views is slightly smaller than full phantom cube, so some regions close to the edges do not contain displacement in the volumes computed from axial measurements.

Examples of estimated elasticity volumes and the difference between the estimates and the ground truth are shown in [Figure 6.5](#). In all cases a stiff spherical inclusion is visible in a soft background. The difference images highlight the largest errors near the border between the background and inclusion. The inclusion appears to generally be underestimated, while the background appears to generally be overestimated. There is a band of underestimated background values around the boundaries of the ROI which seems to grow in spatial extent with increased simulated calibration error.

The RMS error in the estimated elasticity volumes is depicted in [Figure 6.6](#). The RMS error is averaged over 50 randomized trials at each of the calibration error settings to create one point on the plot. The RMS error for the elasticity estimated based on the ANSYS displacements is 3.50 kPa. Adding the steps of projecting the displacements onto the axial directions, adding speckle tracking noise at a 40 dB SNR, interpolating displacements to a common grid, and computing the orthogonal displacement components increases the mean RMS error in the elasticity estimates

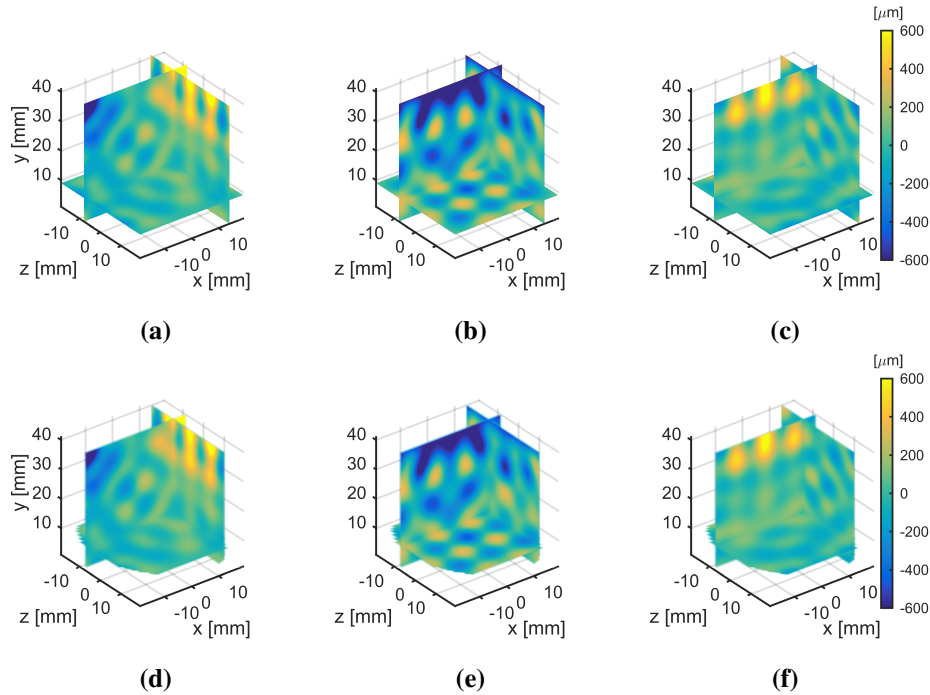


Figure 6.4: The real part of the complex displacement phasors over the volume shown in three orthogonal cross-sectional slices. The displacements in the x , y , and z directions are depicted from left to right, with the top row displaying the FEM solution computed by ANSYS, and the bottom row showing an example of the displacements computed from Equation 6.7 using three simulated axial measurements (with no calibration error applied).

to 6.22 kPa (with no calibration error applied). As expected, the error increases with increasing calibration error in translation and rotation, both in isolation and combined. For low calibration errors (< 1 mm and 2°), the elasticity error increases slowly (< 0.5 kPa) as calibration error increases. The last value on the 3° curve at 2 mm is beyond the range of the plot as the error increases greatly to 494 kPa.

6.4 Discussion

A significant source of the error in the elasticity estimates is caused by several types of errors in the displacement measurements. Neglecting calibration and speckle

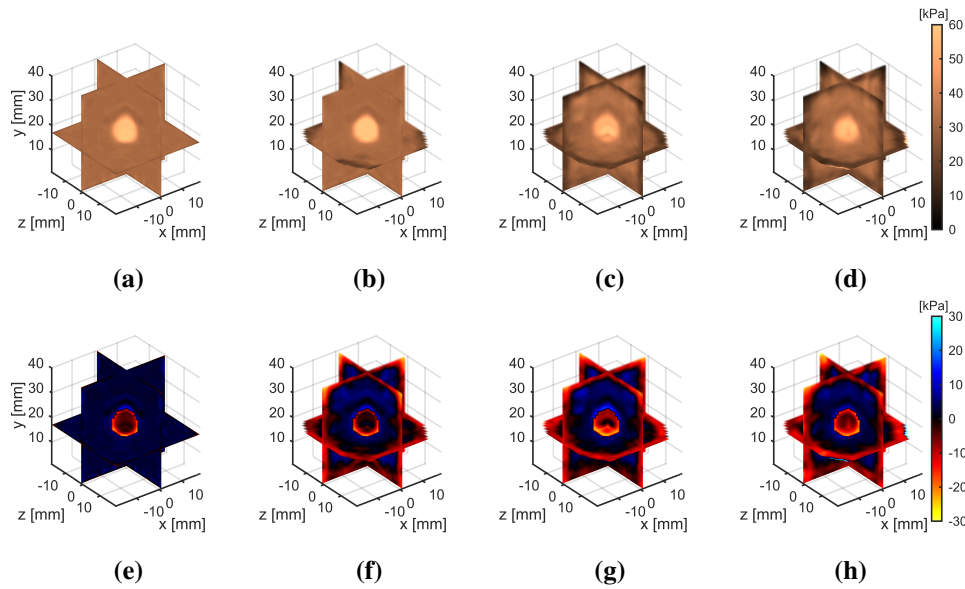


Figure 6.5: The (top row) estimated elasticity and (bottom row) difference in elasticity from ground truth. The estimated elasticity volumes are shown using input displacement (a) computed by ANSYS, and computed from three simulated views with (b) no calibration error, (c) 1 mm and 1° calibration error, and (d) 2 mm and 3° calibration error. The difference between the estimated elasticity and ground truth are shown in the same order as the estimated elasticity. Positive values indicate overestimation and negative underestimation in the difference images.

tracking noise, the displacements already accumulate errors from the three interpolation steps: (1) from the irregular tetrahedral FEM mesh in ANSYS to a regular grid in Matlab using the ANSYS element shape functions; (2) from the regular grid computed in (1) to the irregularly spaced ultrasound measurement points (i.e. the centres of each pixel after scan conversion from transducer to Cartesian coordinates) using 3D linear interpolation; and (3) from the ultrasound measurement points to the common regular grid for the overlapping measurements from each view using 3D linear interpolation. Due to the motor rotation to create the swept ultrasound volume, the intersecting beam angles are not always orthogonal, so after adding speckle tracking noise a spatially dependent projection error is created. This may partially explain why the elasticity estimates are poorer towards the edges of the

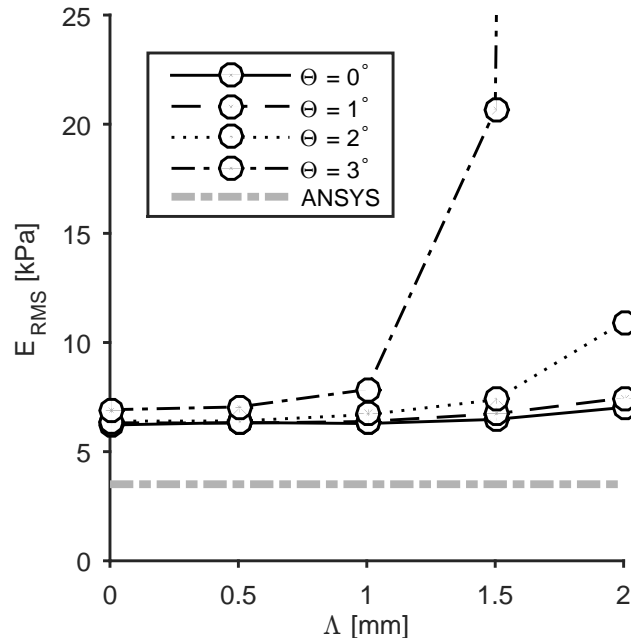


Figure 6.6: The mean RMS error in the estimated elasticity computed over the entire volume for all 50 trial randomized realizations of error, at each calibration error setting ranging from 0 mm to 2 mm in translation and 0° to 3° in rotation.

volume. For low calibration error levels, the elasticity error seems to be dominated by displacement SNR, however as the calibration error increases the elasticity error can grow by orders of magnitude.

Part of the elasticity error is also caused by differences between the inverse model and the forward model, as evidenced by the error produced when the displacements from the ANSYS solution are used directly as the input for the inversion algorithm. These discrepancies include differences in the assumptions used to derive the equations of motion, approximations used to discretize continuous quantities, mesh and element definitions, node placement and resolution, and algorithms used to compute derivatives, integrals, and solve equations.

The results presented in Figure 6.5 demonstrate the elasticity error is higher in regions where the elasticity suddenly changes from the soft background to the stiff

inclusion. This error is partially caused by the mesh, where some elements span the interface of regions of different elasticity. Since an element can only represent a single value of elasticity, it will contain some mix between the two elasticities within it. An optimized mesh adapted for the specific spatial distribution of elasticity, which could be approximated from a quasi-static strain image, would reduce these errors near the interface of the soft and stiff elasticity regions [117].

Inaccurate elasticity estimation, especially at the boundaries between regions of different elasticity, is also caused by the sparsity regularization, where the truncated DCT causes ringing artefacts near step changes in elasticity [135]. Using a different sparsity promoting transform, or a more intelligent method of choosing DCT coefficients could help reduce the ringing artefacts. For example, if a quasi-static strain image is available it can be used as an approximation of the spatial distribution of the shear modulus for selecting the sparsity pattern [138].

For consistency, the same mesh was used for the elasticity inversion of the ANSYS solution was also used for all of the simulated ultrasound displacement measurements. This resulted in some of the nodes falling outside of the overlapping region of the volumes. This might explain why the elasticity estimates for the simulated ultrasound measurements have a larger error towards the edges of the overlapping region. A special mesh designed for the irregular geometry of the overlapping region might help to eliminate the edge error.

The error in ultrasound speckle tracking displacement measurements was modelled as voxel-wise additive Gaussian noise. However, the quality of displacement measurements in real ultrasound signals is spatially dependent. Attenuation of the ultrasound signal with depth causes the SNR of the ultrasound signal and thus the displacement measurement quality to decrease with depth. The PSF of the ultrasound system also varies across the image plane, with the finest resolution located near the transmit focus depth and poorer resolution in the shallow and deep regions. The PSF also is poorer toward the lateral edges of the image as the beam cannot be properly focussed without array elements extending beyond the width of the image. Finally, displacement estimates are also more strongly influenced by high amplitude echoes in the RF signal.

The calibration error model used in this work kept the measured data constant and introduced an error in the measurement location and direction. An alternative

way to model the calibration error would be to fix the location and direction (i.e. the calibration says there is perfect alignment), while the measured data is actually acquired at a different location at a different projection angle. Neither approach models the experimental conditions closer than the other, however there could be some difference in simulated results. The approach used in this work changes the measurement direction matrix in Equation 6.4, and the alternative approach does not modify the measurement direction matrix but changes the measured displacements (a in Equation 6.1), while both approaches model misregistration of the volumes as in Equation 6.8.

This study neglected errors caused by refraction of the ultrasound beam when crossing between regions with different propagation speeds, and improper estimation of echo depth due to difference in the speed of sound used by the scanner and the true propagation speed of the echoes. The nature of these errors is similar to the calibration error that was modelled, however the errors would be spatially variant, depending on the underlying tissue composition and structure. The magnitude of the errors would likely be similar to the calibration error modelled in this work. For example, in the breast with a subcutaneous layer of fat followed by glandular tissue, the ultrasound speed can be expected to be 1480 m/s and 1580 m/s, respectively [92]. For an incident angle of 10° between the ultrasound beam and the transition layer between the fat and glandular tissue, the change in beam angle is 0.68° , and at 45° incidence the change is 1.7° . A previous study modelling the combined misregistration caused by refraction and speed of sound depth misplacement in 2D for orthogonal coplanar linear arrays estimated less than 1.0 mm error for breast tissue for imaging depths up to 30 mm [4].

An implicit assumption in this work is that displacement measurements can be acquired synchronously across all three volumes. The techniques described in Chapter 2 should be sufficient, with either accurate time stamp information for each ultrasound acquisition combined with phase compensation, or a trigger between the excitation and ultrasound scanner.

A long term goal of this research direction is to apply this multi-view approach clinically as a 3D elastography breast cancer system. An effort was made to design the transducer and view geometry such that it could be applied to the breast, either through direct skin contact or through a water bath similar to other similar

approaches [32, 211]. The elastic boundary conditions should not change between view acquisitions, so for direct skin contact this system would probably be best realized using multiple transducers rigidly fixed together or a customized transducer with multiple view directions [4]. For a water bath system, a single transducer could be used instead and rotated to each view position.

6.5 Conclusion

This work simulated acquiring volumetric ultrasound axial motion measurements of harmonically excited tissue from three different view points which are combined to solve for the full motion vector. The modelled geometry could feasibly be used in a clinical breast scanner for cancer imaging. Realistic calibration errors in spatially aligning the three volumes were studied. The proposed three view method can reliably solve for high quality 3D displacement vectors suitable for elasticity estimation based on an full 3D model of tissue mechanics.

Chapter 7

Conclusion

7.1 Summary

In this chapter, a full analysis of the research and its conclusions is presented in light of current research in the field. The contributions of the thesis are delineated and the limitations of the approaches undertaken in this thesis are described. The chapter is concluded with a description of possible future research directions.

In Chapter 2 the design and implementation of a 3D ultrasound elastography system was described. This system realizes a generalized modular system based on several previously developed specialized systems [23, 98, 191], and introduced the first implementation of a 3D band pass based system with an Ultrasonix ultrasound scanner. Simulations demonstrated the robustness of estimating motion amplitude and phase as a function of the number of samples used, the uncertainty in sampling rate, and errors in ultrasound speckle tracking based displacement measurements. B-MODE images collected on a quality assurance phantom showed no substantial degradation of SNR by introducing extra hardware for precise 3D ultrasound motor control. An analysis of experimental measurements of motion showed a gradual drift in motion phase as well as a false wave pattern appearing from motion compensation, and methods for correcting for these errors were presented. Experimental measurements of absolute elasticity values were collected on a CIRS 049 elastography phantom. Consistent elasticity measurements were produced from multiple acquisitions and different excitation conditions. The elasticity values were in agree-

ment with previous measurements of the phantom [22, 135–137].

In Chapter 3 the 3D ultrasound elastography system developed in Chapter 2 was used to quantify the elasticity and viscosity of healthy *ex vivo* placenta tissue. Measurements were collected from six placenta samples using vibrations over a band of 60 Hz to 200 Hz. Mean measurements of Young’s moduli matched previously reported measurements of healthy placenta tissue in the literature [51, 70, 159, 185, 229, 301]. This chapter presented the first elastography research to fit Voigt, Maxwell, and Zener rheological models to fit the placenta dispersion measurements. The Voigt model provided the best fit to the measurements, agreeing with conclusions from elastography measurements of bovine muscle [54] and porcine liver [64]. The strong viscous behaviour measured in this chapter matches observations from conventional mechanical testing of the placenta [333].

In Chapter 4, a novel calibration method, $W_{2D \rightarrow 3D}$, is described for simultaneously calibrating the motor parameters of a 3D ultrasound transducer and determining the rigid transform from the ultrasound data to a tracked sensor. Previous 3D ultrasound spatial calibration research has assumed that the motor parameters are known *a priori*, however it has been suggested that this may contribute to errors in the calibration result [258], and may be a reason that, prior to the results presented in Chapter 4, no 3D ultrasound calibration technique has demonstrated calibration error under 1 mm. The novel method uses accurate 2D ultrasound calibration at multiple locations along the motor sweep to fit the path of the ultrasound image. The technique is general and can make use of the diverse set of 2D calibration methods described in the literature. Chapter 4 also presents a novel 3D ultrasound calibration method that uses assumed motor parameters and uses planar features and a closed form solution. Finally, a method for extending the widely used N-wire technique to add additional data points from the usually ignored edges of the N-shapes. Overall, the $W_{2D \rightarrow 3D}$ method performed best. It improves the accuracy of 3D scan conversion in general, which can help improve the accuracy of any 3D ultrasound elastography technique using a swept motor ultrasound transducer, as well as any elastography technique that uses a tracked 3D ultrasound transducer, such as the multiple view method described in Chapter 6.

In Chapter 5 a novel method for measuring dynamic shear waves with volumetric ultrasound using a synchronization scheme was described. The method used the

$W_{2D \rightarrow 3D}$ calibration from Chapter 4 for scan conversion to Cartesian coordinates. This chapter reported the first results of measuring the full 3D displacement vector over a volume using a swept motor 3D ultrasound transducer for shear waves generated using excitation frequencies on the order of hundreds of cycles per second. A novel method of regularizing the displacement measurements by applying an incompressibility constraint based on tissue motion physics was developed which reduced noise in the displacement measurements without distorting the overall wave pattern. Elasticity measurements on a CIRS 049 elastography phantom were calculated using two previously developed inversion algorithms (LFE [200], and shear-FEM [137]) and 3D measurements (both regularized and unprocessed) are contrasted with 1D measurements. The elasticity estimated using the shear-FEM algorithm with 3D regularized displacement measurements provided the most accurate depiction of the true elasticity contrast and expected elasticity profile.

In Chapter 6 a method for measuring the full 3D displacement vector over a volume was investigated using the axial displacement measurement from three approximately orthogonal ultrasound views, as a potentially more accurate measurement method compared to Chapter 5. A simulation of a practical geometry for a clinical breast scanning system was used to evaluate the proposed approach, with calibration errors added to study the effect of misalignment of the views. Based on the level of calibration errors found in Chapter 4, accurate estimates of elasticity can be obtained of a stiff sphere located in a soft background in a simulated phantom. Previous work on using multiple views to improve ultrasound motion measurement demonstrates promise for applying this approach clinically [33, 118, 211].

At this point, it can be stated that the primary objectives of the thesis have been achieved. In particular,

- A modular 3D elastography research platform was developed and used to compare and optimize parameter selection for different techniques and equipment.
- The 3D elastography research platform was tested through simulations and experiments on tissue mimicking phantoms and *ex vivo* tissue.
- Two highly accurate ultrasound calibration techniques were developed that

can be applied to 3D elastography.

- A method for measuring the full shear wave motion vector field over a volume with 3D ultrasound was developed and tested on a tissue mimicking phantom.
- A method for combining multiple ultrasound volumes from different views to determine the full shear wave motion vector field over a volume was investigated through simulation incorporating realistic modelling of spatial calibration.

In summary, the hypothesis of this thesis, that a 3D approach to measurement can be used with ultrasound elastography to provide accurate measurements of tissue elasticity, is confirmed through numerical simulations and experiments on tissue-mimicking phantoms and *ex vivo* tissue.

7.2 Contributions

The contributions of this thesis are summarized as follows:

- A modular 3D ultrasound elastography research platform, *swave*, enabling easy implementation of different algorithms and use of different hardware. The system allows for comparison of different elastography approaches and can help in the development of new elastography techniques.
- Extending *swave* and implementing a technique for measuring the viscoelastic parameters in the first application of *swave* to placenta tissue. The technique uses longitudinal mechanical vibration and measures the wave pattern within the placenta with a 3D ultrasound transducer using the band pass motion sampling technique. Elasticity estimates are consistent with previous elastography measurements of placenta reported in the literature.
- A novel technique to calibrate a 3D swept motor ultrasound transducer without knowledge of the transducer's motor parameters (called $W_{2D \rightarrow 3D}$ in Chapter 4). The technique fits a rigid transformation path through multiple 2D ultrasound calibration solutions obtained along the motor path. The technique can use the solution from any 2D calibration method, and is implemented with the closed form multi-wedge method [215].

- A novel technique to calibrate a 3D swept motor ultrasound transducer using closed-form solution based on planar image features (called P_{3D} in Chapter 4). The solution uses the plane parameters fit to the segmented lines in each 2D image slice along the motor sweep and calculates the pose of the ultrasound volume with respect to the phantom's coordinate system. The closed-form solution, unlike iterative solutions, is fast to compute, not subject to sub-optimal local minima, and is not sensitive to initial estimates for the calibration parameters.
- A novel extension of the N-wire ultrasound calibration technique to solve for the location of the two edge points of each N-shape instead of ignoring them for the registration between the ultrasound and phantom points (called N_{3D}^{Full} in Chapter 4). The conventional approach only uses the centre point from the diagonal of the N-shape because its location in phantom coordinates can be computed using only ratios from the ultrasound image, and in general there can be ambiguity in determining the edge points in phantom coordinates. The new approach uses a specific placement of multiple N-shapes to uniquely identify the edge points by constraining all of the points from a given image to be located on a plane.
- A novel technique to measure dynamic shear wave vectors with 3D ultrasound for SWAVE. The approach synchronizes the acquisition of each beam line with the mechanical excitation that produces the shear waves. The trigger from the exciter to the ultrasound scanner is shifted in phase relative to the excitation signal such that multiple motion states are observed in the ultrasound data. The displacement between synchronous ultrasound volumes is measured using 3D cross-correlation with polynomial fitting for sub-sample precision, and scan conversion to convert from transducer to Cartesian displacements.
- A novel technique to apply regularization to 3D displacement measurements of soft tissue motion for SWAVE. The technique applies a divergence penalty that encourages solutions with incompressible tissue motion which is expected in most elastography imaging scenarios. The solution can be computed directly using matrix inversion and has demonstrated a qualitative re-

duction in displacement measurement noise for 3D shear wave measurements.

- A code base to solve for the three components of a motion vector given three overlapping volumes of motion measurements and the relative rigid transformations between each volume.

7.3 Limitations

The results reported in this thesis are very promising, however the proposed techniques suffer from some limitations which will pose challenges for adoption of the techniques in clinical practice.

The methods in this thesis assume that the transducer is stationary during acquisition. For the experiments in this thesis, the transducer was always fixed using a clamp. In a clinical setting, this would require the radiologist to hold their hand steady for a few seconds while a volume is acquired. For the 3D vector motion measurement described in Chapter 5, where the acquisition time is significantly longer, the transducer would likely need to be fixed.

Even with a perfectly fixed transducer, the *in vivo* setting poses new challenges. Patient movement, breathing, and cardiac motion can all cause unwanted motions in the measured displacement field. In the worst case, large motions can move the tracked scatterers outside of the field of view, making it impossible to continuously measure tissue displacements. For smaller motions, these can disrupt the excitation wave field and destroy the repeatability of the excitation which is assumed by the phase compensation algorithm.

Another practical consideration is the application of excitation to the tissue. The design of excitation devices for generating waves in deeply situated organs is a challenging task. Attenuation also constrains the range of excitation frequencies that can penetrate the organ of interest. The ideal excitation frequencies are also related to the elasticity of the tissue, as this affects the wavelength and resulting resolution of the elasticity images. The ability to measure waves in the liver, created by vibrations from a small disk applied to the surface of the body, with 3D ultrasound has been demonstrated up to depths of 15 cm for excitation frequencies up to 60 Hz, and to depths of 8 cm for excitation frequencies up to 100 Hz [23].

For elasticity inversion, in this thesis the tissue has been modelled as linear and isotropic, with a constant density equal to the density of water. Aside from the dispersion analysis of the placenta measurements in Chapter 3, this thesis also assumes that the tissue is perfectly elastic with no viscous losses. The assumption of linearity is reasonable because the magnitude of the deformations is on the order of microns of displacement. It should be noted that real tissue is expected to behave in a nonlinear fashion for increasing levels of strain. This could affect the repeatability of elasticity measurements as the level of pre-compression could differ between measurements. While some tissues, such as liver, are close to isotropic on the macro scale, other tissues such as muscle can have different elastic properties in different directions, and the methods developed in this thesis may not properly characterize these tissues. Most soft tissues imaged with ultrasound elastography have a high water content and have a density close to 1000 kg/m^3 , any deviation from this density will cause errors in the elasticity measurement.

7.4 Future Work

The SWAVE system could be enhanced by including other inversion algorithms, such as a GPU accelerated FEM inversion. The SWAVE system could also be extended to include angular compounding, similar to the 2D system described by Zahiri-Azar *et al.* [348], which would provide 2D displacement vectors over a volume, allowing for more sophisticated inversion algorithms to be used. Another extension to the SWAVE system could be to work with parallel received pre-beamformed data, for example by using the SonixDAQ add-on to the Ultrasonix systems. This would enable shorter acquisition times and could be used to measure 2D displacement vectors using the transverse oscillation technique [186]. The use of matrix array transducers with the SWAVE system would also reduce the acquisition time by eliminating the need to move a motor in the transducer, and could improve image quality with the greater ability to focus acoustic beams. Matrix arrays may also allow for 3D angular compounding for measurement of the full motion vector.

Further *ex vivo* measurements of placenta tissue, especially from pregnancies diagnosed with preeclampsia and IUGR would determine if the SWAVE system is capable of differentiating between normal and abnormal placenta tissue. The vis-

coelastic model fitting could be extended to produce high resolution spatial maps of viscous properties over a volume. A careful comparison between viscoelastic parameters, B-MODE features, and histology would be useful in understanding the biophysical basis for changes in the viscoelastic properties, and could help explain any observed changes in abnormal placenta tissue. If the SWAVE system proves to be a useful tool for diagnosing placenta abnormalities, an *in vivo* study of the optimal excitation design and placement would be valuable for creating a clinically viable product.

The calibration methods developed in this thesis can be extended to work with curvilinear transducers. The wedge phantom may need to be modified to optimize the image quality for the different geometry of a curvilinear transducer. It would be interesting to extend the $W_{2D \rightarrow 3D}$ method to also solve for the radius of curvature of the array and the element pitch and study if solving for these parameters can reduce calibration errors as solving for the 3D motor parameters. A study of the calibration error as a function of the number of 2D calibration solutions (each at a unique motor position) used in the 3D calibration fitting procedure would be of interest for determining the optimal number of calibrations to perform. Integrating the calibration algorithms into a powerful open-source toolkit, such as the PLUS toolkit [178], would make it easier for other researchers to use and would be beneficial by enabling the software to provide real-time feedback on the calibration quality and full control and synchronization of the spatial tracker and ultrasound scanner from a single interface.

The measurement of the full 3D shear wave motion vector could be tested with different modulus contrast (e.g. with a soft inclusion) to further investigate its performance in comparison to 1D tracking and MRE measurements with various inversion algorithms. With a goal of ultimately applying the technique *in vivo*, one of the faster acquisition schemes described in Chapter 5 should be implemented. To further decrease the acquisition time, the number of phase offsets might be reduced. A study of the displacement tracking error as a function of the number of acquired phase offsets would be valuable for determining the minimum number of offsets needed for a desired accuracy. Measurement of multi-frequency excitation is a natural extension of the work, which should also help improve the accuracy of the elasticity inversion.

A dedicated apparatus for multiple view ultrasound acquisition should be developed for use in *ex vivo* and *in vivo* settings. The apparatus could be realized with multiple 3D transducers fixed using a manufactured holder. A two view implementation providing 2D displacement over a volume could also be studied as it would provide advantages in acquisition rate and cost. The two view implementation could use a curl-based inversion such as the c-FEM [136]. It may also be possible to use divergence regularization, such as the algorithm described in Chapter 5, to estimate all three components of the vector from measurements of only two projections of the vector.

Bibliography

- [1] J. Abeysekera, R. Rohling, and S. Salcudean, “Vibro-elastography: Absolute elasticity from motorized 3D ultrasound measurements of harmonic motion vectors”, in *IEEE International Ultrasonics Symposium*, 2015, pp. 1–4 (→ page v).
- [2] J. M. Abeysekera and R. Rohling, “Alignment and calibration of dual ultrasound transducers using a wedge phantom”, *Ultrasound in Medicine and Biology*, vol. 37, no. 2, pp. 271–279, 2011 (→ page 154).
- [3] J. M. Abeysekera, M. Honarvar, R. Rohling, and S. E. Salcudean, “3D ultrasound shear wave absolute vibro-elastography (SWAVE) from full vector motion field measurements”, submitted (→ page v).
- [4] J. M. Abeysekera, R. Zahiri-Azar, O. Goksel, R. Rohling, and S. E. Salcudean, “Analysis of 2-D motion tracking in ultrasound with dual transducers”, *Ultrasonics*, vol. 52, no. 1, pp. 156–168, 2012 (→ pages 5, 40, 137, 161, 193, 198, 215, 216).
- [5] J. M. Abeysekera, M. Honarvar, S. E. Salcudean, and R. Rohling, “Combining axial measures to estimate 3D motion over an ultrasound volume”, in *Twelfth International Tissue Elasticity Conference*, 2013, p. 101 (→ pages vi, 193).
- [6] J. M. Abeysekera, M. Najafi, R. Rohling, and S. E. Salcudean, “Calibration for position tracking of swept motor 3-D ultrasound”, *Ultrasound in medicine and biology*, vol. 40, no. 6, pp. 1356–1371, 2014 (→ page v).
- [7] T. K. Adebar, M. C. Yip, S. E. Salcudean, R. N. Rohling, C. Y. Ngan, and S. L. Goldenberg, “Registration of 3D ultrasound through an air-tissue boundary”, *IEEE Transactions on Medical Imaging*, vol. 31, no. 11, pp. 2133–2142, 2012 (→ page 155).

- [8] S. Ahmad, R. Cao, T. Varghese, L. Bidaut, and G. Nabi, “Transrectal quantitative shear wave elastography in the detection and characterisation of prostate cancer”, *Surgical endoscopy*, vol. 27, no. 9, pp. 3280–3287, 2013 (→ page 70).
- [9] H. Akaike, “A new look at the statistical model identification”, *IEEE Transactions on Automatic Control*, vol. 19, no. 6, pp. 716–723, 1974 (→ page 285).
- [10] A. Al-Sharadqah and N. Chernov, “Error analysis for circle fitting algorithms”, *Electronic Journal of Statistics*, vol. 3, pp. 886–911, 2009 (→ page 152).
- [11] S. K. Alam and J. Ophir, “The effect of nonlinear signal transformations on bias errors in elastography”, *IEEE Transactions on Ultrasonics, Ferroelectrics, and Frequency Control*, vol. 47, no. 1, pp. 297–303, 2000 (→ page 43).
- [12] M. Ali, D. Magee, and U. Dasgupta, “Signal processing overview of ultrasound systems for medical imaging”, Texas Instruments, Texas, White Paper SPRAB12, 2008 (→ page 14).
- [13] S. L. Altmann, *Rotations, quaternions, and double groups*. Clarendon Press, Oxford University Press, 1986 (→ pages 153, 277).
- [14] . American Institute of Ultrasound in Medicine, “AIUM practice guideline for the performance of obstetric ultrasound examinations”, *Journal of Ultrasound in Medicine*, vol. 32, no. 6, pp. 1083–1101, 2013 (→ page 118).
- [15] M. E. Anderson, “Multi-dimensional velocity estimation with ultrasound using spatial quadrature”, *IEEE Transactions on Ultrasonics, Ferroelectrics, and Frequency Control*, vol. 45, no. 3, pp. 852–861, 1998 (→ page 40).
- [16] B. A. J. Angelsen, *Ultrasound Imaging*. Trondheim, Norway: Emantec, 2000, vol. I (→ page 4).
- [17] B. A. J. Angelsen, H. Torp, S. Holm, K. Kristoffersen, and T. A. Whittingham, “Which transducer array is best?”, *European Journal of Ultrasound*, vol. 2, no. 2, pp. 151–164, 1995 (→ page 18).
- [18] M. Arigovindan, M. Suhling, C. Jansen, P. Hunziker, and M. Unser, “Full motion and flow field recovery from Echo Doppler data”, *IEEE Transactions on Medical Imaging*, vol. 26, no. 1, pp. 31–45, 2007 (→ page 168).

- [19] M. Azizian and R. Patel, “Intraoperative 3D stereo visualization for image-guided cardiac ablation”, in *Proceedings of SPIE*, vol. 7964, 2011, 79640F (→ page 137).
- [20] A. Baghani, H. Eskandari, S. Salcudean, and R. Rohling, “Measurement of viscoelastic properties of tissue-mimicking material using longitudinal wave excitation”, *IEEE Transactions on Ultrasonics, Ferroelectrics and Frequency Control*, vol. 56, no. 7, pp. 1405–1418, 2009 (→ page 54).
- [21] A. Baghani, A. Brant, S. Salcudean, and R. Rohling, “A high-frame-rate ultrasound system for the study of tissue motions”, *IEEE Transactions on Ultrasonics, Ferroelectrics, and Frequency Control*, vol. 57, no. 7, pp. 1535–1547, 2010 (→ pages 53, 79, 83, 165).
- [22] A. Baghani, S. Salcudean, M. Honarvar, R. Sahebjavaher, R. Rohling, and R. Sinkus, “Travelling wave expansion: A model fitting approach to the inverse problem of elasticity reconstruction”, *IEEE Transactions on Medical Imaging*, vol. 30, no. 8, pp. 1555–1565, 2011 (→ pages 55, 111, 178, 184, 188, 192, 218).
- [23] A. Baghani, H. Eskandari, W. Wang, D. Da Costa, M. Lathiff, R. Sahebjavaher, S. Salcudean, and R. Rohling, “Real-time quantitative elasticity imaging of deep tissue using free-hand conventional ultrasound”, in *Medical Image Computing and Computer-Assisted Intervention*, 2012, pp. 617–624 (→ pages 71, 109, 118, 137, 217, 222).
- [24] J. M. Balter, J. N. Wright, L. J. Newell, B. Friemel, S. Dimmer, Y. Cheng, J. Wong, E. Vertatschitsch, and T. P. Mate, “Accuracy of a wireless localization system for radiotherapy”, *International Journal of Radiation Oncology Biology Physics*, vol. 61, no. 3, pp. 933–937, 2005 (→ page 68).
- [25] J. Bamber, D. Cosgrove, C. F. Dietrich, J. Fromageau, J. Bojunga, F. Calliada, V. Cantisani, J. M. Correas, M. D’Onofrio, E. E. Drakonaki, M. Fink, M. Friedrich-Rust, O. H. Gilja, R. F. Havre, C. Jenssen, A. S. Klauser, R. Ohlinger, A. Saftoiu, F. Schaefer, I. Sporea, and F. Piscaglia, “EFSUMB guidelines and recommendations on the clinical use of ultrasound elastography. Part 1: Basic principles and technology”, *Ultraschall in der Medizin*, vol. 34, no. 2, pp. 169–184, 2013 (→ page 163).
- [26] J. R. Barton and B. M. Sibai, “Prediction and prevention of recurrent preeclampsia”, *Obstetrics and Gynecology*, vol. 112, no. 2, pp. 359–372, 2008 (→ page 115).

- [27] M. Baumann, V. Daanen, A. Leroy, and J. Troccaz, “3-D ultrasound probe calibration for computer-guided diagnosis and therapy”, in *Computer Vision Approaches to Medical Image Analysis*, 2006, pp. 248–259 (→ pages 61, 138, 148).
- [28] P. Beigi, R. Rohling, T. Salcudean, V. A. Lessoway, and G. C. Ng, “Needle trajectory and tip localization in real-time 3-D ultrasound using a moving stylus”, *Ultrasound in medicine and biology*, vol. 41, no. 7, pp. 2057–2070, 2015 (→ page 136).
- [29] N. Benech, J. Brum, S. Catheline, T. Gallot, and C. Negreira, “Near-field effects in Green’s function retrieval from cross-correlation of elastic fields: Experimental study with application to elastography”, *The Journal of the Acoustical Society of America*, vol. 133, no. 5, pp. 2755–2766, 2013 (→ page 59).
- [30] N. Benech, J. Brum, C. Negreira, and S. Catheline, “Elasticity estimation by time-reversal of shear waves”, in *IEEE International Ultrasonics Symposium*, 2007, pp. 2263–2266 (→ page 58).
- [31] N. Benech, S. Catheline, J. Brum, T. Gallot, and C. Negreira, “1-D elasticity assessment in soft solids from shear wave correlation: The time-reversal approach”, *IEEE Transactions on Ultrasonics, Ferroelectrics, and Frequency Control*, vol. 56, no. 11, pp. 2400–2410, 2009 (→ pages 58, 59).
- [32] J. Bercoff, S. Chaffai, M. Tanter, L. Sandrin, S. Catheline, M. Fink, J.-L. Gennisson, and M. Meunier, “In vivo breast tumor detection using transient elastography”, *Ultrasound in medicine and biology*, vol. 29, no. 10, pp. 1387–1396, 2003 (→ pages 5, 50, 216).
- [33] J. Bercoff, R. Sinkus, M. Tanter, and M. Fink, “3D ultrasound-based dynamic and transient elastography: First in vitro results”, in *IEEE Ultrasonics Symposium*, vol. 1, 2004, pp. 28–31 (→ pages 40, 166, 193, 199, 219).
- [34] J. Bercoff, M. Tanter, and M. Fink, “Supersonic shear imaging: A new technique for soft tissue elasticity mapping”, *IEEE Transactions on Ultrasonics, Ferroelectrics, and Frequency Control*, vol. 51, no. 4, pp. 396–409, 2004 (→ pages 50, 70).
- [35] C. Bergmeir, M. Seitel, C. Frank, R. D. Simone, H.-P. Meinzer, and I. Wolf, “Comparing calibration approaches for 3D ultrasound probes”, *International Journal of Computer Assisted Radiology and Surgery*, vol. 4, no. 2, pp. 203–213, 2009 (→ pages 62, 138, 160).

- [36] S. Bharat, T. G. Fisher, T. Varghese, T. J. Hall, J. Jiang, E. L. Madsen, J. A. Zagzebski, and F. T. Lee, “Three-dimensional electrode displacement elastography using the siemens C7F2 fourSight four-dimensional ultrasound transducer”, *Ultrasound in medicine and biology*, vol. 34, no. 8, pp. 1307–1316, 2008 (→ page 4).
- [37] M. Bilgen, “Target detectability in acoustic elastography”, *IEEE Transactions on Ultrasonics, Ferroelectrics, and Frequency Control*, vol. 46, no. 5, pp. 1128–1133, 1999 (→ page 179).
- [38] J. Bishop, G. Poole, M. Leitch, and D. B. Plewes, “Magnetic resonance imaging of shear wave propagation in excised tissue”, *Journal of Magnetic Resonance Imaging*, vol. 8, no. 6, pp. 1257–1265, 1998 (→ page 78).
- [39] E. Boctor, A. Viswanathan, M. Choti, R. H. Taylor, G. Fichtinger, and G. Hager, “A novel closed form solution for ultrasound calibration”, in *IEEE International Symposium on Biomedical Imaging: Nano to Macro*, vol. 1, 2004, pp. 527–530 (→ pages 62, 154).
- [40] E. M. Boctor, A. Jain, M. A. Choti, R. H. Taylor, and G. Fichtinger, “Rapid calibration method for registration and 3D tracking of ultrasound images using spatial localizer”, in *Proceedings of SPIE*, 2003, pp. 521–532 (→ page 61).
- [41] E. M. Boctor, I. Iordachita, G. Fichtinger, and G. D. Hager, “Ultrasound self-calibration”, in *Proceedings of SPIE*, 2006, 61412N–1–61412N–12 (→ page 62).
- [42] L. N. Bohs and G. E. Trahey, “A novel method for angle independent ultrasonic imaging of blood flow and tissue motion”, *IEEE Transactions on Biomedical Engineering*, vol. 38, no. 3, pp. 280–286, 1991 (→ pages 4, 40, 167, 197).
- [43] O. Bonnefous and P. Pesque, “Time domain formulation of pulse-Doppler ultrasound and blood velocity estimation by cross correlation”, *Ultrasonic Imaging*, vol. 8, no. 2, pp. 73–85, 1986 (→ page 36).
- [44] O. Bottema and B. Roth, *Theoretical kinematics*. Dover Publications, 1979 (→ page 277).
- [45] L. G. Bouchet, S. L. Meeks, G. Goodchild, F. J. Bova, J. M. Buatti, and W. A. Friedman, “Calibration of three-dimensional ultrasound images for image-guided radiation therapy”, *Physics in Medicine and Biology*, vol. 46, no. 2, pp. 559–577, 2001 (→ page 138).

- [46] J. Braun, K. Braun, and I. Sack, “Electromagnetic actuator for generating variably oriented shear waves in MR elastography”, *Magnetic resonance in medicine*, vol. 50, no. 1, pp. 220–222, 2003 (→ page 78).
- [47] B. Brendel, S. Winter, and H. Ermert, “A simple and accurate calibration method for 3D freehand ultrasound”, *Biomedizinische Technik*, vol. 49, no. 2, pp. 872–873, 2004 (→ page 61).
- [48] D. Brodsky and H. Christou, “Current concepts in intrauterine growth restriction”, *Journal of Intensive Care Medicine*, vol. 19, no. 6, pp. 307–319, 2004 (→ page 114).
- [49] R. O. Bude and J. M. Rubin, “Power Doppler sonography”, *Radiology*, vol. 200, no. 1, pp. 21–23, 1996 (→ page 29).
- [50] S. R. Buss and J. P. Fillmore, “Spherical averages and applications to spherical splines and interpolation”, *ACM Transactions on Graphics*, vol. 20, no. 2, pp. 95–126, 2001 (→ pages 152, 153).
- [51] S. Callé, M.-C. Dumoux, E. Nicolas, J.-P. Remenieras, E. Simon, and F. Perrotin, “Ex vivo measurement of shear wave speed dispersion in placenta using transient elastography”, in *IEEE International Ultrasonics Symposium*, 2015, pp. 1–4 (→ pages 115, 130, 132, 218).
- [52] V. Cantisani, P. Lodise, H. Grazhdani, E. Mancuso, E. Maggini, G. Di Rocco, F. D’Ambrosio, F. Calliada, A. Redler, P. Ricci, and C. Catalano, “Ultrasound elastography in the evaluation of thyroid pathology. current status”, *European Journal of Radiology*, vol. 83, no. 3, pp. 420–428, 2014 (→ page 70).
- [53] L. Castéra, J. Vergniol, J. Foucher, B. Le Bail, E. Chanteloup, M. Haaser, M. Darriet, P. Couzigou, and V. de Lédinghen, “Prospective comparison of transient elastography, Fibrotest, APRI, and liver biopsy for the assessment of fibrosis in chronic hepatitis C”, *Gastroenterology*, vol. 128, no. 2, pp. 343–350, 2005 (→ pages 2, 163, 189).
- [54] S. Catheline, J.-L. Gennisson, G. Delon, M. Fink, R. Sinkus, S. Abouelkaram, and J. Culioli, “Measurement of viscoelastic properties of homogeneous soft solid using transient elastography: An inverse problem approach”, *The Journal of the Acoustical Society of America*, vol. 116, no. 6, pp. 3734–3741, 2004 (→ pages 33, 50, 218).
- [55] S. Catheline, N. Bencech, J. Brum, and C. Negreira, “Time reversal of elastic waves in soft solids”, *Physical review letters*, vol. 100, no. 6, 064301–1–064301–4, 2008 (→ page 59).

- [56] S. Catheline, R. Souchon, M. Rupin, J. Brum, A. Dinh, and J.-Y. Chapelon, “Tomography from diffuse waves: Passive shear wave imaging using low frame rate scanners”, *Applied Physics Letters*, vol. 103, no. 1, 014101–1–014101–5, 2013 (→ page 59).
- [57] I. Céspedes, Y. Huang, J. Ophir, and S. Spratt, “Methods for estimation of subsample time delays of digitized echo signals”, *Ultrasonic Imaging*, vol. 17, no. 2, pp. 142–171, 1995 (→ pages 37, 81).
- [58] I. Céspedes and J. Ophir, “Reduction of image noise in elastography”, *Ultrasonic Imaging*, vol. 15, no. 2, pp. 89–102, 1993 (→ pages 43, 165).
- [59] C. Chatfield, *The Analysis of Time Series: An Introduction*, 6th ed. Boca Raton: CRC Press, 2004 (→ page 26).
- [60] P. Chaturvedi, M. F. Insana, and T. J. Hall, “2-D companding for noise reduction in strain imaging”, *IEEE Transactions on Ultrasonics, Ferroelectrics and Frequency Control*, vol. 45, no. 1, pp. 179–191, 1998 (→ pages 39, 43, 198).
- [61] E. C. Chen, A. J. McLeod, J. S. Baxter, and T. M. Peters, “An iterative closest point framework for ultrasound calibration”, in *Augmented Environments for Computer-Assisted Interventions*, 2015, pp. 69–79 (→ page 63).
- [62] H. Chen, H. Shi, and T. Varghese, “Improvement of elastographic displacement estimation using a two-step cross-correlation method”, *Ultrasound in medicine and biology*, vol. 33, no. 1, pp. 48–56, 2007 (→ page 37).
- [63] S. Chen, M. Fatemi, and J. F. Greenleaf, “Quantifying elasticity and viscosity from measurement of shear wave speed dispersion”, *The Journal of the Acoustical Society of America*, vol. 115, no. 6, pp. 2781–2785, 2004 (→ pages 51, 115).
- [64] S. Chen, M. W. Urban, C. Pislaru, R. Kinnick, Y. Zheng, A. Yao, and J. F. Greenleaf, “Shearwave dispersion ultrasound vibrometry (SDUV) for measuring tissue elasticity and viscosity”, *IEEE Transactions on Ultrasonics, Ferroelectrics, and Frequency Control*, vol. 56, no. 1, pp. 55–62, 2009 (→ page 218).
- [65] T. K. Chen, A. D. Thurston, R. E. Ellis, and P. Abolmaesumi, “A real-time freehand ultrasound calibration system with automatic accuracy feedback and control”, *Ultrasound in Medicine and Biology*, vol. 35, no. 1, pp. 79–93, 2009 (→ pages 62, 146).

- [66] X. Chen, M. J. Zohdy, S. Y. Emelianov, and M. O'Donnell, "Lateral speckle tracking using synthetic lateral phase", *IEEE Transactions on Ultrasonics, Ferroelectrics, and Frequency Control*, vol. 51, no. 5, pp. 540–550, 2004 (→ page 40).
- [67] X. Chen, H. Xie, R. Erkamp, K. Kim, C. Jia, J. M. Rubin, and M. O'Donnell, "3-D correlation-based speckle tracking", *Ultrasonic Imaging*, vol. 27, no. 1, pp. 21–36, 2005 (→ pages 39, 164).
- [68] A. Cheng, M. K. Ackerman, G. S. Chirikjian, and E. M. Boctor, "Design and development of an ultrasound calibration phantom and system", in *Proceedings of SPIE*, 2014, 903624–1–903624–8 (→ page 62).
- [69] D. Christensen, *Ultrasonic Bioinstrumentation*. New York: Wiley, 1988 (→ pages 4, 10).
- [70] C. Cimsit, T. Yoldemir, and I. N. Akpınar, "Shear wave elastography in placental dysfunction comparison of elasticity values in normal and preeclamptic pregnancies in the second trimester", *Journal of Ultrasound in Medicine*, vol. 34, no. 1, pp. 151–159, 2015 (→ pages 115, 116, 132, 218).
- [71] ———, "Strain elastography in placental dysfunction: Placental elasticity differences in normal and preeclamptic pregnancies in the second trimester", *Archives of gynecology and obstetrics*, vol. 291, no. 4, pp. 811–817, 2015 (→ page 115).
- [72] J. S. Cnossen, R. K. Morris, G. ter Riet, B. W. Mol, J. A. van der Post, A. Coomarasamy, A. H. Zwinderman, S. C. Robson, P. J. Bindels, J. Kleijnen, and K. S. Khan, "Use of uterine artery Doppler ultrasonography to predict pre-eclampsia and intrauterine growth restriction: A systematic review and bivariable meta-analysis", *Canadian Medical Association Journal*, vol. 178, no. 6, pp. 701–711, 2008 (→ page 115).
- [73] R. S. C. Cobbold, *Foundations of biomedical ultrasound*. New York: Oxford University Press, 2007 (→ page 10).
- [74] N. A. Cohn, S. Y. Emelianov, M. A. Lubinski, and M. O'Donnell, "An elasticity microscope. Part I: Methods", *IEEE Transactions on Ultrasonics, Ferroelectrics, and Frequency Control*, vol. 44, no. 6, pp. 1304–1319, 1997 (→ page 36).

- [75] R. M. Comeau, A. F. Sadikot, A. Fenster, and T. M. Peters, “Intraoperative ultrasound for guidance and tissue shift correction in image-guided neurosurgery”, *Medical Physics*, vol. 27, no. 4, pp. 787–800, 2000 (→ page 140).
- [76] J. J. Dahl, G. F. Pinton, M. L. Palmeri, V. Agrawal, K. R. Nightingale, and G. E. Trahey, “A parallel tracking method for acoustic radiation force impulse imaging”, *IEEE Transactions on Ultrasonics, Ferroelectrics, and Frequency Control*, vol. 54, no. 2, pp. 301–312, 2007 (→ page 165).
- [77] S. Dandekar, Y. Li, J. Molloy, and J. Hossack, “A phantom with reduced complexity for spatial 3-D ultrasound calibration”, *Ultrasound in Medicine and Biology*, vol. 31, no. 8, pp. 1083–1093, 2005 (→ page 61).
- [78] M. I. Daoud, P. Mousavi, F. Imani, R. Rohling, and P. Abolmaesumi, “Tissue classification using ultrasound-induced variations in acoustic backscattering features”, *IEEE Transactions on Biomedical Engineering*, vol. 60, no. 2, pp. 310–320, 2013 (→ page 195).
- [79] C. De Korte, S. Carlier, F. Mastik, M. Doyley, A. Van Der Steen, P. Serruys, and N. Bom, “Morphological and mechanical information of coronary arteries obtained with intravascular elastography”, *European Heart Journal*, vol. 23, pp. 405–413, 2002 (→ page 69).
- [80] L. Debernard, G. E. Leclerc, L. Robert, F. Charleux, and S. F. Bensamoun, “In vivo characterization of the muscle viscoelasticity in passive and active conditions using multifrequency MR elastography”, *Journal of Musculoskeletal Research*, vol. 16, no. 2, 1350008–1–1350008–10, 2013 (→ page 133).
- [81] T. Deffieux, G. Montaldo, M. Tanter, and M. Fink, “Shear wave spectroscopy for in vivo quantification of human soft tissues visco-elasticity”, *IEEE Transactions on Medical Imaging*, vol. 28, no. 3, pp. 313–322, 2009 (→ pages 115, 195).
- [82] P. R. Detmer, G. Bashein, T. Hodges, K. W. Beach, E. P. Filer, D. H. Burns, and D. E. Strandness, “3D ultrasonic image feature localization based on magnetic scanhead tracking: In vitro calibration and validation”, *Ultrasound in medicine and biology*, vol. 20, no. 9, pp. 923–936, 1994 (→ page 61).
- [83] R. J. DeWall, T. Varghese, and E. L. Madsen, “Shear wave velocity imaging using transient electrode perturbation: Phantom and ex vivo validation”, *IEEE Transactions on Medical Imaging*, vol. 30, no. 3, pp. 666–678, 2011 (→ pages 166, 192, 194).

- [84] M. D’Onofrio, A. Gallotti, and R. P. Mucelli, “Tissue quantification with acoustic radiation force impulse imaging: Measurement repeatability and normal values in the healthy liver”, *American Journal of Roentgenology*, vol. 195, no. 1, pp. 132–136, 2010 (→ page 70).
- [85] D. B. Downey, A. Fenster, and J. C. Williams, “Clinical utility of three-dimensional US”, *Radiographics*, vol. 20, no. 2, pp. 559–571, 2000 (→ pages 4, 136).
- [86] M. M. Doyley, P. M. Meaney, and J. C. Bamber, “Evaluation of an iterative reconstruction method for quantitative elastography”, *Physics in Medicine and Biology*, vol. 45, no. 6, pp. 1521–1540, 2000 (→ pages 2, 44, 164).
- [87] M. M. Doyley, J. B. Weaver, E. E. W. Van Houten, F. E. Kennedy, and K. D. Paulsen, “Thresholds for detecting and characterizing focal lesions using steady-state MR elastography”, *Medical Physics*, vol. 30, no. 4, pp. 495–504, 2003 (→ pages 71, 164).
- [88] M. A. Dresner, G. H. Rose, P. J. Rossman, R. Muthupillai, A. Manduca, and R. L. Ehman, “Magnetic resonance elastography of skeletal muscle”, *Journal of Magnetic Resonance Imaging*, vol. 13, no. 2, pp. 269–276, 2001 (→ page 54).
- [89] F. A. Duck, *Physical properties of tissue*. San Diego: Academic Press, 1990 (→ page 34).
- [90] B. Dunmire, K. W. Beach, K.-H. Labs, M. Plett, and D. E. Strandness Jr, “Cross-beam vector Doppler ultrasound for angle-independent velocity measurements”, *Ultrasound in Medicine and Biology*, vol. 26, no. 8, pp. 1213–1235, 2000 (→ page 40).
- [91] V. Dutt, R. R. Kinnick, R. Muthupillai, T. E. Oliphant, R. L. Ehman, and J. F. Greenleaf, “Acoustic shear-wave imaging using echo ultrasound compared to magnetic resonance elastography”, *Ultrasound in Medicine and Biology*, vol. 26, no. 3, pp. 397–403, 2000 (→ pages 165, 192).
- [92] P. D. Edmonds, C. L. Mortensen, J. R. Hill, S. K. Holland, J. F. Jensen, P. Schattner, and A. D. Valdes, “Ultrasound tissue characterization of breast biopsy specimens”, *Ultrasonic Imaging*, vol. 13, no. 2, pp. 162–185, 1991 (→ page 215).
- [93] D. W. Eggert, A. Lorusso, and R. B. Fisher, “Estimating 3-D rigid body transformations: A comparison of four major algorithms”, *Machine Vision and Applications*, vol. 9, no. 5-6, pp. 272–290, 1997 (→ page 60).

- [94] V. Egorov and A. P. Sarvazyan, “Mechanical imaging of the breast”, *IEEE Transactions on Medical Imaging*, vol. 27, no. 9, pp. 1275–1287, 2008 (→ page 2).
- [95] H. Eskandari, S. E. Salcudean, and R. Rohling, “Tissue strain imaging using a wavelet transform-based peak search algorithm”, *IEEE Transactions on Ultrasonics, Ferroelectrics and Frequency Control*, vol. 54, no. 6, pp. 1118–1130, 2007 (→ page 39).
- [96] H. Eskandari, S. E. Salcudean, R. Rohling, and J. Ohayon, “Viscoelastic characterization of soft tissue from dynamic finite element models”, *Physics in Medicine and Biology*, vol. 53, pp. 6569–6590, 2008 (→ pages 4, 53, 197).
- [97] H. Eskandari, S. E. Salcudean, and R. Rohling, “Viscoelastic parameter estimation based on spectral analysis”, *IEEE Transactions on Ultrasonics, Ferroelectrics, and Frequency Control*, vol. 55, no. 7, pp. 1611–1625, 2008 (→ pages 49, 134, 195).
- [98] H. Eskandari, O. Goksel, S. E. Salcudean, and R. Rohling, “Bandpass sampling of high-frequency tissue motion”, *IEEE Transactions on Ultrasonics, Ferroelectrics, and Frequency Control*, vol. 58, no. 7, pp. 1332–1343, 2011 (→ pages 71, 79, 164, 217).
- [99] H. Eskandari, S. E. Salcudean, R. Rohling, and I. Bell, “Real-time solution of the finite element inverse problem of viscoelasticity”, *Inverse Problems*, vol. 27, no. 8, p. 085 002, 2011 (→ pages 53, 198).
- [100] K. R. Etzel and J. M. McCarthy, “A metric for spatial displacement using biquaternions on $SO(4)$ ”, in *IEEE International Conference on Robotics and Automation*, vol. 4, 1996, pp. 3185–3190 (→ page 283).
- [101] A. Evans, P. Whelehan, K. Thomson, K. Brauer, L. Jordan, C. Purdie, D. McLean, L. Baker, S. Vinnicombe, and A. Thompson, “Differentiating benign from malignant solid breast masses: Value of shear wave elastography according to lesion stiffness combined with greyscale ultrasound according to BI-RADS classification”, *British journal of cancer*, vol. 107, no. 2, pp. 224–229, 2012 (→ pages 2, 163, 189).
- [102] D. H. Evans, J. A. Jensen, and M. B. Nielsen, “Ultrasonic colour Doppler imaging”, *Interface Focus*, pp. 490–502, 2011 (→ page 26).
- [103] M. Fink, D. Cassereau, A. Derode, C. Prada, P. Roux, M. Tanter, J.-l. Thomas, and F. Wu, “Time-reversed acoustics”, *Reports on progress in Physics*, vol. 63, no. 12, pp. 1933–1995, 2000 (→ page 57).

- [104] M. Fink, G. Montaldo, and M. Tanter, “Time-reversal acoustics in biomedical engineering”, *Annual review of biomedical engineering*, vol. 5, no. 1, pp. 465–497, 2003 (→ page 59).
- [105] T. G. Fisher, T. J. Hall, S. Panda, M. S. Richards, P. E. Barbone, J. Jiang, J. Resnick, and S. Barnes, “Volumetric elasticity imaging with a 2-D CMUT array”, *Ultrasound in Medicine and Biology*, vol. 36, no. 6, pp. 978–990, 2010 (→ pages 39, 164).
- [106] P. T. Fletcher, “Geodesic regression on Riemannian manifolds”, in *Third International Workshop on Mathematical Foundations of Computational Anatomy-Geometrical and Statistical Methods for Modelling Biological Shape Variability*, 2011, pp. 75–86 (→ page 152).
- [107] P. T. Fletcher, C. Lu, S. M. Pizer, and S. Joshi, “Principal geodesic analysis for the study of nonlinear statistics of shape”, *IEEE Transactions on Medical Imaging*, vol. 23, no. 8, pp. 995–1005, 2004 (→ page 283).
- [108] J. Foucher, E. Chanteloup, J. Vergniol, L. Castera, B. Le Bail, X. Adhoute, J. Bertet, P. Couzigou, and V. de Ledinghen, “Diagnosis of cirrhosis by transient elastography (FibroScan): A prospective study”, *Gut*, vol. 55, no. 3, pp. 403–408, 2006 (→ page 69).
- [109] M. D. Fox, “Multiple crossed-beam ultrasound Doppler velocimetry”, *IEEE Transactions on Sonics and Ultrasonics*, vol. 25, no. 5, pp. 281–286, 1978 (→ page 198).
- [110] S. M. Frew, “Viscoelastic imaging methods using acoustic radiation force”, Master’s thesis, University of British Columbia, 2010 (→ page 49).
- [111] Y. C. Fung, *Biomechanics: Mechanical Properties of Living Tissues*, 2nd. New York: Springer, 1993 (→ pages 33, 120).
- [112] T. Gallot, S. Catheline, P. Roux, J. Brum, N. Benech, and C. Negreira, “Passive elastography: Shear-wave tomography from physiological-noise correlation in soft tissues.”, *IEEE Transactions on Ultrasonics, Ferroelectrics, and Frequency Control*, vol. 58, no. 6, pp. 1122–1126, 2011 (→ page 59).
- [113] L. Gao, K. J. Parker, and S. K. Alam, “Sonoelasticity imaging: Theory and experimental verification”, *Journal of the Acoustical Society of America*, vol. 97, no. 6, pp. 3875–3886, 1995 (→ pages 46, 78).
- [114] B. S. Garra, E. I. Cespedes, J. Ophir, S. R. Spratt, R. A. Zuurbier, C. M. Magnant, and M. F. Pennanen, “Elastography of breast lesions: Initial clinical results”, *Radiology*, vol. 202, no. 1, pp. 79–86, 1997 (→ page 69).

- [115] K. J. Glaser and R. L. Ehman, “Perspectives on the development of elastography”, in *Magnetic Resonance Elastography*, S. K. Venkatesh and R. L. Ehman, Eds., New York: Springer, 2014, ch. 2, pp. 3–18 (→ page 2).
- [116] S. Goenezen, J.-F. Dord, Z. Sink, P. E. Barbone, J. Jiang, T. J. Hall, and A. A. Oberai, “Linear and nonlinear elastic modulus imaging: An application to breast cancer diagnosis”, *IEEE Transactions on Medical Imaging*, vol. 31, no. 8, pp. 1628–1637, 2012 (→ page 35).
- [117] O. Goksel, H. Eskandari, and S. E. Salcudean, “Mesh adaptation for improving elasticity reconstruction using the FEM inverse problem”, *Medical Imaging, IEEE Transactions on*, vol. 32, no. 2, pp. 408–418, 2013 (→ page 214).
- [118] A. Gomez, K. Pushparajah, J. M. Simpson, D. Giese, T. Schaeffter, and G. Penney, “A sensitivity analysis on 3D velocity reconstruction from multiple registered echo Doppler views”, *Medical Image Analysis*, vol. 17, no. 6, pp. 616–631, 2013 (→ pages 198, 219).
- [119] M. A. Green, G. Geng, E. Qin, R. Sinkus, S. C. Gandevia, and L. E. Bilston, “Measuring anisotropic muscle stiffness properties using elastography”, *NMR in Biomedicine*, vol. 26, no. 11, pp. 1387–1394, 2013 (→ page 34).
- [120] L. Guo, Y. Xu, Z. Xu, and J. Jiang, “A PDE-based regularization algorithm toward reducing speckle tracking noise: A feasibility study for ultrasound breast elastography”, *Ultrasonic Imaging*, pp. 1–17, 2014 (→ page 168).
- [121] X. Guo, A. Cheng, H. K. Zhang, H.-J. Kang, R. Etienne-Cummings, and E. M. Boctor, “Active echo: A new paradigm for ultrasound calibration”, in *Medical Image Computing and Computer-Assisted Intervention*, 2014, pp. 397–404 (→ page 61).
- [122] I. Hacihaliloglu, R. Abugharbieh, A. J. Hodgson, and R. N. Rohling, “Bone surface localization in ultrasound using image phase-based features”, *Ultrasound in Medicine & Biology*, vol. 35, no. 9, pp. 1475–1487, 2009 (→ page 155).
- [123] T. J. Hall, Y. Zhu, and C. S. Spalding, “In vivo real-time freehand palpation imaging”, *Ultrasound in Medicine & Biology*, vol. 29, no. 3, pp. 427–435, 2003 (→ page 42).
- [124] T. J. Hall, A. Milkowski, B. Garra, P. Carson, M. Palmeri, K. Nightingale, T. Lynch, A. Alturki, M. Andre, S. Audiere, *et al.*, “RSNA/QIBA: Shear wave speed as a biomarker for liver fibrosis staging”, in *IEEE International Ultrasonics Symposium*, 2013, pp. 397–400 (→ page 189).

- [125] H. H. G. Hansen, R. G. P. Lopata, T. Idzenga, and C. L. De Korte, “Full 2D displacement vector and strain tensor estimation for superficial tissue using beam-steered ultrasound imaging”, *Physics in Medicine and biology*, vol. 55, no. 11, pp. 3201–3218, 2010 (→ page 40).
- [126] H. H. G. Hansen, R. G. P. Lopata, and C. L. de Korte, “Noninvasive carotid strain imaging using angular compounding at large beam steered angles: Validation in vessel phantoms”, *IEEE Transactions on Medical Imaging*, vol. 28, no. 6, pp. 872–880, 2009 (→ page 198).
- [127] P. C. Hansen, V. Pereyra, and G. Scherer, *Least Squares Data Fitting with Applications*. Baltimore: The Johns Hopkins University Press, 2012 (→ pages 174, 188, 190).
- [128] P. A. Harris, R. Taylor, R. Thielke, J. Payne, N. Gonzalez, and J. G. Conde, “Research electronic data capture (REDCap)—a metadata-driven methodology and workflow process for providing translational research informatics support”, *Journal of biomedical informatics*, vol. 42, no. 2, pp. 377–381, 2009 (→ page 116).
- [129] A. Hartov, S. D. Eisner, W. Roberts, K. D. Paulsen, L. A. Platenik, and M. I. Miga, “Error analysis for a free-hand three-dimensional ultrasound system for neuronavigation”, *Neurosurgical Focus*, vol. 6, no. 3, E7–E21, 1999 (→ page 62).
- [130] I. A. Hein and W. D. O’Brien Jr, “Current time-domain methods for assessing tissue motion by analysis from reflected ultrasound echoes—A review”, *IEEE Transactions on Ultrasonics, Ferroelectrics and Frequency Control*, vol. 40, no. 2, pp. 84–102, 1993 (→ page 36).
- [131] A. H. Henni, C. Schmitt, and G. Cloutier, “Three-dimensional transient and harmonic shear-wave scattering by a soft cylinder for dynamic vascular elastography”, *The Journal of the Acoustical Society of America*, vol. 124, no. 4, pp. 2394–2405, 2008 (→ pages 165, 192).
- [132] M. Hladunewich, S. A. Karumanchi, and R. Lafayette, “Pathophysiology of the clinical manifestations of preeclampsia”, *Clinical Journal of the American Society of Nephrology*, vol. 2, no. 3, pp. 543–549, 2007 (→ page 114).
- [133] J. Holen, R. C. Waag, and R. Gramiak, “Representations of rapidly oscillating structures on the Doppler display”, *Ultrasound in medicine and biology*, vol. 11, no. 2, pp. 267–272, 1985 (→ page 41).

- [134] P. J. Hollender, S. J. Rosenzweig, K. R. Nightingale, and G. E. Trahey, “Single-and multiple-track-location shear wave and acoustic radiation force impulse imaging: Matched comparison of contrast, contrast-to-noise ratio and resolution”, *Ultrasound in medicine and biology*, vol. 41, no. 4, pp. 1043–1057, 2015 (→ page 51).
- [135] M. Honarvar, R. S. Sahebjavaher, S. E. Salcudean, and R. Rohling, “Sparsity regularization in dynamic elastography”, *Physics in Medicine and Biology*, vol. 57, no. 19, pp. 5909–5927, 2012 (→ pages 54, 111, 163, 176, 208, 214, 218).
- [136] M. Honarvar, R. Sahebjavaher, R. Sinkus, R. Rohling, and S. E. Salcudean, “Curl-based finite element reconstruction of the shear modulus without assuming local homogeneity: Time harmonic case”, *IEEE Transactions on Medical Imaging*, vol. 32, no. 12, pp. 2189–2199, 2013 (→ pages 54, 107, 111, 195, 218, 225).
- [137] M. Honarvar, J. Lobo, O. Mohareri, S. E. Salcudean, and R. Rohling, “Direct vibro-elastography FEM inversion in Cartesian and cylindrical coordinate systems without the local homogeneity assumption”, *Physics in medicine and biology*, vol. 60, no. 9, pp. 3847–3868, 2015 (→ pages 54, 111, 137, 175, 218, 219).
- [138] M. Honarvar, “Dynamic elastography with finite element-based inversion”, PhD thesis, University of British Columbia, 2015 (→ pages 52, 175, 176, 204, 214).
- [139] B. K. P. Horn, “Closed-form solution of absolute orientation using unit quaternions”, *Journal of the Optical Society of America A*, vol. 4, no. 4, pp. 629–642, 1987 (→ pages 147, 149, 150).
- [140] P. R. Hoskins, *Diagnostic Ultrasound: Physics and Equipment*, 2nd ed. New York: Cambridge University Press, 2010 (→ pages 10, 17, 22).
- [141] R. J. Housden, A. H. Gee, G. M. Treece, and R. W. Prager, “3-D ultrasonic strain imaging using freehand scanning and a mechanically-swept probe”, *IEEE Transactions on Ultrasonics, Ferroelectrics, and Frequency Control*, vol. 57, no. 2, pp. 501–506, 2010 (→ page 189).
- [142] P.-W. Hsu, G. M. Treece, R. W. Prager, N. E. Houghton, and A. H. Gee, “Comparison of freehand 3-D ultrasound calibration techniques using a stylus”, *Ultrasound in medicine and biology*, vol. 34, no. 10, pp. 1610–1621, 2008 (→ page 62).

- [143] P.-W. Hsu, R. W. Prager, A. H. Gee, and G. M. Treece, “Freehand 3D ultrasound calibration: A review”, in *Advanced imaging in biology and medicine*, C. W. Sensen and B. Hallgrímsson, Eds., Springer-Verlag, Berlin, 2008, ch. 3, pp. 47–84 (→ pages 5, 138).
- [144] S.-R. Huang, R. M. Lerner, and K. J. Parker, “On estimating the amplitude of harmonic vibration from the Doppler spectrum of reflected signals”, *The Journal of the Acoustical Society of America*, vol. 88, no. 6, pp. 2702–2712, 1990 (→ page 41).
- [145] L. Huwart, F. Peeters, R. Sinkus, L. Annet, N. Salameh, L. C. ter Beek, Y. Horsmans, and B. E. Van Beers, “Liver fibrosis: Non-invasive assessment with MR elastography”, *NMR in Biomedicine*, vol. 19, no. 2, pp. 173–179, 2006 (→ pages 2, 163).
- [146] M. F. Insana, C. Pellot-Barakat, M. Sridhar, and K. K. Lindfors, “Viscoelastic imaging of breast tumor microenvironment with ultrasound”, *Journal of mammary gland biology and neoplasia*, vol. 9, no. 4, pp. 393–404, 2004 (→ page 33).
- [147] A. Itoh, E. Ueno, E. Tohno, H. Kamma, H. Takahashi, T. Shiina, M. Yamakawa, and T. Matsumura, “Breast disease: Clinical application of US elastography for diagnosis”, *Radiology*, vol. 239, no. 2, pp. 341–350, 2006 (→ pages 2, 163).
- [148] J. A. Jensen, “Field: A program for simulating ultrasound systems”, in *10th Nordic-Baltic Conference on Biomedical Imaging Published in Medical and Biological Engineering and Computing*, vol. 34, 1996, pp. 351–353 (→ page 16).
- [149] J. A. Jensen and P. Munk, “A new method for estimation of velocity vectors”, *IEEE Transactions on Ultrasonics, Ferroelectrics, and Frequency Control*, vol. 45, no. 3, pp. 837–851, 1998 (→ page 40).
- [150] C. Jia, R. Olafsson, K. Kim, T. J. Kolias, J. M. Rubin, W. F. Weitzel, R. S. Witte, S.-W. Huang, M. S. Richards, C. X. Deng, and M. O’Donnell, “Two-dimensional strain imaging of controlled rabbit hearts”, *Ultrasound in Medicine and Biology*, vol. 35, no. 9, pp. 1488–1501, 2009 (→ page 198).
- [151] J. Jiang and T. J. Hall, “A generalized speckle tracking algorithm for ultrasonic strain imaging using dynamic programming”, *Ultrasound in Medicine and Biology*, vol. 35, no. 11, pp. 1863–1879, 2009 (→ page 167).

- [152] Y. Jiang, H. Fujiwara, and G. Nakamura, “Approximate steady state models for magnetic resonance elastography”, *SIAM Journal on Applied Mathematics*, vol. 71, no. 6, pp. 1965–1989, 2011 (→ page 194).
- [153] I. T. Jolliffe, *Principal Component Analysis*, 2nd. New York: Springer-Verlag, 2002 (→ page 149).
- [154] F. Kallel and M. Bertrand, “Tissue elasticity reconstruction using linear perturbation method”, *IEEE Transactions on Medical Imaging*, vol. 15, no. 3, pp. 299–313, 1996 (→ page 44).
- [155] F. Kallel and J. Ophir, “A least-squares strain estimator for elastography”, *Ultrasonic Imaging*, vol. 19, no. 3, pp. 195–208, 1997 (→ page 42).
- [156] F. Kallel, M. Bertrand, and J. Meunier, “Speckle motion artifact under tissue rotation”, *IEEE Transactions on Ultrasonics, Ferroelectrics, and Frequency Control*, vol. 41, no. 1, pp. 105–122, 1994 (→ page 36).
- [157] C. G. Kaplan, “Gross pathology of the placenta: Weight, shape, size, colour”, *Journal of Clinical Pathology*, vol. 61, no. 12, pp. 1285–1295, 2008 (→ page 118).
- [158] C. Kasai, K. Namekawa, A. Koyano, and R. Omoto, “Real-time two-dimensional blood flow imaging using an autocorrelation technique”, *IEEE Transactions on Sonics and Ultrasonics*, vol. 32, no. 3, pp. 458–464, 1985 (→ page 26).
- [159] F. Kılıç, Y. Kayadibi, M. A. Yüksel, İ. Adaletli, F. E. Ustabaşioğlu, M. Öncül, R. Madazlı, M. H. Yılmaz, İ. Mihmanlı, and F. Kantarcı, “Shear wave elastography of placenta: In vivo quantitation of placental elasticity in preeclampsia”, *Diagnostic and Interventional Radiology*, vol. 21, pp. 202–207, 2015 (→ pages 115, 131, 132, 218).
- [160] R. J. Kingma, “Novel stand-off pads for Ultrasound-CT registration and elastography”, Master’s thesis, University of British Columbia, 2012 (→ page 46).
- [161] L. E. Kinsler, A. R. Frey, A. B. Coppens, and J. V. Sanders, *Fundamentals of Acoustics*, 4th ed. New York: Wiley, 2000 (→ pages 10, 32).
- [162] D. Klatt, U. Hamhaber, P. Asbach, J. Braun, and I. Sack, “Noninvasive assessment of the rheological behavior of human organs using multifrequency MR elastography: A study of brain and liver viscoelasticity”, *Physics in Medicine and Biology*, vol. 52, no. 24, pp. 7281–7294, 2007 (→ pages 34, 115, 133, 168, 194, 195).

- [163] H. Knutsson, C.-F. Westin, and G. Granlund, “Local multiscale frequency and bandwidth estimation”, in *IEEE International Conference on Image Processing*, vol. 1, 1994, pp. 36–40 (→ pages 54, 87).
- [164] H. Kolsky, *Stress Waves in Solids*. Oxford: Clarendon Press, 1953 (→ pages 32, 78).
- [165] E. E. Konofagou and J. Ophir, “Precision estimation and imaging of normal and shear components of the 3D strain tensor in elastography”, *Physics in Medicine and Biology*, vol. 45, no. 6, pp. 1553–1563, 2000 (→ page 40).
- [166] E. E. Konofagou, T. Varghese, and J. Ophir, “Theoretical bounds on the estimation of transverse displacement, transverse strain and poisson’s ratio in elastography”, *Ultrasonic Imaging*, vol. 22, no. 3, pp. 153–177, 2000 (→ page 191).
- [167] S. Korukonda and M. M. Doyley, “Estimating axial and lateral strain using a synthetic aperture elastographic imaging system”, *Ultrasound in Medicine and Biology*, vol. 37, no. 11, pp. 1893–1908, 2011 (→ pages 5, 40, 167, 197).
- [168] J. Kowal, C. A. Amstutz, M. Caversaccio, and L. P. Nolte, “On the development and comparative evaluation of an ultrasound B-mode probe calibration method”, *Computer Aided Surgery*, vol. 8, no. 3, pp. 107–119, 2003 (→ page 62).
- [169] F. W. Kremkau, “Doppler principles”, *Seminars in Roentgenology*, vol. 27, no. 1, pp. 6–16, 1992 (→ page 23).
- [170] O. D. Kripfgans, J. M. Rubin, A. L. Hall, and J. B. Fowlkes, “Vector Doppler imaging of a spinning disc ultrasound Doppler phantom”, *Ultrasound in Medicine & Biology*, vol. 32, no. 7, pp. 1037–1046, 2006 (→ page 40).
- [171] T. A. Krouskop, T. M. Wheeler, F. Kallel, B. S. Garra, and T. Hall, “Elastic moduli of breast and prostate tissues under compression”, *Ultrasonic imaging*, vol. 20, no. 4, pp. 260–274, 1998 (→ page 35).
- [172] J. F. Krücker, C. R. Meyer, G. L. LeCarpentier, J. B. Fowlkes, and P. L. Carson, “3D spatial compounding of ultrasound images using image-based nonrigid registration.”, *Ultrasound in Medicine & Biology*, vol. 26, no. 9, pp. 1475–1488, 2000 (→ page 137).

- [173] S. A. Kruse, J. A. Smith, A. J. Lawrence, M. A. Dresner, A. Manduca, J. F. Greenleaf, and R. L. Ehman, “Tissue characterization using magnetic resonance elastography: Preliminary results”, *Physics in Medicine and Biology*, vol. 45, no. 6, pp. 1579–1590, 2000 (→ pages 33, 78).
- [174] J. J. Kuffner, “Effective sampling and distance metrics for 3D rigid body path planning”, in *IEEE International Conference on Robotics and Automation*, vol. 4, 2004, pp. 3993–3998 (→ page 208).
- [175] A. Lang, V. Parthasarathy, and A. Jain, “Calibration of 3D ultrasound to an electromagnetic tracking system”, in *Proceedings of SPIE*, vol. 7968, 2011, 79680W (→ page 138).
- [176] T. Lange and S. Eulenstein, “Calibration of swept-volume 3-D ultrasound”, in *Medical Image Understanding and Analysis*, 2002, pp. 29–32 (→ pages 62, 160).
- [177] T. Lange, S. Kraft, S. Eulenstein, H. Lamecker, and P. M. Schlag, “Automatic calibration of 3D ultrasound probes”, in *Bildverarbeitung für die Medizin*, 2011, pp. 169–173 (→ pages 138, 148).
- [178] A. Lasso, T. Heffter, A. Rankin, C. Pinter, T. Ungi, and G. Fichtinger, “Plus: Open-source toolkit for ultrasound-guided intervention systems”, *IEEE Transactions on Biomedical Engineering*, vol. 61, no. 10, pp. 2527–2537, 2014 (→ page 224).
- [179] J. S. Lau, S. N. Saw, M. L. Buist, A. Biswas, C. N. Z. Mattar, and C. H. Yap, “Mechanical testing and non-linear viscoelastic modelling of the human placenta in normal and growth restricted pregnancies”, *Journal of Biomechanics*, 2015 (→ page 115).
- [180] G. E. Leclerc, F. Charleux, L. Robert, M.-C. Ho Ba Tho, C. Rhein, J.-P. Latrive, and S. F. Bensamoun, “Analysis of liver viscosity behavior as a function of multifrequency magnetic resonance elastography (MMRE) postprocessing”, *Journal of Magnetic Resonance Imaging*, vol. 38, no. 2, pp. 422–428, 2013 (→ page 54).
- [181] W.-N. Lee, M. Pernot, M. Couade, E. Messas, P. Bruneval, A. Bel, A. Hagége, M. Fink, and M. Tanter, “Mapping myocardial fiber orientation using echocardiography-based shear wave imaging”, *IEEE Transactions on Medical Imaging*, vol. 31, no. 3, pp. 554–562, 2012 (→ page 34).
- [182] D. F. Leotta, P. R. Detmer, and R. W. Martin, “Performance of a miniature magnetic position sensor for three-dimensional ultrasound imaging”, *Ultrasound in Medicine & Biology*, vol. 23, no. 4, pp. 597–609, 1997 (→ pages 61, 138).

- [183] R. M. Lerner, S. R. Huang, and K. J. Parker, ““Sonoelasticity” images derived from ultrasound signals in mechanically vibrated tissues”, *Ultrasound in medicine and biology*, vol. 16, no. 3, pp. 231–239, 1990 (→ page 46).
- [184] S. F. Levinson, M. Shinagawa, and T. Sato, “Sonoelastic determination of human skeletal muscle elasticity”, *Journal of biomechanics*, vol. 28, no. 10, pp. 1145–1154, 1995 (→ page 54).
- [185] W. J. Li, Z. T. Wei, R. L. Yan, and Y. L. Zhang, “Detection of placenta elasticity modulus by quantitative real-time shear wave imaging”, *Clinical and Experimental Obstetrics and Gynecology*, vol. 39, no. 4, pp. 470–473, 2012 (→ pages 115, 131, 132, 218).
- [186] H. Liebgott, A. Basarab, P. Gueth, D. Friboulet, and P. Delachartre, “Transverse oscillations for tissue motion estimation”, *Ultrasonics*, vol. 50, no. 6, pp. 548–555, 2010 (→ pages 40, 167, 223).
- [187] J. E. Lindop, G. M. Treece, A. H. Gee, and R. W. Prager, “3D elastography using freehand ultrasound”, *Ultrasound in Medicine and Biology*, vol. 32, no. 4, pp. 529–545, 2006 (→ pages 5, 167, 197).
- [188] ———, “Estimation of displacement location for enhanced strain imaging”, *IEEE Transactions on Ultrasonics, Ferroelectrics, and Frequency Control*, vol. 54, no. 9, pp. 1751–1771, 2007 (→ page 43).
- [189] F. Lindseth, T. Langø, J. Bang, and T. A. N. Hernes, “Accuracy evaluation of a 3D ultrasound-based neuronavigation system”, *Computer Aided Surgery*, vol. 7, no. 4, pp. 197–222, 2002 (→ page 138).
- [190] F. Lindseth, G. A. Tangen, T. Langø, and J. Bang, “Probe calibration for freehand 3-D ultrasound”, *Ultrasound in medicine and biology*, vol. 29, no. 11, pp. 1607–1623, 2003 (→ page 62).
- [191] J. Lobo, A. Baghani, H. Eskandari, S. Mahdavi, R. Rohling, L. Goldernberg, W. J. Morris, and S. Salcudean, “Prostate vibro-elastography: Multi-frequency 1D over 3D steady-state shear wave imaging for quantitative elastic modulus measurement”, in *IEEE International Ultrasonics Symposium*, 2015, pp. 1–4 (→ pages 71, 134, 217).
- [192] J. Loncaric, “Smooth invariant interpolation of rotations”, PhD thesis, Harvard University, 1985 (→ page 283).

- [193] R. G. P. Lopata, M. M. Nillesen, I. H. Gerrits, J. M. Thijssen, L. Kapusta, and C. L. de Korte, “4D cardiac strain imaging: Methods and initial results”, in *IEEE Ultrasonics Symposium*, 2007, pp. 872–875 (→ page 165).
- [194] T. Loupas, J. T. Powers, and R. W. Gill, “An axial velocity estimator for ultrasound blood flow imaging, based on a full evaluation of the Doppler equation by means of a two-dimensional autocorrelation approach”, *IEEE Transactions on Ultrasonics, Ferroelectrics, and Frequency Control*, vol. 42, no. 4, pp. 672–688, 1995 (→ pages 28, 38).
- [195] M. A. Lubinski, S. Y. Emelianov, K. R. Raghavan, A. E. Yagle, A. R. Skovoroda, and M. O’Donnell, “Lateral displacement estimation using tissue incompressibility”, *IEEE Transactions on Ultrasonics, Ferroelectrics, and Frequency Control*, vol. 43, no. 2, pp. 247–256, 1996 (→ pages 40, 168).
- [196] M. Lubinski, S. Y. Emelianov, and M. O’Donnell, “Speckle tracking methods for ultrasonic elasticity imaging using short-time correlation”, *IEEE Transactions on Ultrasonics, Ferroelectrics, and Frequency Control*, vol. 46, no. 1, pp. 82–96, 1999 (→ page 38).
- [197] V. Macellari, “Costel: A computer peripheral remote sensing device for 3-dimensional monitoring of human motion”, *Medical and Biological Engineering and Computing*, vol. 21, no. 3, pp. 311–318, 1983 (→ page 67).
- [198] J. E. MacSweeney, D. O. Cosgrove, and J. Arenson, “Colour Doppler energy (power) mode ultrasound”, *Clinical radiology*, vol. 51, no. 6, pp. 387–390, 1996 (→ page 29).
- [199] A. Manduca, T. E. Oliphant, M. A. Dresner, J. L. Mahowald, S. A. Kruse, E. Amromin, J. P. Felmlee, J. F. Greenleaf, and R. L. Ehman, “Magnetic resonance elastography: Non-invasive mapping of tissue elasticity”, *Medical Image Analysis*, vol. 5, no. 4, pp. 237–254, 2001 (→ pages 54, 55, 107, 118, 166, 175, 189).
- [200] A. Manduca, D. S. Lake, S. Kruse, and R. L. Ehman, “Spatio-temporal directional filtering for improved inversion of MR elastography images”, *Medical image analysis*, vol. 7, no. 4, pp. 465–473, 2003 (→ pages 55, 87, 168, 219).

- [201] T. Matsumura, R. Shinomura, T. Mitake, H. Kanda, M. Yamakawa, and T. Shiina, “Estimation of pressure-distribution effects upon elasticity imaging”, in *IEEE Ultrasonics Symposium*, vol. 3, 2005, pp. 1759–1762 (→ page 46).
- [202] R. L. Maurice and M. Bertrand, “Lagrangian speckle model and tissue-motion estimation-theory”, *IEEE Transactions on Medical Imaging*, vol. 18, no. 7, pp. 593–603, 1999 (→ page 38).
- [203] S. A. McAleavey, M. Menon, and J. Orszulak, “Shear-modulus estimation by application of spatially-modulated impulsive acoustic radiation force”, *Ultrasonic imaging*, vol. 29, no. 2, pp. 87–104, 2007 (→ page 52).
- [204] K. P. McGee, D. Lake, Y. Mariappan, R. D. Hubmayr, A. Manduca, K. Ansell, and R. L. Ehman, “Calculation of shear stiffness in noise dominated magnetic resonance elastography data based on principal frequency estimation”, *Physics in medicine and biology*, vol. 56, no. 14, pp. 4291–4309, 2011 (→ page 55).
- [205] D. C. Mellema, P. Song, A. Manduca, M. W. Urban, R. R. Kinnick, J. F. Greenleaf, and S. Chen, “A high frame-rate and low-cost elastography system by generating shear waves through continuous vibration of the ultrasound transducer”, in *IEEE International Ultrasonics Symposium*, 2015, pp. 1–4 (→ pages 53, 70).
- [206] L. Mercier, T. Langø, F. Lindseth, and L. D. Collins, “A review of calibration techniques for freehand 3-D ultrasound systems”, *Ultrasound in Medicine & Biology*, vol. 31, no. 4, pp. 449–471, 2005 (→ pages 5, 138).
- [207] J. Meunier and M. Bertrand, “Ultrasonic speckle motion inherent to tissue motion: Theory and simulation”, in *IEEE Ultrasonics Symposium*, 1989, pp. 865–868 (→ page 36).
- [208] O. V. Michailovich and A. Tannenbaum, “Despeckling of medical ultrasound images”, *IEEE Transactions on Ultrasonics, Ferroelectrics, and Frequency Control*, vol. 53, no. 1, pp. 64–78, 2006 (→ page 11).
- [209] G. F. Miller and H. Pursey, “The field and radiation impedance of mechanical radiators on the free surface of a semi-infinite isotropic solid”, in *Proceedings of the Royal Society of London A: Mathematical, Physical and Engineering Sciences*, vol. 223, 1954, pp. 521–541 (→ page 78).

- [210] M. Moradi, S. S. Mahdavi, G. Nir, O. Mohareri, A. Koupparis, L.-O. Gagnon, L. Fazli, R. G. Casey, J. Ischia, E. C. Jones, S. L. Goldenerg, and S. E. Salcudean, “Multiparametric 3D in vivo ultrasound vibroelastography imaging of prostate cancer: Preliminary results”, *Medical physics*, vol. 41, no. 7, 073505–1–073505–12, 2014 (→ page 48).
- [211] M. Muller, J.-L. Gennisson, T. Deffieux, R. Sinkus, P. Annic, G. Montaldo, M. Tanter, and M. Fink, “Full 3D inversion of the viscoelasticity wave propagation problem for 3D ultrasound elastography in breast cancer diagnosis”, in *IEEE Ultrasonics Symposium*, 2007, pp. 672–675 (→ pages 5, 40, 166, 193, 199, 216, 219).
- [212] D. M. Muratore and R. L. Galloway, “Beam calibration without a phantom for creating a 3-D freehand ultrasound system”, *Ultrasound in medicine and biology*, vol. 27, no. 11, pp. 1557–1566, 2001 (→ page 62).
- [213] K. J. Murphy and J. M. Rubin, “Power Doppler: It’s a good thing”, in *Seminars in Ultrasound, CT and MRI*, vol. 18, 1997, pp. 13–21 (→ page 29).
- [214] R. Muthupillai, D. J. Lomas, P. J. Rossman, J. F. Greenleaf, A. Manduca, and R. L. Ehman, “Magnetic resonance elastography by direct visualization of propagating acoustic strain waves”, *Science*, vol. 269, no. 5232, pp. 1854–1857, 1995 (→ pages 52, 54, 70).
- [215] M. Najafi, N. Afsham, P. Abolmaesumi, and R. Rohling, “A closed-form differential formulation for ultrasound spatial calibration”, in *Information Processing in Computer-Assisted Interventions*, 2012, pp. 44–53 (→ pages 139, 148, 151, 155, 220).
- [216] M. Najafi, N. Afsham, P. Abolmaesumi, and R. Rohling, “Single wall closed-form differential ultrasound calibration”, in *Proceedings of SPIE*, vol. 8316, 2012, 83162A (→ page 149).
- [217] ———, “A closed-form differential formulation for ultrasound spatial calibration: Single wall phantom”, *Ultrasound in medicine and biology*, vol. 41, no. 4, pp. 1079–1094, 2015 (→ page 62).
- [218] M. Najafi, P. Abolmaesumi, and R. Rohling, “Single-camera closed-form real-time needle tracking for ultrasound-guided needle insertion”, *Ultrasound in medicine and biology*, vol. 41, no. 10, pp. 2663–2676, 2015 (→ page 60).

- [219] T. R. Nelson and T. T. Elvins, “Visualization of 3D ultrasound data”, *IEEE Computer Graphics and Applications*, vol. 13, no. 6, pp. 50–57, 1993 (→ pages 4, 136).
- [220] T. R. Nelson and D. H. Pretorius, “Three-dimensional ultrasound imaging”, *Ultrasound in Medicine and Biology*, vol. 24, no. 9, pp. 1243–1270, 1998 (→ page 164).
- [221] K. Nightingale, S. McAleavey, and G. Trahey, “Shear-wave generation using acoustic radiation force: In vivo and ex vivo results”, *Ultrasound in medicine and biology*, vol. 29, no. 12, pp. 1715–1723, 2003 (→ page 50).
- [222] K. R. Nightingale, M. L. Palmeri, R. W. Nightingale, and G. E. Trahey, “On the feasibility of remote palpation using acoustic radiation force”, *The Journal of the Acoustical Society of America*, vol. 110, no. 1, pp. 625–634, 2001 (→ pages 47, 70).
- [223] K. Nightingale, “Acoustic radiation force impulse (ARFI) imaging: A review”, *Current medical imaging reviews*, vol. 7, no. 4, pp. 328–339, 2011 (→ pages 49, 50).
- [224] C. P. Oates, “Towards an ideal blood analogue for Doppler ultrasound phantoms”, *Physics in Medicine and Biology*, vol. 36, no. 11, pp. 1433–1442, 1991 (→ page 141).
- [225] A. A. Oberai, N. H. Gokhale, M. M. Doyley, and J. C. Bamber, “Evaluation of the adjoint equation based algorithm for elasticity imaging”, *Physics in Medicine and Biology*, vol. 49, no. 13, pp. 2955–2974, 2004 (→ page 45).
- [226] M. O’Donnell, A. R. Skovoroda, B. M. Shapo, and S. Y. Emelianov, “Internal displacement and strain imaging using ultrasonic speckle tracking”, *IEEE Transactions on Ultrasonics, Ferroelectrics, and Frequency Control*, vol. 41, no. 3, pp. 314–325, 1994 (→ page 38).
- [227] H. L. Oestreicher, “Field and impedance of an oscillating sphere in a viscoelastic medium with an application to biophysics”, *The Journal of the Acoustical Society of America*, vol. 23, no. 6, pp. 707–714, 1951 (→ page 120).
- [228] J. J. O’Hagan and A. Samani, “Measurement of the hyperelastic properties of 44 pathological ex vivo breast tissue samples”, *Physics in Medicine and Biology*, vol. 54, no. 8, pp. 2557–2569, 2009 (→ page 35).

- [229] T. Ohmaru, Y. Fujita, M. Sugitani, M. Shimokawa, K. Fukushima, and K. Kato, “Placental elasticity evaluation using virtual touch tissue quantification during pregnancy”, *Placenta*, vol. 36, no. 8, pp. 915–920, 2015 (→ pages 115, 118, 132, 218).
- [230] T. E. Oliphant, R. R. Kinnick, A. Manduca, R. L. Ehman, and J. E. Greenleaf, “An error analysis of Helmholtz inversion for incompressible shear, vibration elastography with application to filter-design for tissue characterization”, in *IEEE Ultrasonics Symposium*, vol. 2, 2000, pp. 1795–1798 (→ pages 54, 87).
- [231] T. E. Oliphant, A. Manduca, R. L. Ehman, and J. F. Greenleaf, “Complex-valued stiffness reconstruction for magnetic resonance elastography by algebraic inversion of the differential equation”, *Magnetic Resonance in Medicine*, vol. 45, no. 2, pp. 299–310, 2001 (→ pages 53, 167).
- [232] T. E. Oliphant, “Direct methods for dynamic elastography reconstruction: Optimal inversion of the interior Helmholtz problem”, PhD thesis, Mayo Graduate School, 2001 (→ page 30).
- [233] J. Ophir, I. Cespedes, Y. Ponnekanti, Y. Yazdi, and X. Li, “Elastography: A quantitative method for imaging the elasticity of biological tissues”, *Ultrasonic Imaging*, vol. 13, no. 2, pp. 111–134, 1991 (→ page 42).
- [234] J. Ophir, I. Cespedes, B. Garra, H. Ponnekanti, Y. Huang, and N. Maklad, “Elastography: Ultrasonic imaging of tissue strain and elastic modulus in vivo”, *European Journal of Ultrasound*, vol. 3, no. 1, pp. 49–70, 1996 (→ page 43).
- [235] J. Ophir, S. Alam, B. Garra, F. Kallel, E. Konofagou, T. Krouskop, and T. Varghese, “Elastography: Ultrasonic estimation and imaging of the elastic properties of tissues”, *Proceedings of the Institution of Mechanical Engineers, Part H: Journal of Engineering in Medicine*, vol. 213, no. 3, pp. 203–233, 1999 (→ page 43).
- [236] J. Ophir, S. K. Alam, B. S. Garra, F. Kallel, E. E. Konofagou, T. Krouskop, C. R. B. Merritt, R. Righetti, R. Souchon, S. Srinivasan, and T. Varghese, “Elastography: Imaging the elastic properties of soft tissues with ultrasound”, *Journal of Medical Ultrasonics*, vol. 29, no. 4, pp. 155–171, 2002 (→ page 163).

- [237] D. F. Pace, A. D. Wiles, J. Moore, C. Wedlake, D. G. Gobbi, and T. M. Peters, “Validation of four-dimensional ultrasound for targeting in minimally-invasive beating-heart surgery”, in *Proceedings of SPIE*, vol. 7261, 2009, p. 726 115 (→ page 137).
- [238] N. Pagoulatos, D. R. Haynor, and Y. Kim, “A fast calibration method for 3-D tracking of ultrasound images using a spatial localizer”, *Ultrasound in Medicine & Biology*, vol. 27, no. 9, pp. 1219–1229, 2001 (→ pages 62, 140).
- [239] L. Pallwein, M. Mitterberger, P. Struve, W. Horninger, F. Aigner, G. Bartsch, J. Gradl, M. Schurich, F. Pedross, and F. Frauscher, “Comparison of sonoelastography guided biopsy with systematic biopsy: Impact on prostate cancer detection”, *European radiology*, vol. 17, no. 9, pp. 2278–2285, 2007 (→ pages 2, 163).
- [240] M. L. Palmeri and K. R. Nightingale, “On the thermal effects associated with radiation force imaging of soft tissue”, *IEEE Transactions on Ultrasonics, Ferroelectrics, and Frequency Control*, vol. 51, no. 5, pp. 551–565, 2004 (→ page 70).
- [241] M. L. Palmeri, M. H. Wang, J. J. Dahl, K. D. Frinkley, and K. R. Nightingale, “Quantifying hepatic shear modulus in vivo using acoustic radiation force”, *Ultrasound in medicine and biology*, vol. 34, no. 4, pp. 546–558, 2008 (→ page 50).
- [242] S. Papazoglou, S. Hirsch, J. Braun, and I. Sack, “Multifrequency inversion in magnetic resonance elastography”, *Physics in Medicine and Biology*, vol. 57, no. 8, pp. 2329–2346, 2012 (→ page 195).
- [243] E. Park and A. M. Maniatty, “Shear modulus reconstruction in dynamic elastography: Time harmonic case”, *Physics in medicine and biology*, vol. 51, no. 15, pp. 3697–3721, 2006 (→ pages 54, 168).
- [244] F. C. Park, “Distance metrics on the rigid-body motions with applications to mechanism design”, *Journal of Mechanical Design*, vol. 117, no. 1, pp. 48–54, 1995 (→ page 283).
- [245] F. C. Park and B. Ravani, “Smooth invariant interpolation of rotations”, *ACM Transactions on Graphics*, vol. 16, no. 3, pp. 277–295, 1997 (→ page 152).
- [246] K. J. Parker, “A microchannel flow model for soft tissue elasticity”, *Physics in medicine and biology*, vol. 59, no. 15, pp. 4443–4457, 2014 (→ page 134).

- [247] K. Pathak, A. Birk, N. Vaškevičius, and J. Poppinga, “Fast registration based on noisy planes with unknown correspondences for 3-D mapping”, *IEEE Transactions on Robotics*, vol. 26, no. 3, pp. 424–441, 2010 (→ page 147).
- [248] C. Pellot-Barakat, F. Frouin, M. F. Insana, and A. Herment, “Ultrasound elastography based on multiscale estimations of regularized displacement fields”, *IEEE Transactions on Medical Imaging*, vol. 23, no. 2, pp. 153–163, 2004 (→ page 167).
- [249] O. Péria, L. Chevalier, A. François-Joubert, J.-P. Caravel, S. Dalsoglio, S. Lavallée, and P. Cinquin, “Using a 3D position sensor for registration of SPECT and US images of the kidney”, in *Computer vision, virtual reality and robotics in medicine*, 1995, pp. 23–29 (→ page 62).
- [250] M. Pernot, K. Fujikura, S. D. Fung-Kee-Fung, and E. E. Konofagou, “ECG-gated, mechanical and electromechanical wave imaging of cardiovascular tissues in vivo”, *Ultrasound in Medicine and Biology*, vol. 33, no. 7, pp. 1075–1085, 2007 (→ pages 165, 192, 194).
- [251] A. Pesavento, C. Perrey, M. Krueger, and H. Ermert, “A time-efficient and accurate strain estimation concept for ultrasonic elastography using iterative phase zero estimation”, *IEEE Transactions on Ultrasonics, Ferroelectrics, and Frequency Control*, vol. 46, no. 5, pp. 1057–1067, 1999 (→ page 38).
- [252] Y. Petrank, L. Huang, and M. O’Donnell, “Reduced peak-hopping artifacts in ultrasonic strain estimation using the Viterbi algorithm”, *IEEE Transactions on Ultrasonics, Ferroelectrics, and Frequency Control*, vol. 56, no. 7, pp. 1359–1367, 2009 (→ page 37).
- [253] G. F. Pinton and G. E. Trahey, “Continuous delay estimation with polynomial splines”, *IEEE Transactions on Ultrasonics, Ferroelectrics, and Frequency Control*, vol. 53, no. 11, pp. 2026–2035, 2006 (→ pages 37, 39).
- [254] G. F. Pinton, J. J. Dahl, and G. E. Trahey, “Rapid tracking of small displacements with ultrasound”, *IEEE Transactions on Ultrasonics, Ferroelectrics, and Frequency Control*, vol. 53, no. 6, pp. 1103–1117, 2006 (→ pages 38, 47, 91, 164).
- [255] D. B. Plewes, J. Bishop, A. Samani, and J. Sciarretta, “Visualization and quantification of breast cancer biomechanical properties with magnetic resonance elastography”, *Physics in medicine and biology*, vol. 45, no. 6, pp. 1591–1610, 2000 (→ page 45).

- [256] H. Ponnekanti, J. Ophir, and I. Cespedes, “Ultrasonic imaging of the stress distribution in elastic media due to an external compressor”, *Ultrasound in medicine and biology*, vol. 20, no. 1, pp. 27–33, 1994 (→ page 43).
- [257] H. Ponnekanti, J. Ophir, Y. Huang, and I. Céspedes, “Fundamental mechanical limitations on the visualization of elasticity contrast in elastography”, *Ultrasound in medicine and biology*, vol. 21, no. 4, pp. 533–543, 1995 (→ page 180).
- [258] T. C. Poon and R. N. Rohling, “Tracking a 3-D ultrasound probe with constantly visible fiducials”, *Ultrasound in Medicine & Biology*, vol. 33, no. 1, pp. 152–157, 2007 (→ pages 138, 155, 160, 218).
- [259] T. C. Poon and R. N. Rohling, “Comparison of calibration methods for spatial tracking of a 3-D ultrasound probe”, *Ultrasound in Medicine & Biology*, vol. 31, no. 8, pp. 1095–1108, 2005 (→ pages 63, 138, 148, 160).
- [260] E. R. Pospisil, R. Rohling, R. Zahiri-Azar, and S. E. Salcudean, “4-D x 3-D ultrasound: Real-time scan conversion, filtering, and display of displacement vectors with a motorized curvilinear transducer”, *IEEE Transactions on Ultrasonics, Ferroelectrics and Frequency Control*, vol. 57, no. 10, pp. 2271–2283, 2010 (→ pages 136, 169, 174, 191).
- [261] J. Powers and F. Kremkau, “Medical ultrasound systems”, *Interface focus*, vol. 1, no. 4, pp. 477–489, 2011 (→ page 28).
- [262] R. W. Prager, R. N. Rohling, A. H. Gee, and L. Berman, “Rapid calibration for 3-D freehand ultrasound.”, *Ultrasound in Medicine & Biology*, vol. 24, no. 6, pp. 855–869, 1998 (→ pages 61, 138, 140, 149).
- [263] J. L. Prince and J. M. Links, *Medical imaging signals and systems*. Upper Saddle River, NJ: Pearson Prentice Hall, 2006 (→ page 1).
- [264] J. Provost, C. Papadacci, J. E. Arango, M. Imbault, M. Fink, J.-L. Gennisson, M. Tanter, and M. Pernot, “3D ultrafast ultrasound imaging in vivo”, *Physics in Medicine and Biology*, vol. 59, no. 19, pp. L1–L13, 2014 (→ page 166).
- [265] Y. Qiu, M. Sridhar, J. K. Tsou, K. K. Lindfors, and M. F. Insana, “Ultrasonic viscoelasticity imaging of nonpalpable breast tumors: Preliminary results”, *Academic radiology*, vol. 15, no. 12, pp. 1526–1533, 2008 (→ page 44).
- [266] F. H. Raab, E. B. Blood, T. O. Steiner, and H. R. Jones, “Magnetic position and orientation tracking system”, *IEEE Transactions on Aerospace and Electronic Systems*, no. 5, pp. 709–718, 1979 (→ page 67).

- [267] M. Rao, H. Shi, and T. Varghese, “Spatial-angular compounding for elastography using beam steering on linear array transducers”, *Medical Physics*, vol. 33, no. 3, pp. 618–627, 2006 (→ pages 167, 198).
- [268] M. Rao, Q. Chen, H. Shi, T. Varghese, E. L. Madsen, J. A. Zagzebski, and T. A. Wilson, “Normal and shear strain estimation using beam steering on linear-array transducers”, *Ultrasound in Medicine and Biology*, vol. 33, no. 1, pp. 57–66, 2007 (→ page 40).
- [269] M. S. Richards, P. E. Barbone, and A. A. Oberai, “Quantitative three-dimensional elasticity imaging from quasi-static deformation: A phantom study”, *Physics in Medicine and Biology*, vol. 54, no. 3, pp. 757–779, 2009 (→ pages 168, 191).
- [270] R. Righetti, J. Ophir, and P. Ktonas, “Axial resolution in elastography”, *Ultrasound in Medicine and Biology*, vol. 28, no. 1, pp. 101–113, 2002 (→ pages 37, 167).
- [271] R. Righetti, M. Righetti, J. Ophir, and T. A. Krouskop, “The feasibility of estimating and imaging the mechanical behavior of poroelastic materials using axial strain elastography”, *Physics in medicine and biology*, vol. 52, no. 11, pp. 3241–3259, 2007 (→ page 44).
- [272] H. Rivaz, E. M. Boctor, M. A. Choti, and G. D. Hager, “Real-time regularized ultrasound elastography”, *IEEE Transactions on Medical Imaging*, vol. 30, no. 4, pp. 928–945, 2011 (→ page 167).
- [273] A. Romano, M. Scheel, S. Hirsch, J. Braun, and I. Sack, “In vivo waveguide elastography of white matter tracts in the human brain”, *Magnetic Resonance in Medicine*, vol. 68, no. 5, pp. 1410–1422, 2012 (→ page 34).
- [274] A. J. Romano, J. J. Shirron, J. Bucaro, *et al.*, “On the noninvasive determination of material parameters from a knowledge of elastic displacements theory and numerical simulation”, *IEEE Transactions on Ultrasonics, Ferroelectrics, and Frequency Control*, vol. 45, no. 3, pp. 751–759, 1998 (→ page 53).
- [275] F. Rousseau, P. Hellier, and C. Barillot, “Robust and automatic calibration method for 3D freehand ultrasound”, in *Medical Image Computing and Computer-Assisted Intervention*, 2003, pp. 440–448 (→ pages 61, 138).
- [276] H. F. Routh, “Doppler ultrasound”, *IEEE Engineering in Medicine and Biology*, vol. 15, no. 6, pp. 31–40, 1996 (→ page 24).

- [277] J. M. Rubin, R. O. Bude, P. L. Carson, R. L. Bree, and R. S. Adler, “Power Doppler US: A potentially useful alternative to mean frequency-based color Doppler US”, *Radiology*, vol. 190, no. 3, pp. 853–856, 1994 (→ page 29).
- [278] R. S. Sahebjavaher, A. Baghani, M. Honarvar, R. Sinkus, and S. E. Salcudean, “Transperineal prostate MR elastography: Initial in vivo results”, *Magnetic Resonance in Medicine*, vol. 69, no. 2, pp. 411–420, 2013 (→ page 52).
- [279] R. S. Sahebjavaher, S. Frew, A. Bylinskii, L. Beek, P. Garteiser, M. Honarvar, R. Sinkus, and S. Salcudean, “Prostate MR elastography with transperineal electromagnetic actuation and a fast fractionally encoded steady-state gradient echo sequence”, *NMR in Biomedicine*, vol. 27, no. 7, pp. 784–794, 2014 (→ page 208).
- [280] S. Saitoh, M. Izumi, and Y. Mine, “A dual frequency ultrasonic probe for medical applications”, *IEEE Transactions on Ultrasonics, Ferroelectrics, and Frequency Control*, vol. 42, no. 2, pp. 294–300, 1995 (→ page 24).
- [281] S. E. Salcudean, D. French, S. Bachmann, R. Zahiri-Azar, X. Wen, and W. J. Morris, “Viscoelasticity modeling of the prostate region using vibro-elastography”, in *Medical Image Computing and Computer-Assisted Intervention*, 2006, pp. 389–396 (→ pages 48, 194).
- [282] S. E. Salcudean, R. Sahebjavaher, O. Goksel, A. Baghani, S. Mahdavi, G. Nir, R. Sinkus, and M. Moradi, “Biomechanical modeling of the prostate for procedure guidance and simulation”, in *Soft Tissue Biomechanical Modeling for Computer Assisted Surgery*, 2012, pp. 169–198 (→ pages 2, 163).
- [283] L. Sandrin, M. Tanter, J. L. Gennisson, S. Catheline, and M. Fink, “Shear elasticity probe for soft tissues with 1-D transient elastography”, *IEEE Transactions on Ultrasonics, Ferroelectrics, and Frequency Control*, vol. 49, no. 4, pp. 436–446, 2002 (→ pages 49, 193).
- [284] L. Sandrin, M. Tanter, S. Catheline, and M. Fink, “Shear modulus imaging with 2-D transient elastography”, *IEEE Transactions on Ultrasonics, Ferroelectrics, and Frequency Control*, vol. 49, no. 4, pp. 426–435, 2002 (→ page 50).
- [285] S. Sankaran and P. M. Kyle, “Aetiology and pathogenesis of IUGR”, *Best practice and research: Clinical obstetrics and gynaecology*, vol. 23, no. 6, pp. 765–777, 2009 (→ page 114).

- [286] A. P. Sarvazyan, A. R. Skovoroda, S. Y. Emelianov, J. B. Fowlkes, J. G. Pipe, R. S. Adler, R. B. Buxton, and P. L. Carson, “Biophysical bases of elasticity imaging”, in *Acoustical imaging*, 1995, pp. 223–240 (→ page 33).
- [287] A. Sarvazyan, “Elastic properties of soft tissue”, in *Handbook of Elastic Properties of Solids, Liquids, and Gases*, M. Levy, H. E. Bass, and R. R. Stern, Eds., vol. 3, 2001, ch. 5, pp. 107–127 (→ page 32).
- [288] A. P. Sarvazyan, O. V. Rudenko, S. D. Swanson, J. B. Fowlkes, and S. Y. Emelianov, “Shear wave elasticity imaging: A new ultrasonic technology of medical diagnostics”, *Ultrasound in medicine and biology*, vol. 24, no. 9, pp. 1419–1435, 1998 (→ page 50).
- [289] K. Shoemake, “Animating rotation with quaternion curves”, *ACM SIGGRAPH computer graphics*, vol. 19, no. 3, pp. 245–254, 1985 (→ page 152).
- [290] R. Sinkus, J. Lorenzen, D. Schrader, M. Lorenzen, M. Dargatz, and D. Holz, “High-resolution tensor MR elastography for breast tumour detection”, *Physics in Medicine and Biology*, vol. 45, no. 6, pp. 1649–1664, 2000 (→ pages 53, 70, 78, 166, 194).
- [291] R. Sinkus, M. Tanter, S. Catheline, J. Lorenzen, C. Kuhl, E. Sondermann, and M. Fink, “Imaging anisotropic and viscous properties of breast tissue by magnetic resonance-elastography”, *Magnetic resonance in medicine*, vol. 53, no. 2, pp. 372–387, 2005 (→ pages 34, 168).
- [292] R. Sinkus, M. Tanter, T. Xydeas, S. Catheline, J. Bercoff, and M. Fink, “Viscoelastic shear properties of in vivo breast lesions measured by MR elastography”, *Magnetic Resonance Imaging*, vol. 23, pp. 159–165, 2005 (→ pages 53, 133, 168).
- [293] R. Sinkus, K. Siegmann, T. Xydeas, M. Tanter, C. Claussen, and M. Fink, “MR elastography of breast lesions: Understanding the solid/liquid duality can improve the specificity of contrast-enhanced MR mammography”, *Magnetic Resonance in Medicine*, vol. 58, no. 6, pp. 1135–1144, 2007 (→ page 33).
- [294] A. R. Skovoroda, S. Y. Emelianov, and M. O’Donnell, “Tissue elasticity reconstruction based on ultrasonic displacement and strain images”, *IEEE Transactions on Ultrasonics, Ferroelectrics, and Frequency Control*, vol. 42, no. 4, pp. 747–765, 1995 (→ page 44).

- [295] P. Song, H. Zhao, A. Manduca, M. Urban, J. Greenleaf, and S. Chen, “Comb-push ultrasound shear elastography (CUSE): A novel method for two-dimensional shear elasticity imaging of soft tissues”, *IEEE Transactions on Medical Imaging*, vol. 31, no. 9, pp. 1821–1832, 2012 (→ pages 51, 189).
- [296] T. K. Song and S. B. Park, “A new digital phased array system for dynamic focusing and steering with reduced sampling rate”, *Ultrasonic Imaging*, vol. 12, no. 1, pp. 1–16, 1990 (→ page 20).
- [297] I. Sporea, M. Vlad, S. Bota, R. Sirli, A. Popescu, M. Danila, M. Sendroiu, and I. Zosin, “Thyroid stiffness assessment by acoustic radiation force impulse elastography (ARFI).”, *Ultraschall in der Medizin*, vol. 32, no. 3, pp. 281–285, 2011 (→ page 69).
- [298] S. Srinivasan and J. Ophir, “A zero-crossing strain estimator for elastography”, *Ultrasound in Medicine and Biology*, vol. 29, no. 2, pp. 227–238, 2003 (→ page 39).
- [299] D. D. Steele, T. L. Chenevert, A. R. Skovoroda, and S. Y. Emelianov, “Three-dimensional static displacement, stimulated echo NMR elasticity imaging”, *Physics in Medicine and Biology*, vol. 45, no. 6, pp. 1633–1648, 2000 (→ pages 164, 197).
- [300] R. F. Steidel Jr, *An Introduction to Mechanical Vibrations*, 3rd ed. New York: John Wiley & Sons, 1989 (→ page 195).
- [301] M. Sugitani, Y. Fujita, Y. Yumoto, K. Fukushima, T. Takeuchi, M. Shimokawa, and K. Kato, “A new method for measurement of placental elasticity: Acoustic radiation force impulse imaging”, *Placenta*, vol. 34, no. 11, pp. 1009–1013, 2013 (→ pages 115, 131, 132, 218).
- [302] C. Sumi, “Displacement vector measurement using instantaneous ultrasound signal phase—multidimensional autocorrelation and Doppler methods”, *IEEE Transactions on Ultrasonics, Ferroelectrics and Frequency Control*, vol. 55, no. 1, pp. 24–43, 2008 (→ page 40).
- [303] C. Sumi, “Ultrasonic axial strain measurement for lateral tissue deformation”, *Ultrasound in Medicine & Biology*, vol. 33, no. 11, pp. 1830–1837, 2007 (→ page 198).
- [304] C. Sumi and T. Itoh, “Spatially variant regularization of lateral displacement measurement using variance”, *Ultrasonics*, vol. 49, no. 4–5, pp. 459–465, 2009 (→ page 191).

- [305] C. Sumi, A. Suzuki, and K. Nakayama, “Estimation of shear modulus distribution in soft tissue from strain distribution”, *IEEE Transactions on Biomedical Engineering*, vol. 42, no. 2, pp. 193–202, 1995 (→ page 44).
- [306] T. L. Szabo, *Diagnostic Ultrasound Imaging: Inside Out*, 2nd ed. Oxford: Elsevier, 2014 (→ pages 11, 15).
- [307] H. Takahashi, N. Ono, Y. Eguchi, T. Eguchi, Y. Kitajima, Y. Kawaguchi, S. Nakashita, I. Ozaki, T. Mizuta, S. Toda, *et al.*, “Evaluation of acoustic radiation force impulse elastography for fibrosis staging of chronic liver disease: A pilot study”, *Liver International*, vol. 30, no. 4, pp. 538–545, 2010 (→ page 70).
- [308] A. Tang, G. Cloutier, N. M. Szeverenyi, and C. B. Sirlin, “Ultrasound elastography and MR elastography for assessing liver fibrosis: Part 1, principles and techniques”, *American Journal of Roentgenology*, vol. 205, W1–W11, 2015 (→ page 163).
- [309] M. Tanter and M. Fink, “Ultrafast imaging in biomedical ultrasound”, *IEEE Transactions on Ultrasonics, Ferroelectrics, and Frequency Control*, vol. 61, no. 1, pp. 102–119, 2014 (→ pages 166, 192).
- [310] M. Tanter, J. Bercoff, L. Sandrin, and M. Fink, “Ultrafast compound imaging for 2D motion vector estimation: Application to transient elastography”, *IEEE Transactions on Ultrasonics, Ferroelectrics and Frequency Control*, vol. 49, no. 10, pp. 1363–1374, 2002 (→ pages 40, 49).
- [311] M. Tanter, J. Bercoff, A. Athanasiou, T. Deffieux, J.-L. Gennisson, G. Montaldo, M. Muller, A. Tardivon, and M. Fink, “Quantitative assessment of breast lesion viscoelasticity: Initial clinical results using supersonic shear imaging”, *Ultrasound in medicine and biology*, vol. 34, no. 9, pp. 1373–1386, 2008 (→ page 51).
- [312] L. S. Taylor, B. C. Porter, D. J. Rubens, and K. J. Parker, “Three-dimensional sonoelastography: Principles and practices”, *Physics in medicine and biology*, vol. 45, no. 6, pp. 1477–1494, 2000 (→ pages 46, 88).
- [313] U. Techavipoo, Q. Chen, T. Varghese, and J. A. Zagzebski, “Estimation of displacement vectors and strain tensors in elastography using angular insonifications”, *IEEE Transactions on Medical Imaging*, vol. 23, no. 12, pp. 1479–1489, 2004 (→ pages 40, 204).

- [314] A. Thitaikumar, L. M. Mobbs, C. M. Kraemer-Chant, B. S. Garra, and J. Ophir, “Breast tumor classification using axial shear strain elastography: A feasibility study”, *Physics in medicine and biology*, vol. 53, no. 17, pp. 4809–4823, 2008 (→ page 43).
- [315] S. Tong, H. N. Cardinal, D. B. Downey, and A. Fenster, “Analysis of linear, area and volume distortion in 3D ultrasound imaging”, *Ultrasound in Medicine & Biology*, vol. 24, no. 3, pp. 355–373, 1998 (→ page 139).
- [316] G. E. Trahey, P. D. Freiburger, L. F. Nock, and D. C. Sullivan, “In vivo measurements of ultrasonic beam distortion in the breast”, *Ultrasonic Imaging*, vol. 13, no. 1, pp. 71–90, 1991 (→ page 17).
- [317] G. M. Treece, J. E. Lindop, A. H. Gee, and R. W. Prager, “Freehand ultrasound elastography with a 3-D probe”, *Ultrasound in Medicine and Biology*, vol. 34, no. 3, pp. 463–474, 2008 (→ page 164).
- [318] M. Tsubai, N. Ueno, O. Fukuda, and M. Akiyama, “Development of an ultrasonic probe with measurement of contact pressure distribution”, in *SICE-ICASE International Joint Conference*, 2006, pp. 3827–3830 (→ page 45).
- [319] E. Turgay, S. Salcudean, and R. Rohling, “Identifying the mechanical properties of tissue by ultrasound strain imaging”, *Ultrasound in medicine and biology*, vol. 32, no. 2, pp. 221–235, 2006 (→ pages 47, 49, 195).
- [320] J. Udesen, F. Gran, K. L. Hansen, J. A. Jensen, C. Thomsen, and M. B. Nielsen, “High frame-rate blood vector velocity imaging using plane waves: Simulations and preliminary experiments”, *IEEE Transactions on Ultrasonics, Ferroelectrics, and Frequency Control*, vol. 55, no. 8, pp. 1729–1743, 2008 (→ page 166).
- [321] E. E. W. Van Houten, M. I. Miga, J. B. Weaver, F. E. Kennedy, and K. D. Paulsen, “Three-dimensional subzone-based reconstruction algorithm for MR elastography”, *Magnetic Resonance in Medicine*, vol. 45, no. 5, pp. 827–837, 2001 (→ page 53).
- [322] E. E. Van Houten, M. M. Doyley, F. E. Kennedy, J. B. Weaver, and K. D. Paulsen, “Initial in vivo experience with steady-state subzone-based MR elastography of the human breast”, *Journal of Magnetic Resonance Imaging*, vol. 17, no. 1, pp. 72–85, 2003 (→ page 78).
- [323] J. Vappou, C. Maleke, and E. E. Konofagou, “Quantitative viscoelastic parameters measured by harmonic motion imaging”, *Physics in medicine and biology*, vol. 54, no. 11, pp. 3579–3594, 2009 (→ page 134).

- [324] T. Varghese, J. Ophir, E. Konofagou, F. Kallel, and R. Righetti, “Tradeoffs in elastographic imaging”, *Ultrasonic Imaging*, vol. 23, no. 4, pp. 216–248, 2001 (→ page 179).
- [325] F. Viola and W. Walker, “A spline-based algorithm for continuous time-delay estimation using sampled data”, *IEEE Transactions on Ultrasonics, Ferroelectrics, and Frequency Control*, vol. 52, no. 1, pp. 80–93, 2005 (→ page 39).
- [326] F. Viola and W. F. Walker, “A comparison of the performance of time-delay estimators in medical ultrasound”, *IEEE Transactions on Ultrasonics, Ferroelectrics, and Frequency Control*, vol. 50, no. 4, pp. 392–401, 2003 (→ pages 37, 164).
- [327] R. F. Wagner, S. W. Smith, J. M. Sandrik, and H. Lopez, “Statistics of speckle in ultrasound B-scans”, *IEEE Transactions on Sonics and Ultrasonics*, vol. 30, no. 3, pp. 156–163, 1983 (→ page 11).
- [328] W. F. Walker and G. E. Trahey, “A fundamental limit on delay estimation using partially correlated speckle signals”, *IEEE Transactions on Ultrasonics, Ferroelectrics and Frequency Control*, vol. 42, no. 2, pp. 301–308, 1995 (→ page 203).
- [329] K. Walsh, D. Dumont, M. Palmeri, and B. Byram, “On-axis radiation-force-based quantitative stiffness estimation with a Bayesian displacement estimator”, in *IEEE International Ultrasonics Symposium*, 2015, pp. 1–4 (→ page 50).
- [330] M. Wang, B. Byram, M. Palmeri, N. Rouze, and K. Nightingale, “Imaging transverse isotropic properties of muscle by monitoring acoustic radiation force induced shear waves using a 2-D matrix ultrasound array”, *IEEE Transactions on Medical Imaging*, vol. 32, no. 9, pp. 1671–1684, 2013 (→ page 71).
- [331] ———, “On the precision of time-of-flight shear wave speed estimation in homogeneous soft solids: Initial results using a matrix array transducer”, *IEEE Transactions on Ultrasonics, Ferroelectrics, and Frequency Control*, vol. 60, no. 4, pp. 758–770, 2013 (→ page 71).
- [332] M. Waterstone, S. Bewley, and C. Wolfe, “Incidence and predictors of severe obstetric morbidity: Case-control study”, *BMJ*, vol. 322, no. 7294, pp. 1089–1094, 2001 (→ page 114).

- [333] B. C. Weed, A. Borazjani, S. S. Patnaik, R. Prabhu, M. Horstemeyer, P. L. Ryan, T. Franz, L. N. Williams, and J. Liao, “Stress state and strain rate dependence of the human placenta”, *Annals of biomedical engineering*, vol. 40, no. 10, pp. 2255–2265, 2012 (→ pages 115, 133, 218).
- [334] J. N. Welch, M. Bax, K. Mori, T. Krummel, R. Shahidi, and C. R. Maurer Jr, “A fast and accurate method of ultrasound probe calibration for image-guided surgery”, in *Computer Assisted Radiology and Surgery*, 2002, pp. 1078–1078 (→ page 63).
- [335] J. Weng, P. Cohen, and M. Herniou, “Camera calibration with distortion models and accuracy evaluation”, *IEEE Transactions on Pattern Analysis and Machine Intelligence*, no. 10, pp. 965–980, 1992 (→ page 67).
- [336] A. D. Wiles, D. G. Thompson, and D. D. Frantz, “Accuracy assessment and interpretation for optical tracking systems”, in *Proceedings of SPIE*, vol. 5367, 2004, pp. 421–432 (→ page 67).
- [337] T. Wu, J. P. Felmlee, J. F. Greenleaf, S. J. Riederer, and R. L. Ehman, “MR imaging of shear waves generated by focused ultrasound”, *Magnetic Resonance in Medicine*, vol. 43, no. 1, pp. 111–115, 2000 (→ page 54).
- [338] Z. Wu, L. S. Taylor, D. J. Rubens, and K. J. Parker, “Sonoelastographic imaging of interference patterns for estimation of the shear velocity of homogeneous biomaterials”, *Physics in medicine and biology*, vol. 49, no. 6, pp. 911–922, 2004 (→ page 56).
- [339] Y. Yamakoshi, J. Sato, and T. Sato, “Ultrasonic imaging of internal vibration of soft tissue under forced vibration”, *IEEE Transactions on Ultrasonics, Ferroelectrics, and Frequency Control*, vol. 37, no. 2, pp. 45–53, 1990 (→ pages 42, 54, 70, 78).
- [340] C. X. Yan, B. Goulet, J. Pelletier, S. J.-S. Chen, D. Tampieri, and D. L. Collins, “Towards accurate, robust and practical ultrasound-CT registration of vertebrae for image-guided spine surgery”, *International Journal of Computer Assisted Radiology and Surgery*, vol. 6, no. 4, pp. 523–537, 2011 (→ page 60).
- [341] F. Yeung, S. F. Levinson, D. Fu, and K. J. Parker, “Feature-adaptive motion tracking of ultrasound image sequences using a deformable mesh”, *IEEE Transactions on Medical Imaging*, vol. 17, no. 6, pp. 945–956, 1998 (→ page 167).

- [342] M. Yin, J. A. Talwalkar, K. J. Glaser, A. Manduca, R. C. Grimm, P. J. Rossman, J. L. Fidler, and R. L. Ehman, “Assessment of hepatic fibrosis with magnetic resonance elastography”, *Clinical Gastroenterology and Hepatology*, vol. 5, no. 10, pp. 1207–1213, 2007 (→ page 194).
- [343] M. Yin, O. Rouvière, K. J. Glaser, and R. L. Ehman, “Diffraction-biased shear wave fields generated with longitudinal magnetic resonance elastography drivers”, *Magnetic resonance imaging*, vol. 26, no. 6, pp. 770–780, 2008 (→ pages 4, 71).
- [344] L. Yuan and P. C. Pedersen, “Stress field calculation for quantitative ultrasound elastography via integration of force sensors”, in *IEEE Bioengineering Conference*, 2010, pp. 1–2 (→ page 45).
- [345] R. Zahiri-Azar and S. E. Salcudean, “Motion estimation in ultrasound images using time domain cross correlation with prior estimates”, *IEEE Transactions on Biomedical Engineering*, vol. 53, no. 10, pp. 1990–2000, 2006 (→ pages 37, 81, 164, 171).
- [346] ———, “Time-delay estimation in ultrasound echo signals using individual sample tracking”, *IEEE Transactions on Ultrasonics, Ferroelectrics and Frequency Control*, vol. 55, no. 12, pp. 2640–2650, 2008 (→ page 39).
- [347] R. Zahiri-Azar, O. Goksel, T. S. Yao, E. Dehghan, J. Yan, and S. E. Salcudean, “Methods for the estimation of sub-sample motion of digitized ultrasound echo signals in two dimensions”, in *IEEE Engineering in Medicine and Biology Society*, 2008, pp. 5581–5584 (→ page 39).
- [348] R. Zahiri-Azar, A. Baghani, S. E. Salcudean, and R. Rohling, “2-D high-frame-rate dynamic elastography using delay compensated and angularly compounded motion vectors: Preliminary results”, *IEEE Transactions on Ultrasonics, Ferroelectrics and Frequency Control*, vol. 57, no. 11, pp. 2421–2436, 2010 (→ pages 198, 223).
- [349] R. Zahiri-Azar, O. Goksel, and S. E. Salcudean, “Sub-sample displacement estimation from digitized ultrasound RF signals using multi-dimensional polynomial fitting of the cross-correlation function”, *IEEE Transactions on Ultrasonics, Ferroelectrics, and Frequency Control*, vol. 57, no. 11, pp. 2403–2420, 2010 (→ pages 39, 171).
- [350] R. Zahiri-Azar, A. Baghani, S. E. Salcudean, and R. Rohling, “Frequency-locked pulse sequencer for high-frame-rate monochromatic tissue motion imaging”, *IEEE Transactions on Ultrasonics*,

Ferroelectrics, and Frequency Control, vol. 58, no. 4, pp. 680–684, 2011 (→ pages 166, 192).

- [351] R. Zahiri-Azar, C. Leung, T. K. Chen, K. Dickie, J. Dixon, K.-K. Chan, and L. Pelissier, “An automated breast ultrasound system for elastography”, in *IEEE International Ultrasonics Symposium*, 2012, pp. 1–4 (→ page 194).
- [352] Y. Zhang, A. A. Oberai, P. E. Barbone, and I. Harari, “Solution of the time-harmonic viscoelastic inverse problem with interior data in two dimensions”, *International Journal for Numerical Methods in Engineering*, vol. 92, no. 13, pp. 1100–1116, 2012 (→ page 53).
- [353] H. Zhao, P. Song, D. D. Meixner, R. R. Kinnick, M. Callstrom, W. Sanchez, M. Urban, A. Manduca, J. Greenleaf, and S. Chen, “External vibration multi-directional ultrasound shearwave elastography (EVMUSE): Application in liver fibrosis staging”, *IEEE Transactions on Medical Imaging*, vol. 33, no. 11, pp. 2140–2148, 2014 (→ page 78).
- [354] Y. Zhu, T. J. Hall, and J. Jiang, “A finite-element approach for Young’s modulus reconstruction”, *IEEE Transactions on Medical Imaging*, vol. 22, no. 7, pp. 890–901, 2003 (→ page 45).
- [355] A. Zorgani, R. Souchon, A.-H. Dinh, J.-Y. Chapelon, J.-M. Ménager, S. Lounis, O. Rouvière, and S. Catheline, “Brain palpation from physiological vibrations using MRI”, *Proceedings of the National Academy of Sciences*, vol. 112, no. 42, pp. 12 917–12 921, 2015 (→ page 59).

Appendix A

Index Notation

Index notation provides a useful tool for representing vector and tensor calculus. The indices are written as subscripts to specify a component of a vector (e.g. a_i) or a tensor (e.g. A_{kl}) in a Cartesian coordinate system.

The Einstein summation convention is used for repeated indices. For example, the dot product between two vectors can be represented as

$$a_i b_i = \sum_{i=1}^3 a_i b_i = \mathbf{a} \cdot \mathbf{b}. \quad (\text{A.1})$$

Similarly, the double dot product between tensors can be written

$$A_{ij} B_{ij} = \sum_{i=1}^3 \sum_{j=1}^3 a_{ij} b_{ij} = \mathbf{A} : \mathbf{B}. \quad (\text{A.2})$$

Two symbols which are commonly used are the Kronecker delta symbol,

$$\delta_{ij} = \begin{cases} 0 & i \neq j \\ 1 & i = j \end{cases}, \quad (\text{A.3})$$

and the Levi-Civita symbol

$$\epsilon_{ijk} = 0 \quad \text{if any of } i, j, \text{ or } k \text{ are equal,} \quad (\text{A.4})$$

otherwise

$$\epsilon_{123} = \epsilon_{231} = \epsilon_{312} = -\epsilon_{321} = -\epsilon_{213} = -\epsilon_{132} = 1. \quad (\text{A.5})$$

The Levi-Civita symbol can be used to represent components of the vector cross product

$$\epsilon_{ijk}a_jb_k = (\mathbf{a} \times \mathbf{b})_i. \quad (\text{A.6})$$

Spatial derivatives are represented using a comma between indices. For example

$$u_{i,j} = \frac{\partial u_i}{\partial x_j}. \quad (\text{A.7})$$

The following are representations of common vector calculus operators such as divergence, curl, and the Laplacian in index notation

$$u_{i,i} = \sum_{i=1}^3 \frac{\partial u_i}{\partial x_i} = (\nabla \cdot \mathbf{u})_i, \quad (\text{A.8})$$

$$\epsilon_{ijk}u_{k,j} = (\nabla \times \mathbf{u})_i, \quad (\text{A.9})$$

$$u_{i,jj} = \sum_{j=1}^3 \frac{\partial^2 u_i}{\partial x_j^2} = \nabla^2 \mathbf{u}_i. \quad (\text{A.10})$$

Appendix B

Placenta Study Consent Form

The consent form used for the placenta study in Chapter 3 is provided in the following six pages. Personal information, such as phone numbers and e-mail addresses, has been redacted.



**CHILDREN'S & WOMEN'S HEALTH
CENTRE OF BRITISH COLUMBIA**

AN AGENCY OF THE PROVINCIAL HEALTH SERVICES AUTHORITY

Research Study Information and Consent Form

STUDY TITLE: Shear Wave Absolute VibroElastography in Utero (SWAVE-U)
Phase 1: Definition of the Normal Placenta Elasticity

Principal Investigator: Dr. Jeff Terry, Clinical Assistant Professor
Department of Pathology & Laboratory Medicine
University of British Columbia
Children's & Women's Health Centre of BC
Phone: [REDACTED], ext. [REDACTED]
Email: [REDACTED]

Co-Investigators: Dr. Rob Rohling, Professor
Department of Electrical & Computer Engineering,
University of British Columbia

Dr. Denise Pugash, Clinical Professor
Department of Radiology,
University of British Columbia
BC Women's Health Centre

Dr. Chantal Mayer, Clinical Assistant Professor
Department of Obstetrics and Gynecology
BC Women's Health Centre

Dr. Christof Senger, Clinical Assistant Professor
Department of Pathology & Laboratory Medicine
Children's & Women's Health Centre of BC

1. BACKGROUND & INVITATION

The placenta (afterbirth) is a temporary organ that joins the mother and baby in the womb. Many pregnancy related health problems are linked to the placenta. Ultrasound is a safe, practical, and cost-effective method for examining the placenta. However it is only useful for detecting large abnormalities. During ultrasound, high frequency sound waves bounce off of tissues to create an image. Researchers have recently developed a new system (Shear Wave Absolute VibroElastography (SWAVE)) which could be used with ultrasound to create a different image which reflects the density and elastic properties of the tissue. This could allow doctors to detect more subtle abnormalities and lead to earlier disease diagnosis and treatments. In this study we will collect placentas and examine them to learn what normal placentas look like using this new system (SWAVE).

You have been invited to take part in this research study because you are scheduled to deliver your baby by caesarean section at BC Women's Health Centre and no problems are expected.

2. YOUR PARTICIPATION IS VOLUNTARY

Your participation is voluntary. You have the right to refuse to participate in this study. If you decide to participate now, you may still choose to withdraw from the study at a later date without any negative consequences to the medical care, education, or other services to which you are entitled or are presently receiving. If you do not wish to participate, you do not have to provide any reason.

If you wish to take part in this study, you will be asked to sign this form. Please take time to read the information carefully and to discuss it with your family, friends, and doctor before you decide.

3. WHO IS CONDUCTING THE STUDY?

The study is being conducted by researchers at the Children's and Women's Health Centre of BC and at the University of British Columbia.

4. WHAT IS THE PURPOSE OF THE STUDY?

Currently, we do not know what placentas look like using the SWAVE device. This study will determine what normal placentas look like using SWAVE. We can then use this information as a reference for future studies, which will compare normal placenta images with abnormal placenta images. Together, this knowledge will enable us to determine if SWAVE can be used with ultrasound to detect subtle abnormalities in pregnancy.

5. WHO CAN PARTICIPATE IN THIS STUDY?

You may participate in this study if you are pregnant, with no significant complications, and are scheduled to deliver your child at BC Women's Health Centre. No other conditions need to be met to take part in this study.

You may have been invited to donate your cord blood to Canadian Blood Services(CBS). You may participate in this study without any impact to your CBS donation.

6. WHO SHOULD NOT PARTICIPATE IN THIS STUDY?

If your doctor has told you of an abnormality in your pregnancy, you might not be eligible to participate. The study personnel will be able to determine if you are eligible if you are unsure.

7. WHAT DOES THE STUDY INVOLVE?

Approximately 90 patients will take part in this study. If you agree to take part in the study, we will collect your placenta and examine it using SWAVE. If any clinical investigations of your placenta are needed, these will take place before your placenta is

handed to the study team. Your placenta will then be examined under a microscope and with an ultrasound wand using SWAVE. A small portion of your placenta will then be examined to assess the flow of oxygen. After the study examination, small portions of placental tissue will be kept for quality purposes for approximately 5 years after the study. If you have consented to donate placental tissue to the BC Children's Hospital Biobank (BCCHB), a portion will also be sent there. Otherwise, the remainder of your placenta will be destroyed according to usual hospital procedures.

We will also review your medical records for information about your age, any conditions which might affect your pregnancy (e.g., smoking history, diabetes, high blood pressure). We will also review medical records to collect information about your baby's health including gestational age, birth weight.

No new tests, procedures or visits to your doctor are required for the study. Your participation in this study will not affect your care or your baby's care in any way.

8. WHAT ARE MY RESPONSIBILITIES?

All information required for this study is already collected as part of clinical care. There are no added responsibilities for you to participate in this study.

9. WHAT ARE THE POTENTIAL BENEFITS OF PARTICIPATING?

Neither you nor your child will directly benefit from participating in the study. However, we hope that the results of the study will be useful for examining pregnant women in the future.

10. WHAT ARE THE ALTERNATIVES TO THE STUDY PARTICIPATION?

Participating in this study is voluntary. You may choose not to participate in this study without any affect on the care you receive.

There are also choices available to you when considering how your samples and medical information will be handled at the end of this study. You may donate specimens, including leftover placental tissue, to the BC Children's Hospital Biobank for use in future research. If you are interested in participating in the Biobank, a separate consent form will be provided. Please indicate your choice below as to how you wish to have your samples and medical information handled.

- I have previously signed or would be willing to sign the consent form for the BC Children's Hospital BioBank and I wish to have my samples and medical information deposited in the BC Children's Hospital BioBank for use in future research.
- I wish to have my samples and medical information destroyed at the end of the study.

11. WHAT HAPPENS IF I DECIDE TO WITHDRAW MY CONSENT TO PARTICIPATE?

You may withdraw from this study at any time without giving any reason. If you choose to enter the study and then decide to withdraw at a later time, you have the right to request the withdrawal of your information collected during the study. This request will be respected to the extent possible. Please note however that there may be exceptions where the data and/or samples will not be able to be withdrawn for example where the data and/or sample is no longer identifiable (meaning it cannot be linked in any way back to your identity) or where the data has been merged with other data. If you would like to request the withdrawal of your data and/or samples, please let your study doctor know.

12. WILL MY TAKING PART IN THIS STUDY BE KEPT CONFIDENTIAL?

Your confidentiality will be respected. However, research records and medical records identifying you or your child may be inspected in the presence of the Investigator or her designate and by members of the Children's and Women's Hospital Research Ethics Board for the purpose of monitoring the research. No information or records that disclose your identity will be removed or released without your consent unless required by law.

Your full date and time of delivery will be collected in the study database in order that we can measure the amount of time between delivery and SWAVE examination. This is the only personal identifying information that will be collected in the study database, and care will be taken not to share this information outside of the study team. You will be assigned a unique study number as a participant in this study. This number will not include any personal information that could identify you (e.g., it will not include a Personal Health Number, SIN, name, etc.). This number will be used on any research-related information collected about you during the course of this study, so that your identity as a participant in this study will be kept confidential. Information that contains your identity will remain only with the Principal Investigator and/or designate. A list that matches your name to the unique identifier that is used on your research-related information will not be removed or released without your consent unless required by law.

Your rights to privacy are legally protected by federal and provincial laws that require safeguards to insure that your privacy is respected and also give you the right of access to the information about you and, if need be, an opportunity to correct any errors in this information. Further details about these laws are available on request to your study doctor.

13. WHAT HAPPENS IF SOMETHING GOES WRONG?

By signing this form, you do not give up any of your legal rights and you do not release the study doctor, participating institutions, or anyone else from their legal and professional duties.

14. WHAT WILL THE STUDY COST ME?

There will be no cost to you for participating in the study.

15. WHO DO I CONTACT IF I HAVE QUESTIONS ABOUT THE STUDY DURING MY PARTICIPATION?

If you have any questions or would like further information about this study, you can contact Dr. Jeff Terry at [REDACTED], ext [REDACTED], or [REDACTED].

16. WHO DO I CONTACT IF I HAVE ANY QUESTIONS OR CONCERNS ABOUT MY RIGHTS AS A PARTICIPANT?

If you have any concerns or complaints about your rights as a research participant and/or your experiences while participating in this study, contact the Research Participant Complaint Line in the University of British Columbia Office of Research Ethics by e-mail at [REDACTED] or by phone at [REDACTED] (Toll Free: [REDACTED]).

17. CONSENT TO PARTICIPATE

My signature on this consent form means:

- I have read and understood the participant information and consent form.
- I have been able to ask questions and have had satisfactory responses to my questions.
- I understand that all of the information collected will be kept confidential and that the results will only be used for scientific purposes.
- I understand that my participation in this study is voluntary and that I am completely free to refuse to participate in this study at any time without changing in any way the quality of care that I receive.
- I authorize access to my and my child's medical record and placenta, as described in this consent form.
- I understand that I am not waiving any of my legal rights as a result of signing this consent form.

I will receive a signed copy of this consent form for my own records.

I consent to participate in this study.

Participant's Signature Printed name Date

Signature of person obtaining consent Printed name Date

Language of translation (if applicable): _____

Signature of translator Printed name Date

Appendix C

N-wire Ambiguity

This appendix demonstrates the ambiguity in the transducer orientation based on inter-point distance measures of N-wire features in ultrasound images. The ambiguity makes it difficult to determine the location of the outside edge points of the N-wire in phantom coordinates. One possible solution is presented in Chapter 4. The phantom geometry used in the paper is considered in this appendix while considering different numbers and combinations of N-wires. The figures show renderings of a L14-5/38 linear array to simplify the understanding of each of the slices obtained from the motorized 4DL14-5/38 transducer.

The phantom contains three rows of N-wires as described in the Section 4.2. The inter-point distances (left/right) from the top N-wire to the bottom are 15/20, 21.6/13.4, and 13.1/16.1 mm, matching the distances in Figure 4.5.

First, consider only one N-wire at a time. Using the distances measured in the ultrasound image, a line can be drawn across the N-wire model, where the angled wire cuts the line into two segments with lengths matching the ultrasound measurements. There are two possible lines that can satisfy the measurements. The two lines for each of the three N-wires are shown in Figure C.1. In Figure C.1(a)–(c), the transducer is in the same pose. This happens to be the pose that satisfies the inter-point distances for all three N-wires simultaneously. In Figure C.1(d)–(f), the transducer translates slightly between N-wire choices, and is rotated compared to Figure C.1(a)–(c). It should be noted that the transducer in Figure C.1 can be rotated about the a line’s axis and still satisfy the measurements. The transducer is

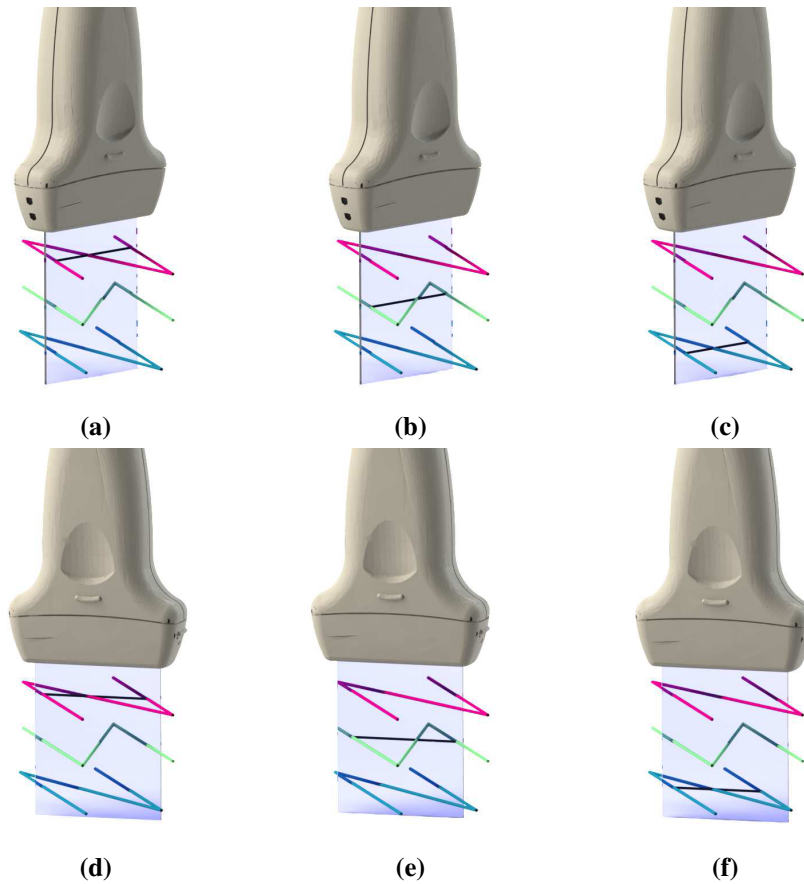


Figure C.1: By observation of the inter-point distances for one N-wire at a time, the transducer orientation can be constrained to rotate about an axis. The inter-point distances allow for two possible axes for each N-wire. For simplicity, the transducer is shown only orthogonal to the plane of the N-wire. The first set of possible axes (black) for the (a) top, (b) middle, and (c) bottom N-wires, and the second set of axes for the (d) top, (e) middle, and (f) bottom.

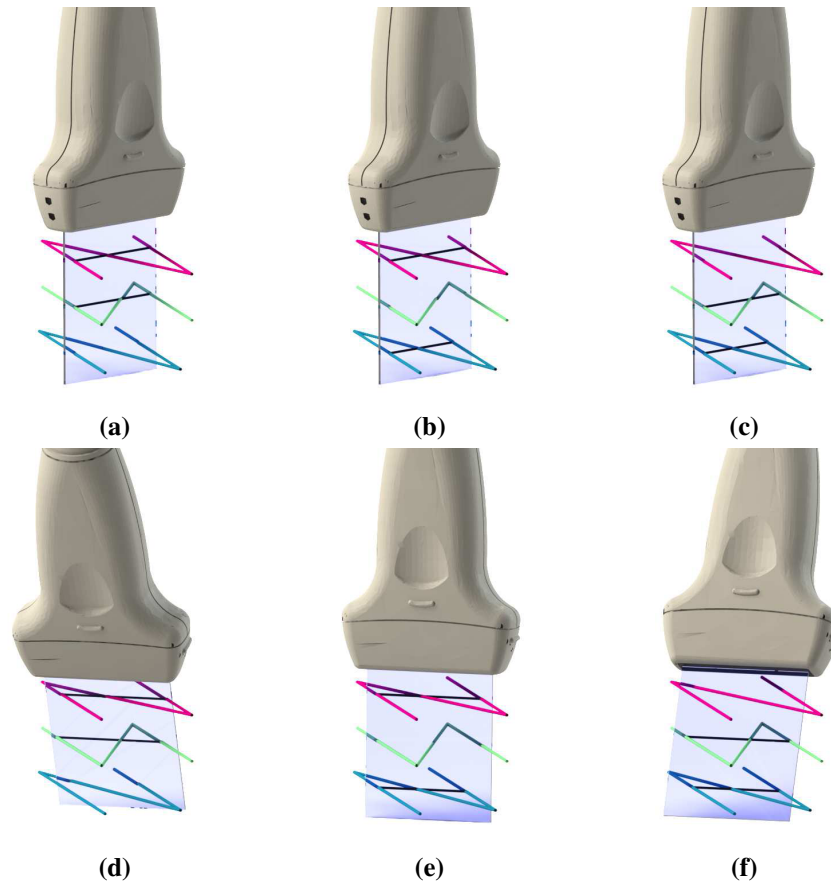


Figure C.2: By observation of the inter-point distances for two N-wires at a time, the transducer orientation can be fully constrained. Only combinations of the axes for each N-wire (black) between two of the first row of Figure C.1 or two of the second row of Figure C.1 are shown, as a plane cannot be fit to two lines for combinations across the rows.

shown only orthogonal to the plane of the N-wires for simplicity. It is clear that since there are multiple transducer poses that satisfy the measurements, the outside edge points cannot be determined.

It is also illustrative to consider more than one N-wire at a time. If two N-wires are considered, then there are 12 possible combinations of the axes from Figure C.1; three choices in N-wires, and two possible axes for each N-wire ($3 \times 2 \times 2 = 12$). However, only six combinations are coplanar. The non-planar combinations are

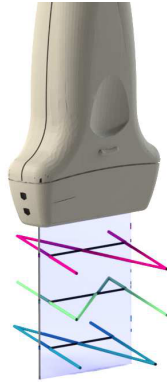


Figure C.3: Observing the inter-point distances for all three N-wires at the same time allows for only one coplanar solution.

not physically realizable because the image is planar. In Figure C.2(a)–(c), the transducer is again in the same pose throughout, which is the correct pose to satisfy all three N-wires simultaneously. In Figure C.2(d)–(f), the transducer clearly needs to change pose to fit the different combinations of two N-wires and would not satisfy all three simultaneously.

Finally, considering all three rows of N-wires at the same time results in only one possible combination that remains coplanar. The solution is presented in Figure C.3. Now that the pose is uniquely defined the outside edge points can be located in the phantom coordinates and included in the corresponding point algorithm for calibration.

Appendix D

Logarithm and Exponential Maps of Dual Quaternions

This appendix describes how to find the logarithm of a dual quaternion of the form

$$\hat{q} = q + \epsilon \frac{1}{2} t q, \quad (\text{D.1})$$

and how to perform the inverse mapping from the tangent space back to the manifold with the exponential mapping. Using Taylor expansion, it is found that Equation D.1 is equivalent to [44]

$$\hat{q} = q e^{\epsilon \frac{1}{2} \vec{t}}. \quad (\text{D.2})$$

The quaternion, q , defined by

$$q = \cos\left(\frac{1}{2}\theta\right) + \sin\left(\frac{1}{2}\theta\right)\vec{u}, \quad (\text{D.3})$$

describes a rotation around the axis \vec{u} by an angle θ . This can be written in the form [13]

$$q = e^{\frac{1}{2}\theta\vec{u}}. \quad (\text{D.4})$$

Then taking the logarithm of Equation D.2

$$\log(\hat{q}) = \frac{1}{2}\theta\vec{u} + \epsilon\frac{1}{2}\vec{t}. \quad (\text{D.5})$$

Now the exponential mapping to the manifold is derived given a dual vector in the dual quaternion tangent space

$$\hat{x} = \frac{1}{2}\vec{a} + \epsilon\frac{1}{2}\vec{b}, \quad (\text{D.6})$$

$$\hat{q} = \exp(\hat{x}). \quad (\text{D.7})$$

Comparing Equation D.6 to Equation D.5, the components of the dual quaternion can be found. Since \vec{u} is a unit vector

$$\theta = \|\vec{a}\|, \quad (\text{D.8})$$

and

$$\vec{u} = \frac{\vec{a}}{\theta}. \quad (\text{D.9})$$

The translation is simply

$$\vec{t} = \vec{b}. \quad (\text{D.10})$$

Now the quaternion can be constructed as in Equation D.3, and the dual quaternion using Equation D.1.

Appendix E

Solving for Geodesic Direction on the Quaternion Manifold

This appendix describes the method for solving for the tangent vector that defines the direction of the best fit geodesic on the quaternion manifold for the $W_{2D \rightarrow 3D}$ calibration method described in Section 4.2.4. The tangent vector is found using a gradient descent algorithm. The initial guess is the tangent vector from the mean quaternion to the last quaternion in the set

$$\vec{v} = \log(q_m^* q_N). \quad (\text{E.1})$$

The objective is to minimize the sum of the geodesic distances between the quaternion sample points and the best fit geodesic. However, since the sample points are all located near the mean, the geodesic distance can be approximated in the tangent space. The quaternions are mapped to the tangent space at q_m

$$\vec{p}_i = \log(q_m^* q_i). \quad (\text{E.2})$$

Now we need to minimize the sum of the orthogonal distances between the \vec{p}_i and

the line described by \vec{v} . The squared distance can be computed using

$$\begin{aligned} d_i^2 &= \frac{\|\vec{v} \times \vec{p}_i\|^2}{\|\vec{v}\|^2} \\ &= \frac{\|[\vec{p}_i]_{\times}^T \vec{v}\|^2}{\|\vec{v}\|^2}, \end{aligned} \quad (\text{E.3})$$

where \times represents the cross product operator, and $[\cdot]_{\times}$ is a skew symmetric matrix. To minimize the distances, we require the gradient of (E.3). If we let $h = \|[\vec{p}_i]_{\times}^T \vec{v}\|^2$, and $g = \|\vec{v}\|^2$, then the familiar quotient rule results in

$$\frac{d(d_i^2)}{d\vec{v}} = \frac{\frac{dh}{d\vec{v}}g - \frac{dg}{d\vec{v}}h}{g^2}. \quad (\text{E.4})$$

The derivatives of h and g are given by

$$\frac{dh}{d\vec{v}} = 2 [\vec{p}_i]_{\times} [\vec{p}_i]_{\times}^T \vec{v}, \quad (\text{E.5})$$

and

$$\frac{dg}{d\vec{v}} = 2\vec{v}. \quad (\text{E.6})$$

It would be convenient to parametrize the geodesic in (4.13) such that the scalar parameter $t \in [0, 1]$, with 0 corresponding to the start of the geodesic path, 0.5 at the mean quaternion, and 1 at the end of the path. However, \vec{v} is arbitrarily scaled and is located at q_m . We can instead define a new scalar parameter, s , as a function of t which uses the projections of the first and last quaternions mapped to the tangent space onto \vec{v}

$$s(t) = a + t(b - a), \quad (\text{E.7})$$

where

$$a = \frac{\vec{p}_1 \cdot \vec{v}}{\|\vec{p}_1\| \|\vec{v}\|}, \quad (\text{E.8})$$

and

$$b = \frac{\vec{p}_N \cdot \vec{v}}{\|\vec{p}_N\| \|\vec{v}\|}. \quad (\text{E.9})$$

Now the best fit geodesic can be described by

$$q = q_m \exp (s\vec{v}) . \quad (\text{E.10})$$

The distance metric, as described in Equation E.3, for solving for the direction of the best fit geodesic is bi-invariant (i.e. independent of the choice of coordinate system). For an arbitrary quaternion, a , left-invariance is shown by left multiplying all of the quaternions by a and demonstrating that the distance is the same as without a . The initial guess for the direction is given by

$$\begin{aligned} \vec{v} &= \log ((aq_m)^* aq_N) \\ &= \log (q_m^* a^* aq_N) \\ &= \log (q_m^* q_N) , \end{aligned} \quad (\text{E.11})$$

which is the same as in Equation E.1. Similarly, the quaternions mapped to the tangent space at q_m are

$$\begin{aligned} \vec{p}_i &= \log (q_m^* a^* aq_i) \\ &= \log (q_m^* q_N) . \end{aligned} \quad (\text{E.12})$$

Since both \vec{v} and \vec{p}_i are the same, d_i^2 as defined in Equation E.3 must also be the same.

Demonstrating right-invariance is more involved. The initial guess for the direction is now given by

$$\begin{aligned} \vec{v} &= \log ((q_m a)^* q_N a) \\ &= \log (a^* q_m^* q_N a) , \end{aligned} \quad (\text{E.13})$$

and the tangent points by

$$\vec{p}_i = \log (a^* q_m^* q_i a) . \quad (\text{E.14})$$

Note, inside the logarithm the composition of q_m^* and q_i is undergoing rotation by a^* . Since the magnitude of the angle described by $q_m^* q_i$ is unaffected by rotation, only the direction of the rotation axis changes, therefore

$$\log (a^* q_m^* q_i a) = a^* \log (q_m^* q_i) a . \quad (\text{E.15})$$

Now the distance metric becomes

$$d_i^2 = \frac{\| (a^* \log (q_m^* q_N) a) \times (a^* \log (q_m^* q_i) a) \|^2}{\| a^* \log (q_m^* q_N) a \|^2} . \quad (\text{E.16})$$

Recall for two vectors, \vec{x} and \vec{y} , their cross product is

$$\vec{x} \times \vec{y} = \|\vec{x}\| \|\vec{y}\| \sin(\theta) \vec{n} . \quad (\text{E.17})$$

Since the length of the vectors and the angle between them is unaffected by rotation, applying a rotation with matrix R to the two vectors results in the following cross product

$$\begin{aligned} (R\vec{x}) \times (R\vec{y}) &= \|\vec{x}\| \|\vec{y}\| \sin(\theta) R\vec{n} \\ &= R(\vec{x} \times \vec{y}) . \end{aligned} \quad (\text{E.18})$$

Therefore Equation E.16 can be rewritten as

$$\begin{aligned} d_i^2 &= \frac{\| a^* (\log (q_m^* q_N) \times \log (q_m^* q_i)) a \|^2}{\| a^* \log (q_m^* q_N) a \|^2} \\ &= \frac{\| \log (q_m^* q_N) \times \log (q_m^* q_i) \|^2}{\| \log (q_m^* q_N) \|^2} , \end{aligned} \quad (\text{E.19})$$

as desired.

For the fitting procedure used in Chapter 4 to interpolate between calibrations, location and orientation were fit separately. It would seem natural to try to find a

best fit through the rigid body motions described by the calibrations for different slices. Unfortunately there are no bi-invariant Riemannian metrics for rigid body motions in the group $SE(3)$ [192]. Thus a compromise would be required, such as choosing a left-invariant metric [244], or approximating $SE(3)$ with the special orthogonal group, $SO(4)$, which contains bi-invariant metrics [100].

The method for finding the direction of the best fit geodesic relies on a linear approximation of the manifold at the mean to calculate the objective function using Equation E.3. The actual geodesic distance is

$$d_i = \|\log(q_i^* q_m \exp(\log(q_m^* q_i) \cdot \vec{v}))\|. \quad (\text{E.20})$$

Calculating the gradient of this distance is significantly more complicated. The linear approximation using the tangent space can be justified by the closeness of the sample points to the mean. The total sweep angle is approximately $\pm 15^\circ$ from the mean, and assuming good calibration results, the samples will lie within a few degrees of the best fit geodesic. principal geodesic analysis (PGA), which is a generalization of PCA from Euclidean to manifold settings, uses the same approximation with the same justification [107]. In fact, PGA can be used as an alternative to the gradient descent algorithm presented in this paper for finding the direction of greatest variance, which should correspond to the direction of the data. The algorithm starts by finding the mean quaternion and the tangent points at the mean as before. Then the covariance matrix is constructed with

$$\mathbf{C} = \frac{1}{N} \sum_{i=1}^N p_i p_i^T. \quad (\text{E.21})$$

The tangent vector of the best fit geodesic is the eigenvector corresponding the largest eigenvalue of \mathbf{C} , which can be found using Singular Value Decomposition. In practice, it was found that the tangent vector found using PGA was equivalent to the one found using gradient descent to the sixth significant figure after normalization, with the advantage of PGA being 100 times faster to calculate.

Appendix F

Simulation Test of Rotation Fitting Algorithm

This appendix describes a simulation which was used to evaluate the rotation fitting algorithm from Chapter 4 for the $W_{2D \rightarrow 3D}$ calibration interpolation. A set of $n = 8$ quaternions was generated, evenly spaced along a geodesic, starting at the identity rotation, $q_1 = [1, 0, 0, 0]^T$, and following a rotation about the z -axis, $\vec{w} = [0, 0, \pi/4]^T$. Error for each quaternion was simulated with an isotropic Gaussian distribution, with standard deviation σ , in the tangent space, $\vec{\epsilon}$. Thus, each noisy quaternion is described by

$$q_i = q_1 \exp(t_i \vec{w}) \exp(\vec{\epsilon}), \quad (\text{F.1})$$

where $i \in [1 \dots n]$, and

$$t_i = \frac{i-1}{n-1}. \quad (\text{F.2})$$

To evaluate the performance of the fit, an error metric was defined as the geodesic distance between the last quaternion in the simulated set, and the same quaternion using the best fit geodesic

$$E = \|\log((q_1 \exp(\vec{w}))^* (q_m \exp(\vec{v})))\|. \quad (\text{F.3})$$

The simulation was run for three different values of σ ; $\pi/32$, $\pi/16$, and $\pi/8$. As

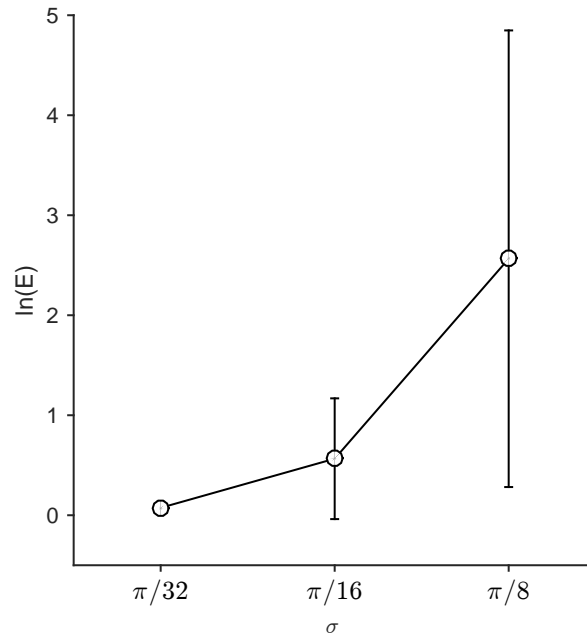


Figure F.1: Plot of the mean and standard deviation of the best fit geodesic error metric after taking the natural logarithm of the set to transform the distribution closer to normal. The values are plotted for three different levels of simulated Gaussian noise, with standard deviation σ , on the eight quaternions used for fitting after 1000 simulation trials for each noise level.

σ is increased, it is expected that the mean and standard deviation of E should also increase. The Log-normal distribution of E provided the best statistical model fit (based on the minimum information theoretical criterion estimate [9]). The mean and standard deviation of E after 1000 simulations for the three different levels of σ are shown in Figure F.1. To visualize the effectiveness of the proposed fitting method in the presence of noise, axes indicating orientation defined by each quaternion are plotted for the noiseless, noisy, and estimated geodesic quaternions for one of the simulations at $\sigma = \pi/16$ in Figure F.2. These results give confidence in the proposed quaternion-based method.

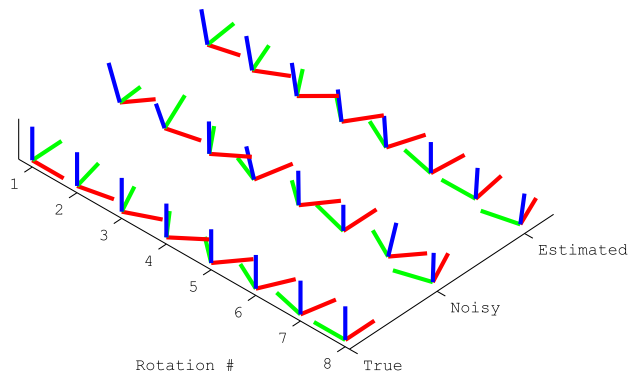


Figure F.2: A visual demonstration of fitting the rotation samples with axes indicating the rotation orientation. The true rotations are equally sampled along a 90 degree rotation about the z -axis. The noisy rotations have isotropic Gaussian noise ($\sigma = \pi/16$) applied to each sample. After fitting the best fit geodesic curve to the noisy samples, eight equally spaced rotations are interpolated from the curve to provide the estimated rotations.

Appendix G

Linear Least Squares Displacement Gradient

This appendix describes a method for calculating the gradient of a scalar field over a small 3D region using linear least squares. This method is used in Chapter 6 for the estimation of displacement gradients in the elasticity inversion algorithm.

Given one of the displacement components, \mathbf{u}_γ , along the γ^{th} direction over a small region of size $n_x \times n_y \times n_z$, the spatial gradient is desired

$$\nabla \mathbf{u}_\gamma = \begin{bmatrix} \frac{\partial \mathbf{u}_\gamma}{\partial r_x} \\ \frac{\partial \mathbf{u}_\gamma}{\partial r_y} \\ \frac{\partial \mathbf{u}_\gamma}{\partial r_z} \end{bmatrix}, \quad (\text{G.1})$$

where \mathbf{r} represents spatial location, defined locally in the region. The derivatives are modelled as partial slope coefficients which fit a hyperplane to the displacement data

$$\mathbf{u}_\gamma = m_x \mathbf{r}_x + m_y \mathbf{r}_y + m_z \mathbf{r}_z + b, \quad (\text{G.2})$$

where b is an offset parameter for the fitted hyperplane. The problem is stated in matrix form as finding the least squares solution to

$$\mathbf{A}\mathbf{g} = \mathbf{u}_\gamma, \quad (\text{G.3})$$

where

$$\mathbf{g} = \begin{bmatrix} b \\ m_x \\ m_y \\ m_z \end{bmatrix}, \quad (\text{G.4})$$

$$\mathbf{A} = \begin{bmatrix} \mathbf{e}_{n_x n_y n_z \times 1} & \mathbf{r}_x & \mathbf{r}_y & \mathbf{r}_x \end{bmatrix}, \quad (\text{G.5})$$

and \mathbf{e} is a vector of ones. Thus the linear least squares gradient over the region is

$$\mathbf{g} = (\mathbf{A}^T \mathbf{A})^{-1} \mathbf{A}^T \mathbf{u}_y. \quad (\text{G.6})$$